

A Thermoplasmonic Platform for Investigating Membrane Repair

Helena Maria Dávidsdóttir Danielsen

PhD Thesis

Abstract

The cell membrane is crucial for cell survival, and ensuring its integrity is essential as the cell experiences injuries throughout its entire life cycle. To maintain cell viability, cells have developed robust plasma membrane repair (PMR) mechanisms. Notably, a deficiency in PMR has been associated with several diseases, such as muscular dystrophies, whereas enhanced PMR, as seen in cancer cells, enables them to cope with the physical stress imposed during migration and invasion.

Despite extensive efforts, the activation and function of the complex PMR machinery remain enigmatic. Nevertheless, numerous mechanisms have been proposed, among which a subset of different proteins have been identified as members of the PMR machinery. Notably, the annexin protein family appears to play a pivotal role in plasma membrane repair processes, with several members being recruited to the site of injury following membrane puncture. To study the intricate repair mechanisms in a near-native environment, an optical platform was developed utilizing thermoplasmonic heating. This platform offers an alternative approach to investigating the plasma membrane repair machinery by locally disrupting membranes without causing extensive damage to the cell.

The findings suggest that the recruitment of annexin A5 (ANXA5) and annexin A2 (ANXA2) is crucial for the process of wound resealing following thermoplasmonic rupture. Specifically, the findings revealed that ANXA5 and ANXA2 were rapidly recruited to the perimeter of the membrane wound, where they formed scaffolds, potentially as part of the PMR machinery. Additionally, a substantial calcium influx was observed as a prerequisite for the activation of ANXA. Despite reports of ANXA5-induced curvature and rolling of model membranes, the geometry of the formed ANXA ring structures remained constant over time and space, indicating that their suggested biophysical functions may be partially inhibited in living cells by the actin cytoskeleton. However, following the thermoplasmonic rupture of cells overexpressing ANXA2, in which the actin cytoskeleton had been disrupted, distinctive changes in the membrane morphology surrounding the wound were observed as a direct biophysical effect of ANXA2, highlighting its correlation with the cortical actin.

Additionally, the thermoplasmonic approach was further developed and used to facilitate intracellular membrane ruptures. The response of actin to nuclear envelope disruption was investigated, revealing a large-scale reorganization of the actin cytoskeleton both during and after disruption. The findings also revealed that the rapid actin polymerization in the perinuclear region was not solely dependent on elevated intracellular calcium levels, but specifically on extracellular calcium influx prior to its assembly. Overall, the thermoplasmonic method holds great potential for studying both plasma membrane and nuclear membrane repair, two intricate processes that are essential for the viability of metastatic cancer cells and may contribute to the development of novel therapeutic strategies.

Abstrakt (Danish)

Cellemembranen er afgørende for cellens overlevelse, og det er vigtigt at sikre dens integritet, da cellen udsættes for skader gennem hele sin levecyklus. For at opretholde cellens vitalitet har cellerne udviklet robuste plasma membran reparations (PMR) mekanismer. Svækkelse af PMR er blevet forbundet med sygdomme, så som muskelsvind, mens en forstærket PMR, som set i cancerceller, gør dem i stand til at håndtere den fysiske belastning, som de udsættes for under migration og invasion. På trods af omfattende forskning, er aktivering og funktionen af det komplekse PMR-maskineri fortsat enigmatisk. Ikke desto mindre, er der blevet foreslået adskillige mekanismer, hvoraf en række forskellige proteiner er blevet identificeret som værende en del af PMR-maskineriet. Især annexin-protein familien lader til at spille en central rolle i plasmamembranreparationsprocesser, idet flere annexin medlemmer rekrutteres til den beskadigede membran, som følge af punktering af membranen. For at studere de intrikate reparationsmekanismer i et næsten naturligt miljø, blev en optisk platform udviklet på basis af termoplasmonisk opvarmning. Denne platform tilbyder en alternativ metode til undersøgelse af plasmamembran reparationsmaskineriet ved lokal beskadigelse af membraner, uden at beskadige cellen i større omfang.

Resultaterne tyder på, at rekrutteringen af annexin A5 (ANXA5) og annexin A2 (ANXA2) er afgørende for genlukningen af membranlæsionen efter termoplasmonisk ruptur. Helt specifikt viste resultaterne, at ANXA5 og ANXA2 hurtigt blev rekrutteret til perimeteren af læsionen, hvor de dannede scaffolds, potentielt som en del af PMR-mekanismen. Desuden blev der observeret et betydeligt calcium-influx som en forudsætning for aktivering af ANXA. På trods af beretninger om ANXA5-induceret krumning og rulning af modelmembraner, forblev geometrien af de dannede ANXA-ringstrukturer konstant over tid og rum. Dette indikerer, at deres foreslåede biofysiske funktion kan være delvist hæmmet i levende celler af aktin-cytoskelettet. Ved termoplasmonisk punktering af celler som overudtrykte ANXA2, hvori aktin-cytoskelettet var opløst, blev der desuden observeret karakteristiske ændringer i membranmorfologien omkring læsionen som en direkte biofysisk effekt af ANXA2, hvilket fremhæver dets korrelation med aktin-cytoskelettet.

Den termoplasmoniske metode blev videreudviklet og anvendt til at punktere intracellulære membraner. Aktinets respons til punktering af kernemembranen blev undersøgt, hvilket afslørede en omfattende reorganisering af aktin-cytoskelettet både under og efter den mekaniske disruption. Resultaterne viste også, at den hurtige aktinpolymerisering i den perinukleare region ikke kun var betinget af en forhøjet intracellulære calcium koncentration, men specifikt af ekstracellulært calcium influx forud for aktinsamlingen. Samlet set rummer den termoplasmoniske metode et stort potentiale til at studere både plasmamembran og kernemembran reparation, to intrikate processer, som er afgørende for overlevelsen af metastaserende kræftceller, og som kan bidrage til udviklingen af unikke terapeutiske strategier.

Acknowledgments

First and foremost, I would like to extend my sincere appreciation to my supervisor, Pól Martin Bendix, who not only gave me the incredible opportunity to pursue my career in the field of experimental science but also for his constant support, immense patience, and encouragement throughout my PhD journey. Your enthusiasm for all aspects of science has been a great source of inspiration for me.

Also, a huge thanks to all the people at the Experimental Biophysics and Optical Manipulation group — both current and former members. You have all been a highlight of my PhD journey, and I appreciate every little discussion, whether scientific or personal. My research would have been impossible without the aid and support from each and every one of you.

A special thanks to Christopher and Safia, whom I have had the privilege of supervising during my time at the Niels Bohr Institute. You have given me invaluable scientific inputs and taught me a lot more than you are probably aware of. I would also like to thank Younes and Guillermo, two exceptional scientists who have been a tremendous source of inspiration to me. In addition, I would also like to extend my heartfelt gratitude to my former and present OT crew, including Pavlina, Alba, Veneta, Hazal, Pablo, Natascha, and Christoffer. You have been an incredible support system throughout my PhD journey, from our shared frustrations to the scientific discussions that kept me on my toes and the chats that kept me sane. Your company, laughter, and conversations have been an essential part of my life in the lab.

I have had the pleasure of collaborating with an incredibly talented group of people throughout several of my projects. I would like to extend my sincere gratitude to Kristina Ganzinger, who hosted me at her lab for four months and introduced me to the fascinating field of immunology, where I learned more than I could have ever bargained for. A special shout-out to the Ganzinger gang, who made my stay invaluable; Nebojsa, your invaluable knowledge and endless brainstorming sessions were truly inspiring. Guusje, thank you for our great teamwork, for our early mornings in the cell lab, for endless cups of coffee (or tea in my case), and for all the laughs. To my jungle officemates, Chris and Chi, thank you for always making my day great. A huge shout-out to Lori, thank you for your encouragement, constant support, hilarious anecdotes, and friendship. And a special thanks to the Amsterdam-residing, former OT crew member and friend, Irene, for your crazy ideas, our countless laughs and discussions, and your encouragement to live life to the fullest.

Additionally, I would like to extend my thanks to Jesper Nylandsted and his team at the

Danish Cancer Society Research Center (DCRC) for their collaboration. A special thanks to the dedicated scientist, Malene, for your invaluable help, support, and insightful discussions on the numerous topics related to annexin and actin, as well as for the great pep talks during those long evenings of nuclear envelope puncture experiments in the basement, while attempting to solve world issues one laser irradiation at a time.

Last but not least, nothing of this could have been possible without my incredible partner, Emma. Thank you for your unwavering support, patience, love, and encouragement, all of which have made it possible for me to pursue my passion within experimental science. To my dearest friends, Idunn, Ida, and Lisa, thank you for your endless support, laughter, and companionship, which have kept me going through the ups and downs of the PhD life. And finally, to my family; my brother Dánjal, thank you for always being there for me, listening to me, and sharing your wisdom and encouragement. To my parents, Sunnvør and Dávid, thank you for believing in me and supporting me in all my endeavors, even the crazier ones.

Abstract	ii
Abstrakt (Danish)	iii
Acknowledgments	v
Contents	vi
List of figures	ix
List of Publications	xi
1 Introduction	2
1.1 Motivation	2
1.2 Biophysics of the cell surface	3
1.2.1 Mechanics of plasma membrane repair	5
1.2.2 Investigations of plasma membrane disruption	6
2 Optics	9
2.1 Optical trapping and imaging of nanoheaters	9
2.1.1 Principles of optical trapping	9
2.2 Thermoplasmonics	12
2.3 Confocal imaging of cells and nanoparticles	17
3 Annexins	21
3.1 Annexins as key regulators in membrane repair	21
3.2 The ANXA response to thermoplasmonic-induced membrane disruption	29
3.3 Annexin A5 response to plasma membrane rupture	34
3.3.1 Annexin A5 mediated repair	34
3.3.2 Analysis of ANXA5 at the wound perimeter	36
3.3.3 The alternative PMR "pocket" model	39
3.3.4 AuNP encapsulation within ANXA5 rings	40
3.3.5 ANXA4 response to intracellular membrane disruption	42
3.3.6 Concluding remarks	44
3.4 Annexin A2 response to plasma membrane rupture	47
3.4.1 Annexin A2 mediated repair	47
3.4.2 Analysis of ANXA2 at the wound perimeter	48
3.4.3 The PMR funnel model	50
3.4.3.1 Wound insight through imaging of extracellular dye	52

3.4.4	Actin disruption by inhibition of actin polymerization	53
3.4.4.1	Analysis of ANXA2 to actin disruption	54
3.4.5	The Annexin flower	55
3.4.5.1	Strategies for wound closure	56
3.4.6	The Annexin flower in three dimensions	57
3.4.6.1	ANXA2-membrane bridges	59
3.4.7	Wound closure and calcium imaging	62
3.4.7.1	Analysis of calcium influx	63
3.4.7.2	The three scenarios	63
3.4.8	Concluding remarks	67
4	Actin and the nuclear envelope	70
4.1	The nuclear envelope	70
4.2	Endocytosis of gold nanoparticles	71
4.3	Actin structure and function	73
4.4	The experimental conditions	74
4.5	Actin response to internal membrane disruption	75
4.6	Actin mechanosensing upon plasma membrane disruption	78
4.7	Nuclear envelope disruption	80
4.7.1	Simultaneous nuclear envelope and plasma membrane disruption	80
4.7.2	Exclusive disruption of the nuclear envelope	82
4.8	Concluding remarks	84
5	Synapse formation and T-cell activation	87
5.1	The immune system	87
5.1.1	T-cells	88
5.1.1.1	The importance of butyrophilins for phosphoantigen sensing	90
5.1.1.2	T-cell activation	90
5.2	The research objective	91
5.3	The novel experimental platform	91
5.4	Exploring the formation of immunological synapses	93
5.4.1	T-cell recognition and response to tumor cells	95
5.4.1.1	The active search for tumor cells	96
5.4.2	Immunological synapse formation upon tumor cells interaction	98
5.4.2.1	Modified immune receptors facilitate tumor interaction	100
5.4.3	T-cell interaction with GPMVs derived from tumor cells	102
5.4.3.1	BTN3A1 localization on tumor cell membranes	104
5.5	Concluding remarks	106
6	Conclusion and future work	108

Bibliography	113
Appendices	128
A Supplementary Figures	129
B Publications	133

List of Figures

1.1	The plasma membrane	4
2.1	The principles of optical trapping	10
2.2	Thermoplasmonic heating	12
2.3	The principles of light-to-heat conversion	15
2.4	The absorption cross-section and its associated temperature profile	16
2.5	The experimental setup	18
3.1	Annexin-mediated PMR models	25
3.2	Model membrane patches exposed to ANXA5 and ANXA2	26
3.3	Structure and function of ANXA5	28
3.4	The thermoplasmonic approach and ANXA response	32
3.5	The biophysical effect of ANXA5	35
3.6	Analysis of ANXA5 ring sizes	36
3.7	Analysis of ANXA5 rings in 3D	37
3.8	Analysis of ANXA5 ring evolution	38
3.9	The ANXA5-mediated PMR "pocket" model	39
3.10	Actin response to PM injury	40
3.11	AuNPs locate within ANXA5 ring structures	41
3.12	ANXA4 response to nuclear envelope disruption	43
3.13	Plasma membrane disruption by nanobubble formation	46
3.14	The biophysical effect of ANXA2	48
3.15	Statistical comparison of ANXA5 and ANXA2 ring sizes	49
3.16	The PMR "funnel" model	51
3.17	Insight into the content within the wound	53
3.18	Inhibition of actin polymerization in cells	54
3.19	Time evolution of the Annexin flower	55
3.20	The Annexin flower in three dimensions	58
3.21	ANXA2-membrane bridges	59
3.22	ANXA2 mediated membrane aggregation	61
3.23	Calcium influx upon plasma membrane rupture	64
3.24	Calcium influx and ANXA2 translocation upon plasma membrane rupture	65
3.25	Calcium influx upon plasma membrane rupture induced cell death	67
4.1	The nuclear envelope	71
4.2	Endocytosis of AuNPs	73
4.3	Actin response to nuclear membrane disruption	76
4.4	Actin response to plasma membrane disruption	79

4.5	Actin response to the nuclear envelope and plasma membrane disruption	81
4.6	Actin response to exclusive nuclear envelope disruption	83
5.1	Schematic illustration of a T-cell and a tumor cell	89
5.2	The 2D membrane-derived experimental platform	92
5.3	A simplified model for T-cell activation upon tumor cell interaction	94
5.4	T-cell sensing via finger-like protrusions	97
5.5	Immunological synapse formation	98
5.6	T-cell response upon $\gamma\delta$ TCR modification	100
5.7	The GPMV experimental condition	103
5.8	T-cell interaction with GPMV surface	104
5.9	BTN localization upon vesiculation	106
A.1	ANXA rings surrounding plasma membrane injuries	129
A.2	Fractions of ANXA rings surrounding plasma membrane injuries	129
A.3	ANXA5 and ANXA4 response to GUV puncture	130
A.4	ANXA2 filled vesicles protruding from the injury site	130
A.5	RFP quenching upon NIR laser irradiation	131
A.6	T-cell behavior in the absence and presence of tumor cells	131
A.7	The speculated cytotoxic attribute of T-cells	132

List of Publications

2020 *Interdisciplinary synergy to reveal mechanisms of annexin-mediated plasma membrane shaping and repair*

Poul Martin Bendix, Adam Cohen Simonsen, Christoffer D. Florentsen, Swantje Christin Häger, Anna Mularski, Ali Asghar Hakami Zanjani, Guillermo Moreno-Pescador, Martin Berg Klenow, Stine Lauritzen Sønder, [Helena M. Danielsen](#), Mohammad Reza Arastoo, Anne Sofie Heitmann, Mayank Prakash Pandey, Frederik Wendelboe Lund, Catarina Dias, Himanshu Khandelia, and Jesper Nylandsted.

Cells 9 (4), 1029

2022 *Thermoplasmonic nano-rupture of cells reveals annexin V function in plasma membrane repair*

Guillermo S. Moreno-Pescador, Dunya S. Aswad, Christoffer D. Florentsen, Azra Bahadori, Mohammad R. Arastoo, [Helena Maria D. Danielsen](#), Anne Sofie B. Heitmann, Theresa L. Boye, Jesper Nylandsted, Lene B. Oddershede, and Poul Martin Bendix.

Nanoscale 14, 7778-7787

2023 *A thermoplasmonic approach for the investigation of plasma membrane repair in living cells and model membranes*

[Helena Maria D. Danielsen](#), Mohammad Reza Arastoo, Guillermo Moreno-Pescador, and Poul Martin Bendix

Journal of Visualized Experiments. Submitted: April 2023

1

Introduction

1.1 Motivation

Cancer is a pervasive and debilitating disease that poses a significant global health challenge, affecting millions of people each year. The World Health Organization has reported that cancer is one of the leading causes of death worldwide, with an estimated 10 million deaths attributed to the disease in 2020 alone[1]. In Denmark, the yearly report on cancer estimates that one out of three people will receive a cancer diagnosis before the age of 75, with more than 50% experiencing secondary effects following recovery[2]. These statistics underscore the urgent need for a better understanding of the mechanisms underlying malignant tumor growth and metastases.

Detecting and treating cancer is a complex process, where one of the primary obstacles is the ability of cancer cells to evade detection by the immune system. This evasion is partly due to the fact that cancer cells often share a similar surface repertoire with the cells from which they originate, making it difficult for the immune system to recognize them as foreign invaders. T-cells have been established as an essential component of the immune system owing to their ability to identify cancer cells through the recognition of specific antigens presented on the tumor surface. These immune cells can initiate cancer cell death through the formation of immunological synapses, which are specialized connections between the two cells[3]. The T-cells are activated as they engage with an antigen-presenting cancer cell, which in turn triggers various signaling cascades involving rapid cytoskeleton rearrangements and cytosolic calcium elevations, which are vital for T-cell activation and the immune response against cancer. This is followed by the recruitment of additional immune cells into the tumor microenvironment, where the secretion of cytotoxic molecules culminates in the death of cancer cells[4]. Therefore, T-cells are pivotal in both identifying and eliminating cancer cells. In Chapter 5, the mechanism of T-cell activation was investigated in an effort to advance the understanding of $\gamma\delta$ T-cell synapse formation and ultimately $\gamma\delta$ T-cell-based immunotherapies.

Metastasis is a hallmark feature of cancer and involves the migration of cancer cells from their primary site to colonize distant organs[5]. During this invasion, cancer cells experience physical stress and deformations, which can cause damage to both the plasma membrane

and nuclear membrane. To overcome these lesions, cancer cells have developed an enhanced plasma membrane repair (PMR) machinery. One of the key components involved in PMR is the annexin protein family, which is activated upon cytosolic calcium elevations and has been proposed to play a major role in PMR by, e.g., preventing wound expansion and inducing membrane resealing by vesicle fusion[6]. In particular, the biophysical response of Annexin A5 and Annexin A2 was studied in Chapter 3 after the plasma membrane was locally disrupted by thermoplasmonic heating. Notably, the PMR machinery maintains the membrane integrity of all cells, where a deficiency in PMR has been associated with several diseases, such as muscular dystrophies, where a failure to repair repeated membrane lesions leads to progressive muscle wasting. In contrast, an enhanced PMR, as for cancer cells, helps them cope with the physical stress imposed during invasion[7]. Moreover, the rapid and dynamic cortical actin cytoskeleton has been identified as another key component in PMR, where it both provides structural support and facilitates membrane repair and reconstruction[8]. In Chapter 4, the actin response was investigated upon membrane rupture, particularly by nuclear envelope disruption, revealing a large-scale reorganization of the actin cytoskeleton and a correlation between actin recruitment and the extent of cytosolic calcium elevation.

In summary, the exploration of the mechanisms underlying the activation of T-cells, along with annexin and actin-mediated PMR, could enhance the biophysical understanding of the intricate interplay between proteins and membranes. As a result, such investigations have the potential to contribute to the development of novel therapeutic strategies.

1.2 Biophysics of the cell surface

The plasma membrane and cytoskeletal cortex

The plasma membrane is a critical component of the cell that shields it from the extracellular environment, measuring 5-10 nm in thickness[8, 9]. With its dynamic and complex structure, the plasma membrane serves as a selective permeable barrier, enabling the exchange of solutes such as nutrients and waste products between the cell and the extracellular environment while also separating the cell's internal contents from the external environment[7, 10]. While the lipid bilayer can vary in composition and organization depending on the specific cell type, all eukaryotic membranes are composed of structural and signaling lipids as well as embedded proteins[11] (Fig. 1.1). The abundance of densely packed phospholipids, sterols, and sphingolipids, such as cholesterol, enhances its resistance to mechanical stress[12, 13].

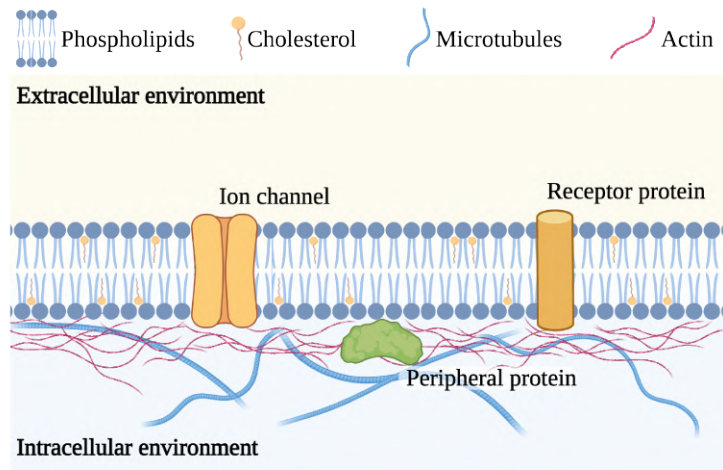


Figure 1.1: The composition of the plasma membrane is schematically illustrated as a lipid bilayer composed of phospholipids, cholesterol, and integral proteins that are embedded within the bilayer, collectively serving as a selective permeable barrier between the extracellular and intracellular environments. Additionally, peripheral proteins, such as annexins, reside within the cell along a network of cytoskeletal proteins, depicted as microtubules and actin filaments.

This dynamic structure enables cells to communicate and interact with each other by translating external signals such as secreted signaling molecules and adhesion-induced tension into intracellular signaling pathways and cellular responses[14]. The cortical actin cytoskeleton, a network of actin filaments located beneath the plasma membrane, provides rigid structural support and reinforcement to the membrane[15, 16]. The cytoskeleton components, including actin filaments, microtubules, and intermediate filaments, as well as various integrated and peripheral proteins and the geometrical properties of the lipids, are collectively responsible for maintaining the structure and shape of the cell [8, 17, 18]. In addition to maintaining the cell's structure, the actin cytoskeleton is involved in numerous cellular processes, including cell migration, intracellular trafficking, division, membrane repair, and sensing in the three-dimensional extracellular space [8, 17, 19].

The assembly of the lipid bilayer is driven by the amphiphilic nature of the phospholipids. The hydrophobic head groups orient towards the exterior of the membrane, while the hydrophobic tails orient inward towards the center of the bilayer. Furthermore, the surface properties of the membrane, as determined by the head group charge of the individual lipids, influence its interaction with proteins[20]. The annexin protein family is an example of proteins that can bind to negatively charged phospholipids in a calcium-dependent manner and play various roles in membrane organization, trafficking, and repair[7, 21]. The transport of cargo across the membrane often necessitates substantial membrane remodeling, such as pore formation, fusion, and fission, which are critical for normal cell function[10, 22, 23].

Despite being permeable to water, the plasma membrane acts as a passive barrier for the

transport of small molecules and ions. To maintain an ion gradient across the membrane, cells utilize active transport facilitated by transmembrane proteins[24]. These membrane-integrated ion pumps play a crucial role in regulating the ion concentration within the cell, such as when intracellular calcium levels are increased due to the 10^4 -fold concentration gradient upon plasma membrane rupture [8, 25, 26]. Given the plasma membrane's multifaceted role, its integrity is crucial for the cell's survival and overall function. To counter the threat of membrane damage, cells have developed robust and sophisticated plasma membrane repair (PMR) mechanisms to ensure their survival[7].

1.2.1 Mechanics of plasma membrane repair

Cells in various regions of the body are exposed to mechanical stress as they move through their physiological environment, including in the skeletal, muscles, gut epithelium, and skin [27, 28, 29, 30, 31], while metastatic cancer cells face additional stress due to their migration and invasion through the dense environment of the body[32]. When the cell membrane is damaged, it triggers a rapid influx of Ca^{2+} from the extracellular environment, owing to the steep Ca^{2+} gradient across the membrane [33]. This influx activates the repair mechanisms, initiating membrane resealing [34, 35]. Studies dating back to the 1930s, using sea urchin eggs in a Ca^{2+} -depleted solution, have demonstrated that membrane repair fails in the absence of Ca^{2+} [36]. Similarly, blocking Ca^{2+} with magnesium resulted in ineffective membrane repair in fibroblasts [37]. These findings not only highlight the crucial role of Ca^{2+} in cell survival but also emphasize its central function in initiating plasma membrane repair [36].

The Ca^{2+} concentration in resting cells is typically in the nanomolar range (100 nM), whereas extracellular Ca^{2+} concentrations are in the millimolar range (1-2 mM) [25, 38, 26], creating a steep Ca^{2+} gradient. This gradient is critical for signaling events since it actively pumps Ca^{2+} out of the cell or into intracellular Ca^{2+} storage organelles to prevent cytotoxicity. However, Ca^{2+} can also be released from these organelles, such as the endoplasmic reticulum (ER), endosomes, lysosomes, Golgi apparatus, and mitochondria, initiating various signaling cascades[4, 39, 40]. The level of Ca^{2+} influx is proportional to the size of the wound; consequently, the size and type of damage can be determining variables for the initial and subsequent responses [34, 35]. Furthermore, it also determines whether one or both sources of Ca^{2+} are employed to initiate the repair response[39].

Membrane repair includes both passive and active processes. Passive resealing occurs for injuries smaller than $0.2 \mu\text{m}$ [41] and depends on the inherent tendency of disordered lipids to close the injury, acting as a driving force to enable membrane closure and reducing membrane tension[42]. However, the close connection between the plasma membrane and the peripheral actin cytoskeleton often prevents the spontaneous releasing of the membrane, which instead can lead to local actin remodelling[42, 43]. The proposed PMR machinery

is primarily an active process that involves not only the lipid bilayer but also protein components, including cytoskeletal reorganization, membrane fusion, and replacement mechanisms [6, 44, 45, 46, 47, 48, 49]. For instance, the cell can repair itself by fusing intracellular vesicles, such as lysosomes, to the injury site, contracting the wound through actin purse-string healing, removing the injured area completely through endocytosis, or shedding the damaged membrane into the extracellular environment as microvesicles[6, 39], as demonstrated in Figure 3.1. Depending on the extent and type of injury, as well as the cell type, different mechanisms may be activated and are most likely cooperating[39], where annexin proteins are believed to play an essential role in various stages of this processes[6].

Furthermore, integral and peripheral membrane proteins are both associated with PMR. Integral proteins, such as ion channels, G protein-coupled receptors, and integrins, are involved in transporting ions across the cell membrane. Located in the cytoplasm, peripheral membrane proteins, such as actin and annexins, temporarily bind to the inner leaflet of the PM and play a variety of roles in enzymatic activity, vesicle transport, spatial organization, and mechanical properties. Some of these proteins may be involved in sensing and generating membrane curvature in response to PM damage, as well as influencing organelle shaping, protein sorting, membrane scission, and membrane fusion[6, 27].

The annexin protein family plays a critical role in plasma membrane repair (PMR) [7, 47, 50, 51, 52, 53, 54]. They are mainly cytosolic and are activated upon PM disruption by the Ca^{2+} influx, which poses an immediate threat to the cell's survival[55]. Although the complete mechanisms of annexin repair are challenging to study, research on individual annexin members has provided insights into their importance and involvement in PMR, which is expanded upon in Chapter 3, due to their abilities to shape membranes and sense curvatures[56].

1.2.2 Investigations of plasma membrane disruption

Numerous approaches have been used to disrupt the plasma membrane in order to study cellular responses and membrane repair. These methods include mechanical disruption using microneedles, agitation with glass microbeads, and cell scraping[52, 57, 58, 59], in addition to heat stress[56] and chemically induced injuries using detergents[31, 60] (as digitonin) or bacterial pore-forming toxins[61, 62] (such as streptolysin O or listeriolysin O) to generate membrane pores for examination of PM integrity. Typically, the effect of chemically induced stress is analyzed by lysing the cells and examining the membrane using mass spectroscopy, with an emphasis on PMR-associated proteins. Microneedle injury is a technique used to explore cellular responses and membrane repair and has been used for puncturing the plasma membrane of *Xenopus* oocytes with a 150- μm diameter needle[57]. This led to an increase of the motorprotein Myosin II around the injury site following actin polymerization, resulting in wound constriction. The microneedle method allows for single-cell investigations and a

high time-and-spatial resolution but does not permit control over the pore size and therefore requires cells that are larger than the typical human cells utilized for PMR cellular response studies, such as HEK293, MCF7, or HeLa cells[31, 47, 52, 63]. Microsized glass beads can be used to inflict larger injuries on cells by gently rolling the beads on top of adhered cells[59] or by shaking the co-incubated beads and cells[56]. This approach offers excellent visualization of membrane disruption in bulk measurements and monitoring of the survival ability of whole cell populations; however, this method does not provide control over the degree and location of the injury.

Optical techniques, such as pulsed lasers, can also be used to rupture the cell membrane. Laser-induced punctures offer superior time and spatial control and are therefore well suited for local disruption of specific regions of the cell. Pulsed lasers have proven beneficial for studying cellular PMR responses and their components, such as actin and annexin proteins[27, 31, 47, 52, 56, 64], and can also be utilized in combination with plasmonic nanoparticles[65, 66, 67, 68, 69]. Pulsed ultraviolet (UV) lasers are particularly effective in controlling the localization of membrane damage in two dimensions and have been used to monitor protein responses upon PM injury. Despite the efficiency of high-powered pulse lasers, the high energy associated with each pulse can cause membrane injuries of several micrometers as well as damage throughout the cell along the laser path. This can induce diffusion, affecting the lipid and protein mobility within the cell, and cause material ablation and protein denaturation within the cell; hence, irradiation of the nucleus and other vital organelles has to be avoided [7].

Thermoplasmonically induced membrane disruption

The thermoplasmonic technique has been utilized to study the protein response to membrane disruption (Fig. 3.4). It employs optical tweezers with a wavelength of 1064 nm and gold nanoparticles (AuNPs) or gold nanoshells (AuNSs), which are efficient nanoheaters[70]. These nanoparticles can induce small, highly localized membrane ruptures, enabling a controlled and localized study of protein-membrane interactions and membrane dynamics in response to membrane damage and Ca^{2+} influx. The plasmonic metal nanoparticles can convert light to heat in a spatially confined area (Fig. 2.2C). This conversion is particularly effective at a specific frequency, which is adjustable by altering the size, shape, and composition of the particles[70]. A significant advantage of the metal NPs is their ability to interact with light outside the visible spectrum, hence generating heat within the biological transparency window[71] while minimizing interaction with biologically relevant molecules, including blood, water, and lipids, in this region of the electromagnetic spectrum[72]. To induce a membrane wound, single NP can be immobilized on a glass surface beneath an adhered cell and irradiated, thereby creating the wound from below (as illustrated in Fig. 3.4C (ii)). This approach enables fluorescent imaging of the entire two-dimensional hole and allows confocal imaging of the annexin protein's response to injury (Fig. 3.4C (iii)). By stacking images in

the z-direction, three-dimensional visualization is possible, which facilitates tracking of the geometry of the wound and the proteins recruited around the hole as it extends through the cell[54]. This technique, therefore, allows for the investigation of PMR response in a nearly native environment[73].

The thermoplasmonic method has also been used to directly monitor the temperature surrounding single AuNPs in both 2D and 3D assays. In these assays, the nanoparticle was irradiated on a lipid bilayer or trapped near a lipid vesicle, enabling the quantification and control of the precise temperature profile surrounding the particle for the study or manipulation of biological specimens[74, 75]. The technique has further been used to investigate potential photothermal applications such as drug delivery and photothermal therapy[76, 77, 78], where its plasmonic heating attribute has been of great interest within the biomedical field for decades. Moreover, the method has been extended to gain a better understanding of intracellular mechanisms by investigating vesicle and cell fusion, which could lead to the creation of novel hybrid cells or the delivery of a drug of interest to a specific cell for studying cellular response or gene expression[79, 80, 81, 82]. The same fusion approach has also been employed to investigate membrane protein phase affinity [83]. Recently, the method has been used to study the annexin protein response to membrane disruption[54, 84], which is further explored in Chapter 3.

2.1 Optical trapping and imaging of nanoheaters

Optical tweezers, or optical traps, have become a widely used method for optically manipulating micro- and nanosized particles by utilizing a highly focused laser beam. Invented by Arthur Ashkin in 1970, the technique was employed to trap living bacteria [85] and has since emerged as a highly valuable tool for investigating biophysical phenomena in biological systems without causing unwanted damage. The groundbreaking invention and biological relevance of Ashkin's contribution to the field was recognized with the 2018 Nobel Prize in Physics [86].

Optical trapping of metallic particles in three dimensions is made possible by utilizing the momentum of photons carried by laser light [87]. Near-infrared (NIR) laser light is particularly useful in biological systems due to its limited interaction with tissue and water since its wavelength falls within the biological transparency window, which spans from $\sim 650\text{-}950\text{ nm}$ and $1000\text{-}1350\text{ nm}$ [72]. Consequently, optical manipulation of particles can be carried out in biological systems in a non-invasive manner.

Optical tweezers can be combined with a scanning confocal microscope, which was developed by M. Minsky in the 1950s [88]. This combination allows for accurate visualization of biological processes with minimal damage. This has proven to be useful in experimental biophysics for investigating physical changes of the membrane such as ruptures, bending, and shape modulations, as well as protein interactions in living cells and in model membrane systems.

2.1.1 Principles of optical trapping

When an object capable of reflecting or refracting light is illuminated, it experiences a force. The force is proportional to the photon momentum, which is determined by the energy and propagation of the light. As the light passes through the object, its momentum is altered due to the change in direction, resulting in a corresponding change in the momentum of the refracted or reflected light. This change in momentum of the light induces an equal and opposite momentum on the particle, according to Newton's Third Law of motion and mo-

momentum conservation. This force, which is equivalent to the change in momentum, leads to a mechanical effect of light on exposed dielectric and metallic particles [87, 89].

Calculating the force exerted by a focused laser beam on a particle requires consideration of the particle's dimension (R) relative to the wavelength of the laser light (λ) [87, 89]. As such, three different regimes must be taken into account: i) the Rayleigh regime ($\lambda \gg R$), where the particle is considerably smaller than the wavelength of light; ii) the Mie regime ($\lambda \ll R$), in which the particle is larger than the wavelength of light; and iii) the intermediate regime ($R \approx \lambda$), where the size of the particle and the wavelength of light are comparable[87].

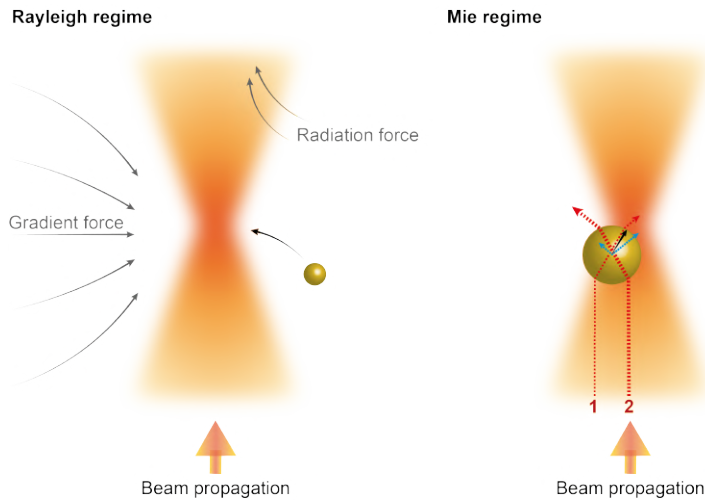


Figure 2.1: The principles of optical trapping are illustrated through the schematic representation of the Rayleigh (left) and Mie (right) regimes. When the size of the particle is smaller than the wavelength of the incoming light ($\lambda \gg R$), the particle is trapped when the gradient force is larger than the radiation force. Conversely, when the particle is larger than the wavelength of light ($\lambda \ll R$), the particle is trapped by momentum conservation based on the Mie conditions.

In this study, particles between 160 and 200 nm in diameter were used, which are significantly smaller than incoming light with a wavelength of 1064 nm. Thus, the forces acting on the particles are in accordance with the Rayleigh regime. In the Rayleigh regime ($\lambda \gg R$), which is the relevant regime when considering thermoplasmonics, the particle behaves as a point dipole induced by the incoming electrical field (E). The trapping force, also known as the gradient force (F_{grad}), arises from the Gaussian intensity gradient of the laser beam. This force pulls the particle towards the center of the beam, in the direction of the highest intensity (Fig. 2.1, left). The gradient force experienced by the particle can be described using Equation 2.1:

$$F_{grad} = -\nabla U = \alpha \nabla E^2 \quad (2.1)$$

The force is derived from the negative gradient of the potential $U = -dE$, where $d = \alpha E$ [87] and the polarizability of the object is given as $\alpha = \frac{8}{3}\pi(kR)^4 R^2 \left(\frac{m^2-1}{m^2+2}\right)^2$. Here, R is the radius of the particle, $m = \frac{n}{n_m}$ represents the relative refractive index, and $k = 2\pi \frac{n_m}{\lambda}$ is the

wavenumber of light [90]. As the intensity and electric field are proportional, the gradient force points towards the focus of the laser beam, thus trapping the particle in the high-intensity region, which is the center of the Gaussian laser beam.

When light interacts with a particle, it can either be scattered or absorbed, resulting in a transfer of momentum that contributes to the scattering and absorption forces. The sum of these forces is known as the radiation force and acts perpendicular to the beam direction, pushing the particle away from the laser focus and displacing it along the propagation of the beam [90]. The radiation force, F_{rad} , can be expressed as:

$$F_{rad} = \frac{n_m}{c} \langle P \rangle (C_{scat} + C_{abs}) \quad (2.2)$$

where C_{scat} and C_{abs} represent the scattering and absorption cross-sections, respectively. n_m is the refraction index of the surrounding medium, c is the speed of light, and $\langle P \rangle$ is the time-averaged Poynting vector, which describes the energy flux and the direction of the radiation force.

The stability of an optical trap is determined by the balance between the gradient force and the radiation force[91]. If the gradient force dominates, it pulls the particle towards the high-intensity region of the electrical field, facilitating stable optical trapping[92]. However, for some particles, such as nanorods or gold nanoshells[93], the radiation force may exceed the gradient force, leading to reduced or lost optical trapping. The scattering and absorption cross-sections play an important role in the thermoplasmonic properties of metallic nanoparticles, as will be discussed in Section 2.2.

For larger particles, $\lambda \ll R$, a more intuitive trapping mechanism exists that relies on tracking the change in momentum as the light beam passes through the particle. Assuming a Gaussian intensity profile, the laser beam has a higher intensity at the center of the trap compared to the edges. This means that the photons in the center of the beam (2) carry more momentum than the peripheral photons (1), as depicted in Figure 2.1 (right). When the incoming light interacts with the particle (indicated by the red arrows), the particle experiences a change in momentum (represented by the blue arrows), which is equal to and opposite to the momentum change of the light, according to the conservation of momentum. As the peripheral photons carry less momentum compared to the photons in the center, the net momentum change pushes the particle toward the center (black arrow), effectively trapping it at the focus point of the laser beam, where the conserved momentum holds the particle in the center of the trap[87].

2.2 Thermoplasmonics

The field of thermoplasmonics is a rapidly expanding area that combines the properties of light with those of plasmonic metal nanoparticles, such as gold nanoparticles (AuNPs). AuNPs have been used for centuries for their decorative properties, as evidenced in the stained glass windows of churches and cathedrals, where the color variations are based on the size, shape, and composition of the particles due to the interaction with sunlight and the refraction and reflection phenomena [70].

The colorful properties of metallic nanoparticles (NPs) were explained by Gustav Mie in 1908, who published a mathematical model that described the scattering and absorption cross-sections of metallic NPs [94]. When light carrying an electromagnetic field interacts with a plasmonic metal nanoparticle (Fig.2.2A), the conduction electrons within the particle are excited, leading to a collective electron oscillation known as plasmon[95] (Fig. 2.2B). When the plasmon resonates with the incoming electromagnetic field, the particle experiences a localized surface plasmon resonance (LSPR), referred to as plasmon resonance[70]. The particle absorbs a significant amount of light at the resonance frequency, which is subsequently released as heat (Fig. 2.2C) in an attempt to restore the system to its equilibrium state, caused by friction between the oscillating electrons and the surrounding metal lattice known as Joule heating or thermoplasmonic heating.

To achieve plasmon resonance in the NIR spectrum, the particle's shape, size, and composition can be adjusted to tune the plasmon resonance frequency, the wavelength with the highest extinction cross-section, to the NIR region. This makes plasmonic nanoparticles highly efficient light-to-heat converters, a property employed in photothermal applications[70, 96, 97].

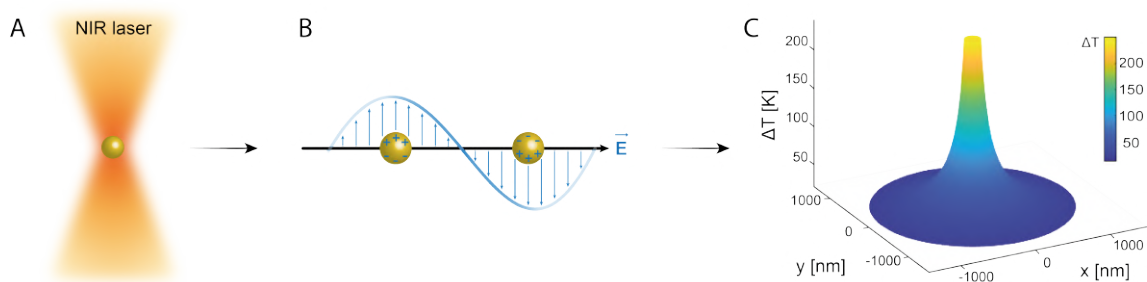


Figure 2.2: A schematic illustration of a gold nanoparticle being illuminated by a NIR laser beam (A). The interaction between the electromagnetic field and the particle's conduction electrons leads to a collective oscillation of the conduction electrons with the electromagnetic field, known as plasmon resonance (B). This process is accompanied by the release of thermoplasmonic heat (C), which has been estimated for a 200 nm AuNP subjected to laser irradiation at a power of 230 mW.

Surface plasmon resonance

Plasmon resonance is dependent on the boundary conditions of the particle and can be distinguished as either bulk plasmon resonance or localized surface plasmon resonance. For small metal nanoparticles, such as AuNPs, the boundary conditions are restricted due to the relative size of the particle in relation to the incoming wavelength, resulting in surface plasmons localized in all three dimensions within the particle, hence localized surface plasmon resonance [98].

Upon illumination, the NPs scatter and absorb light, where the localized surface plasmon resonance frequency corresponds to the wavelength with the most efficient absorption. This frequency is tunable by adjusting the particle's boundary conditions, such as size, shape, and composition. This, in turn, affects the localized surface plasmons, leading to changes in the resonance frequency's spectral localization[70]. Consequently, light scattering and absorption are highly sensitive to small changes in the nanostructure.

The measurement of a particle's scattering and absorption at a specific wavelength is expressed as the extinction cross-section (C_{ext}) and can be calculated as the sum of the scattering and absorption cross-sections ($C_{scat} + C_{abs}$) and applied theoretically using Mie theory to predict the efficiency of the light-to-heat conversion [74].

The extinction cross-section (C_{ext}) of a particle located in a dielectric medium, with permittivity (ϵ_m) at a particular wavelength (λ), can be determined by using the modified approximation proposed by Bohren et al.[99] to solve Maxwell's equations. The extinction cross section is expressed by Equation 2.3, where the wavenumber, κ , is given by $\kappa = 2\pi\sqrt{\epsilon_m/\lambda}$, and α represents the polarizability of the particle.

$$C_{ext} = C_{scat} + C_{abs} = \frac{8\pi}{3}\kappa^4|\alpha|^4 + 4\pi\kappa Im(\alpha) \quad (2.3)$$

The polarizability of the particle, Equation 2.4, is described as a function of the particle's volume (V), dielectric permittivity (ϵ) at frequency ω , and a shape-dependent parameter ϕ .

$$\alpha = \frac{3V}{4\pi} \frac{\epsilon(\omega) - \epsilon_m}{\epsilon(\omega) - \phi\epsilon_m} \quad (2.4)$$

The shape-dependent parameter ϕ for a solid sphere is 2. However, for spheres with a thin metal shell and a dielectric core of radius a_c , ϕ is represented by Equation 2.5.

$$\phi = \frac{3}{f_s} \left(1 + \frac{\epsilon_c}{2\epsilon_m} \right) \quad (2.5)$$

The dielectric function for a metal nanoparticle, $\epsilon(\omega)$, as introduced in Equation 2.4, is represented by $\epsilon(\omega) = \epsilon_1(\omega) + \epsilon_2(\omega)$ [89], which can be simplified using the Drude approximation[95] as shown in Equation 2.6. Here, ω is the frequency, ϵ_{ib} is the contribution from electronic interband transitions, and ω_p is the plasmon frequency of bulk gold. The damping of conduc-

tion electrons in bulk gold is represented by $\gamma_b = \frac{l_b}{v_f}$, where l_b is the electron mean free path and v_f is the Fermi velocity.

$$\epsilon(\omega) = \epsilon_{ib} - \frac{\omega_p^2}{\omega(\omega + i\gamma_b)} \quad (2.6)$$

Equation 2.3 and Equation 2.4 can be combined to estimate the resonance frequency by using Equation 2.7 [100], provided that the dipole assumption and $\gamma_b \ll \omega_p$ are satisfied.

$$\epsilon(\omega_{max}) = \frac{\omega_p}{\sqrt{\epsilon_{ib} + \phi\epsilon_m}} \quad (2.7)$$

The particle's resonance can be tuned to a specific wavelength by adjusting the particle's shape and, consequently, the shape factor ω in Equation 2.7. Although increasing the size of spherical gold nanoparticles leads to a significant rise in absorption, it does not result in a considerable shift in the resonance frequency[89]. The reason for the slight red shift in the resonance frequency observed for larger spherical nanoparticles (Fig. 2.4A), is caused by oscillations other than the oscillations described by Equation 2.7, as it is only valid under the dipole assumption ($R \ll \lambda$) for particles with a radius of 10 nm or less [74]. Notably, larger particles possess quadruple resonance instead of dipole resonance, which leads to a broadening of the absorption resonance peak[70], as illustrated in Figure 2.4A.

Generation of heat by plasmon resonance

The light absorbed by nanoparticles (NPs) leads to the distribution of heat within the irradiated NP and its surroundings. The light-to-heat conversion process is illustrated in Figure 2.3, in which a metallic NP is illuminated with resonant photons. This leads to an excitation of the electron cloud surrounding the particle, causing rapid non-equilibrium heating that is promptly followed by relaxation via electron-electron scattering. This phenomenon results in a swift temperature rise at the particle's surface[101]. As the lattice cools through phonon coupling, the surface temperature returns to equilibrium within a fraction of a microsecond after irradiation, leading to heat dissipation into the surrounding medium of the NP[102], where the heat distribution reaches equilibrium within 100 ns[103].

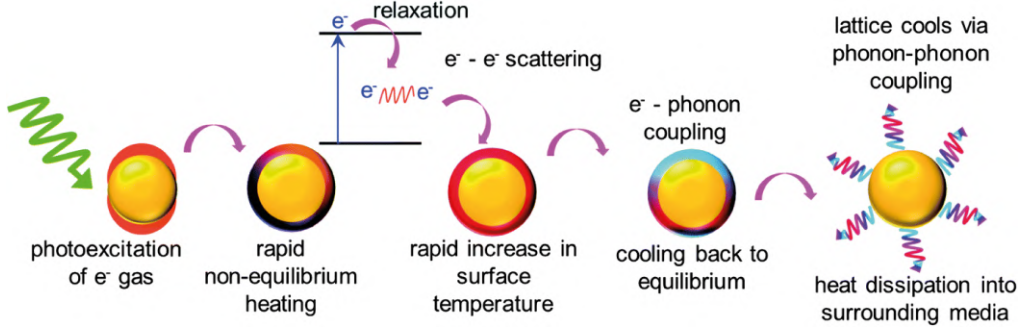


Figure 2.3: A simplified model illustrating the process of light-to-heat conversion in plasmonic gold nanoparticles following photon absorption. The conversion process from light absorption to the release of thermoplasmonic heat is completed within a couple of hundred picoseconds. The figure is adapted from Webb et al.[102].

The process of light-to-heat conversion serves as a crucial mechanism underlying the membrane disruption studies in this project. By irradiating metallic NPs at their resonance wavelength, significant and localized heating can be achieved. The temperature distribution within the NP can be determined by solving the heat transfer equation [104], where the local heat intensity is derived from the light dissipation within the NP[99]. The resulting temperature increase, $\Delta T(r)$, is expressed as a function of distance (r) from the surface of the NP (with radius R) and the source [105]:

$$\Delta T(r) = \frac{VQ}{4\pi\kappa r}, r \geq R \quad (2.8)$$

Here, κ is the thermal conductivity of water (0.58 W/mK at ambient temperature) and Q is a measure of the locally generated heat per unit time and volume (V) within the particle, most of which is produced as Joule heating within the NP[70].

Equation 2.8 can be adapted to relate the increase in temperature, $\Delta T(r)$, to the absorption cross-section, C_{abs} , as a function of distance (r) from the NP surface, relative to the ambient temperature[96]:

$$\Delta T(r) = \frac{IC_{abs}}{4\pi\kappa r}, r \geq R \quad (2.9)$$

The laser power density at the sample plane is denoted by I , where I represents the laser power as a function of the area in focus, measured as $\frac{W}{cm^2}$. The temperature distribution around the NP, generated by Equation 2.8, reaches a steady state within tens of nanoseconds[103], thus satisfying Laplace's equation[54, 70].

The absorption cross-section (C_{abs}) is a key factor in the thermoplasmonic heating generated by nanoparticles, where the immediate heat production can be calculated by multiplying C_{abs} with the known laser intensity (I)[70]. Thus, estimating the value of C_{abs} for a given particle allows for the determination of the temperature increase at its surface using the inverse relation from Equation 2.9. This calculation has been carried out in both two-dimensional

and three-dimensional assays, where the particle is irradiated on a lipid bilayer or in close proximity to lipid vesicles, such as giant unilamellar vesicles (GUVs), with well-defined lipid melting temperature[74, 75]. This enables the exact measurement of the temperature profile around the particle, as the equation accounts for thermal dissipation and heat transfer into the surrounding medium or surface.

Mie theory presents a mathematical framework for characterizing the scattering and absorption cross sections of nanoparticles [94]. This theory was employed to estimate the absorption cross section (C_{abs}) for AuNPs exposed to a 1064 nm NIR laser beam. To calculate C_{abs} , an in-house Matlab workflow was used, which incorporated Mie’s equation along with the NP’s boundary conditions, laser power density, and wavelength. The C_{abs} of nanoparticles, therefore, varies with particle size, which is illustrated in Figure 2.4A for AuNPs with radii ranging from 20 to 100 nm, where the temperature profile for 50 and 100 nm AuNPs was calculated in Figure 2.4B, showing a notable difference in their heating capacity. In spite of this difference, the heated volume surrounding both NPs remained highly confined, with the temperature decreasing by 30-40% at a distance equivalent to the particle radius from the surface. Despite the rapid reduction in heat with increasing distance from the particle, a considerable heating effect can still be observed up to 1 micron from the particle. In previous trapping experiments[93], it was noted that gold nanoparticles were trapped slightly outside the focal region, resulting in a significantly lower intensity exposure than that assumed in the calculations. As a result, the thermoplasmonic approach enables minimally invasive, yet highly localized, efficient heating, such as for the disruption of membranes in living cells [70, 71, 74, 89, 106].

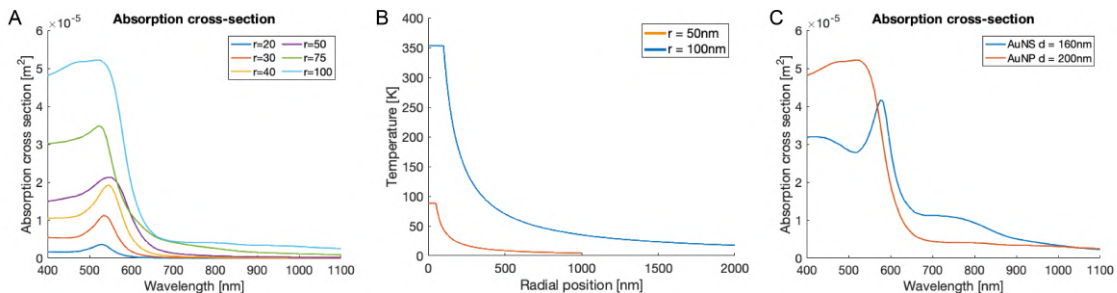


Figure 2.4: The relationship between the absorption cross-section (C_{abs}) as a function of laser wavelength and the particle size and composition. (A) The C_{abs} was determined for AuNPs with radii ranging from 20 to 100 nm, revealing a slight red shift and broadening of the resonance peak with increasing particle size. (B) Using Mie’s equations, the temperature profile was determined for AuNPs with radii of 50 and 100 nm, which were exposed to NIR irradiation at a wavelength of 1064 nm and a laser power of 230 mW. The temperature profile is presented as a function of the radial distance from the particle center. (C) The C_{abs} was calculated for AuNPs and AuNSs with radii of 100 nm and 80 nm, respectively, as a function of wavelength, using the Mie Theory Calculator, nanoComposix[107].

The plasmonic nanoparticle toolbox

Nanoparticles, owing to their ability to efficiently convert light into heat, have been the subject of extensive research in various applications, including gold nanoparticles, gold nanoshells, and other non-spherical nanoparticles, such as gold nanorods and gold nanostars [70]. In this project, gold nanoparticles and gold nanoshells were used. Here, the AuNSs consisted of a silica core measuring 120 ± 4 nm encapsulated by a 20 ± 7 nm gold shell, resulting in a particle size of 160 nm (Nanocomposix). The resonance frequency of the AuNSs can be tuned to specific wavelengths by altering the ratio between the silica core and the gold shell, allowing for the adjustment of the absorption cross-section (C_{abs}) into the near-infrared (NIR) window, hence highly efficient light-to-heat conversion at longer wavelengths[70].

Although the resonance frequency of AuNPs is less adjustable, the absorption cross-section can be slightly shifted and broadened to reach longer wavelengths by increasing the particle size, enabling NIR light absorption (Fig. 2.4A). While AuNSs appear to be more efficient at generating heat at longer wavelengths, the gold shell has a tendency to be thermally unstable at high temperatures[78], whereas solid gold nanoparticles have been found to exhibit higher thermal stability under similar conditions [78, 106]. Furthermore, the absorption cross-sections for 160 nm AuNSs and 200 nm AuNPs at 1064 nm are very similar (Fig. 2.4C), however, given the difference in size, the AuNPs generate more heat than the AuNSs. Accordingly, the stable 200 nm AuNPs (from British Biocell International (BBI)) were chosen as the primary option for plasma membrane disruption in Chapter 3. In contrast, the slightly smaller AuNSs, which were more efficiently internalized by the cells, were selected as the primary choice for intracellular membrane disruption in Chapter 4.

2.3 Confocal imaging of cells and nanoparticles

Combining confocal microscopy with optical tweezers can provide an efficient tool for biophysics studies at the molecular and cellular levels. The confocal microscope offers high-resolution, three-dimensional images, while optical tweezers enable precise, nanoscale force and thermal manipulation. The combination of these techniques permits the simultaneous observation and manipulation of biological samples, such as studies of membrane and protein dynamics, as well as precise measurement of the spatial and temporal dynamics of biological processes.

In our study, a Leica SP5 scanning confocal microscope was employed together with a dual optical trap system powered by a NIR continuous wave laser operating at a wavelength of 1064 nm (neodymium-doped yttrium orthovanadate (Nd:YVO₄), Spectra Physics J201-BL-106C). However, only a single optical trap was utilized for the study, as depicted in the experimental setup illustration in Figure 2.5. The confocal microscope offers a full range of UV, visible,

and IR excitation lasers, including a set of three built-in scanning lasers (argon laser at 485, 477, 488, 514 nm, HeNe 543 nm, and HeNe 633 nm), as well as an integrated Acousto-Optical Beam Splitter (AOBS) with rotating photomultipliers[108]. These features enable accurate imaging and measurement of multiple fluorescently labeled components, provided that the emission and excitation spectra of the selected fluorophores do not overlap. The setup can also be configured to collect reflected light, such as that from AuNPs, rather than fluorescence. The optical trapping and imaging are performed in the same focal plane, with the laser beam focus from the optical trap coinciding with the objective lens of the confocal microscope. The focal plane was achieved using a Leica PL APO, NA=1.2, 63X water immersion objective. While the optical trap was stationary, its position relative to the sample could be adjusted by translating the sample, which was mounted on a piezoelectric stage (PI 731.20, Physik Instrumente, Germany), allowing for nanoscale precision movement in the lateral position.

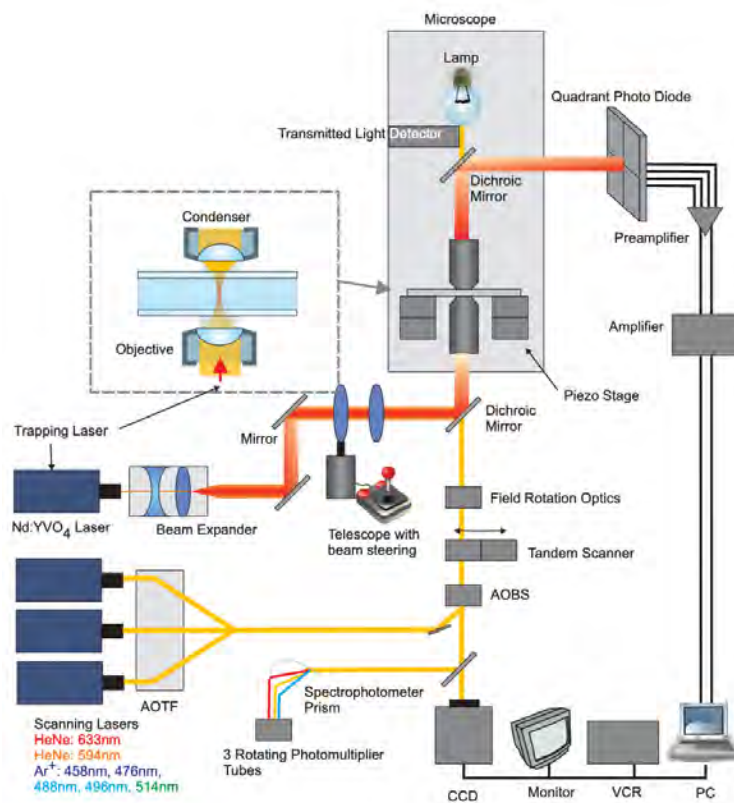


Figure 2.5: The diagrammatic representation of the entire experimental setup includes the optics utilized for forming the optical trap, as well as the confocal scanning system. Specifically, a confocal microscope equipped with a 1064 nm Nd:YVO₄ laser was employed in this study, enabling the simultaneous detection of fluorescence and reflection from fluorophores and gold nanoparticles, respectively. Figure adapted from Richardson et al.[108].

When comparing confocal microscopy to widefield microscopy, several advantages in terms of image quality and resolution become evident. The use of a pinhole in confocal microscopy effectively reduces out-of-focus light, resulting in improved axial and lateral resolution. Additionally, confocal microscopy reduces sample damage, making it a more suitable technique for

live cell imaging and providing clearer visualization of internal cellular structures in three dimensions. The confocal microscope employs a sequential scanning technique, where the laser beam is scanned over the sample point by point and the emitted fluorescence and reflection signal are collected through a pinhole positioned in front of the emission detector, typically a Photo Multiplier Tube (PMT). The pinhole only allows light from the focal plane, eliminating out-of-focus light from the sample and producing images with high spatial resolution while also reducing background noise[109, 110]. However, the reduction in out-of-focus light in confocal microscopy can lead to an overall reduction in signal intensity, which can make it challenging to identify weak signals.

The resolution of optical microscopes is limited by the diffraction of light, which imposes a fundamental diffraction limit and sets a minimum size for objects that can be resolved by light microscopes. The Rayleigh criterion defines resolution as the minimum distance between two points that can be optically distinguished as two separate entities. In essence, the size of the diffraction pattern generated by the objective determines the resolution of the optical system. The Airy disk, named after mathematician and astronomer Sir George Biddell Airy, illustrates the diffraction pattern, where the minimum lateral distance between two objects is equal to the radius of the central Airy disk. The smaller the diffraction pattern, hence the Airy disk, the higher the resolution of the system[111].

Additionally, the resolution is influenced by both the wavelength of light (λ) and the numerical aperture of the objective (NA_{obj}), where the latter refers to the maximum collection angle of light and is directly proportional to the lateral resolution. The numerical aperture is defined as $NA_{obj} = n \sin(\theta)$, where n is the refractive index of the image medium (1.33 for water) and θ is the light's half-angle[109]. The overall resolution is determined by both the lateral and axial resolution limits, which together represent the diffraction limit. The diffraction limit is the theoretical minimum resolution of a microscope system. The resolution can be approximated using the equations presented below[111], where the lateral resolution, $d_{lateral}$, relates to the wavelength of light (λ) and the numerical aperture of the objective (NA_{obj}), while the axial resolution, d_{axial} , also relates to the refractive index of the image medium (n):

$$d_{lateral} = \frac{0.51\lambda}{NA_{obj}} \quad (2.10)$$

$$d_{axial} = \frac{0.88\lambda}{n - \sqrt{n^2 - NA_{obj}^2}} \quad (2.11)$$

Typically, the estimated minimum distance (d) for lateral resolution in confocal optical microscopes falls between 200 and 230 nm[112], while the minimum distance for axial resolution is above 500 nm[109]. For instance, when two GFP molecules are excited with a 488nm laser, the two molecules can be observed as separate entities with a minimum distance of 207 nm

in the lateral direction and 567 nm in the axial direction, using a 1.2 numerical aperture. Since the samples are observed in a single focus plane, the lateral resolution is of utmost importance. Confocal microscopes use a pinhole to create a narrow point spread function (PSF), which is essential for high lateral and axial resolution. However, the resolution equations do not account for the PSF, and therefore the actual resolution of the system may be underestimated[111].

In summary, the simultaneous visualization and manipulation of biological samples along with the trapping of metallic nanoparticles can be achieved through the integration of confocal microscopy and optical tweezers. Among the metallic nanoparticles, AuNPs possess the ability to act as efficient light-to-heat converters and can be utilized to locally disrupt cell membranes. It is important to note that particles with diameters between 160 and 200 nm may not be resolved individually. However, in our experiments, the resolution of particles is secondary to the temperature increase generated upon irradiation, which facilitates the study of membrane proteins. Moreover, Chapter 3 demonstrates that the combination of confocal microscopy in reflection mode provides clear visualization of AuNPs with high signal intensity.

From these considerations, it can be concluded that the use of nanoparticles along with NIR laser irradiation has considerable potential for nanoscale biomedical and biophysical research, owing to its non-invasive characteristic in biological tissues. Along with the ability of the particles to scatter light, enabling particle visualization, and their pronounced absorption in the NIR region, which consequently generates a heating effect in the metallic nanoparticles[113], will be explored in the following chapters.

3

Annexins

The plasma membrane is an indispensable component of eukaryotic cells, serving as a protective barrier and a dynamic platform for cell signaling and function. In the event of membrane damage, the cell relies on its rapid plasma membrane repair mechanisms, which involve various proteins that aid in preserving cellular homeostasis and protect the cell from the detrimental effect of membrane disruption[36, 37]. The association between PMR deficiency and several degenerative diseases, such as muscular dystrophy, highlights the importance of the mechanism, where repeated membrane damage can result in progressive muscle degeneration. In contrast, some cancer cells, particularly those in metastatic breast cancer, exhibit heightened PMR, which appears to enhance the cells' capacity to endure membrane damage during invasion[7].

Depending on the severity and nature of the injury, membrane repair is facilitated by either passive or active processes. Smaller injuries with a diameter of less than 0.2 microns can spontaneously reseal through the natural reorganization of phospholipids in the membrane[41], whereas larger wounds require active processes as the close coupling between the plasma membrane and the cortical actin cytoskeleton generates membrane tension around the injury site[6]. The self-resealing properties of phospholipids are only one component of the resealing process, which also involves cytoskeletal reorganization, membrane fusion, and membrane replacement[6, 50]. Several cytosolic proteins, including the annexin protein family, are believed to be involved in various steps of the repair process in a Ca^{2+} -dependent manner, while non- Ca^{2+} -dependent proteins, such as the endosomal sorting complex required for transport (ESCRT-III), are thought to aid in the removal of damaged membranes[6]. Overall, plasma membrane repair is an intricate and dynamic series of events that are essential for cell survival and proper functioning.

3.1 Annexins as key regulators in membrane repair

The annexin (ANXA) protein family owes its nomenclature to the Greek term "annex", which denotes its propensity to bind or hold membranes together. This diverse group of proteins is characterized by over 160 family members distributed throughout the animal and plant kingdoms. In humans, 12 distinct annexins, namely ANXA1-ANXA11 and ANXA13, have been identified [114, 115].

The annexin proteins are a group of soluble, hydrophilic proteins that are predominantly found in the cytosol. These proteins have the ability to bind to negatively charged phospholipids in a Ca^{2+} -dependent manner[116]. Annexins are known to associate with organelle membranes and the inner leaflet of the plasma membrane, where this interaction is reversible upon the removal of calcium ions. The ANXAs share several structural similarities and consist of two principal domains: the conserved core domain and the N-terminal region. The core domain, which is the unique COOH-terminal, is composed of four annexin repeats, each containing approximately 70 amino acid residues, except for ANXA6, which has twice as many annexin repeats compared to other members[114]. Each annexin repeat is composed of five alpha-helical domains linked by short loops or turns, which contribute to the formation of a slightly curved disc. The core domain is considered to be the membrane binding domain as it contains Ca^{2+} binding sites[21]. In the presence of free Ca^{2+} , the protein binds to Ca^{2+} and undergoes a conformational change that allows the convex side of the core domain to bind to negatively charged phospholipids near the rupture site[6, 114]. However, the sensitivity to calcium ions and specificity for phospholipid headgroups may vary among individual annexin proteins, resulting in distinct recruitment patterns[7, 114]. Additionally, the unique NH₂-terminal region of the annexin is found on the concave side of the core domain and ranges in length from a few to several hundred residues[114, 116]. This diverse region is considered to be the primary regulator of annexin function, influencing the protein's stability and facilitating interactions with intracellular proteins such as members of the S100 protein family[52]. Despite a substantial biochemical and structural understanding of annexins, their physiological function remains a subject of ongoing research and requires further investigation[114].

Annexin mediated plasma membrane repair

Although studying annexin-mediated repair poses various challenges, researchers have gained insight into its role in plasma membrane repair primarily through the investigation of individual annexin members. Figure 3.1 depicts how annexins, in conjunction with other proteins, are believed to be associated with multiple functions and steps of the membrane repair process. These processes are believed to be interrelated and may even work together during plasma membrane repair[6].

The cortical actin cytoskeleton plays a pivotal role in many cellular processes, including cell motility, organelle movement, cell division, and plasma membrane repair[8]. However, its direct connection to the plasma membrane can elevate membrane tension, hindering spontaneous resealing of larger injuries [53]. To overcome this barrier, various processes can reduce the membrane tension in the vicinity of the injury, one of which involves exocytosis (Fig. 3.1A). This process entails the fusion of intracellular vesicles, such as lysosomes or endosomes, near the wound perimeter, bringing the wound edges closer together for eventual

resealing[6, 41, 117]. Additionally, intracellular vesicles generated by massive endocytosis from the surrounding membrane[118] can fuse together, forming a patch that directly fuses with the free edges of the damaged plasma membrane, thus covering the wound[6] (Fig. 3.1B).

ANXA2 has been observed to accumulate around the wound perimeter in dysferlin-deficient muscle fibers and has been postulated to play a role in PMR by fusing intracellular vesicles with the damaged membrane, owing to its ability to aggregate and fuse liposomes in vitro[119, 120]. Furthermore, ANXA2 is known to form complexes with members of the S100 protein family and bind to components of the actin cytoskeleton, which can alter actin dynamics and regulate intracellular fusion[52]. Importantly, the actin cytoskeleton participates in PMR by promoting exocytic events through the localized transport of vesicles to the injured membrane via myosin motors[7]. ANXA6 has also been detected near the injury site in muscle cells, and its characteristic dimeric structure has led to the suggestion that it constricts the membrane during wound closure by cross-linking two parts of the membrane[31]. This wound constriction is believed to be actin-dependent[8] and coincides with the recruitment of ANXA1, ANXA2, and ANXA5[7].

Small membrane injuries or pores can be removed through vesicle internalization or shedding. Endocytosis facilitates the internalization of the damaged membrane, a process that involves several annexins, including ANXA1, ANXA2, ANXA6, and ANXA8, at different stages of the endocytotic process. This process can depend on clathrin and dynamin, which organize the necessary proteins for inward budding (Fig. 3.1C), while the vesicle scission is facilitated by actin polymerization[6]. In addition, small membrane injuries can be removed by shedding microparticles, where ectosomes are released into the extracellular environment, which has been observed in muscle cells (Fig. 3.1D). ESCRT-III is thought to drive this process, which is mediated by the Ca^{2+} -activated ALG2 protein as the initiator[121]. ANXA7 facilitates the assembly of the ESCRT-III complex, while ANXA1 and ANXA6 are also believed to be involved in the shedding process, as they have been detected in shedded ectosomes from human embryonic kidney cells after exposure to pore-forming toxins[6].

The reduction of membrane tension can be achieved through local actin depolymerization, facilitated by the influx of calcium ions. This phenomenon is followed by a re-polymerization process[122, 123], which reinforces the cortical actin at the wound site, indicating a possible adaptive strategy for cells to counteract repetitive injuries. The plasma membrane and cortical actin cytoskeleton were proposed to be contracted by an actomyosin ring (Fig. 3.1E) using a *Xenopus* oocyte model[124]. This contraction is analogous to pulling a purse string, which is further elaborated on in Section 3.4.5.1. Moreover, ANXA2 and S100A11 are known to be overexpressed in multiple types of cancer and have been found to play a crucial role in membrane repair[52]. Following Ca^{2+} influx, the ANXA2-S100A11 complex is activated

and recruited to the site of repair, where it mediates actin polymerization and couples the actin cortex to the plasma membrane, thus defining the repair site [6]. Apart from binding to the actin cytoskeleton, the complex has also been shown to modify actin dynamics and regulate intracellular vesicle fusion[52]. Overexpression of the ANXA2-S100A11 complex in cancer cells has been linked to metastasis and poor prognosis, while cells lacking the complex show compromised plasma membrane repair and limited invasive abilities[52, 125], indicating that the complex plays a critical role in maintaining membrane integrity[50].

Moreover, the wound contraction mediated by the actomyosin ring can result in the formation of a bleb containing the damaged membrane, which in turn is removed with the scission of bleb[6] (Fig. 3.1F). While the ANXA2-S100A11 complex localizes near the site of repair, ANXA1 localizes directly at the injury site. Recent studies report that ANXA1 accumulates within the neck of the bleb, eventually forming a plug that prevents both extracellular influx and intracellular efflux[126]. The complex resealing process likely requires immediate patching, followed by reconstruction of the membrane and the associated actin cortex[6].

Apart from mediating repair by fusion and excision of membranes, annexins, such as ANXA5, have also been found to facilitate wound stabilization by forming 2D scaffolds at the injured plasma membrane[47, 127]. Upon Ca^{2+} influx, ANXA5 self-assembles into trimers on the inner leaflet of the plasma membrane (Fig. 3.3B and C), constructing 2D arrays that reinforce the plasma membrane and limit further expansion of the wound [6, 127, 128] (Fig. 3.1G).

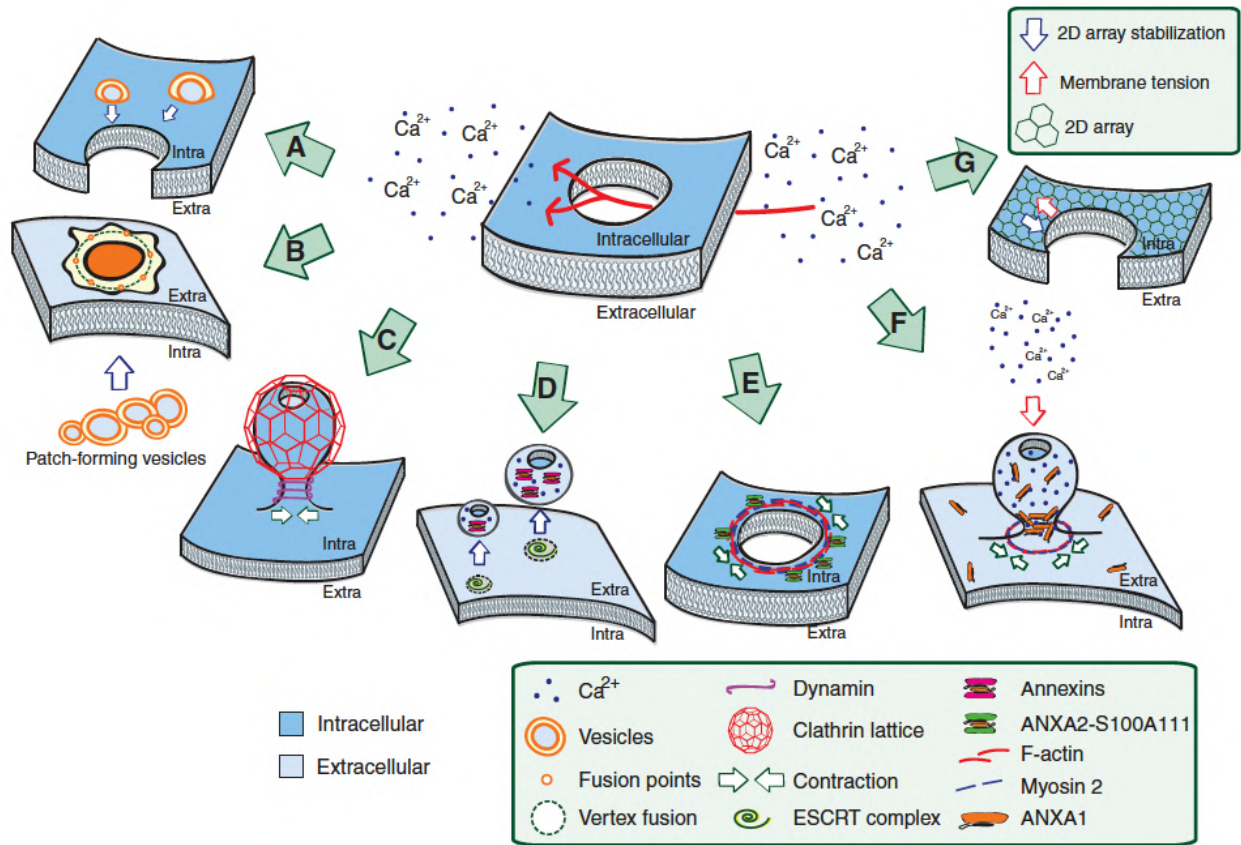


Figure 3.1: A schematic representation of various proposed mechanisms involved in plasma membrane repair (PMR). (A) Exocytosis-mediated PMR is achieved through tension reduction, whereby the fusion of vesicles around the wound perimeter reduces the membrane tension caused by the cortical actin cytoskeleton. This initial step brings the wound edges together for eventual resealing. (B) Exocytosis-mediated PMR occurs through patch fusion, where a substantial generation of intracellular vesicles leads to the formation of a patch that, through multiple fusion points between the plasma and patch membrane, fuses to cover the hole. (C) Endocytosis-mediated PMR employs clathrin and dynamin-dependent or independent pathways to remove pores or small plasma membrane injuries through endocytosis. Alternatively, (D) microparticle shedding-mediated PMR eliminates pores or small plasma membrane injuries via ectosome shedding. (E) Actomyosin purse-string contraction involves bringing the undamaged plasma membrane and the underlying cortical cytoskeleton together via a contractile actomyosin ring, analogous to pulling a purse string. (F) PMR by bleb formation is achieved through the contraction of the cortical actomyosin, which eliminates the damaged membrane by forming a bleb that contains the wound. Finally, (G) wound stabilization can be facilitated by the formation of 2D arrays. This can be achieved by ANXA5, which self-assembles into trimers on the inner leaflet of the plasma membrane upon Ca^{2+} influx, constructing 2D arrays that strengthen the plasma membrane and prevent further expansion of the wound. Figure adapted from Boye et al.[6].

Annexins and membrane curvatures

The proposed mechanisms for plasma membrane repair share a common characteristic, namely the bending of the cell membrane. The plasma membrane is conceptually perceived as a

two-dimensional sheet embedded in a three-dimensional space. Annexin proteins, with their curved binding surface, are anticipated not only to induce this membrane bending but also to selectively bind to membranes with specific local curvatures[63, 129].

A recent study investigated the physiological function of individual annexins by introducing them to isolated membrane patches on supported lipid bilayers in a calcium-containing medium (Fig. 3.2). These patches were characterized by their stable, free edges at the patch border, which served as a model for the free membrane edges at the injury site[130]. As individual annexins were added to the membrane patch, the patch displayed different morphologies, suggesting different mechanisms within the protein family. The annexin proteins were expected to induce curvature and membrane remodeling due to their structural similarities, particularly the convex shape of their membrane-binding core domain (Fig. 3.3A). Consequently, similar membrane morphologies were expected to be associated with similar ANXA amino acid sequences[131].

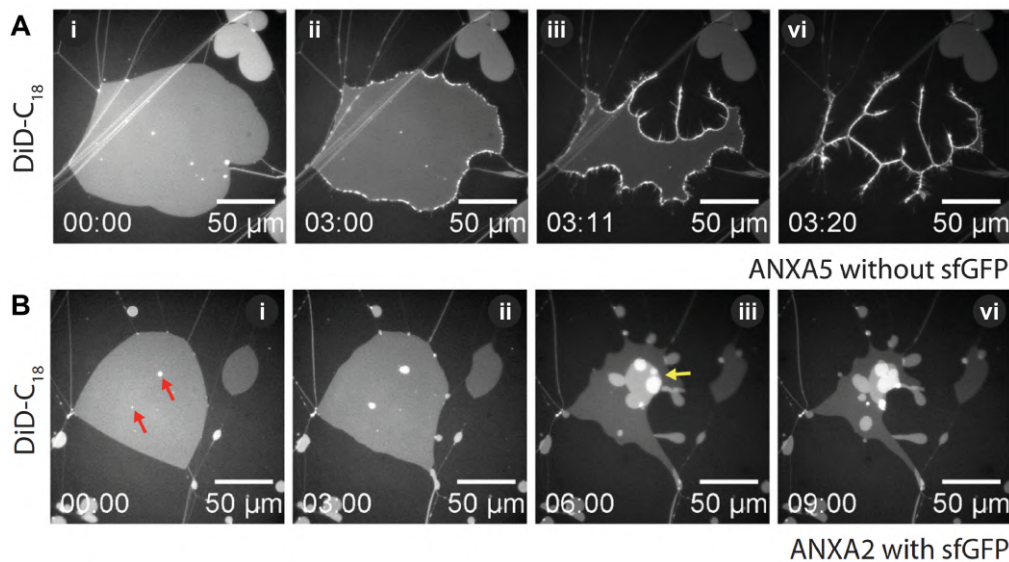


Figure 3.2: The alterations in the morphology of flat membrane patches exposed to ANXAs imply different biophysical mechanisms for the individual ANXA protein family members. This was illustrated in a series of fluorescent images displaying the response of open-edge membrane patches (DiDC18) to ANXA5 (A) and ANXA2 (B) exposure. Specifically, (A) ANXA5 induces rolling of the membrane patch, which was initiated from the free edges and eventually led to the entire patch being rolled up over time. In contrast, (B) ANXA2 induces membrane contraction and blebbing, which emanated from the initial defect sites (denoted by the red arrows) and progressed into blebs (denoted by the yellow arrows) over time. The figure was adapted from Boye et al.[131].

ANXA5 and ANXA4, two members of the annexin protein family, share several similarities, including similar amino acid sequences, sensitivity to Ca^{2+} , and the ability to self-assemble into trimers and form 2D arrays on the membrane (Fig. 3.3B) in response to membrane damage within seconds [41, 132]. Moreover, both ANXA4 and ANXA5 have been observed

to induce membrane rolling by binding to free membrane edges, ultimately causing complete rolling up of the entire cell-sized membrane patch (Fig. 3.2A), indicating their ability to induce spontaneous curvature[7, 131]. It is expected that the same curvature is generated at the injury site, where ANXA5 binds to the inner leaflet of the damaged plasma membrane in a Ca^{2+} -dependent manner. However, as the membrane of living cells does not undergo complete rolling up upon injury, Boye et al.[31] proposed that a balance between the curvature and membrane tension, resulting in the formation of a stable neck shape at the injury site (Fig. 3.5D). The curvature of a plasma membrane can be quantified by measuring the radius of a circle fitted at the point where the curvature is evaluated. This curvature can be mathematically separated into two distinct components, referred to as the principal curvatures: $c_1 = 1/r_1$ and $c_2 = 1/r_2$, representing the extreme high and low curvature, respectively, at the local point of interest[18]. In addition to the large-scale membrane rolling mediated by ANXA4 and ANXA5, ANXA3 and ANXA13 induce rolling with a fragmented morphology, observed as fragmented branches formed perpendicular to the membrane, while ANXA7 and ANXA11 induce rolling and dynamic membrane aggregates, but not vesicles[131]. While the study by Boye et al.[131] demonstrated that ANXA5 promotes membrane rolling, ANXA1, ANXA2, and ANXA6 induce membrane contraction, where ANXA1 and ANXA2 subsequently induce folding and blebbing of the membrane patch, respectively (Fig. 3.2B), indicating an ability to bind asymmetrically to membranes and thus support PMR. ANXA6's unique dimeric structure has been suggested to be the reason for the observed restriction of the membrane patch, where this constriction force enables the formation of membrane folds[131]. Interestingly, although ANXA1, ANXA2, and ANXA6 share similar sequences and are identified as membrane crosslinkers[41], they exhibit functional differences, which are thought to be facilitated by the N-terminal domain[133]. Furthermore, the two-dimensional ANXA5 and ANXA4 protein arrays surrounding the wound, combined with membrane rolling, may create substantial friction between the membrane and protein lattice, thus preventing the wound from expanding during repair. While membrane repair may also be facilitated by additional mechanisms, such as the fusion of intracellular vesicles to the rupture site (Fig. 3.3C), potentially assisted by ANXA2[16], or membrane wound constriction by ANXA6[31], their functions within cellular repair remains to be elucidated.

The translocation of ANXAs at the injury site is vital for the subsequent bending, constriction, and resealing of the damaged membrane, where their rapid recruitment suggests that this process may be regulated by changes in the plasma membrane curvature. The curved binding domain of the annexin protein could imply that it can sense curvature and, as a result, preferentially bind to a membrane with a specific curvature[129]. Moreno et al.[63] investigated this ability by extracting nanotubes from giant plasma membrane vesicles (GPMVs) containing annexins, revealing that ANXA5 and ANXA4 are sensitive to curvature as they accumulated within the nanotube with high membrane curvature. In contrast, ANXA2 showed

no affinity for curvature. The observation that ANXA5 and ANXA4 are capable of sensing curvature[63], and trimerizing and inducing rolling of membranes[6], supports the hypothesis that trimerization is a critical aspect of curvature sensing. This finding links the shaping of the membrane and curvature sensing in a feedback loop, where the initial curvature sensing leads to further recruitment of additional annexins, thereby amplifying the response to the bending of the membrane[7]. While ANXA2 can generate curvature upon binding, it lacks the ability to sense cylindrical curvatures, which suggests that ANXA2 could be recruited by higher membrane curvatures than investigated by Moreno et al.[63] or that it is recruited through alternative mechanisms[131].

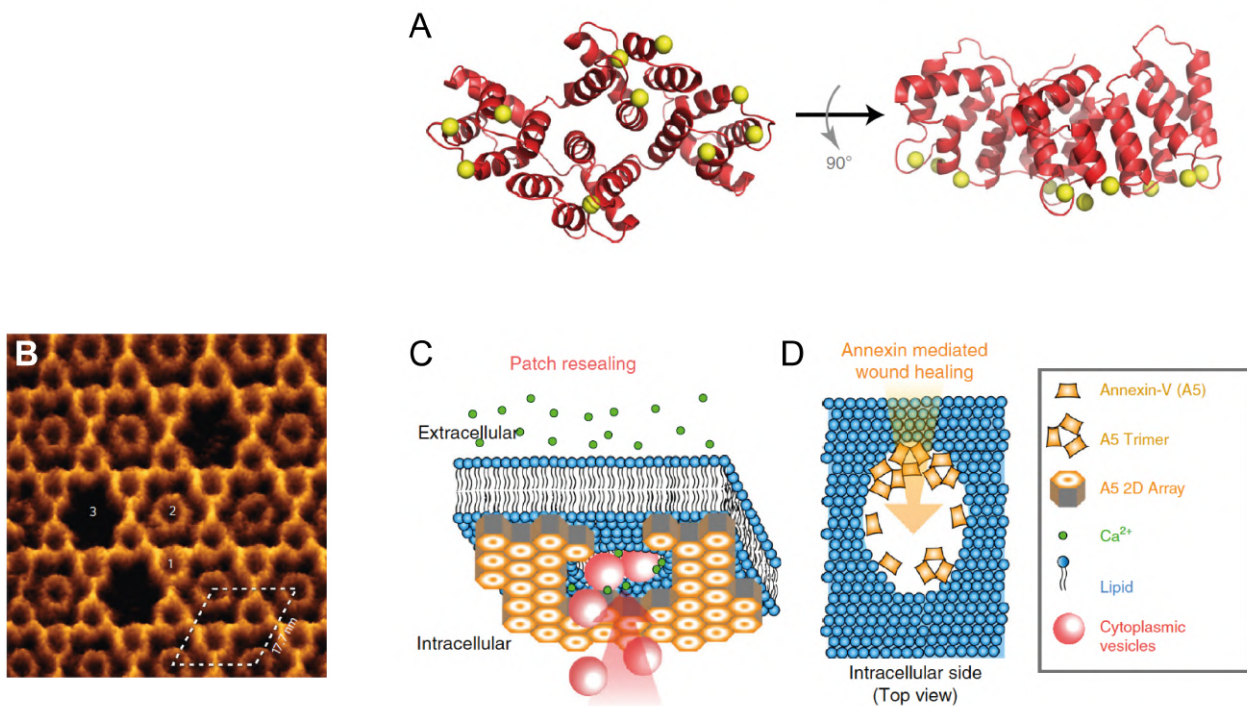


Figure 3.3: Structure and function of Annexin A5 (ANXA5). (A) The ANXA5 structure (PDB: 1A8A) is viewed from the bottom (left) and the side (right). The membrane binding core domain, which is slightly curved, is bound to calcium ions represented by the yellow spheres. (B) The high-resolution AFM topography image of ANXA5 grown on a lipid bilayer in the presence of calcium shows the ANXA5 oligomerization pattern of the two-dimensional array (scaffold). Two PMR models are proposed to be mediated by ANXA5 upon Ca^{2+} influx: patch resealing (C) and annexin-mediated wound healing (D). For the patch resealing model (C), the ANXA5 scaffolds at the injury site aid in stabilization and prevent further expansion of the wound, which is followed by patching of the wound via intracellular vesicle fusion. The annexin-mediated resealing model (D) is facilitated by ANXA5 assembling along the wound's edge promoting wound closure. Figures A, C, and D are adapted from Lin et al.[127] and Figure B is adapted from Miyagi et al.[132].

3.2 The ANXA response to thermoplasmonic-induced membrane disruption

A variety of techniques have been devised to cause mechanical and chemical damage to cell membranes. Of particular note, these techniques have revealed the recruitment of the proteins necessary for membrane repair, including annexins, actin, and ESCRT-III, to the site of membrane injury, which has also been observed upon laser-induced damage. This indicates that laser-induced plasma membrane injuries may offer valuable insights into the mechanisms underlying membrane repair since all types of injuries converge at the point of Ca^{2+} influx, which is a key stimulus for plasma membrane repair[7].

This chapter explores the response of annexin proteins, specifically ANXA5 and ANXA2, to membrane disruption inflicted by thermoplasmonics, as detailed in Sections 3.3 and 3.4, respectively. To observe the protein response to membrane injury, human embryonic kidney (HEK293T) cells were transfected with either ANXAs fluorescently tagged with GFP, as illustrated in Figure 3.4A.

To generate local membrane injuries, a focused NIR laser ($\lambda = 1064 \text{ nm}$) was utilized, given its low interaction with biological tissue[71]. The heating generated by a 200 nm AuNP upon irradiation with the NIR laser was predicted in Figure 2.4B (denoted by the blue line) using Mie theory, where the heat is highly confined to the radius of the particle from its surface in all three dimensions as it decreases rapidly with the distance from the AuNP center. The extent of the injury can be controlled by adjusting the size, shape, and composition of the nanoparticle as well as the laser power, generating injuries from nanometers to several micrometers in size. This phenomenon was exploited to create highly localized membrane ruptures, where the response of the fluorescently labeled proteins can then be monitored with optical microscopy, with a time resolution of less than one second.

It is worth noting that the use of low laser power can generate membrane permeabilization[134], whereas high laser power can result in temperatures around the NP that surpass the boiling point of water, even if the glass surface has a cooling effect. According to the study by Bendix et al.[74], which was based on direct measurements of AuNPs on supported lipid bilayers, the formation of nanobubbles (NB) surrounding the NPs occurs between 200 and 300 °C. The initiation of nanoscale bubbles can be explained by the classical nucleation theory, where the formation and expansion of the bubble, according to Laplace Law, are caused by an increase in pressure within the bubble, as denoted in Equation 3.1 [135]. As a result, the surface tension of the bubble is heightened, leading to an effective increase in the boiling temperature.

$$P_{NB} = P_{\infty} + \frac{2\gamma}{a} \quad (3.1)$$

In this context, the pressure existing within the nanobubble, denoted as P_{NB} , can be described in terms of three key factors: the surface tension of the air-water interface (γ), namely the nanobubble surface tension, the ambient pressure (P_∞), and the radius of the nanobubble (a).

However, the expansion of the bubble can be counteracted by an energy barrier, as given by the Equation 3.2 [135]. This energy barrier represents the minimum amount of energy required to establish an air-water interface, which must be surpassed for the bubble to expand. These phenomena contribute to the observed superheating in liquid water, a state wherein the liquid is heated beyond its boiling point, reaching temperatures of 220 °C or higher[74, 135, 136].

$$\Delta E = 4\pi a^2 \gamma \quad (3.2)$$

Taken together, the surface tension of the nanobubble results in an increase in the boiling temperature relative to bulk water. This finding is supported by the study of Sasikumar et al.[136], which used molecular dynamics simulations to examine the heat transfer characteristics surrounding a strongly heated nanoparticle in a fluid. The results revealed that NB formation indeed occurs at temperatures exceeding 200 °C, where the likelihood of bubble formation and expansion increases with increasing surface curvature of the particle. Additionally, the presence of bubbles was also proven experimentally by Baffou et al.[135], who investigated the characteristics of NBs formed from plasmonic nanoparticles in water, revealing that these bubbles consist solely of air molecules and not of vapor or steam as otherwise assumed.

If bubble formation occurs on or around a particle, thermal conduction away from the particle is impeded due to the insulating effect of the air-water interface. This leads to a notable increase in temperature and NB expansion, which, in turn, creates a positive feedback loop as long as the particle continues to absorb photons[70]. This often results in either particle displacement from the laser focus or particle fragmentation. It is important to note that gold nanoshells cannot tolerate high temperatures and will degrade under these conditions, as observed by high-resolution microscopy[78]. Once the laser heating is turned off, the system is expected to return to a state of equilibrium, causing the bubble to shrink. Baffou et al.[135] reported that the duration of this process can vary from seconds to several hours, depending on the initial radius of the bubble. The shrinkable of the bubble can be approximated using Equation 3.3 [135]:

$$\tau_{NB} = \frac{P_\infty K}{6RTD\gamma} a^3 \quad (3.3)$$

Where the lifetime of the nanobubble (τ_{NB}) is proportional to the volume of the bubble (a^3). Additionally, P_∞ signifies the ambient pressure, K represents the Henry coefficient, R denotes the gas constant, T signifies the nanobubble temperature, D stands for the diameter of the

laser beam, and γ represents the surface tension of the air-water interface. This simplified formula revealed that bubbles with a radius smaller than one micrometer will shrink within one second[135].

The membrane ruptures in this study could therefore be a result of small transient nanobubbles or simply due to membrane poration by local heating. Nevertheless, to achieve optimal imaging of the response of ANXA to thermoplasmonic membrane rupture, single nanoparticles were immobilized on the glass surface beneath the cell, allowing for a two-dimensional visualization of the injury (Fig. 3.4 B and C).

The results revealed an immediate influx of Ca^{2+} upon membrane rupture, which is necessary for the binding of ANXA to the plasma membrane as part of the PMR machinery. The Ca^{2+} influx triggered a translocation and upconcentration of ANXA5 and ANXA2 around the site of injury (Fig. 3.4C). To minimize the thermal impact on the cell, the particles were briefly irradiated for about one second. After a few seconds, ANXA5 and ANXA2 had formed a stable ring-like structure around the wound, as depicted in Figure 3.4D and E, respectively. These observations were consistent with previous studies on ANXA5[128] and ANXA2[116], where a similar response to plasma membrane injuries was reported using a pulsed laser source[31, 56]. The ANXA2 and ANXA5 responses and translocations were comparable, with objectively similar ring structures (Fig. A.1), varying in size and shape. This variability may arise from several factors, including cell-cycle conditions, temperature differences resulting from nanoparticle heating, ANXA transfection efficiency, or the extent of cell attachment to the glass surface in the vicinity of the wound. In some cases, only a fraction of the ANXA ring was evident (Fig. A.2), which could be due to asymmetric adhesion of the plasma membrane to the surface, interaction with the actin cortex beneath the plasma membrane, or an unfavorable membrane disruption in certain parts of the injured membrane.

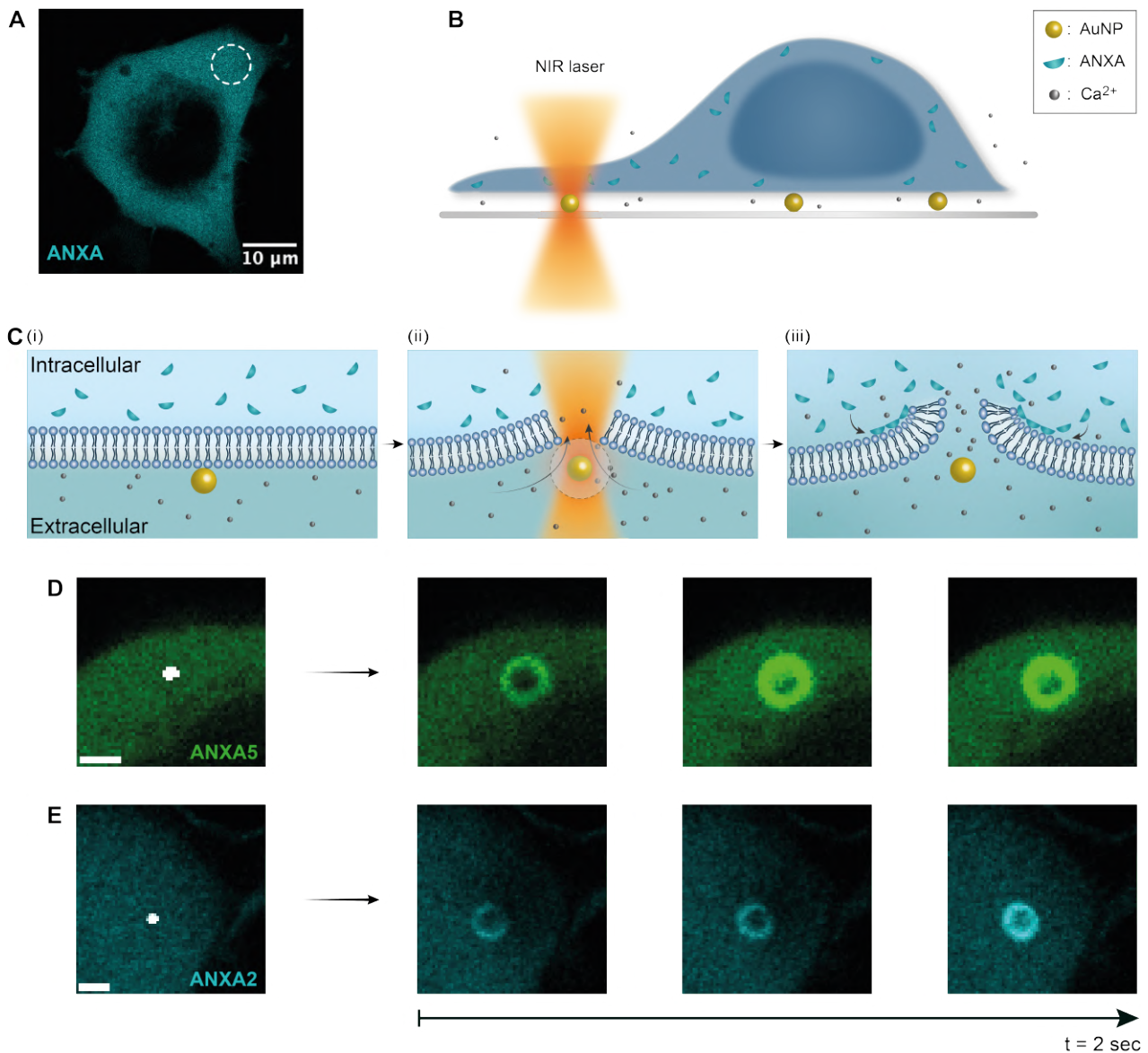


Figure 3.4: The thermoplasmonic approach and the ANXA response to plasma membrane rupture. (A) HEK293T cells expressing ANXA (B) were located on top of immobilized AuNPs located on the surface. (C) A region of interest is schematically illustrated, (i) where the plasma membrane (PM) serves as an initial barrier between the intracellular and extracellular environments, with cytosolic ANXA proteins present in the former and Ca^{2+} ions present in the latter. (ii) Upon irradiation with a 1064 nm NIR laser, the nanoparticle generates significant heat, possibly leading to the formation of nanobubbles at the AuNP surface, resulting in PM rupture and an immediate flux of Ca^{2+} into the cell. (iii) This results in activation of the PMR machinery and the recruitment of ANXAs to the site of injury, where they bind to negatively charged phospholipids on the inner leaflet of the damaged membrane. The confocal imaging of ANXA5 (D) and ANXA2 (E) demonstrates rapid ANXA recruitment to the injury site, forming a ring-like structure around the wound within seconds. A typical region of interest is indicated by the dashed circle in panel A, and the irradiation site is represented by the reflection of the AuNP (white dot) prior to laser irradiation, as shown in panels D and E. Panels D and E are accompanied by scale bars measuring 2 μm .

Cell viability was evaluated by assessing the binding of ANXA5 and ANXA2 to internal

membranes, a common approach used in cell viability studies to demonstrate apoptosis[137]. Excessive Ca^{2+} influx induces ANXA5 translocation from the cytosol to the internal membranes, which was observed to occur within seconds to a few minutes upon cell apoptosis. The majority of thermoplasmonically injured cells exhibited no ANXA5 or ANXA2 binding to the internal membranes, except at the wound site, indicating successful repair. Membrane ruptures and subsequent ANXA responses followed by cell death or injuries resulting from AuNP aggregation were excluded from the analysis of the ANXA response in membrane repair.

As previously mentioned, temperatures exceeding ~ 220 °C can generate nanobubbles on the surface of AuNPs [74, 135, 136], depicted in Figure 3.4C(ii), which can cause tremendous heat and rip the membrane apart at the injury site. Additionally, to achieve optimal precision and efficacy of membrane disruption, it is essential to ensure that the axial position of the laser focus coincides with the confocal focus. This alignment optimizes the intensity of AuNP imaging, leading to a maximum local temperature increase and therefore membrane injury at lower laser power[73]. However, as the alignment of the laser focus with the particle's location is a manual process, it may create a variation in membrane rupture efficiency and subsequently contribute to the varying ANXA ring sizes. Despite this potential limitation, the thermoplasmonic approach provides a unique tool for studying cellular responses and plasma membrane repair in a nearly native environment, almost without compromising cell viability.

3.3 Annexin A5 response to plasma membrane rupture

The primary aim of this study was to investigate the annexin A5 (ANXA5) protein response upon plasma membrane repair (PMR) triggered by the influx of extracellular calcium. To achieve this, the thermoplasmonic approach was utilized to disrupt the plasma membrane (see Section 3.2). The main findings of this investigation revealed that ANXA5 accumulates around the site of injury, where the geometry of the wound and the ANXA5 ring structure remained constant throughout time and space. A previously proposed mechanism for PMR involved an inward bending and contraction of the membrane wound, resulting in the formation of an inward budding membrane funnel. However, the present findings did not support this model, suggesting an alternative ANXA5-mediated PMR mechanism taking the complexity of the cellular environment into account. This model was based on the ability of ANXA5 to induce membrane curvature and rolling, and the membrane tension imposed by the underlying actin cytoskeleton, hereby folding the plasma membrane on top of itself facilitated by ANXA5's N-terminal domain. ANXA5 was suggested to mediate PMR by preventing further expansion of the wound, leading to successful membrane restoration through additional repair mechanisms.

3.3.1 Annexin A5 mediated repair

ANXA5 is known to create scaffolds on the plasma membrane in the presence of elevated calcium levels[127]. Furthermore, ANXA5 has been found to induce membrane curvature and roll membrane edges[131], as well as sense curvature[63]. Upon cell membrane disruption, the injury site has been proposed to be formed into a neck shape (Fig. 3.5C) due to a balance between the induced curvature (Fig. 3.5B) and the tension imposed by the underlying actin cytoskeleton[31]. This ultimately results in the inward budding of the injury site and the formation of a funnel shape[31]. Despite these reports, the response of ANXA5 to highly confined PM injuries in living cells induced by thermoplasmonics remains unexplored. As a result, the focus of this investigation will be to explore this area of research in greater depth.

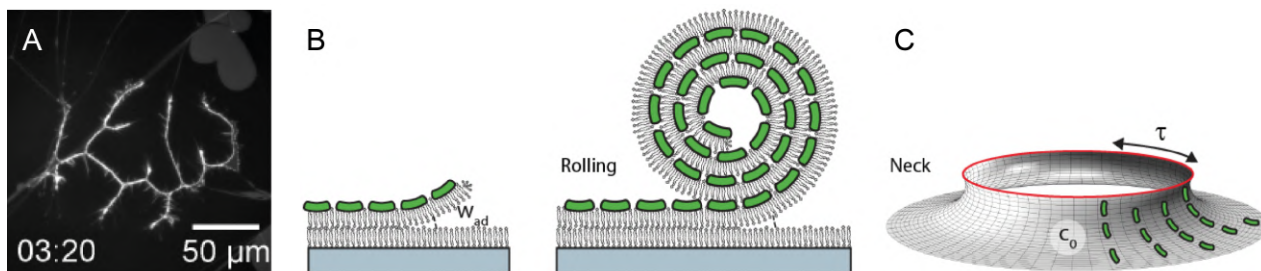


Figure 3.5: The confocal image (A) and schematic illustration (B) demonstrate ANXA5’s ability to induce curvature on a flat membrane patch in the presence of calcium. (B) ANXA5 (green) binds to the free edges of the membrane patch, representing the free edges at a wounded membrane[130], and induces spontaneous curvature. This results in a rolling morphology of the patch with a membrane adhesion energy, w_{ad} . (C) This mechanism is applied to the geometry of a wounded plasma membrane, where the edge tension (τ) and spontaneous curvature (c_0) cooperate to create a stable neck conformation. The figure was adapted from Bendix et al.[7].

This study utilized both AuNPs ($d = 200$ nm) and AuNSs ($d = 160$ nm) which were irradiated with laser powers of 230-295 mW. As described in Section 2.2, the AuNSs are designed to be resonant with NIR light, while the AuNPs exhibit significant absorption in the NIR region. This property allows both particles to generate high absorption and heat upon NIR laser irradiation. Although solid AuNPs have been shown to exhibit higher thermal stability than AuNS[78, 106], they need to be slightly larger in diameter than AuNS to achieve the same heating.

Upon rupture of the plasma membrane, ANXA5 was observed to translocate to the injury site, which is consistent with previous observations following pulsed laser irradiation. Interestingly, the ANXA ring-like structure surrounding the wound has been observed to persist up to one hour, contrary to recent findings reported by Boye et al.[31], where the ANXA accumulation disappeared from the injury site within 15 seconds. Although the previous study investigated ANXA4, given the similarities between ANXA5 and ANXA4, it was expected that ANXA5 would similarly bind to the wound perimeter, induce curvature, and generate a wound neck-like membrane formation associated with the proposed funnel geometry of the wound[31], as depicted in Figure 3.16.

In some cases, ANXA5 rings were observed to span up to several micrometers. The size of these ring structures can be explained by the factors mentioned previously, such as varying rupture efficiency or NB formation, which can lead to explosive heat generation and larger injuries. As depicted in Figure 3.11A and 3.11B, two injuries enclosed by an ANXA5 ring, measuring ~ 2.3 and $3.2 \mu m$ in diameter, were observed in the same cell. The presence of cytosolic ANXA5 following plasma membrane disruption indicates that the cell has undergone successful repair. Larger injuries were observed to exhibit a cytosolic signal within the ANXA5 ring’s otherwise dark center (Fig. 3.13A), an observation not made for smaller in-

juries or ANXA2 ring structures. Assuming the wound takes the shape of an inward-budding funnel, the cytosolic ANXA5 signal in the center of the injury could be attributed to the funnel’s top sagging down into the focal plane due to the wound’s size or to cytosolic content being fused to the edges of the neck mediated by other PMR mechanisms (Section 3.1). Hence, future investigations into endosomal and lysosomal recruitment and translocation would be of great interest to gain a better understanding of the events occurring inside the wound.

3.3.2 Analysis of ANXA5 at the wound perimeter

To investigate whether individual annexins affect the perimeter of the wound differently, the annexin ring diameters were quantified based on the full-width-half-maximum of the intensity line profile, as demonstrated in Figure 3.6B. Specifically, the radius of the ring was calculated by measuring the distance from the center to the external radius of the curve (R_{ext}) of the collapsed intensity profile (Fig. 3.6D). A total of 135 cell injuries were analysed[54], and the resulting ANXA5 ring sizes were presented in a histogram, as displayed in Figure 3.6C. The heterogeneous distribution of ANXA5 ring sizes, ranging from hundreds of nanometers to several micrometers, implicates a variation in the efficiency of PMR within the same cell line. Such variations could be attributed to the factor mentioned earlier (see Section 3.2).

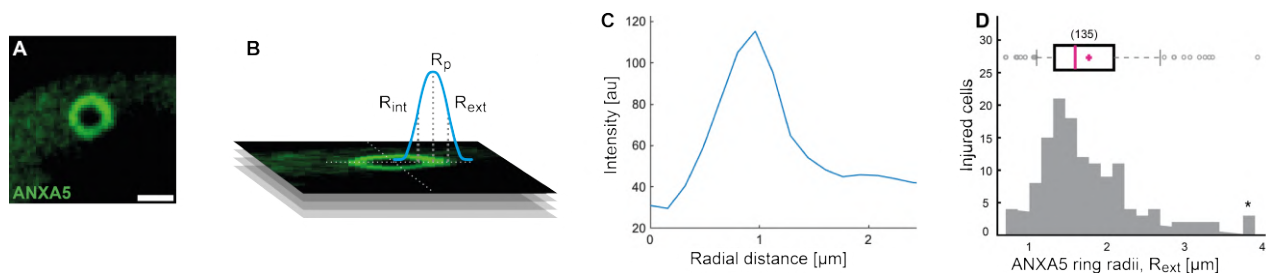


Figure 3.6: The ANXA5 ring sizes surrounding the wound sites were quantitatively analyzed. (A) The confocal fluorescence image depicts an ANXA5 ring structure obtained by thermoplasmonic membrane disruption in HEK293T expressing ANXA5-GFP, with a scale bar measuring 2 μm . (B) The ANXA5 ring size analysis is based on the full-width-half-maximum of the intensity line profile. The ANXA intensity is scanned from the center of the ring to its outer perimeter and the averaged intensity for the entire scanning range is fitted to a one-dimensional Gaussian curve. The maximal intensity is denoted as R_p and the full-width-half-maximum (FWHM) intensities are denoted as R_{ext} and R_{int} . The radius of an ANXA ring is determined by measuring the distance from the center of the ring to the external radius, R_{ext} . (C) The typical intensity plot, derived from panel A, visualizes the fluorescence intensity line profile as a function of radial distance from the center of an ANXA5 ring. (D) The histogram displays ANXA5 ring radii measured for all experiments[54], showing a heterogeneous distribution of ring sizes. A boxplot, obtained from the histogram, is superimposed on the upper part of the graph, providing further insights into the distribution of the ANXA5 ring sizes. Figures B and D are edited from Moreno et al.[54].

Given that the wound morphology has been proposed to resemble a funnel shape budding into the cell[31], the three-dimensional structure of the membrane wound was investigated.

To achieve this, a z-stack series was employed to capture the injury from the bottom of the cell and throughout the cell cytosol. The wound geometry was determined by analyzing the intensity profile of the ANXA5 ring, as depicted in Figure 3.6B, for each slide throughout the cell (Fig. 3.7A). The coordinates for the center of the ring were held constant for all images within the z-stack, and the radius of the ANXA5 ring was calculated for all slices and fitted to first-order polynomials, giving the radius as a function of z-height for each injury (Fig. 3.7B).

Surprisingly, contrary to the anticipated decrease in ANXA5 ring radii with increasing z-height, in line with the funnel hypothesis, the ANXA5 ring radii showed no significant variation throughout the cell. This was further corroborated by the absence of a wound slope along the wound depth (Fig. 3.7C), obtained from the radius profile along the z-direction. This finding is inconsistent with the funnel hypothesis and rather suggests a cylindrical shape that extends several micrometers into the cell. Given ANXA5's ability to induce membrane curvature and rolling, the absence of an observed wound slope could be attributed to the rolling of the membrane along the inner leaflet, as depicted in Figure 3.5A and B. This rolling could potentially account for the high concentration and long-lasting ANXA5 ring structure since ANXA5 would be trapped between different membrane layers in the rolled-up membrane.

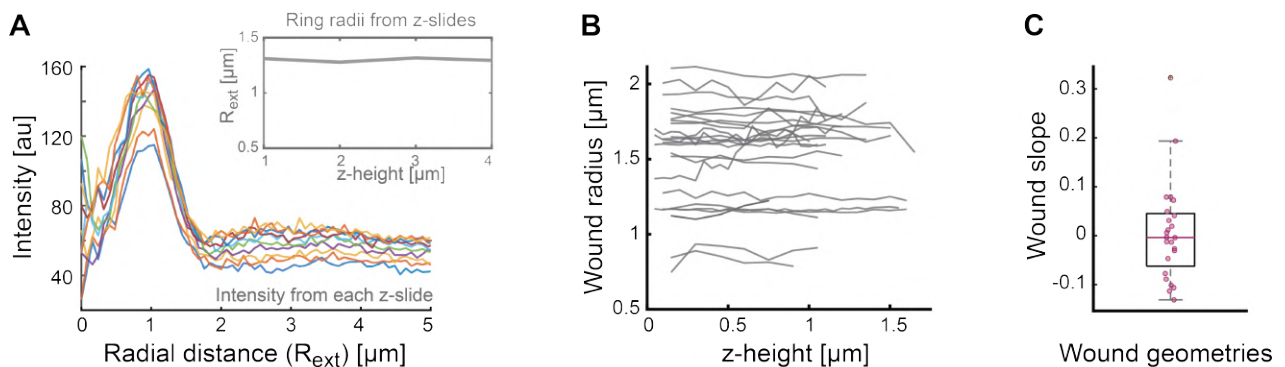


Figure 3.7: A quantitative analysis of ANXA5 ring sizes surrounding the wound along z-height. (A) The fluorescence intensity line profiles across an ANXA5 ring were obtained for each slice of the z-stack based on the workflow presented in Fig. 3.6A. The inset illustrates the variation in radius size along each slice of the z-stack. (B) The ANXA5 ring radii were determined for all slices as a function of wound depth for each injury. (C) The wound geometry is depicted as the slope of ring radius versus wound depth, which was extracted from the data in panel B. The results show a wound slope of zero for most cases. The figures are edited from Moreno et al. [54].

To investigate if the ANXA5-induced membrane rolling attribute was responsible for the absence of a wound slope, the wound, and ANXA5 ring were monitored over time, as illustrated in Figure 3.8A. The ANXA5 ring structure reached its final radius within one second following laser irradiation (Fig. 3.8C), where the intensity increase during this short time period indicates a gradual recruitment of ANXA5 to the membrane rupture. However, the width of

the wound and ANXA5 ring did not exhibit a gradual increase, which was unexpected, as ANXA5 was anticipated to induce membrane rolling of the free wound edges.

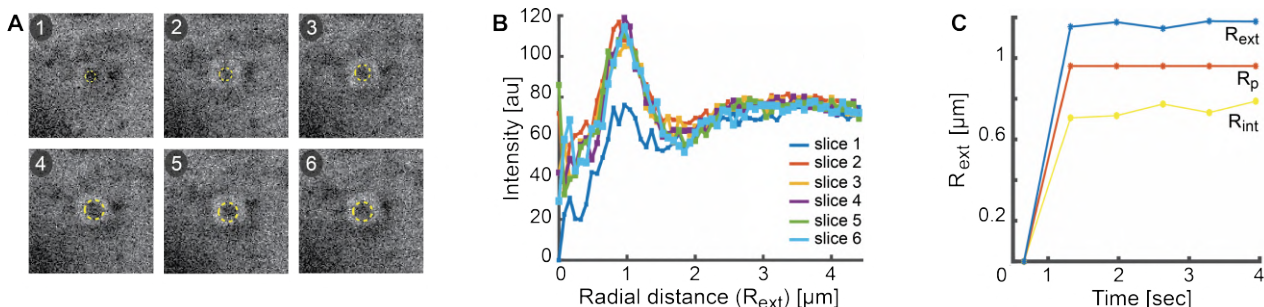


Figure 3.8: A quantitative analysis of the time evolution of an ANXA5 ring surrounding the wound. (A) The confocal images demonstrate the time-dependent evolution of a wound and ANXA5 ring, where ANXA5 is observed to accumulate at the wound perimeter immediately after injury, followed by wound stabilization. The images are captured at a time interval of 0.66 seconds per frame, denoted as frames 1-6. (B) The fluorescence intensity line profiles were generated across the ANXA5 ring for time intervals 1-6, as depicted in panel A, denoted as slices 1-6. (C) The time evolution of the ANXA5 ring radii from panel B is displayed as a function of time, showing that the ring radius remains stable following ANXA5 ring formation. The figures are edited from Moreno et al.[54].

To explore whether the lack of membrane rolling was influenced by the membrane's adhesion to the surface, Moreno et al.[54] investigated the ANXA5 repair response in the absence of surface contact. This was achieved by optically trapping an AuNP in three dimensions and inducing a membrane injury on the side of the cell (Fig. A.3D). This revealed an accumulation of ANXA5 around the injury site, which was similar to the observations in the present study, and occasionally noted a slight inward bending of the ANXA5-enriched area. To further elucidate the mechanistic effect of ANXA5 upon membrane disruption, recombinant ANXA4 or ANXA5 was encapsulated within giant unilamellar vesicles (GUVs), whereafter the vesicle membrane was locally disrupted. These findings revealed that similar to ANXA5, ANXA4 rapidly formed a ring-like structure at the injured membrane (Fig. A.3B), which then proceeded to expand the wound and eventually roll up the entire membrane (Fig. A.3C). This attribute is consistent with observations of ANXA5 function in other model membrane systems[131]. Furthermore, this characteristic was established to be a biophysical mechanism of ANXA5 and ANXA4, as injured GUV membranes, absent of ANXA, were able to facilitate rapid membrane repair by membrane line tension (Fig. A.3A).

The collective findings suggest that ANXA5 plays a vital role in plasma membrane repair of larger wounds by creating ANXA5 scaffolding around the wound perimeter, potentially enabling vesicle recruitment and clustering at the wound site[54]. Notably, ANXA5 was found to translocate only near the wound site and not to other regions of the membrane, indicating that it selectively binds to the injured membrane in the presence of high levels of Ca^{2+} . However, when the geometry of the wound was investigated in living cells following

thermoplasmonic membrane disruption, no wound slope or expansion was observed over time, indicating that ANXA5 does not induce significant inward bending or rolling of the injured membrane. Instead, the protein appears to cluster around the injury site.

3.3.3 The alternative PMR "pocket" model

Previous studies demonstrated that ANXA5 can induce curvature at free membrane edges and facilitate membrane rolling in the absence of cortical actin. However, as the present study was conducted in living cells, the presence of the underlying actin cytoskeleton acts as a rigid support and exerts tension on the plasma membrane, possibly inhibiting membrane rolling. In contrast to the proposed balance between actin-imposed tension and membrane rolling[131], the current observations did not lead to an inward budding funnel, suggesting a more intricate membrane stabilization mechanism within cells.

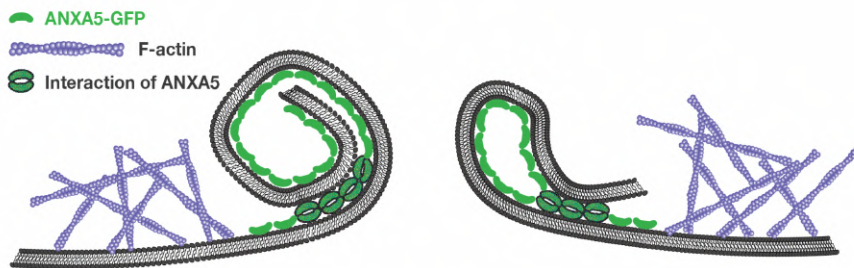


Figure 3.9: A schematic illustration of the proposed PMR “pocket” model mediated by ANXA5 at the injury site. Upon injury, ANXA5 binds to the free membrane edges, inducing a local bending of the membrane. The interaction between ANXA5 and the actin cytoskeleton prevents membrane rolling, thus inhibiting wound expansion. The membrane is then folded on top of itself, creating a membrane “pocket”, as a result of ANXA5-ANXA5 interactions facilitated by its N-terminal region. Figure adapted from Moreno et al.[54]

An alternative PMR model is proposed in Figure 3.9, suggesting that ANXA5 locally bends the membrane inwards as it binds to the damaged membrane. The membrane rolling is counteracted by the presence of the actin cytoskeleton, resulting in the membrane folding back onto itself, thus creating a membrane “pocket”. This process is mediated by ANXA5, where the N-terminal region facilitates the interaction between two ANXA5 proteins, thereby “closing” the pocket. This process is further supported by ANXA5’s ability to aggregate GUVs, creating a flat membrane contact area between adjacent vesicles upon ANXA5 addition to a GUV-containing suspension[54] (Fig. A.3E). This mechanism is believed to aid in PMR as ANXA5 extensively binds to disrupted membranes, resulting in a connected protein scaffold[128], counteracting wound expansion while enabling other membrane repair components to access the injury site and facilitate PMR, such as intracellular vesicle recruitment, vesicle clustering, and fusion at the injury site.

Notably, if the temperature around the AuNP exceeds 200 °C, a nanobubble may nucle-

ate from the nanoparticle[70, 74], generating significant heat that could explosively displace the membrane from the injury site. In this case, ANXA5 is still expected to bind to the damaged membrane and mediate PMR via the "pocket" formation. Furthermore, this proposed model for ANXA5-mediated PMR aligns well with the heterogeneity of the ANXA5-ring structures obtained throughout this study, as it potentially leads to a variation in rupture and wound size. Although the wound is stabilized and successfully repaired, the exact mechanism involved in the process and what occurs within the wound require further investigation.

Actin accumulation at the injury site

The "pocket" model proposes that the actin cytoskeleton plays a role in inhibiting ANXA5-mediated membrane rolling[131], which could involve local actin polymerization at the site of injury[31]. Figure 3.10 presents initial findings that support this hypothesis demonstrating that actin accumulates at the wound site and forms a ring-like structure similar to that of ANXA5. Moreover, the recruitment and participation of actin following thermoplasmonically induced PM disruption further corroborate the proposed "pocket" model, where its presence suggests that actin may counteract membrane rolling while also strengthening the damaged membrane, thereby enabling cooperative PMR mechanisms. To gain a more thorough understanding of the interaction between the actin network and ANXA5 proteins during membrane repair, it would be beneficial to repeat the experiments with both ANXA5 and filamentous actin labeling.

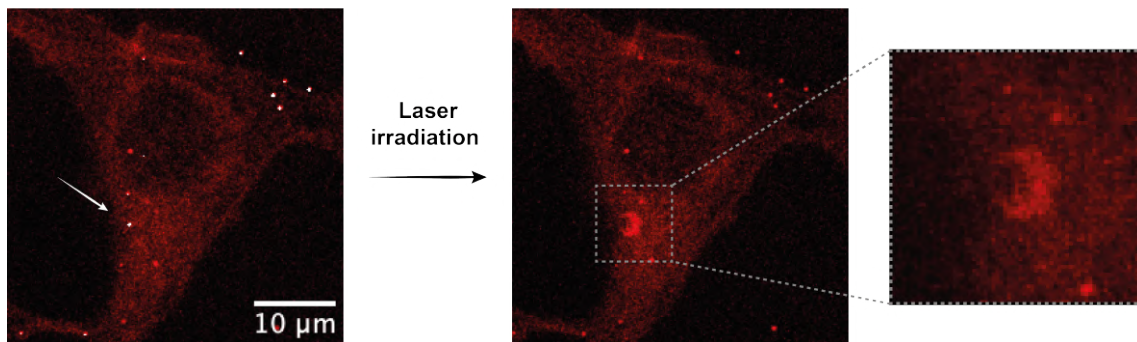


Figure 3.10: The confocal images depict a HEK293T cell where actin is labelled with SPY650-FastAct (red). The images are captured before and after NIR laser irradiation, which reveals an accumulation of actin around the injury site. The injury site is denoted by the white arrow, and the reflection of single 200 nm AuNPs is visualized as white dots.

3.3.4 AuNP encapsulation within ANXA5 rings

AuNPs were occasionally observed within the ANXA5 ring structure, as shown in Figures 3.11A and B. Prior to irradiation, the AuNPs were located at the injury site but were rapidly moved into the ANXA5 ring structure following irradiation. The displacement of the AuNPs is suggested to be a stochastic process where the AuNPs are displaced out of focus due to

the explosive heat generated upon irradiation, where their relocation could be coincidental. Furthermore, the AuNP located within the larger injury (Fig. 3.11B) was observed to move within the ring structure over time, as seen in Figure 3.11C, which was obtained ~ 10 minutes after the initial image. The movement of the particle within the ANXA5 ring suggests fluidity within the circle and could potentially be attributed to changes in lipid order within the ANXA5 ring. This hypothesis could be confirmed or dismissed by studying the variation in lipid order using the membrane order-sensitive probe, push-pull pyrene[138], or the environment-sensitive plasma membrane incorporating dye, Laurdan[127], in future experiments.

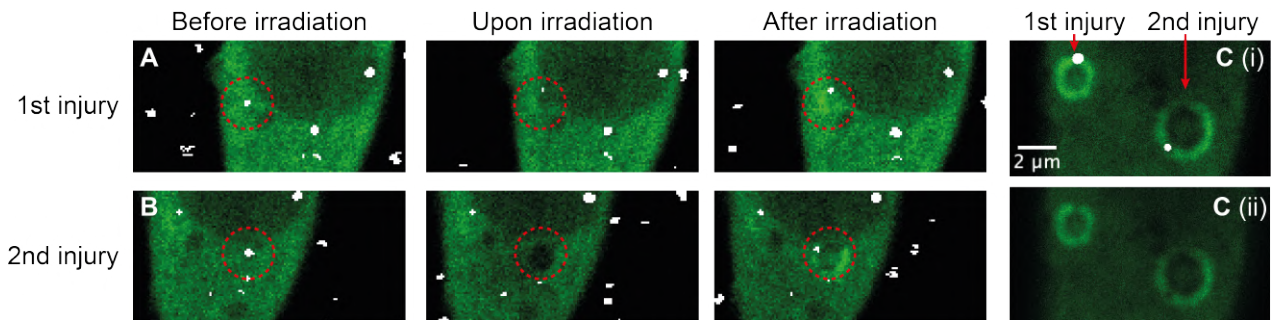


Figure 3.11: The confocal images depict a HEK293T cell transfected with ANXA5-GFP subjected to two PM injuries. (A) The first injury site exhibits an AuNP at the irradiation site (red dashed circle) that is rapidly relocated into the wound perimeter upon laser irradiation. The same process is observed for the second injury (B) where the AuNP appeared in the ANXA5 ring after laser irradiation. The confocal images presented in (A) and (B) were acquired with a 0.66-second time interval before, upon, and after irradiation. (C) The confocal image of the two ANXA5 rings was obtained ~ 10 min after the second injury. (i) The 200 nm AuNPs are visualized by their reflection, appearing as white dots, and were observed to be embedded within the ANXA5 rings. Notably, (ii) their presence appeared to inhibit the ANXA5 fluorescent signal locally.

Another potential explanation for the displacement of the AuNP could be attributed to the “pocket” model. Here, the AuNP could be captured within a membrane “pocket” that forms as the membrane is torn or bent inward, subsequently folding onto itself and the AuNP. The observation of particle movement within the ANXA5 ring may indicate that larger ruptures create larger “pockets”, or that different mechanisms are at play depending on factors such as cell cycle, extent of rupture, and membrane adhesion at the injury site.

Notably, a dark dot was observed at the site of AuNP placement within the ANXA5-GFP ring (Fig. 3.11C (ii)), which may suggest that ANXA5 is unable to bind to the AuNP-embedded membrane. However, it is more likely that the absence of GFP signal in this area is due to fluorescence quenching by the AuNP[139], as GFP is known to be temperature-sensitive[140]. This temperature sensitivity was evident during laser irradiation (Fig. 3.11B), where the GFP fluorescence signal disappeared upon laser irradiation and quickly returned after the

laser was turned off, which was a common observation. However, the exact reason for the AuNP's displacements remains unclear, while the most probable explanation would be due to a stochastic process with a coincidental relocation of the AuNP.

3.3.5 ANXA4 response to intracellular membrane disruption

The cell is subjected to physical stress and deformations throughout its entire cell cycle, which may lead to lesions and damage in both the plasma membrane and its nucleus[6, 141]. This activates the PMR machinery, in which ANXA4 is thought to play a crucial role[31]. ANXA4 has been observed to function similarly to ANXA5[131] and is suggested to prevent wound expansion and promote resealing[31, 129]. In collaboration with the Danish Cancer Society Research Center, the ANXA4 response was investigated upon nuclear envelope disruption using the thermoplasmonic approach, with a detailed description of the experimental conditions and procedures elaborated in Chapter 4. The main findings of this study revealed that ANXA4 is immediately recruited to the injury site at the nucleus, where it forms a ring-like structure, a similar response as observed for ANXA5 to PM disruption.

The nuclear membrane was visualized by labeling nucleoporin 153 (NUP153), a molecular transport regulating protein [142] that is a component in the nuclear envelope-embedded nuclear pore complex (see Section 4.1 for further information), while the cytosolic ANXA4 was labeled with RFP. Gold nanoparticles ($d = 80$ nm) localized at the nuclear membrane were irradiated (Fig. 3.12A), which resulted in an immediate translocation of ANXA4 to the injury site (Fig. 3.12B). A second irradiation at higher laser power led to the recruitment of ANXA4 around the injury site (Fig. 3.12C) forming an ANXA4 ring-structure within one second, while the nuclear membrane appeared disrupted (Fig. 3.12D, indicated by the yellow arrow). After 20 seconds (Fig. 3.12F), the morphology of the nuclear membrane appeared to have returned to its original form, while the ANXA4 ring structure remained stable and clearly visible.

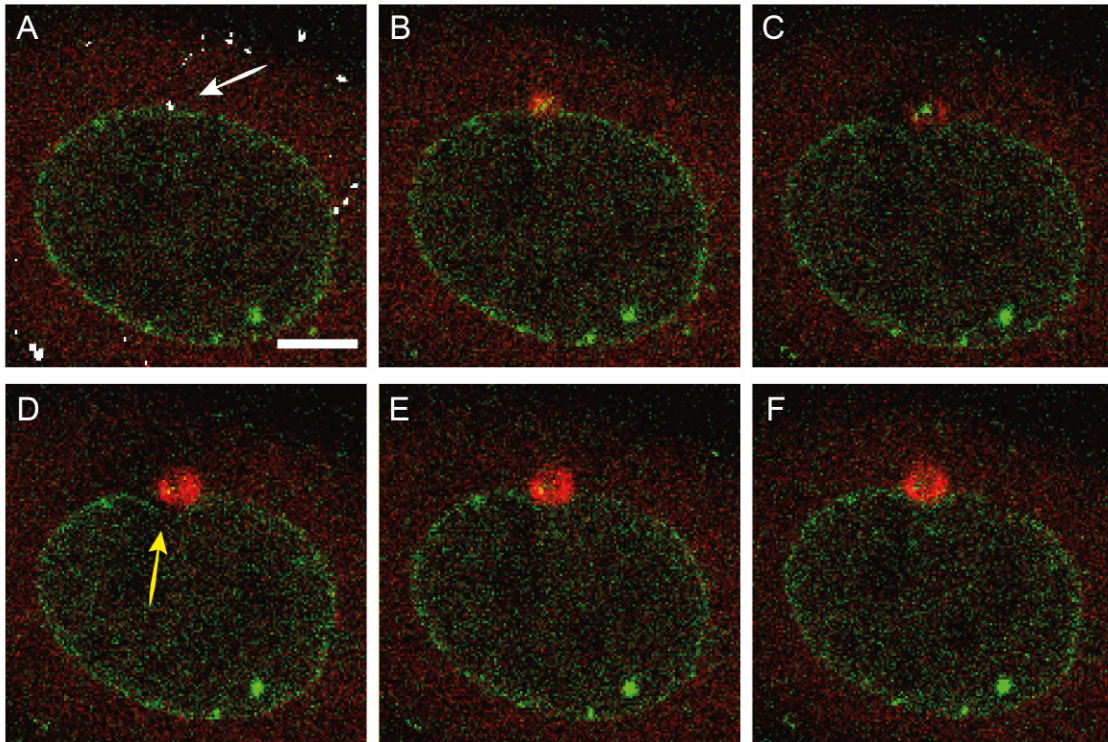


Figure 3.12: The confocal images display a MCF7 cell expressing ANXA4-RFP (red), observable in the cytosol, and NUP153-GFP (green) visualizing the nuclear envelope. (A) Prior to laser irradiation, the injury site is represented by the white arrow, and the white dots are the reflection from 80 nm AuNPs. (B) Following the initial brief irradiation, a slight yet immediate upconcentration of ANXA4 is observed. (C) Subsequently, the AuNS is irradiated once again, resulting in a slight alteration in the nuclear membrane morphology at the injury site and the formation of an ANXA4 ring-like structure. (D) 1 second after the second irradiation in panel C, a clear ANXA4 ring structure emerges, with a slight rupture of the nuclear membrane indicated by the yellow arrow. (E) 2 seconds after panel C, the image indicates an intact nuclear membrane following the curve of the ANXA4 ring. (F) Finally, the image captured 20 seconds after panel C shows a clear and stable ANXA4 ring structure and a slight recovery of the previously deformed nucleus. The scale bar measures 5 μm .

The irradiation of AuNPs at the nucleus can cause disruption of the nuclear envelope as well as permeabilization of the plasma membrane. ANXA4 was observed to accumulate at the nuclear envelope regardless of nuclear membrane or plasma membrane disruption (data not shown). Although the recruitment of ANXA4 to the wound area may be triggered by extracellular Ca^{2+} influx upon PM permeabilization, ANXA4 was not observed to accumulate at the plasma membrane in the present study. This suggests that the recruitment of ANXA4 is initiated by Ca^{2+} bursts from intracellular Ca^{2+} storage organelles[143]. Whether ANXA4 is aiding in nuclear membrane repair, similar to its role in PMR[31, 41], remains to be further investigated. Nonetheless, the similarity between the ANXA4 and ANXA5 responses upon thermoplasmonic membrane disruption is apparent. Further elaboration on nuclear envelope disruption and the subsequent actin response can be found in Chapter 4.

3.3.6 Concluding remarks

Although the exact function of ANXAs in membrane repair is not well understood, it is known that ANXA5 is rapidly recruited to the injury site when the plasma membrane is disrupted. ANXA5 appeared to cluster around the wound, presumably generating a local curvature; however, the study revealed no changes in the wound or ANXA5 ring geometry over time or space. Moreover, ANXA5 has been observed to induce membrane curvature and rolling of model membrane patches[131], where the rolling of the membrane edges could explain the bright, long-lasting ANXA ring surrounding the hole after thermoplasmonic membrane rupture. However, the plasma membrane is supported by the cortical actin cytoskeleton in living cells, where the tension imposed on the plasma membrane by the actin cortex possibly inhibits ANXA5 from rolling up the entire membrane, as otherwise observed in model membrane systems[41, 54, 131]. Rather, ANXA5 is suggested to locally bend the membrane inwards and fold the membrane on top of itself, forming a membrane pocket. This gave rise to the proposed PMR "pocket" model mediated by ANXA5[54] aiding in wound stabilization.

Due to limited biophysical investigations of ANXA function upon membrane rupture in living cells, assigning a specific mechanism to the observation of ANXA5 rings in response to thermoplasmonically induced membrane injury proved to be a challenge. As a result, this led to various speculations in an attempt to understand this phenomenon. These speculations were primarily based on ANXA5's ability to induce membrane curvature and rolling, plasma membrane tension imposed by the actin cortex, and the formation of nanobubbles at the AuNP surface.

The findings revealed that ANXA5 rings are formed at injury sites as a response to local membrane ruptures. These rings have a darker center, and for larger injuries, a completely dark ring could be observed within the ANXA5 (Fig. 3.13A). The mechanisms behind this observation are not clear; however, one suggestion is that the plasma membrane is explosively displaced at the injury site, leading to membrane accumulation at the wound perimeter, as depicted in Figure 3.13D1. The outer membrane leaflet, which contains fewer phosphatidylserine (PS) lipids than the inner leaflet[144], is present at the perimeter, and as ANXAs are known to bind to PS lipids[56], the annexin proteins are not expected to bind to the membrane cluster but rather to the inner leaflet in the vicinity of the hole. The dark circle, lacking ANXA5, observed within the ANXA5 ring could therefore be due to the clustered membrane. However, if this were the case, the ANXA5 ring would be expected to disappear from the injury site after membrane repair, as they have been observed to disappear from PM injury sites within 15 seconds after pulsed laser irradiation[31]. Therefore, the observations of stable, long-lasting ANXA5 rings do not support this speculation.

Another suggestion for the ANXA5 ring formation, illustrated in Figure 3.13D2, is that

ANXA5 starts to roll the membrane edges immediately after the membrane is torn open. However, before the membrane is completely rolled up to the hole perimeter, it binds to the plasma membrane. The rolled edges, decorated with ANXA5, attach to the inner leaflet of the plasma membrane mediated by the ANXA5 N-terminal domain[54], similar to the proposed “pocket” model, and could account for the prolonged observation of the ANXA5 ring around the wound. Moreover, this process is proposed to happen rapidly, where sufficient Ca^{2+} levels for ANXA5 binding may not be obtained within the membrane pocket, which could give rise to the dark, ANXA5-devoid area within the ANXA5 ring. However, if this mechanism was at play, cytosolic ANXA5 fluorescence would be expected to be observed within the pocket as well as in the rest of the cell.

To explore the content within the ANXA5 ring structure, the extracellular medium was supplemented with a small fluorescent molecule (Alexa Hydrazide 633) prior to membrane injury. The resulting observations demonstrated that Alexa hydrazide accumulated within the ANXA5 ring, at the location that was previously believed to be “dark” (Fig. 3.17C), hence within the wound, confirming the presence of extracellular content within the wound. Overall, this study highlights the challenges of fully comprehending the underlying mechanisms of plasma membrane repair and the necessity for further investigations to pinpoint the molecular components involved in membrane repair in living cells.

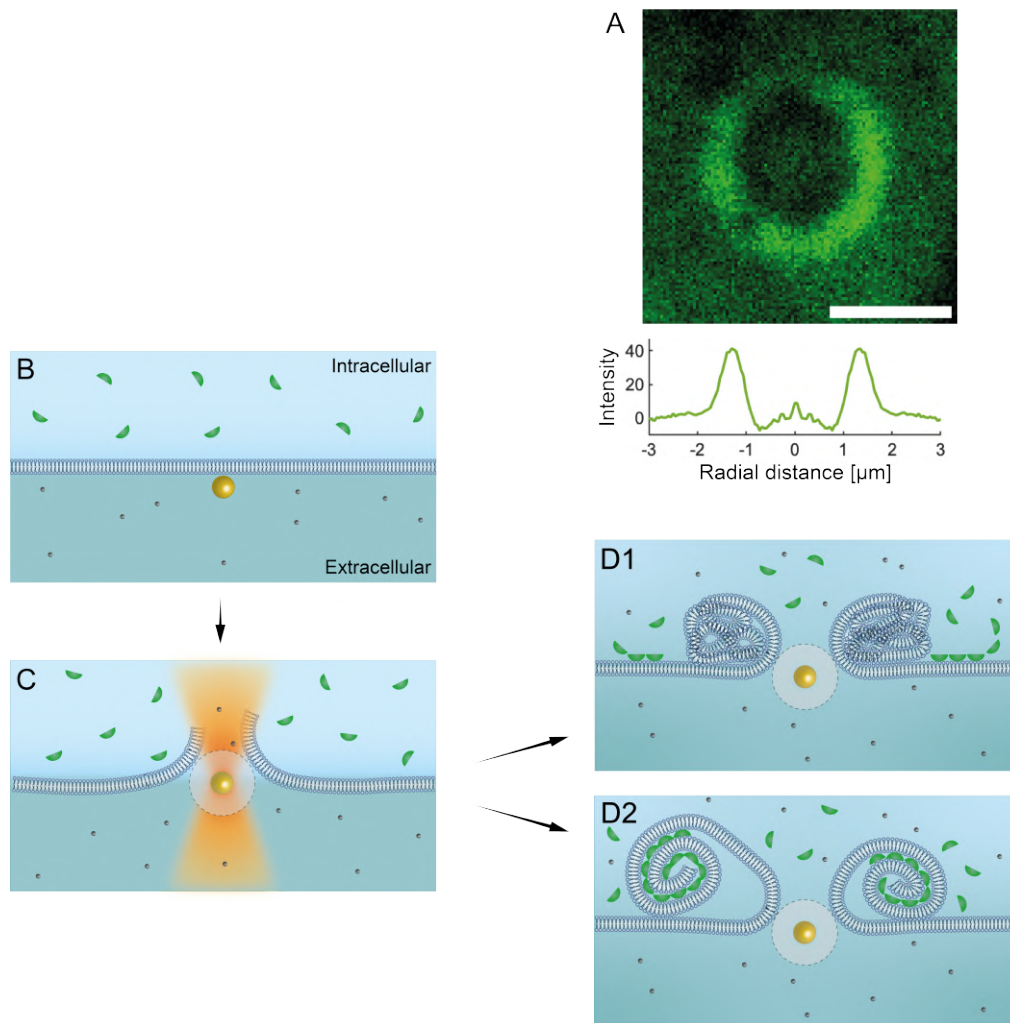


Figure 3.13: A schematic representation of the thermoplasmonic method and the ANXA response to plasma membrane (PM) rupture. (A) The confocal image depicts a PM injury surrounded by an ANXA5 ring structure, with a scale bar measuring $2 \mu\text{m}$. The corresponding intensity line profile is presented in the lower figure, where the center of the circle is situated at $0 \mu\text{m}$. The cytosolic ANXA5 intensity is depicted at the beginning of the intensity profile, followed by an increase in ANXA5 intensity at the wound perimeter, a dark circle just within the ANXA5 circle (presumably lacking ANXA5), and finally a slight increase in ANXA5 intensity at the center of the wound. (B) The PM serves as a barrier between the intracellular and extracellular milieus, where cytosolic ANXA proteins reside in the former and Ca^{2+} ions in the latter. (C) Upon exposure to a 1064 nm NIR laser, the nanoparticle generates substantial heat, leading to the formation of nanobubbles. This results in the explosive displacement of the PM and an influx of Ca^{2+} into the cell. The explosive PM rupture can lead to two scenarios, as illustrated in panel D. Firstly, (D1) the membrane can accumulate at the injury site, where ANXA5 binds to the negatively charged phosphatidylserine lipids on the inner leaflet of the damaged membrane next to the clustered membrane. Alternatively, (D2) ANXA5 can induce rolling of the membrane edges, which then rapidly bind to the inner leaflet of the plasma membrane via the N-terminal domain of ANXA5, creating a membrane “pocket”.

3.4 Annexin A2 response to plasma membrane rupture

Another main objective of the study was to investigate the response of annexin A2 (ANXA2) proteins upon plasma membrane repair triggered by extracellular calcium influx using the thermoplasmonic approach (Section 3.2). The findings revealed that upon plasma membrane repair the interplay between calcium influx and ANXA2 translocation unfolds in sequential steps, where the time of wound closure takes priority. Moreover, the biophysical mechanism of ANXA2 was investigated by disrupting the underlying actin cytoskeleton. Confocal microscopy was employed to visualize ANXA2, which revealed that ANXA2 formed a ring-like structure around the injury site in both actin-intact and actin-disrupted cells, demonstrating a consistent wound geometry and ANXA2 ring structure over time and space. However, in 25% of the actin-disrupted cells, a distinct ANXA2 response was observed, with vesicle structures protruding from the ANXA2 ring structure, resembling flower petals, hence entitling the phenomenon the “Annexin flower”. The impact of actin disruption revealed a correlation between the actin cytoskeleton and ANXA2 blebbing mechanism in human embryonic kidney cells.

3.4.1 Annexin A2 mediated repair

As evidenced by previous studies, ANXA2 has been shown to form scaffolds on model membrane surfaces[133] and promote membrane curvature[131], resulting in the contraction of the membrane into vesicular structures when exposed to high calcium levels (see Figure 3.14). It has therefore been suggested that ANXA2 binds asymmetrically to membranes, promoting curvature, and facilitating plasma membrane repair[131]. Moreover, ANXA2 does not seem to sense high membrane curvature, according to the study by Moreno et al.[63], due to its inability to form trimers, thus implying that its recruitment mechanism differs from that of ANXA5. This dissimilarity is believed to stem from structural differences between the two proteins, specifically in their N-terminal domain, which has also been postulated to be responsible for their functional differences in facilitating plasma membrane repair.

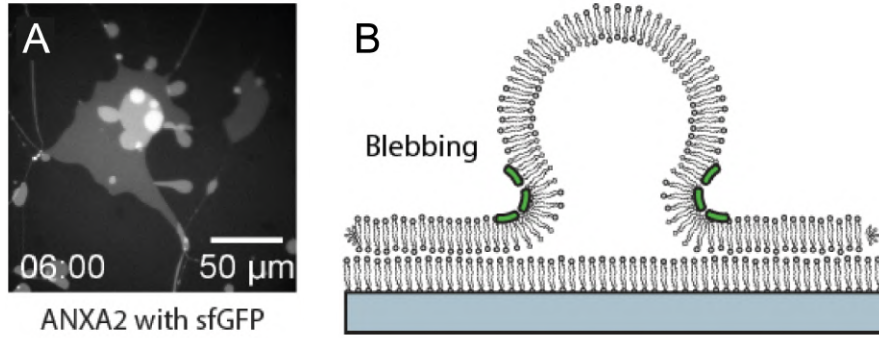


Figure 3.14: The membrane shaping ability of ANXA2 was explored on supported membrane patches. The confocal image (A) and schematic illustration (B) demonstrate ANXA2’s ability to induce curvature of a model membrane patch in the presence of calcium. (B) ANXA2 (green) contacts the membrane patch upon interaction, resulting in the formation of vesicular structures emanating from the surface, as depicted in panel A, where ANXA2 is located at the neck of the vesicle. The figure was adapted from Bendix et al.[7].

ANXA2 is predominantly found in the cell cytosol in two forms: as monomers[145] or heterotrimeric complexes with its binding partner S100A10 (ANXA2-S100A10) from the calcium-binding S100 protein family[116]. Despite having different biochemical properties, such as different Ca^{2+} sensitivity[133], both ANXA2 forms are believed to function together with the underlying actin cytoskeleton[146, 147]. Numerous studies have been dedicated to uncovering the mechanisms and strategies involved in PMR, as demonstrated in Figure 3.1. Additionally, ANXA2 has been implicated in lipid aggregation and has been shown to facilitate processes such as membrane indentation and vesicle budding, membrane-membrane interconnection, and fusion of intracellular vesicles with the plasma membrane [116, 119, 133, 144]. The ability of ANXA2 to induce blebbing on flat membrane patches[131], along with the actin-mediated repair processes[8], has given rise to the two PMR strategies, namely the purse-string contraction mechanism and the bleb formation mechanism, as depicted in Figures 3.1E and F, respectively, which will be elaborated on in section 3.4.5.1.

3.4.2 Analysis of ANXA2 at the wound perimeter

The ANXA2 response was investigated in living cells following plasma membrane injury induced by the thermoplasmonic method employing 200 nm AuNPs. As depicted in Figure 3.4D, a cell expressing ANXA2 is subjected to membrane damage, where the increase in intracellular Ca^{2+} triggers PMR. Within a second after laser irradiation, ANXA2 translocated to the injury site and formed a stable ring-like structure surrounding the wound, similar to ANXA5. These observations are in agreement with previous reports on ANXA2 response to PM disruption using a pulsed laser source[56], where ANXA2 accumulation peaked at the injury site within 35-45 seconds in HeLa cells, although molecular dynamic simulations suggest that ANXA2 binds to the plasma membrane within 500 ns[56].

The ANXA2 rings were analyzed based on the full-width-half-maximum of the intensity line profile, identical to the ANXA5 analysis discussed in Section 3.3.2. A total of 74 plasma membrane injuries were quantified, revealing a Gaussian distribution of ANXA2 ring sizes, ranging from 0.42 to 1.95 μm in radius. Since the ANXA2 and ANXA5 data were obtained under similar conditions in terms of cell type and experimental conditions, it allowed for a direct comparison of the two ANXA ring analyses. The analysis indicated a statistically significant difference between the ANXA5 and ANXA2 ring sizes (see Figure 3.15) determined by the Welsh's t-test assuming unequal variances. Notably, although the data were obtained under similar conditions, it was collected over several months, and variations in cell medium, cell condition, and transfection efficiency can lead to slight differences in the ANXA ring size. However, these variations do not compromise the statistical difference between the two ANXA rings. Additionally, the wound evolution and geometry were analyzed and found to be similar for the two cases, where both ANXA ring structures reached their final radius and maximum intensity within 1 second, which is significantly faster than reported for pulsed laser ablations[56].

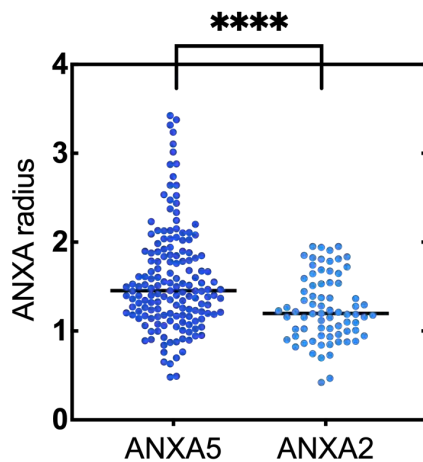


Figure 3.15: The ANXA ring radii for ANXA5 and ANXA2 are represented by the dark blue and light blue dots, respectively. The p-value, based on the statistical analysis of the ANXA rings using the Welsh's t-test (assuming unequal variances), is $p \leq 0.0001$, indicating that the ANXA5 ring sizes differ significantly from the ANXA2 ring structures.

While the ANXA2 rings were not expected to expand over time, as ANXA2 has not been reported to induce membrane rolling, the analysis did not indicate any geometrical changes in the wound along the z-height either. This suggests that ANXA2 forms a stable, three-dimensional ANXA2 ring structure that acts as a scaffold around the wound perimeter, similar to ANXA5. However, the significant difference in ANXA ring sizes could be attributed to the different functions of ANXA2 and ANXA5, where Mulaski et al.[41] reported that the two proteins translocate to different sites at the injury upon PMR, assuming the PMR "funnel" model[31].

3.4.3 The PMR funnel model

Boye et al.[31] proposed a PMR model, depicted in Figure 3.16A, for ANXA4 and ANXA6, which was subsequently expanded by Mulaski et al.[41] in Figure 3.16B to include ANXA1 and ANXA2. Both models assume that the ANXAs exist as monomers that are evenly distributed in the cytoplasm of uninjured cells and are recruited to the membrane wound edges following PM injury to facilitate PMR that is triggered by an influx of Ca^{2+} . The ANXAs were proposed to alter the shape of the wound, creating a membrane funnel that protrudes into the cytoplasm. This wound geometry was based on the biophysical mechanism of ANXA observed on flat membrane patches in the presence of Ca^{2+} [31]. The location of ANXA-mediated binding to the funnel was determined by additional membrane patch experiments with co-ANXA incubation and AFM analysis[41] as well as observing their translocation in injured MCF7 cells by UV pulsed laser irradiation, which created 1-3 μm sized injuries [31].

Similar to ANXA5, ANXA4 was found to bind to the free edges of the membrane patch, thereby inducing curvature that ultimately led to the rolling of the entire patch[31, 41]. ANXA4 self-assembles into trimers at the site of injury, thereby inducing local curvature and bending of the wounded edges into the cytosol while simultaneously restricting wound expansion[128]. ANXA1 and ANXA2, on the other hand, function as specialized membrane crosslinkers by preferentially binding to the free membrane edges and positioning themselves as recruitment sites for intracellular vesicles[41]. Prior to rolling, ANXA2 is proposed to locate at the wound edges without mixing with ANXA4 (as depicted in Fig. 3.16B), resulting in ANXA2 binding to the top of the funnel, while ANXA4 is located at the vicinity of the wound (Fig. 3.16A and B). Moreover, the PMR models suggest different binding sites for ANXA6, either mixing with ANXA4 (Fig. 3.16B) or binding to the free wound edges (Fig. 3.16A), similar to ANXA2. In both cases, ANXA6 is suggested to cross-bridge vesicles to the injury site based on its dimeric structure. Additionally, due to its ability to constrict and shrink membrane patches, ANXA6 is thought to contract the wound edges, ultimately leading to membrane resealing by intracellular vesicle fusion[31]. Finally, subsequent repair steps would include local actin polymerization and vesicle fusion to fully repair and restore the membrane after injury.

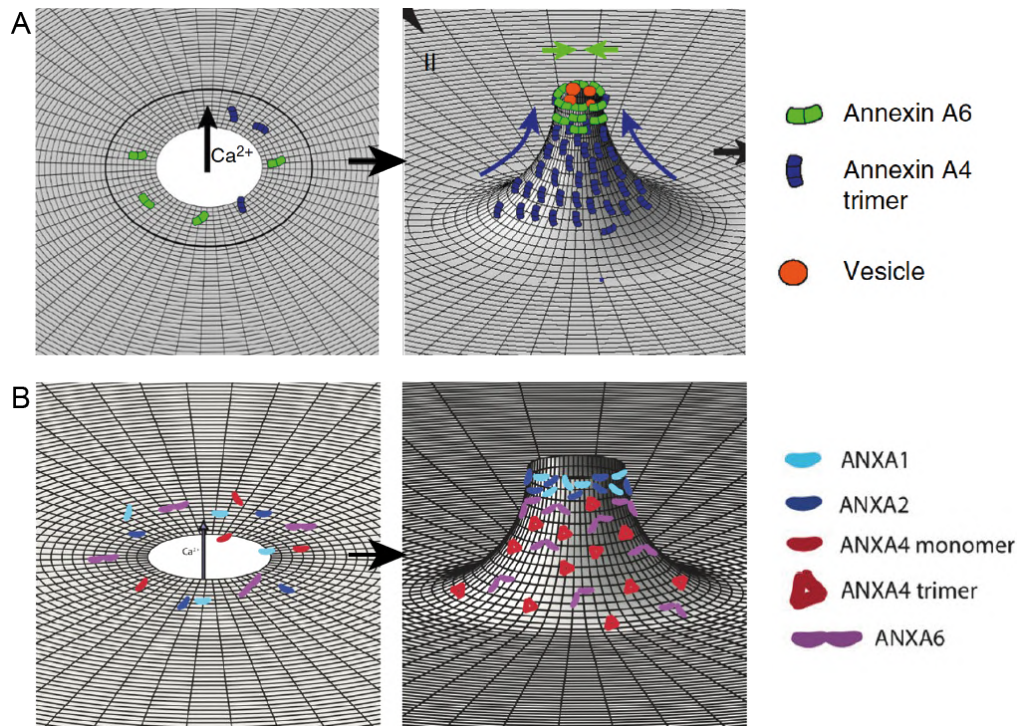


Figure 3.16: The proposed "funnel" model for plasma membrane repair is initiated by (A) ANXA4 and ANXA6 along with (B) ANXA1 and ANXA2. The ANXA proteins exist as monomers in the cytosol of uninjured cells. However, upon PM injury Ca^{2+} influx triggers ANXA recruitment to the injury site. ANXA4 subsequently self-assembles into trimers that induce a local out-of-plane curvature. ANXA6 fuses intracellular vesicles to the membrane and is either located with ANXA4 (B) or at the wound edges (A), where it also initiates wound constriction. Together, ANXA4 and ANXA6 induce curvature and wound constriction, which facilitates the funnel shape. (B) ANXA1 and ANXA2 preferentially bind to free membrane edges and position themselves as binding sites for adjacent membranes, such as intracellular vesicles. The repair process is followed by local actin polymerization and intracellular vesicle fusion to fully repair and restore the membrane. Figure (A) is adapted from Boye et al.[31], while figure (B) is adapted from Mularski et al.[41].

It is worth highlighting that the PMR models (Fig. 3.16) primarily rely on experiments conducted on model membrane patches. The cellular experiments that support these models were conducted using UV-pulsed laser irradiation, which causes membrane injuries throughout the entire cell along the propagating laser beam. While the pulsed laser-induced injury is local, the nature of the wound has not been thoroughly investigated. It can be speculated that, rather than creating a single local injury at the plasma membrane, the pulsed laser may induce membrane permeabilization, resulting in multiple nanoscopic pores forming simultaneously at the injury site. These small injuries could potentially support the proposed ANXA6-mediated membrane constriction. However, for larger injuries, the ANXA6-mediated wound constriction remains speculative, as it is uncertain how ANXA6 would be able to constrict and contract the fluid lipids at the wound edges for eventual resealing.

The results obtained by the thermoplasmonic method do not support the proposed PMR

”funnel” model, and the significant difference in ANXA ring sizes between ANXA5 and ANXA2 is therefore not suggested to be due to their locations on the membrane funnel. Instead, the study revealed that the rapid recruitment and accumulation of ANXA2 and ANXA5 occurred rapidly, implying that the ring structures are induced by an explosive rupture of the membrane, presumably caused by nanobubble formation at the surface of the AuNPs[74, 135]. The NB approach has been extensively investigated and demonstrated to be an effective membrane disruption approach[65, 148, 149, 69], where this study presumably has demonstrated its applicability in a biological system. While the nanobubble formation may make the thermoplasmonic approach less controllable than previously expected, the observed ANXA response to membrane rupture remains valid. As previously mentioned, ANXA5 and ANXA2 are known to have distinct biophysical functions[131] (Fig. 3.2), which is believed to be reflected in and quantified by their ANXA ring sizes upon thermoplasmonic PM rupture. This further suggests that the membrane rolling mechanism of ANXA5 is responsible for the generally larger size of ANXA5 rings relative to the ANXA2 rings. However, the significant difference in the sizes of ANXA2 and ANXA5 rings remains to be fully elucidated.

3.4.3.1 Wound insight through imaging of extracellular dye

Although the plasma membrane injuries can be induced by nanobubble formation facilitated by thermoplasmonic heating, ANXA2 and ANXA5 were still able to bind to the damaged membrane and enable the successful repair of the plasma membrane. However, the precise mechanisms underlying this repair process and the events occurring within the wound remain unclear. Typically, the rim of the wound is visualized as bright fluorescence due to the accumulation of ANXA at the injury site, while the center of the ring appears darker than the surrounding cytosolic content (Fig. A.1). Occasionally, a completely dark ring within the ANXA rim (Fig. 3.17C (ii)) is observed, suggesting a region devoid of ANXA.

To investigate the content and geometry of the wound, a small far-red fluorescent molecule, Alexa Hydrazide 633, was added to the extracellular medium before injuring the plasma membrane. Following rupture, ANXA2 (Fig. 3.17A (ii)) and ANXA5 (Fig. 3.17C (ii)) immediately translocated to the site of injury, forming a ring structure as previously reported. Alexa hydrazide 633 was observed to accumulate inside the ANXA ring, confirming the presence of extracellular content within the wound. Figure 3.17A and Figure 3.17C depict the three-dimensional wound structure by z-stack imaging from the cell surface into the cytosol. The images show Alexa hydrazide with either ANXA2 or ANXA5, respectively, at the site of injury, where Alexa hydrazide appeared to form a ring structure within the ANXA ring (Fig. 3.17B and D). The ANXA and Alexa hydrazide rings are presumed to co-exist on each side of the plasma membrane and extend along the z-height into the cell until both fade away, leaving only the ANXA cytosolic signal (Fig. 3.17A). It is assumed that the wound has been repaired at this point and does not extend beyond this z-height. Local actin polymerization is

believed to follow the repair process to fully restore the membrane after injury[31]. However, the exact events occurring within the wound, besides containing extracellular content, remain unknown.

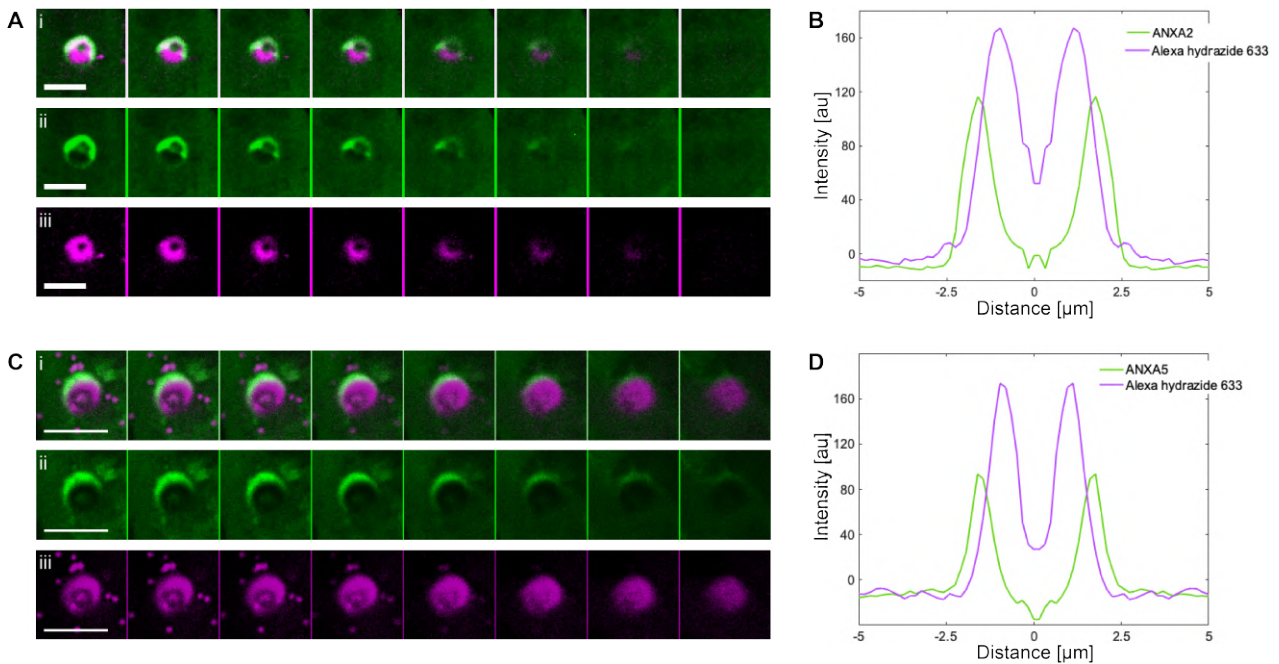


Figure 3.17: The confocal images depict a plasma membrane injury in HEK293T cells. The images were acquired as a z-stack series, starting at the membrane surface and progressing into the cell, with scale bars measuring 5 μm . To investigate the content and geometry of the wound, Alexa hydrazide 633 (iii) was added to the extracellular medium, while ANXA2-GFP (A,ii) and ANXA5-GFP (C,ii) were observed around the injury site. The intensities of both Alexa hydrazide and ANXA were quantified as a function of distance from the center of the ring, where the ring radii were determined based on the full-width-half-maximum of the intensity line profile. (A) The ring radii for ANXA2 were measured to be 2.15 μm and 1.59 μm for Alexa hydrazide, while (D) the ring radii for ANXA5 measured 1.91 μm and 1.35 μm for Alexa hydrazide.

3.4.4 Actin disruption by inhibition of actin polymerization

The plasma membrane is closely associated with the underlying actin cytoskeleton, which both provides structural support and exerts tension on the membrane[150]. When the cell membrane undergoes rupture, a rapid influx of extracellular Ca^{2+} occurs, triggering actin cytoskeletal remodeling. The Ca^{2+} influx promotes depolymerization of actin filaments, thereby reducing tension near the injury site[122]. This is followed by a rapid re-polymerization that reinforces the cortical actin at the injury site[122, 123], which is believed to counteract repetitive injuries as an adaptive strategy[31]. Jaiswal et al.[52] reported that the ANXA2-S100A11 complex mediates F-actin polymerization at the injury site, linking the actin cytoskeleton to the plasma membrane and defining the repair site. Moreover, the ability of ANXA2 to restrict actin depolymerization and promote new actin formation at the injury site has been suggested to enable contraction of the plasma membrane and the underlying actin cytoskeleton via ac-

tomyosin ring formation[6], clearly indicating a correlation between ANXA2 and the actin network.

To explore the response of ANXA2 to plasma membrane rupture, in an environment that lacks the constraints imposed by the actin cortex in living cells, an *ex vivo* condition was employed by disrupting the actin cytoskeleton using the actin-depolymerizing drug Cytochalasin D (CytoD). This prevented the association and dissociation of actin monomers, hereby disassembling filamentous actin and inhibiting further polymerization[151, 152]. Following this treatment, the plasma membrane was disrupted by brief NIR irradiation of surface-immobilized 200 nm AuNP with a laser power of ~ 230 mW. The intact actin cytoskeleton, visualized by the SPY650-FastAct fluorescent dye, was homogeneously dispersed within non-treated cells (Fig. 3.18A), whereas the disrupted actin network (Fig. 3.18B) appeared agglomerated at the cell periphery. Although actin filaments were still present, the cortical actin network was not expected to function optimally.

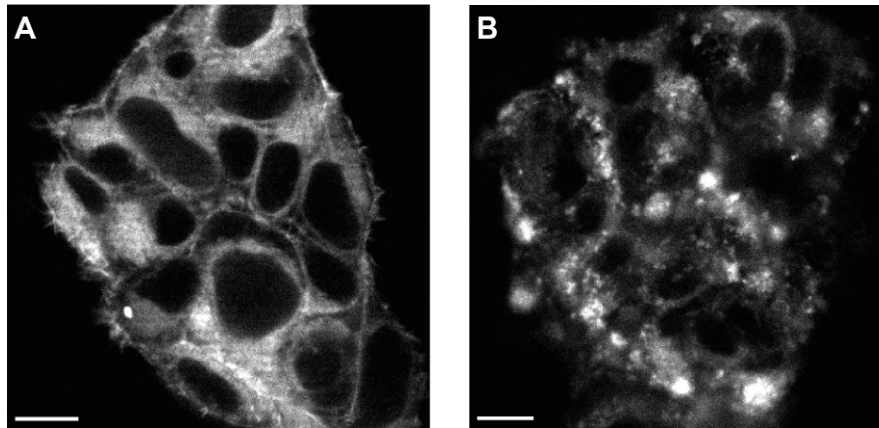


Figure 3.18: The confocal images of HEK293T cell clusters, wherein actin was labeled with SPY650-FastAct showcase (A) the intact actin cytoskeleton, whereas (B) demonstrates the actin cytoskeleton following treatment with the actin-depolymerizing drug Cytochalasin D. The scale bars measure $10 \mu\text{m}$.

3.4.4.1 Analysis of ANXA2 to actin disruption

The present study showed an accumulation of ANXA2 around the wound perimeter after PM disruption regardless of the inhibition of actin polymerization. Despite previous reports of ANXA2-induced contraction of model membranes into vesicular structures[131], the analysis of 39 plasma membrane injuries demonstrated that the recruitment, size, and geometry of ANXA2 rings in actin-disrupted cells were statistically indifferent from those in cells with intact actin. These findings can be attributed to the partial functionality of the actin network, as observed in Figure 4B, where it remained present in the cell, albeit appearing agglomerated at the cell periphery following actin polymerization inhibition.

3.4.5 The Annexin flower

However, a new phenomenon was observed exclusively in actin-disrupted cells. Following PM rupture and subsequent formation of the ANXA2 ring structure at the wound perimeter, several circular structures, resembling flower petals, were observed to nucleate from the ANXA2 ring, as shown in Figure 3.19, naming the discovered phenomenon the "Annexin flower". The observation of the Annexin flower can be attributed disrupted actin network (Fig. 3.19B) and is thought to be linked to the blebbing mechanism of ANXA2, which has been demonstrated on model membrane patches upon ANXA2 exposure[131] (Fig. 3.2B). Therefore, the present finding demonstrates that a direct biophysical effect of ANXA2-induced blebbing also can occur within living cells in which the membrane is not constrained by a rigid actin cortex.

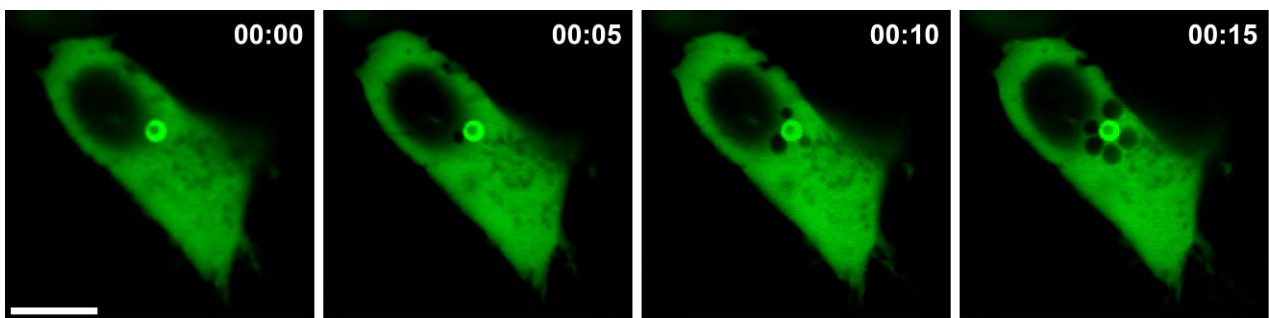


Figure 3.19: The Annexin flower was observed to develop over time after laser-induced membrane injury. The confocal images illustrate an actin-disrupted HEK293T cell expressing ANXA2-GFP. The evolution of the Annexin flower is observed as vesicular structures emanate from the ANXA2 ring over time (0-15 sec). This observation is suggested to be a direct biophysical effect of ANXA2. The scale bar represents 10 μm .

The vesicular "petal" structures, commonly referred to as blebs, are spherical membrane protrusions that are closely associated with the underlying actin cytoskeleton[31]. In cells with a normally functioning actin network, bleb formation and expansion can be triggered by either local disruption of the membrane and actin or by a local detachment of the actin network from the plasma membrane. Additionally, the reassembly of the actin cytoskeleton is reported to facilitate the retraction of the blebs[153, 154]. Laser ablation, as reported by Tineves et al.[153], mimics the natural bleb nucleation process. Based on the spherical structure and the rapid expansion of the blebs, it was proposed that the hydrostatic pressure, generated by the contraction of the underlying actin cytoskeleton, is responsible for bleb expansion. This internal pressure drives bleb nucleation and expansion in regions where the actin cortex has been weakened[153], which could partially account for the development of ANXA2-filled blebs observed at plasma membrane injury sites in cells with intact actin (Fig. A.4).

It is postulated that the blebs in the Annexin flower form due to the inability of actin reassembly, resulting in inward budding, as demonstrated in the z-stack imaging series presented in Figure 3.20. This stands in contrast to the outward blebbing observed in cells with intact actin (Fig. A.4), thus highlighting the intricate interplay between ANXA2 and the actin

cytoskeleton. The observations demonstrate that inhibition of actin polymerization enables ANXA2-mediated blebbing on damaged cell membranes. The blebs possibly nucleate from membrane artifact site in the ANXA2 ring, similar to the observation in Figure 3.2B, leading to an inward-budding due to the absence of hydrostatic pressure within the cell. Additionally, the ANXA2-induced blebbing mechanism observed for the Annexin flower is believed to be strongly associated with the reports by Boye et al.[31] on ANXA2's capability to induce vesicular structure budding out of plane on membrane patches (Fig. 3.2B). These observations have led to various potential strategies for plasma membrane repair involving ANXA2, as elaborated in Section 3.1. Notably, two strategies emphasize the interplay between ANXA2 and the cortical actin cytoskeleton[6].

3.4.5.1 Strategies for wound closure

Upon PM injury, Ca^{2+} flow into the cell and locally depolymerizes filamentous actin, while activating the PMR machinery, which in turn recruits ANXA2 to the injury site. ANXA2 then inhibits depolymerization, allowing for local repolymerization, leading to actin accumulation and actin remodeling at the repair site[43]. This process results in the formation of an actomyosin complex, comprising filamentous actin and motorprotein myosin II[6], surrounding the wound perimeter[124]. In this context, Boye et al.[31] proposed two potential mechanisms for wound resealing: contraction of the wound edges or removal of the injury through bleb formation.

The first proposed strategy involves the formation of a contractile actomyosin ring[124], which brings together the damaged membrane edges and underlying actin cytoskeleton analogous to pulling a purse string (Fig. 3.1E). This process is cooperated by the ANXA2-S100A11 complex and filamentous actin for eventual resealing[6, 52]. However, despite the accumulation of ANXA2 and actomyosin at the repair site, it remains unclear whether the actomyosin ring can make contact with the fluid membrane edges due to slippage between the two, indicating a possible limitation of this approach.

The second strategy for wound repair is an extension of the first, which seeks to promote PMR through membrane excision (Fig. 3.1F). This process relies on the relationship between bleb formation and the actin network[153], including the actomyosin ring, as bleb formation has been associated with high myosin II activity[154, 155]. Following membrane contraction by the actomyosin ring, a bleb is formed containing the damaged membrane, where ANXA2 facilitates repair by blocking the wound through the fusion of intracellular vesicles, hereby sealing the damaged membrane [6]. However, actomyosin formation and accumulation have been reported to occur within minutes, rendering this strategy too slow for wound closure[6]. Nonetheless, a strong correlation between bleb formation and actin cytoskeletal tension has been established, whereby an increase in tension leads to bleb expansion[153]. Blebs have

been observed to be stable for several minutes before retraction, indicating that the membrane resealing process involves multiple steps, including immediate patching of the wound and slower reconstruction of the actin cytoskeleton and the plasma membrane before restoring membrane integrity.

The occurrence of the Annexin flower may be facilitated by the formation of the actomyosin ring, which is assisted by ANXA2 at the site of injury. This process could potentially result in the isolation of the damaged membranes at the wound perimeter through bleb formation followed by membrane excision. The ANXA2 ring structure could serve as a precursor step to the excision of the damaged membrane. However, in the absence of a fully functioning actin network, the removal of the damaged membrane cannot be accomplished. Consequently, neither of the PMR strategies can account for the stable ANXA2 ring structures or the expansion of bleb nucleating from the ANXA2 ring.

Given the thermoplasmonic method's potential for creating injuries through explosive heat via nanobubble formation[70, 74], it was speculated that the nucleation of nanobubbles from the surface of the AuNP was the reason for the physical origin of the blebs nucleating from the ANXA2 ring. However, it was expected that if the blebs were a result of nanobubble formation, they would shrink in size after laser heating has ceased, since the nanobubble expands only as long as the particle is being irradiated, as elaborated upon in Section 3.2. As the blebs continued to expand even after the cessation of irradiation, suggests that nanobubble formation was the least likely explanation for the generation and expansion of the blebs.

Despite the inability of the proposed PMR strategies or nanobubble formation to explain the Annexin flower formation, the nucleation and expansion of the blebs in the ANXA2 ring indicate an ANXA2-mediated PMR mechanism. The findings demonstrate ANXA2's capacity to induce curvature and lipid aggregation, consistent with previous research, including the study by Drücker et al.[116], which reported ANXA2-induced membrane indentation, inward budding in GUVs, as well as membrane aggregation and interconnection.

3.4.6 The Annexin flower in three dimensions

The Annexin flower developed immediately after membrane injury (Fig. 3.20A) and is visualized in three dimensions in Figure 3.20B acquired by z-stack imaging from the membrane surface at the site of PM injury progressing into to the cytosol. Four blebs were observed to nucleate from the ANXA2 ring (Fig. 3.20A), which expanded in size as they protruded into the cytosol (Fig. 3.20B). These observations were consistent with the ANXA2-mediated out-of-plane blebbing response on membrane patches[131], as observed in Figure 3.14A. Eventually, the four blebs merged into three compartments (Fig. 3.20B, last image) that seemed to be directly linked within the cell, with the ANXA2 ring becoming less distinguishable. The lack

of fluorescent intensity within the bleb compartments suggests an absence of ANXA2, instead, ANXA2 appears to be bound to the bleb peripheries. The vesicular membranes appeared to be interconnected, likely due to membrane-ANXA2 crosslinking, forming membrane-ANXA2 bridges that seem to recede as the blebs grow in size towards the cytosol.

The laser irradiation subjects the cell to mechanical stress, prompting translocation of ANXA2 to the injury site, inducing local membrane curvature, and the formation of a bottleneck structure, as illustrated in Figure 3.14B. Subsequently, blebs emerge and expand due to the pressure gradients acting along the structures, with the internal pressure eventually increasing as the mechanical stress decreases as the blebs protrude into the cytosol, allowing for the expansion of the compartments. It is postulated that the bleb perimeter from the Annexin flower was composed of damaged membranes tightly associated with the ANXA2 ring via ANXA2-membrane binding. The number of blebs nucleating from the ANXA2 varied, which could be explained by the membrane patch experiments, where the blebs originated from defect membrane sites[131]. This observation supported the hypothesis that the blebs comprised damaged membranes at the wound perimeter.

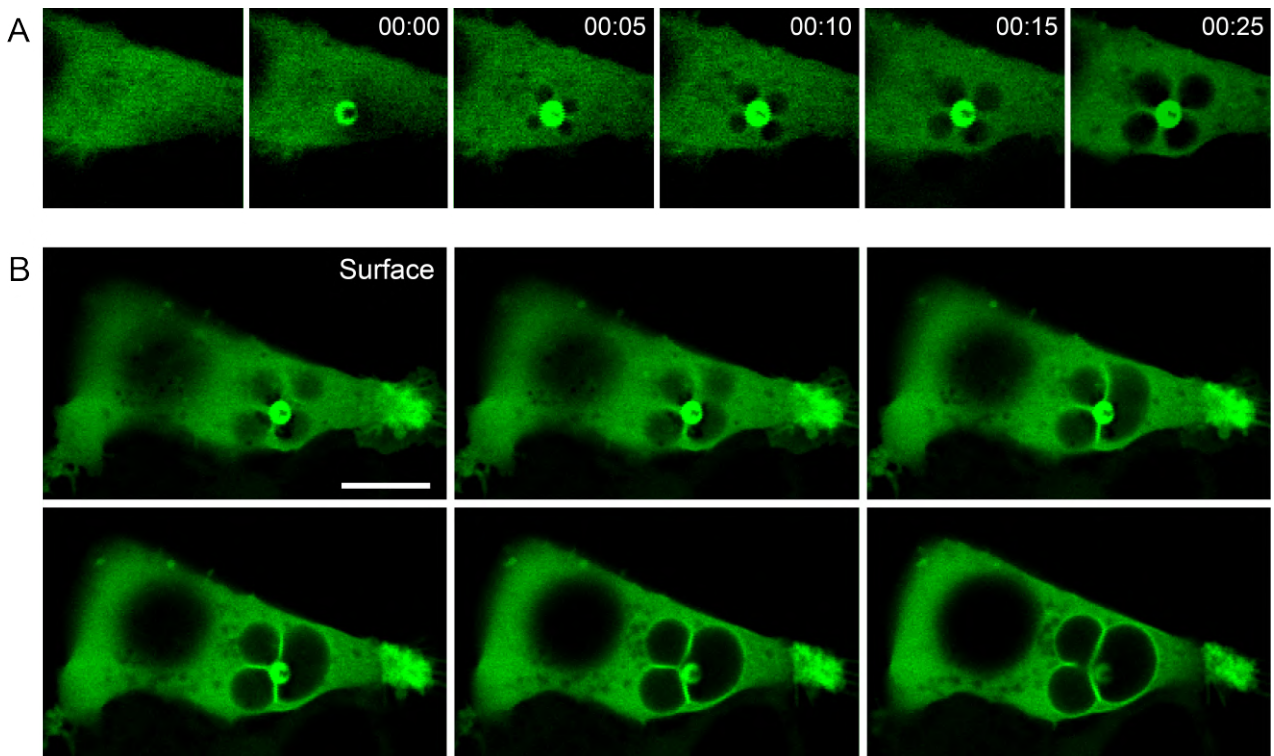


Figure 3.20: The confocal images illustrate a HEK293T cell expressing ANXA2-GFP in an environment where actin polymerization is inhibited. (A) The Annexin flower is observed to develop over time (0-25 sec). Upon laser irradiation, ANXA2 accumulates at the injury site (0 sec), which is rapidly followed by bleb nucleation and expansion from the ANXA2 ring structure. (B) A three-dimensional view of the injury site was obtained by z-stack imaging, displaying the Annexin flower from the cell surface into the cytosol, where the four blebs observed at the surface appeared to become three as they propagate into the surface. The scale bar represents 10 μm .

3.4.6.1 ANXA2-membrane bridges

The ANXA2 proteins were observed to accumulate at the periphery of the blebs, where the adjacent membranes appeared interconnected, based on the flat contact area and the increased ANXA2 intensity in this region. A quantitative analysis was performed on the three main membrane-ANXA2 bridges, denoted as bridge A, B, and C in Figure 3.21D, by measuring the intensity as a function of distance spanning across the cytosol, the blebs, and the ANXA2-membrane bridges. The ANXA2-membrane bridges are visualized as intensity peaks in Figure 3.21A, B, and C, respectively. The minimum intensity valleys observed next to the peak represented the intensity within the blebs compartments, while the slight increase in intensity represented the cytosolic ANXA2, which corresponds to the mean cytosolic ANXA2 intensity given by the gray line across the intensity plot.

The intensity plots supported the observed ANXA2 accumulation at the membrane bridges. Bridges A, B, and C showed an increase in ANXA2 intensity relative to the mean cytosolic ANXA2 intensity by 41.4%, 50.8%, and 54.7%, respectively. This indicated a significant increase in ANXA2 binding to the membrane bridges, although the variation of the relative ANXA2 accumulation remains to be elucidated. Furthermore, the sudden decrease in intensity in the “valley” confirmed the lack of ANXA2 within the bleb compartments, while further supporting the hypothesis that ANXA2 binds to the disrupted parts of the membrane, inducing curvature and blebbing, as a plausible mechanism to isolate and remove the damaged parts of the plasma membrane. Collectively, the preliminary results are consistent with the reported blebbing mechanism observed on model membrane patches[131].

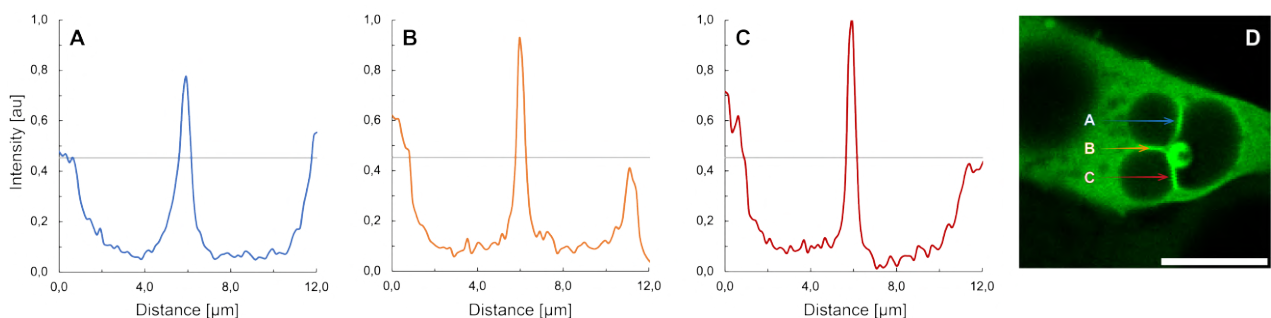


Figure 3.21: The ANXA2-membrane bridges were analyzed by measuring the ANXA2 intensity as a function of distance. To accomplish this, line intensity profiles (A-C) were generated for the corresponding ANXA2-membrane bridges indicated in panel (D). An increase in ANXA2 intensity of 41.4% (blue), 50.8% (orange), and 54.7% (red) was measured for ANXA2-membrane bridges A, B, and C in panel (D), respectively, relative to the mean cytosolic ANXA2 signal (represented by the gray horizontal line). (D) The confocal image displays the Annexin flower presented in Figure 3.20B, at a z-height of $1.65 \mu\text{m}$ above the surface, with a scale bar of $10 \mu\text{m}$.

Furthermore, previous studies have demonstrated that ANXA2 is involved in lipid aggregation [144, 156] and interconnections between adjacent membranes[157]. The formation of intercon-

nections between vesicles is known to result in a membrane deformation of the spherical structures, leading to a flattened region at the contact site[54, 116], which is considered a hallmark of established membrane contact. In the present study, the flattened contact area between adjacent blebs extending from the ANXA2 ring (Fig. 3.21D), coupled with the significant increase in ANXA2 intensity, strongly suggests ANXA2-mediated membrane interconnection of adjacent blebs within the cell. This notion was further supported by the research of Drücker et al.[116] who found that ANXA2 in both its monomeric and heterotetrameric form could mediate adhesion between adjacent GUV membranes in a calcium-dependent manner and aggregate the lipid vesicles through the formation of regular junctions or interconnections. The accumulation of ANXA2 observed at the interconnection site indicated its ability to link two membrane surfaces, which has also been demonstrated by cryo-electron microscopy[157, 158].

Membrane interconnection mediated by ANXA2

The mechanism behind monomeric ANXA2 membrane-membrane adhesion is not fully understood. Nonetheless, it has been proposed that ANXA2 binds with free Ca^{2+} and adopts an "inverted" configuration, allowing it to bind to two adjacent membranes simultaneously[159]. Drücker et al.[116] proposed a model for ANXA2-mediated membrane aggregation and interconnection based on the geometry of the ANXA2 binding core, formed as a slightly curved disc with the Ca^{2+} binding sites located at its convex side. Following Ca^{2+} influx, ANXA2 assumes either one of two orientations, parallel or anti-parallel, to facilitate ANXA2-membrane bridging. The parallel orientation (Fig. 3.22 A1) supports the observed membrane indentations and inward budding process (Fig. 3.22C). The anti-parallel orientation (Fig. 3.22 A2) was proposed to form a rigid scaffold providing binding sites for a second membrane surface, inducing membrane aggregation and interconnection through a zipper-like mechanism[116]. Moreover, ANXA2-S100A10 heterotetrameric complexes were found to induce lipid clustering and GUV aggregation even more efficiently than monomeric ANXA2[116], indicating that S100A10 binding to the ANXA2 N-terminal domain enhanced its lipid segregation properties, possibly by physically linking two membrane-binding ANXA2 moieties[133, 156]. The complex facilitates membrane interconnection by two cores of one complex facing opposite GUV membranes (Fig. 3.22 B1), whereas membrane clustering and indentation required two cores of one complex binding to the same membrane (Fig. 3.22 B2). Lastly, the ANXA2 core domain was found to be necessary and sufficient to trigger domain formation and GUV aggregation, while the N-terminal provided a second membrane site but was dispensable for ANXA2-mediated membrane aggregation[116].

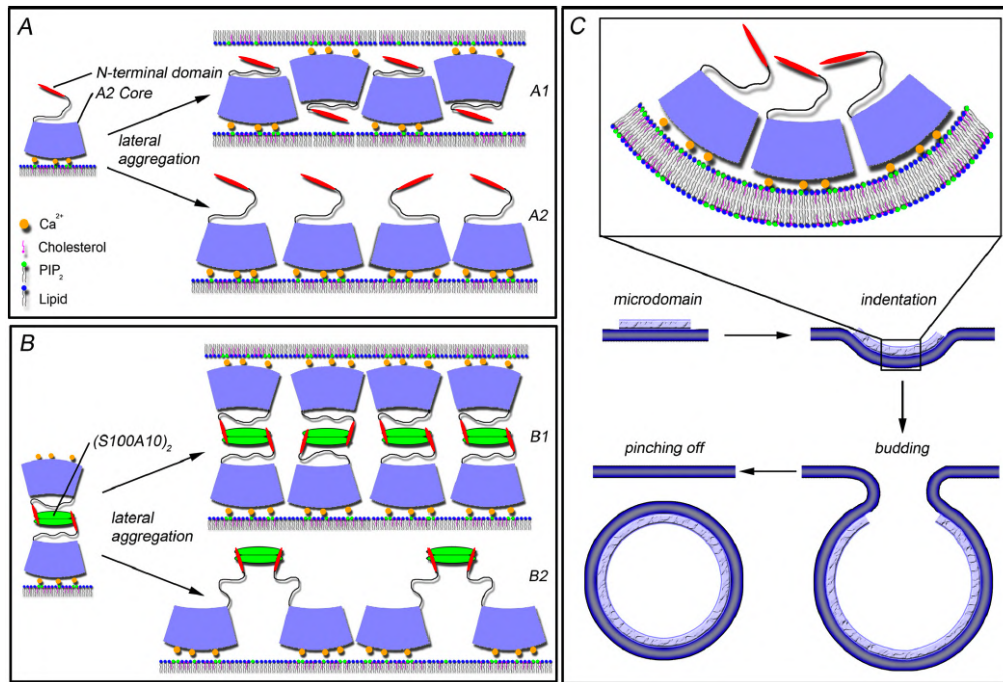


Figure 3.22: The schematic model illustrates two strategies for ANXA2 mediated membrane aggregation process depending on its monomeric and heterotetrameric form. (A) Monomeric ANXA2 mediates membrane aggregation by binding in either an anti-parallel (A1) or a parallel (A2) orientation on a membrane surface. The anti-parallel configuration (A1) is postulated to induce membrane interconnections through a zipper-like mechanism, while the parallel configuration (A2) leads to indentations and an inward budding process as illustrated in (C). Furthermore, the lateral aggregation of the ANXA2-S100A10 heterotetrameric complex is illustrated in (B), where (B1) portrays an orientation where the two core domains face adjacent membranes hereby forming a membrane interconnection. In contrast, (B2) shows parallel aligned core domains facing the same membrane, thereby inducing membrane aggregation and potentially membrane indentation. Finally, (C) displays the ANXA2-mediated vesicle budding in four steps, including microdomain formation, indentation of the membrane, membrane budding, and eventual pinching of the vesicle off. The figure was adapted from Drücker et al[116].

It is worth noting, that the observed inward budding induced by ANXA2 by Drücker et al.[116] was specific to its extracellular localization, implying that living cells would exhibit outward budding since ANXA2 is primarily located in the cytosol. This process has been associated with virus budding[160] and the shedding of plasma membrane vesicles from cancer cells[161], suggesting that it could also partially contribute to the ANXA2-filled vesicles emanating from the ANXA2 wound of normally functioning cells (Fig. A.4). While these observations suggest that ANXA2 can efficiently induce membrane deformations, further evidence is needed to substantiate these claims as a part of the PMR in living cells. To better understand the extent of the biophysical response of ANXA2 to membrane injury, its mechanism could be isolated in model membrane systems with ANXA2 encapsulated within GUVs, similar to the ANXA5 in vitro experiments by Moreno et al.[54]. This could elaborate on the underlying ANXA2 ring formation at the injury site and potentially offer evidence of how the blebs

are formed and expand into the Annexin flower. Furthermore, the contents of the inner compartments of the blebs remain unknown, with the hypotheses proposing the compartments to be filled with extracellular medium due to the lack of ANXA2 intensity. However, additional experiments utilizing extracellular residing fluorescent dyes, such as Alexa Hydrazide 633, should be conducted to test this hypothesis.

3.4.7 Wound closure and calcium imaging

Plasma membrane repair is a complex process that is initiated by the influx of extracellular Ca^{2+} upon PM rupture, facilitated by a steep calcium concentration gradient that exists across the plasma membrane[33]. Consequently, the size of the wound is directly proportional to the level of Ca^{2+} influx, which is a critical determinant of the initial and subsequent responses, including whether passive or active membrane resealing is activated, where the latter involves calcium-dependent proteins such as ANXAs and cytoskeletal remodeling[8, 162]. The main objective of this section was to verify that thermoplasmonic heating in fact leads to Ca^{2+} influx as well as to verify that the Ca^{2+} influx ceases upon successful PMR. This step was necessary to ensure that the observed ANXA response was in fact triggered by Ca^{2+} influx upon PM rupture of the adhered cell surface. Moreover, these initial findings allowed for an estimation of the timescale required for wound closure.

Confocal imaging was employed to monitor the intracellular calcium levels in HEK293T cells following thermoplasmonic injury. To visualize calcium influx, the calcium probe GCaMP6s was used in both its cytosolic[163] and membrane-bound form[164], where GCaMP6s-CAAX specifically targets the plasma membrane. The cells co-expressed one of the green fluorescent calcium probes and ANXA2-RFP. The plasma membrane ruptures were expected to induce a flux of Ca^{2+} ions in and out of the cell, depending on their concentration gradient. The membrane-bound probe was expected to be the most reliable reporter of Ca^{2+} influx due to its relative immobility[162], allowing for visualization of the calcium dynamics at the cell surface. To provide a reference, parallel measurements using the well-established cytosolic probe were also conducted. The qualitative and quantitative Ca^{2+} intensity distribution exhibited the same behavior for both forms, consistent with the previous findings by Klenow et al[162]. Moreover, the preliminary results revealed a varied cellular response to thermoplasmonically induced membrane disruptions, categorizing them into three scenarios. In all three scenarios, an elevation in intracellular Ca^{2+} levels was observed after PM disruption. However, in the first scenario, ANXA2 translocation was not observed. In the second scenario, ANXA2 was recruited to the injury site, forming a ring structure around the injury site and mediating PMR. A similar response was observed for the third scenario, although the cell appeared to be unable to cope with the excessive Ca^{2+} influx, resulting in cell death.

3.4.7.1 Analysis of calcium influx

In this study, local plasma membrane disruption was performed at the cell periphery to minimize damage to intracellular organelles that may compromise cell viability. The spatio-temporal distribution of Ca^{2+} intensity was qualitatively examined for both forms of the GCaMP6s probe and quantitatively analyzed by measuring the Ca^{2+} intensity within the entire cell footprint over time. Prior to laser irradiation, the resting cell exhibited low cytosolic Ca^{2+} intensity, reflecting its intracellular Ca^{2+} concentration at $\sim 100\text{nM}$, indicating cellular homeostasis[165]. Upon membrane rupture, a rapid extracellular Ca^{2+} influx (mM) occurs, driven by the significant Ca^{2+} gradient, until the membrane rupture has closed. The background Ca^{2+} level was set to zero by subtracting the background intensity prior to membrane disruption and post-membrane repair. The maximum intensity was derived by normalizing the mean Ca^{2+} intensity within the cell to one, which provided an intensity curve that exhibited a rapid initial Ca^{2+} intensity increase to a maximum followed by a slower decrease. The observed decrease is thought to occur due to membrane repair, where the intracellular Ca^{2+} levels are no longer in competition with the extracellular Ca^{2+} influx, and the excess Ca^{2+} ions are removed by cellular processes such as Ca^{2+} pumps. Therefore, the time of the intensity peak also indicates the closure time ($t = t_c$) where the wound has resealed, as proposed by Klenow et al.[162].

3.4.7.2 The three scenarios

For the first scenario, cells expressing ANXA2-RFP along with the membrane-bound calcium probe, GCaMP6s-CAAX, were used. Upon PM injury, free Ca^{2+} ions flowed into the cell, causing a conformational change in the probe and an increase in its fluorescent intensity[162]. The Ca^{2+} influx emerging from the site of injury propagates into the cell, as depicted in Figure 3.23A, which was followed by a slower decrease in Ca^{2+} intensity. The qualitative observation was supported by quantitative analysis of the calcium intensity over time (Fig. 3.23C). According to Klenow et al.[162], the time of the intensity peak corresponds to the time of wound closure ($t = t_c$), indicating that the wound is resealed within 6.6 seconds, denoted by the orange dashed line in Figure 3.23C. Since the significant changes in Ca^{2+} intensity were only observed in the injured cell and not in the control cell (Fig. 3.23C), the thermoplasmonic PM rupture is confirmed to be responsible for the observed changes. This further indicates that the rupture must have been significant enough to allow for passive extracellular diffusion, but not significant enough to trigger ANXA2 translocation (Fig. 3.23B). Moreover, it suggests that active PMR strategies were not necessary and that the cell was able to prioritize the return to its pre-injury homeostatic state. As such, spontaneous membrane resealing is indicated. For spontaneous resealing to occur, the wound must be less than $0.2 \mu\text{m}$ [41], which has been proven achievable by the thermoplasmonic approach in model membrane vesicles[134].

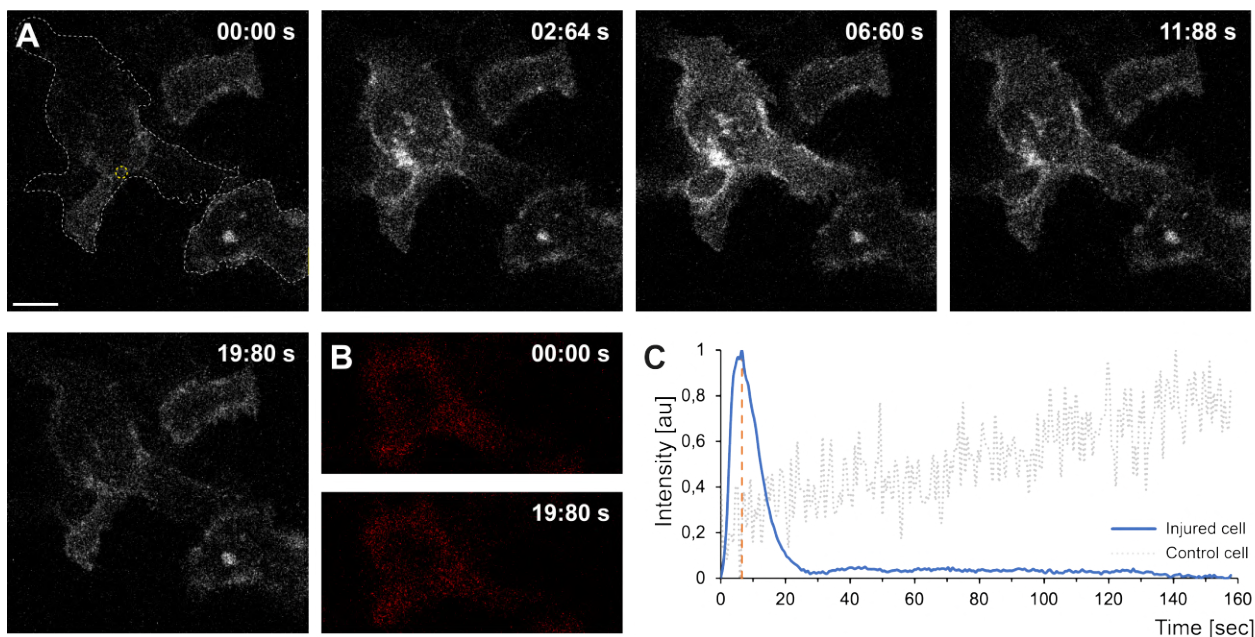


Figure 3.23: Scenario 1 is depicted by time-lapse images of HEK293T cells expressing GCaMP6s-CAAX, a membrane-bound calcium probe (A), and ANXA2-RFP (B). The yellow circle in panel A indicates the puncture site on the membrane before irradiation at 00:00s. Calcium is observed to rapidly flow into the cell, and reaches its maximum intensity at 6.6 seconds, estimated as the wound closure time (indicated by the orange dashed line) followed by a calcium decrease (C). In contrast, (B) displays the ANXA2 intensity before and after irradiation, demonstrating no ANXA2 translocation. (C) represents the GCaMP6s-CAAX calcium intensity for the entire footprint of the cell (enclosed by the gray dashed line in panel A) over time for the injured cell (blue line) in comparison to an uninjured control cell (gray dotted line). The scale bar measures 10 μm .

However, although the wound closure time was consistent with that reported by Klenow et al.[162], spontaneous resealing has been reported to occur on the millisecond time scale for injuries of less than one nanometer in size[42]. This leads to some discrepancies between the proposed wound closure time and the timescale for spontaneous resealing and it proved to be challenging to distinguish the dominant mechanism underlying membrane resealing in this scenario. Suggestively, it could be a combination of membrane deformation and subsequent rearrangement of the intracellular actin network, where the Ca^{2+} influx is due to the opening of Ca^{2+} channels and not a distinct membrane rupture[36], or that the small injury is resealed by actin cytoskeleton relaxation driving the thermodynamically favored passive membrane resealing[53, 122]. Nevertheless, the fact that the Ca^{2+} process was exclusively observed in the injured cell and not in the control cell proves that the cell was indeed experiencing Ca^{2+} influx without activating ANXA2 and actively pumping out the excess calcium to reach its homeostatic Ca^{2+} concentration.

The second and third scenarios displayed a similar trend of increased overall cytosolic Ca^{2+} intensity upon PM disruption. This increase began at the injury site and propagated throughout the cell, as evidenced by Figures 3.24 and Figure 3.25. In both scenarios, the injury was

sufficient to trigger ANXA2 translocation to the wound perimeter, indicating the initiation of active PMR strategies. The maximal calcium intensity was observed within 19 seconds for both scenarios, where the cell was either able to facilitate PMR, as depicted in Scenario 2 (Fig. 3.24), or unable to facilitate wound closure and cope with the excessive influx of Ca^{2+} , as in Scenario 3 (Fig. 3.25), ultimately resulting in cell death.

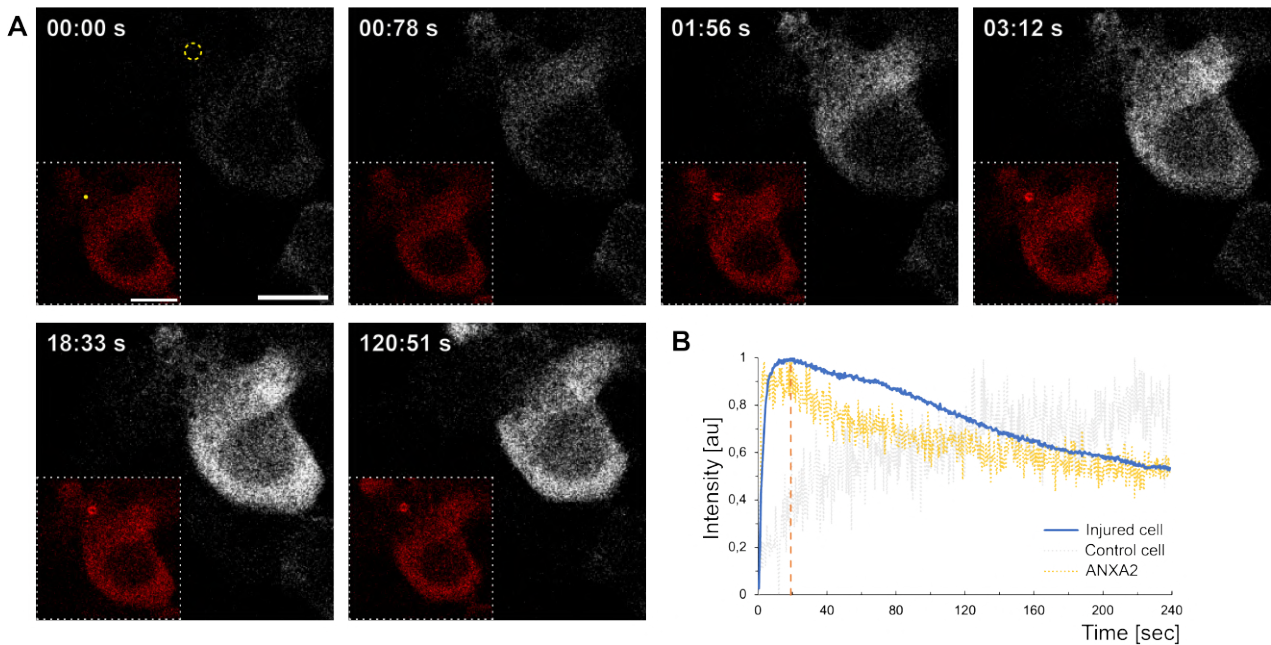


Figure 3.24: Scenario 2 is depicted by time-lapse images of HEK293T cells expressing GCaMP6s, a cytosolic calcium probe (A), and ANXA2-RFP (A red insert). The yellow circles in panel A indicate the puncture site on the membrane before irradiation at 00:00s. Calcium is observed to rapidly flow into the cell upon puncture (0.78s) closely followed by an ANXA2 accumulation at the injury site (1.56s). The calcium signal reaches its maximum intensity at 18.94 seconds, estimated as the wound closure time (indicated by the orange dashed line) followed by calcium decrease (B). (B) represents the GCaMP6s calcium intensity over time for the injured cell (blue line) in comparison to an uninjured control cell (gray dotted line) as well as the ANXA2 intensity measured at the injury site (yellow dotted line). The scale bars measure $10 \mu\text{m}$.

The quantitative analysis of the calcium intensity supported the qualitative observation. In Scenario 2, the rapid Ca^{2+} increase was followed by a gradual decrease in intensity, resulting in a softer intensity peak compared to Scenario 1 and a significantly slower wound closure time of ~ 19 sec (Fig. 3.24B). The gradual decrease in Ca^{2+} and prolonged wound resealing align with literature suggesting that active PMR is a multi-step process[131], thus slower than spontaneous resealing. In Figure 3.24B, the calcium intensity decay appeared linear compared to the exponential decay for scenario 1 (Fig. 3.23C) following wound closure, which has been argued to be the rate Ca^{2+} is pumped out of the cell[162]. Therefore, the gradual decay in Ca^{2+} along with the accumulation of ANXA2 at the injury site further suggests that active PMR strategies have been triggered, where the cell actively prioritizes repairing the injury. Once the wound is resealed and the intracellular Ca^{2+} ions are no longer in competition with

the Ca^{2+} influx, the excess Ca^{2+} is pumped out, with a definable pumping rate, until the Ca^{2+} level within the cell eventually returns to its homeostatic level.

The injury site is proposed to be proportional to the influx volume of calcium ions[33], where larger injuries both depend on the preliminary tension relief through local actin depolymerization and on the additional components mediating PMR. The active PMR observed in scenario 2 is further supported by the prolonged time evolution of the Ca^{2+} intensity compared to scenario 1. Moreover, the accumulation of ANXA2 (Fig. 3.24A, red insert) at the injury site appeared in the presence of millimolar Ca^{2+} levels flowing into the cell due to the 10^4 -fold Ca^{2+} gradient across the plasma membrane [6, 33], indicating a higher intracellular Ca^{2+} concentration than in Scenario 1, again indicating a larger injury and active PMR. When comparing the calcium influx and ANXA2 recruitment in Scenario 2, Ca^{2+} appeared at the injury site immediately upon laser irradiation and membrane rupture (Fig. 3.24A (0.78s)), which was followed by ANXA2 translocation to the injury site within a second post-irradiation (Fig. 3.24A (1:56)). A similar step-wise process was observed for Scenario 3 (Fig. 3.25), indicating that a significant Ca^{2+} influx serves as a prerequisite step and is imperative to trigger ANXA2 recruitment for eventual PMR. Moreover, the slow Ca^{2+} decay rate after presumed wound closure (Fig. 3.24B) aligns with the findings by Klenow et al.[162], who reported the mean timescale for recovery of the calcium concentration to be ~ 8 -10 time slower than the mean timescale for sealing of the hole. Therefore, it can be assumed that the immediate sealing of the plasma membrane wound has priority over the subsequent recovery of cell homeostasis to that of an uninjured cell.

In the third scenario, active PMR was initiated by the influx of extracellular Ca^{2+} , which was observed to propagate from the injury site into the cell, followed by ANXA2 accumulation at the wound perimeter, as illustrated in Figure 3.25A. The quantitative analysis of the membrane-bound calcium probe, GCaMP6s-CAAX, revealed that the maximum calcium intensity was achieved within ~ 18.5 s. However, the cell was incapable of coping with the excessive Ca^{2+} influx. This was evident from the translocation and clustering of ANXA2 at the intracellular membranes (Fig. 3.25A (178.86s)), while the overall Ca^{2+} intensity remained unregulated (Fig. 3.25B), indicating that the cell was unable to close the wound and ultimately resulting in cell death.

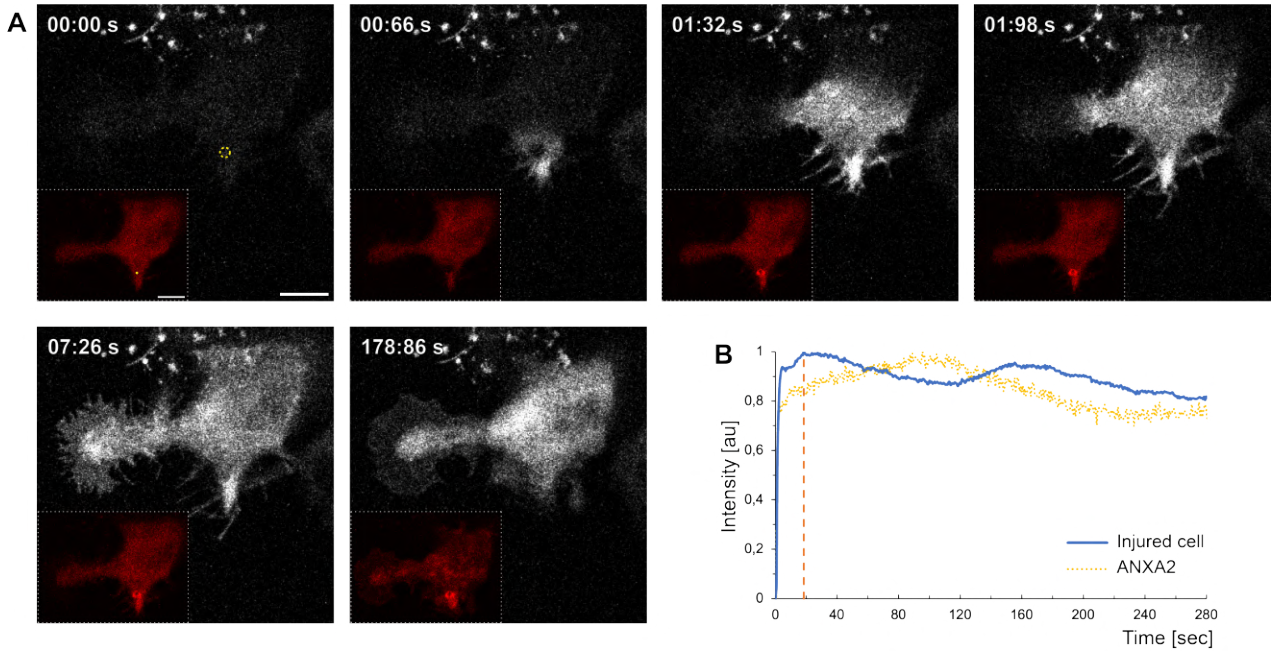


Figure 3.25: Scenario 3 is depicted by time-lapse images of HEK293T cells expressing GCaMP6s-CAAX, a membrane-bound calcium probe (A), and ANXA2-RFP (A red insert). The yellow circle in panel A denotes the puncture site before irradiation at 00:00s. Calcium is observed to rapidly flow into the cell upon puncture (0.66s) closely followed by ANXA2 accumulation at the injury site (1.32s). The calcium signal reaches its maximum intensity at 18.44 seconds, indicated by the orange dashed line, where it appeared to remain stable (B). (B) represents the GCaMP6s-CAAX calcium intensity over time for the injured cell (blue line) and the ANXA2 intensity is measured at the injury site (yellow dotted line). The scale bars measure 10 μm .

3.4.8 Concluding remarks

The repair of the plasma membrane is crucial for maintaining cellular homeostasis after a rupture, where the closure of the wound plays a significant role in promoting cellular recovery. Overall, the findings revealed that both ANXA5 and ANXA2 accumulate in a ring-like structure around the injured plasma membrane. This structure was observed to persist in a stable manner across time and space and is believed to play a significant role in the process of plasma membrane repair, eventually leading to successful wound closure. However, while both proteins share this similarity, the ring sizes of ANXA5 and ANXA2 differ significantly. This difference may be attributed to their distinct biophysical functions, as demonstrated on model membrane patches (Fig. 3.2), where ANXA5 was observed to induce membrane curvature and rolling, while ANXA2 induced membrane contraction and out-of-plane vesicle formation[131]. This biophysical function is suggested to be reflected in the ANXA ring sizes, where the ANXA5-mediated membrane rolling may result in generally larger ANXA5 rings than those of ANXA2. Furthermore, the "Annexin flower" phenomenon was observed exclusively in cells where the actin cytoskeleton was disrupted through the inhibition of actin polymerization. Within the ANXA2 ring structure, the blebbing attribute of ANXA2 was

observed as vesicles emanating from the ring, indicating a correlation between the ANXA2 blebbing mechanism and the actin cytoskeleton. It is believed that these blebs protrude into the cell cytosol, where ANXA2 binds to the membrane neck of the vesicle, as demonstrated in Figure 3.14B. However, the findings of Drücker et al.[116] demonstrated that ANXA2 can also form membrane indentations, as depicted in Figure 3.22C. This suggests the existence of two distinct curvature-generating abilities of ANXA2, indicating a multifunctional nature of the ANXA2 protein in terms of curvature generation.

Moreover, several investigations have examined successful membrane repair, revealing that the time necessary for wound closure is dependent on the extent of the injury and the type of cell. One principal discovery of this study was that extracellular calcium ions were capable of entering the cell upon thermoplasmonically induced injury. This activated the plasma membrane repair machinery, as evidenced by ANXA recruitment to the injury site following Ca^{2+} influx, culminating in successful repair. Furthermore, previous studies have confirmed that the response of ANXA observed in this study occurs independently of the fluorescently coupled protein[31, 131], a finding that is briefly discussed in Chapter 4 upon thermoplasmonic disruption.

HEK293T cells expressing ANXA2-RFP and either cytosolic (GCaMP6s) or membrane-bound calcium (GCaMP6s-CAAX) probes were used to verify the influx of Ca^{2+} upon thermoplasmonically induced plasma membrane disruption. These preliminary findings revealed that the cells indeed experienced a rapid Ca^{2+} influx upon plasma membrane rupture, which could further give an estimate of the wound closure time. This led to three primary observations, designated as scenarios 1-3. In the first scenario, ANXA2 was not observed to be recruited upon Ca^{2+} influx, and the cytosolic Ca^{2+} concentration was observed to decrease over time with an estimated wound closure time of ~ 6.5 seconds. In the second scenario, ANXA2 accumulated at the injury site, forming a ring structure around the wound, with an estimated wound closure time of ~ 19 seconds, followed by a decrease in Ca^{2+} intensity. A similar response was observed in the third scenario, although the cell appeared to be unable to cope with the excessive Ca^{2+} influx, reaching a maximum calcium intensity at ~ 18.5 seconds, where it remained relatively constant. The faster wound closure time observed in scenario 1 could be due to passive resealing, which has been observed upon thermoplasmonic induction of nanoscopic holes in annexin-free GUVs, which were efficiently resealed by membrane line tension[54, 134]. This passive resealing process was supported by the absence of ANXA2 recruitment and the rapid decrease in Ca^{2+} intensity. Interestingly, this wound closure time was consistent with the findings of Klenow et al.[162] who reported a wound closure time of 5-7 seconds in MCF7 cells, although assuming wound closure by active PMR strategies. However, the nature of the wound must be taken into consideration, as Klenow et al.[162] damaged the plasma membrane by pulsed laser irradiation, which may permeabilize the mem-

brane or create multiple pores at the injury site instead of a single hole. This could explain the similar wound closure times, as both would be closed by spontaneous membrane resealing.

In contrast to smaller membrane injuries, larger wounds, e.g., obtained by the microneedle approaches, have been reported to be successfully resealed within seconds[37, 117] or minutes[46, 120]. Active PMR is reported to be a multi-step process involving numerous mechanisms and thus a slower process than passive membrane resealing. As a result, prolonged wound closure time and an extended Ca^{2+} pump rate are observed before the intracellular calcium concentration is restored to its homeostatic level. The findings from scenario 2 support this notion, indicating that the active PMR system operates in several stages, with the actual resealing of the injury taking priority over other mechanisms and occurring as early as possible in the repair sequence. Furthermore, the difference in wound closure time and Ca^{2+} decay rate in scenarios 1 and 2 seem to be dependent on the extent of extracellular Ca^{2+} influx, which is proportional to injury size and determines whether the wound is repaired through passive resealing or active PMR strategies[33]. It is worth noting that even if the simplified explanation states that wound closure occurs prior to other remodeling mechanisms, the immediate resealing and reconstruction of the membrane are likely to occur simultaneously, e.g., the involvement of blebbing and shedding has been proposed to occur in both immediate repair and in membrane and actin remodeling[8]. Essentially, all membrane repair mechanisms are directly or indirectly dependent on this dynamic remodeling of both the plasma membrane and actin cytoskeleton[8, 45].

Given the preliminary nature of the present study, the exact timeframe for wound closure remains ambiguous, and further statistical data is required to draw conclusions. Nonetheless, this study highlights a promising avenue for future research, such as investigating the average wound closure time of membrane pores and the effects of active PMR. It would also be beneficial to explore the average time required to remove excess calcium, i.e., the Ca^{2+} pump rate, as this would allow for comparison with the findings by Klenow et al.[162]. Such investigations could help clarify the difference in the nature of wounds obtained by the two laser irradiation approaches and further enhance the understanding of the general ANXA response to membrane injury. It can, however, be concluded that the disruption of the cell membrane triggers the passive diffusion of extracellular calcium ions into the intracellular environment. This process continues until the wound has been closed, with the extent of wound closure determining the resealing mechanism employed. Spontaneous resealing is predominant in small injuries, during which the cell prioritizes the removal of excess calcium via pumps and protein binding[165]. Conversely, active resealing mechanisms prevail in larger wounds. Notably, a significant Ca^{2+} influx appeared to serve as a prerequisite for ANXA recruitment and accumulation at the injury site, irrespective of the condition of the underlying cortical actin, ultimately leading to membrane repair and restoration.

Actin and the nuclear envelope

Cancer cells are subjected to significant physical stress during their migration and invasion through the compact extracellular matrix within the body. This results in extensive deformation of the cell, which in turn can cause lesions and damage to both the cell plasma membrane and its nucleus[6, 141, 42, 43, 34]. Consequently, the plasma membrane repair machinery is activated, in which ANXAs and actin are identified as key players. The dynamic actin network partakes in both membrane resealing and reconstruction[8], two processes that are believed to be cooperative. Notably, all membrane repair mechanisms depend directly or indirectly on the membrane and actin cytoskeletal remodeling [8, 45]. However, the mechanistic understanding of the actin cytoskeleton dynamics during membrane reconstruction remains to be elucidated.

In this study, the response of the actin cytoskeleton following internal membrane disruption was investigated. In particular, the nuclear envelope was disrupted by combining the well-established thermoplasmonic method's ability to heat nanoparticles[74, 89, 166, 54] with the cell's ability to efficiently endocytose gold nanoparticles[167]. This approach enabled the investigation of protein response to local internal membrane damage, which is essential for a comprehensive understanding of how cells cope with injuries.

In collaboration with the Danish Cancer Society Research Center, the actin response to nuclear envelope disruption in breast cancer (MCF7) cells was investigated. The preliminary findings revealed that a large-scale actin reorganization occurs during and after mechanical disruption, where the rapid actin polymerization at the perinuclear space was not solely dependent on elevated intracellular calcium levels, but specifically on extracellular calcium influx prior to its assembly.

4.1 The nuclear envelope

Initially, the cell nucleus was primarily considered as a physical barrier separating the nucleoplasm, and its genetic material, from the cytoplasm[168]. However, extensive research has revealed its involvement in a multitude of processes, including sensing of mechanical stress and regulation of gene expression[169]. The nuclear envelope is a double-membrane system that encloses the cell nucleus, as depicted in Figure 4.1. It is composed of two lipid bilayers separated by a perinuclear space that typically measures between 30-50 nm[170]. The nuclear

envelope has embedded nuclear pore complexes, which facilitate the exchange of nucleocytoplasmic proteins, thus contributing to the regulation of nuclear-cytoplasmic transport[171]. The outer nuclear membrane is continuous with the endoplasmic reticulum (ER) and possesses similar biochemical characteristics to the peripheral ER[172]. In contrast, the inner nuclear membrane is lined with a filamentous meshwork, referred to as the nuclear lamina, which provides structural support and serves as a binding site for nuclear pore complexes and chromatin [172, 173]. Additionally, the lamina influences the shape and stiffness of the nucleus[169], causing it to be considerably more rigid (~ 5 -10 times) than the surrounding cytoskeleton[174]. In contrast, the plasma membrane consists of a lipid bilayer embedded with numerous integral proteins, which measures between 5-10 nm in thickness and is internally lined by the cortical actin cytoskeleton[8]. As a consequence, the plasma membrane is comparatively less rigid than the nuclear envelope.

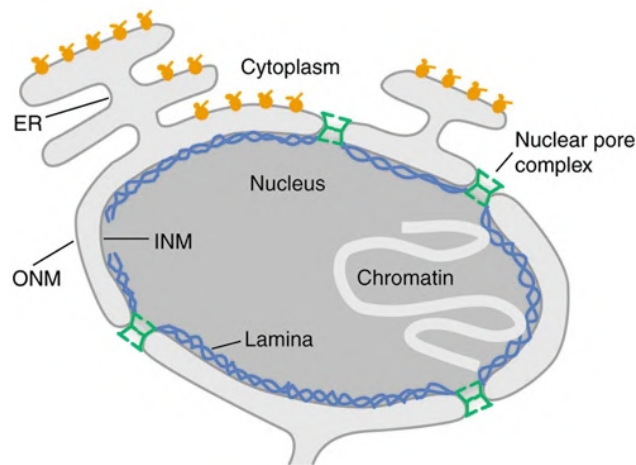


Figure 4.1: The schematic depicts the structure of the nuclear envelope, which is a double-membrane system consisting of an outer nuclear membrane (ONM) and an inner nuclear membrane (INM). This system separates the nucleoplasm from the cytoplasm, where the embedded nuclear pore complexes govern the regulated molecular exchange between these compartments. The ONM is contiguous with the endoplasmic reticulum (ER), while the INM is lined by the nuclear lamina, which serves as a binding site for both nuclear pore complexes and chromatin, while also providing structural support. The figure was adapted from Schirmer et al.[172]

4.2 Endocytosis of gold nanoparticles

Gold nanoparticles have received significant attention within a diverse array of biomedical applications, ranging from bio-imaging to nanomedicine development, due to their surface chemistry, as well as their scattering and absorption properties [77, 167, 175, 176, 177, 178]. One approach leveraging the use of these nanoparticles involves taking advantage of the natural endocytic process, whereby cells internalize extracellular contents, such as AuNPs. Upon

internalization, the particles are delivered to early endosomes, where actin polymerization is believed to play a crucial role in initiating vesicle scission during endocytosis[6]. These endosomes efficiently sort their contents, either by rapidly recycling them back to the plasma membrane for reuse or directing them towards the nucleus as late endosomes and lysosomes for degradation[179].

Gold nanoparticles have been extensively studied for their broad potential for biomedical applications [167, 175, 176, 177, 180, 181, 182], where their biocompatibility and endocytic behavior was found to depend on several factors including size, surface charge, coating, and cell type [176, 180]. Smaller particles and those with positively charged surfaces have been reported to enhance internalization[182, 181, 180], and even non-functionalized, negatively charged particles have been observed to be readily endocytosed by cells[167]. Following endocytosis, AuNPs have been found within membrane-bound enclosures, suggested to be endosomes and/or lysosomes [167, 175, 177], predominantly in the perinuclear region, and to a lesser extent in the cell periphery. Furthermore, AuNPs have not been observed to migrate from the perinuclear region into the nucleus after 24 hours of incubation[167]. The internalized particles have been found as either single particles or agglomerates, with both internalization and agglomeration being concentration dependent[167]. Clathrin-mediated endocytosis, one of the most common receptor-mediated uptake pathways[180], has been suggested as the mechanism for NP internalization. However, as this pathway has been reported to optimally endocytose particles less than 100 nm[183], it is likely that larger particles are less efficiently endocytosed or may be taken up by alternative clathrin-independent pathways.

The current study aimed to investigate the mechanisms associated with nuclear envelope repair and reconstruction subsequent to thermoplasmonic disruption of the nuclear envelope. This was accomplished through the use of laser irradiation of gold nanoparticles that had been internalized in close proximity to the nuclear envelope. Prior to this investigation, the optimal concentration and incubation time of non-functionalized, negatively charged AuNPs (d= 80, 150 nm) and streptavidin-functionalized AuNS (d = 160 nm) were determined, ranging between 8.75-12.5 $\mu\text{g}/\text{ml}$. It has been reported that such concentrations have no cytotoxic effects on the cell up to 24h[167], where nanoparticles have furthermore been reported to be minimally cytotoxic[167, 176, 177] and negatively charged AuNPs are generally considered to be non-toxic[178]. The internalization of these particles was evaluated in breast cancer (MCF7) cells incubated with the nanoparticles for 4h, 16h, or 24h. Both types of nanoparticles were endocytosed and found close to the nuclear perimeter, with a greater number of particles found at the perinuclear space after 16h incubation than for 4h. Cells incubated with NPs for 16-24 hours showed similar NP internalization and localization. However, the cells exposed to NPs for 24h showed actin stress fibers, a stress response likely due to excessive AuNP uptake (data not shown). Streptavidin-functionalized AuNS were found to accumulate

to a greater degree at the perinuclear space than AuNPs, which might be attributed to their functionalization by the linker molecule streptavidin, which targets membrane sites[184]. The optimal experimental conditions were hereby determined, excluding 80 nm-sized AuNP, which were less likely to generate sufficient heat for disrupting both the encapsulating endosomal membrane and the rigid nuclear envelope compared to larger particles. Accordingly, AuNSs were incubated with MCF7 cells for 16h to allow them to be trafficked to the nuclear envelope, as illustrated in Figure 4.2, and minimize cellular stress induction, enabling optical trapping of nanoparticles at the nuclear surface and investigation of the protein response to this disruption.

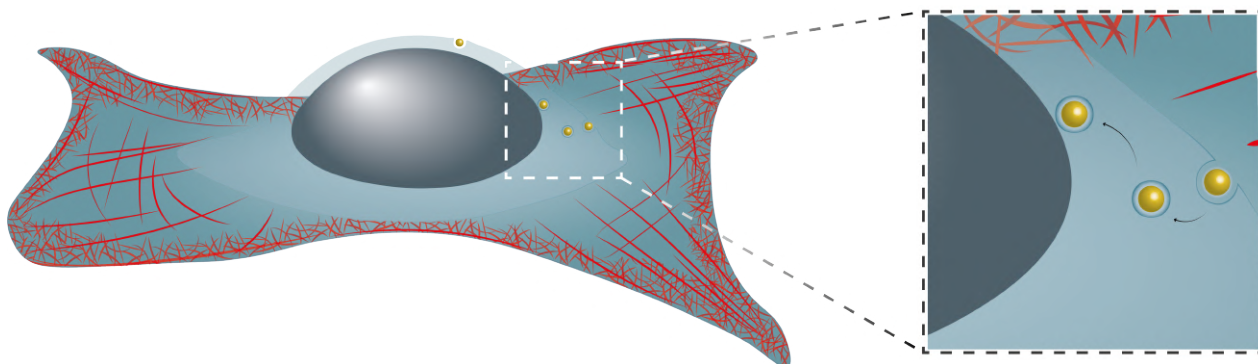


Figure 4.2: A schematic representation of a cell, depicting its cortical actin cytoskeleton. An enlarged view of the nuclear region demonstrates the endocytosis of AuNPs, which are transported to the nuclear envelope, where they can be subjected to irradiation, leading to the disruption of the nuclear envelope.

4.3 Actin structure and function

The cortical actin network is known to enhance membrane tension due to its attachment to the plasma membrane. For efficient membrane resealing, the influx of Ca^{2+} initiates actin cytoskeletal remodeling through local depolymerization of actin filaments into actin monomers[8, 152, 185]. This is followed by a rapid repolymerization that leads to the formation of a dense network of filamentous actin at the injury site, thereby reinforcing the membrane and possibly preventing further damage or facilitating membrane resealing[31].

Several studies have demonstrated that external mechanical forces, such as cell stretching[186], fluid shear stress[187, 188], and optical forces, can induce actin reorganization in cells[152]. Cells have been observed to adapt to their physical microenvironment through specific mechanosensing mechanisms, such as actin assembly in the perinuclear region[152, 189, 190]. This mechanotransduction mechanism is primarily facilitated by the cytoskeleton, which, when subjected to tension forces, can activate molecular sensors, trigger intracellular signaling cascades, and result in a coordinated cellular response that mediates tension levels within the cell[8]. Ele-

vated intracellular Ca^{2+} levels, in conjunction with calcium regulator calmodulin and actin polymerization factor inverted formin-2 (IFN2), have been shown to induce the rapid accumulation of actin around the nucleus in response to both mechanical and biochemical stimuli[152, 189]. This force-induced remodeling of perinuclear actin could be interpreted as an attempt by the cell to protect the nucleus from mechanical-induced ruptures[8]. The repair mechanisms of the plasma membrane and nuclear envelope share similarities, such as the involvement of the endosomal sorting complex required for transport (ESCRT-III) in nuclear envelope repair[168], suggesting a potential overlap between the plasma membrane and nuclear envelope repair mechanisms. This raises the question of whether perinuclear actin remodeling is not only limited to mechanosensing or also involved in nuclear envelope repair.

4.4 The experimental conditions

Although actin has many known functions, and recent studies have reported actin remodeling within the perinuclear space, such experiments have primarily been conducted either in vitro or solely by plasma membrane disruptions. Therefore, this chapter aims to investigate the response of actin to local disruption of the nuclear envelope in order to gain a better understanding of its reorganizing properties and potential role in repairing intracellular membranes in living cells. The experimental setup was similar to that presented in Chapter 3, except that instead of surface-immobilized gold nanoparticles, AuNS were endocytosed into MCF7 cells and internalized near the perinuclear region. Optical trapping and brief irradiation with ~ 230 mW was used in a total of 95 experiments conducted under varying conditions, depending on which proteins were investigated. These experiments included investigation of ANXA4-RFP response following nuclear membrane disruption, as presented in Section 3.3.5, as well as the response of actin tagged with either RFP or SPY650-FastAct, a fluorescent probe optimized for F-actin labeling. The cell nuclear membrane was visualized by coupling GFP to either NUP153 or Lamin B. NUP153 is a nucleoporin, which is an essential component in the nuclear pore complexes, that regulates macromolecular transport[142], while Lamin B1 is a constituent of the intermediate filamentous lamina that provides support to the nuclear envelope[174]. Additionally, two other components, the nuclear localization signal (NLS) and the DNA-specific dye Hoechst 33258, were included in the experiments to further confirm nuclear and plasma membrane disruptions, as elaborated on in the following sections.

The thermoplasmonic approach, as previously introduced in Section 2.2, is well known for generating significant heating in plasmonic nanoparticles. The study by Fraire et al.[69] reported two distinct photothermal effects resulting from the irradiation of AuNP within endosomes. One of these effects induced endosomal membrane permeabilization, which was found to be directly correlated with the clustering of AuNP within the endosome, since clustering generates significantly more heat than a single particle[70]. Additionally, under certain conditions

such as surpassing the energy barrier (Equation 3.2) and the pressure within the NB exceeding the ambient pressure (Equation 3.1), this photothermal effect may give rise to the formation of nanobubbles (NB), which efficiently increase the boiling temperature in water, as describe in Section 3.2. This phenomenon has been previously highlighted by Bauffou et al.[135] and has been reported to occur at temperatures exceeding 200 °C[74, 135, 136]. Moreover, the threshold for NB formation may be affected by the clustering of AuNPs[65], as the collective radius of the aggregate is significantly larger than that of a single particle. However, NB formation within endosomes was reported to be independent of AuNP clustering, possibly due to the rapid nature of the nanoscale bubble phenomenon upon surpassing the NB threshold, independent of the number of AuNPs present within the endosome[69]. Furthermore, Fraire et al.[69] demonstrated that nanobubble formation induced by particle irradiation was particularly efficient in causing endosomal bursting due to its explosive heating. Despite being a more drastic nanoscale event compared to heat diffusion, NB formation was reported to not compromise cell viability or long-term cell homeostasis[69] and is, therefore, an excellent tool for the selective puncture of intracellular membranes.

4.5 Actin response to internal membrane disruption

This study employed confocal imaging to monitor the actin response upon nuclear envelope disruption. Specifically, actin was coupled with RFP, and the nuclear envelope was indirectly visualized through GFP coupling with Lamin B1. Following irradiation of AuNSs the nuclear envelope was presumed to be disrupted, given the deformation of the lamina (Fig. 4.3A, 10 sec) located beneath the inner nuclear membrane. Subsequent to nuclear membrane rupture, actin accumulated at the perinuclear region (Fig. 4.3A, 1 min), presumably mediated by Ca^{2+} influx upon simultaneous PM disruption[152, 189]. Notably, actin accumulation appeared to originate at the irradiation site (Fig. 4.3B, 20 sec), and was followed by a complete actin assembly encircling the nuclear rim (Fig. 4.3A, 03:00), which peaked in intensity at 2.3 min (Fig. 4.3C). The actin ring structure was found to disassemble during the following minutes, consistent with prior research by Shao et al.[152], who noted actin polymerization in the perinuclear region to be a reversible process within two minutes for cells subjected to mechanical stimuli at the cell periphery. In the present case, the nuclear membrane was subjected to rupture, which may explain the actin response, whereby reversible actin polymerization at the nuclear membrane culminated in actin accumulation at the injury site (Fig. 4.3B, 6:00) where it appeared to form a plug (Fig. 4.3B, 12:00), with maximum actin intensity observed at 9.7 min. These observations were consistent with preliminary findings by our collaborators at the Danish Cancer Research Center, who reported a similar actin response and accumulation upon pulsed laser irradiation of the nuclear envelope.

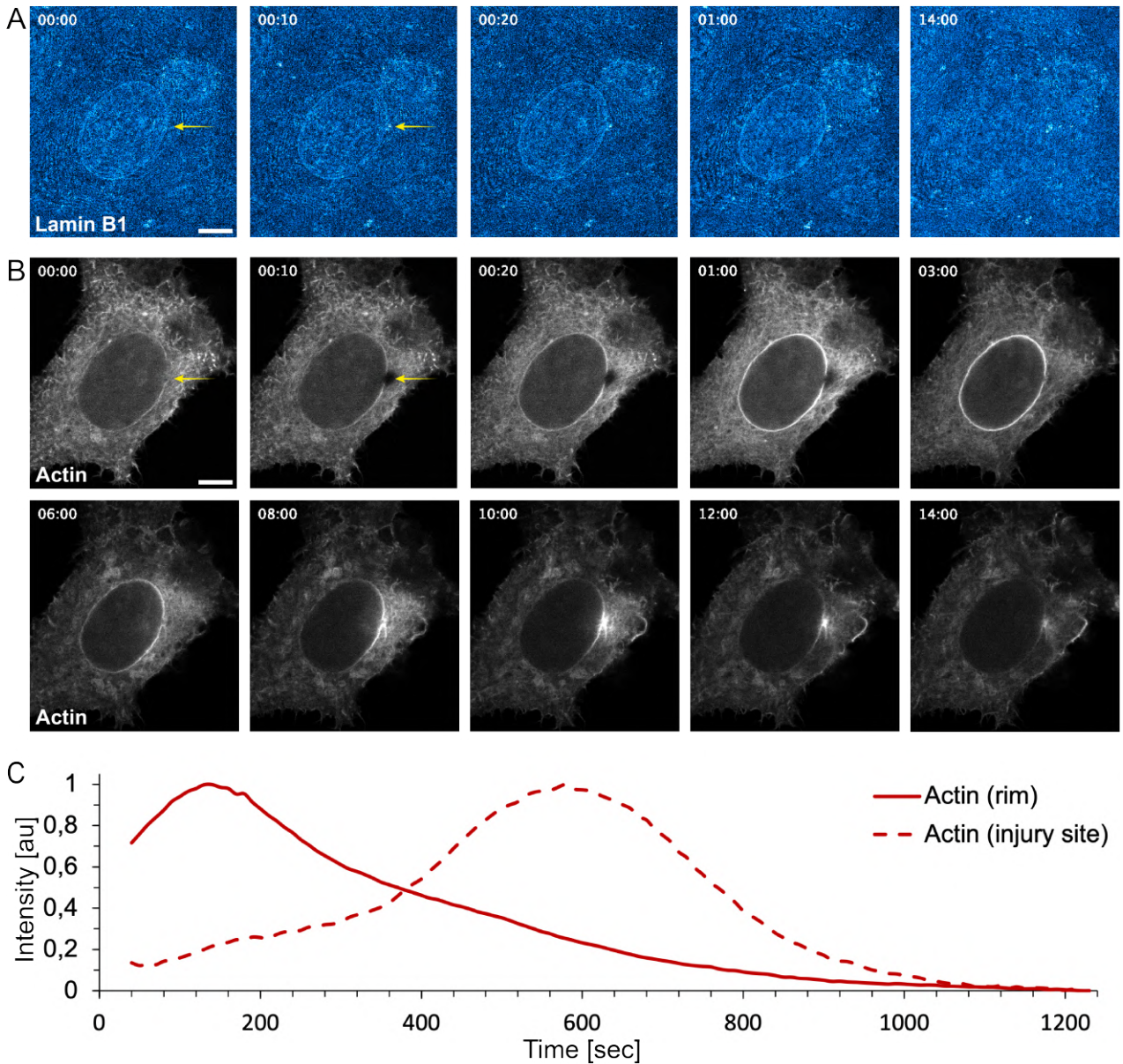


Figure 4.3: Confocal imaging was employed to monitor the response of actin to nuclear envelope disruption in MCF7 cells utilizing AuNSs and thermoplasmonics. The nuclear perimeter was visualized by coupling Lamin B1 with GFP (A), while the actin response was visualized by actin-RFP (B). Images were captured before (00:00), upon (00:10), and after thermoplasmonically induced injury at the nuclear envelope. The irradiation site is highlighted by the yellow arrows, and the scale bars measure $10 \mu\text{m}$. In panel (C), the actin intensity was measured at the perinuclear region (red line) and at the injury site (red dashed line) as a function of time. The perinuclear actin reached a maximum at 2.3 min, after which the actin polymerization was reversed, leading to a decrease in perinuclear intensity, while the actin intensity at the injury site increased and reached a maximum at 9.7 min.

The assembly of perinuclear actin is thought to be a cellular response aimed at protecting the nucleus from mechanical ruptures[8, 152]. Nevertheless, it remains unclear if perinuclear actin remodeling is solely limited to mechanosensing. It has been reported that the plasma membrane and nuclear envelope share similar repair mechanisms, such as the ESCRT-III mediated repair[168]. This suggests that actin-mediated membrane repair could also occur

at the nuclear membrane similar to plasma membrane repair. The observed actin formation in the perinuclear space suggests extracellular calcium influx[152]. This is initiated by the Ca^{2+} influx, which led to local depolymerization of the actin cortex[152], followed by a rapid repolymerization of new actin forming a dense actin network at the injury site, which in turn prevents repeated injury[7]. Actin is also suggested to mediate membrane integrity by wound contraction, where actin and Myosin II form a complex minutes after membrane resealing[6]. This could explain the observed actin translocation over time, where actin initially accumulates at the perinuclear region, protecting the nucleus, while the membrane injury is resealed. The actin polymerization then appears to reverse (Fig. 4.3C, red line) and translocate to the injury site (Fig. 4.3C, red dashed line) after the presumed wound resealing, potentially to reconstruct and strengthen the injured membrane.

The reduction in overall cytosolic actin intensity over time, which suggests a shift in the focal plane, is noteworthy. However, given that the periphery of the membrane remains in focus throughout the timelapse imaging, the shift would be minimal. While the decrease in cytosolic actin intensity and vague Lamin B1 signal can be attributed to bleaching, this does not affect the observed actin response to thermoplasmonic-induced membrane disruption. It is worth noting that the nucleus exhibits slight deformation or a decrease in volume over time after nuclear disruption, which has also been observed by our collaborators. Actin-based mechanisms, such as the membrane contractile abilities of the actin-Myosin II complex, have been proposed to facilitate nuclear deformation, which further can result in altered gene expression due to the reduction in nuclear volume[169]. However, Shao et al.[152] refuted this claim as neither myosin IIA nor myosin IIB was found to be associated with the perinuclear actin rim, and inhibition of myosin II contractility did not affect the formation of this actin structure. Furthermore, the rapid actin polymerization around the nucleus has been shown to depend on calcium bursts[152, 189], as its formation was prevented in a calcium-depleted medium as well as upon treatments that inhibited actin polymerization[152]. It has been proved that mechanical stimulation of cells increases the cytosolic calcium concentration[191, 192], which is a prerequisite to perinuclear actin assembly[152]. Nonetheless, it has been debated whether the polymerization is solely triggered by extracellular influx into the cytoplasm, either through stretch-sensitive channels[192, 193] or by a reversible membrane rupture[54, 76, 49], or whether it can be triggered by the release of calcium from the endoplasmic reticulum (ER)[143, 169].

Previous studies have suggested that the Ca^{2+} -dependent assembly of actin around the nuclear rim is triggered by plasma membrane disruption[152, 189]. However, it remained unclear whether the elevated Ca^{2+} levels in the present study were due to extracellular Ca^{2+} influx or Ca^{2+} release from the ER upon internal thermoplasmonic disruption. To discern between these possibilities, a fluorescent dye, Hoechst 33258, was utilized. The rather membrane-impermeable dye preferentially binds to DNA and thus targets the cell nucleus specifically.

By adding Hoechst 33258 to the extracellular medium, it could be confirmed whether or not the plasma membrane had been disrupted by observing an increase of Hoechst within the nucleus. This would also enable the assessment of whether the observed actin mechanism was solely due to plasma membrane rupture or whether the response was affected by nuclear envelope rupture. As shown in Figure 4.3A, deformation of the lamina network could suggest that the outer double membrane system experienced a force significant enough to disrupt the nuclear membrane, but this remained an assumption. To monitor the disruption of the nuclear envelope, nuclear localization signals (NLS) coupled with GFP were employed. NLS are short peptides that act as signal fragments that transport proteins from the cytoplasm into the nucleus through nuclear pore complexes[171]. NLS coupled with GFP were predominantly observed in the nucleoplasm, and their flow into the cell cytoplasm was expected as the nuclear envelope was ruptured.

4.6 Actin mechanosensing upon plasma membrane disruption

Initially, a control experiment was performed where the peripheral plasma membrane was thermoplasmonically disrupted. To visualize the resulting effects, the F-actin targeting dye SPY650-FastAct was used to label actin, and Hoechst 33258 was introduced to the extracellular medium. The outcome of the control experiment is depicted in Figure 4.4, where the injury site is indicated by the yellow arrow. Following plasma membrane disruption, actin was found to accumulate around the nucleus (Fig. 4.4A and 4.4C, red line), while extracellular cell impermeable Hoechst 33258 accumulated in the nucleus (Fig. 4.4B and 4.4C, gray line). Notably, this event was specific to the injured cell, as the neighboring control cell exhibited no change in either actin response or Hoechst 33258 uptake (Fig. 4.4C, red and gray dotted lines, respectively). These observations are in agreement with previous studies upon both mechanical and chemical stimuli of the plasma membrane, where actin mechanotransduction was triggered by extracellular Ca^{2+} influx[152, 189]. However, in contrast to prior findings, the perinuclear actin did not disassemble during the 4-minute observation period. Additionally, actin was observed to accumulate at the injury site, displaying a rapid increase in intensity upon rupture (Fig. 4.4C, irradiation time is denoted by the blue dashed line) and forming a ringlike structure around the wound. This response appeared to be unique to thermoplasmonic-induced injuries, as it has not been reported in previous studies[152, 189] nor observed by our collaborator upon pulsed laser-induced injuries. As the accumulation of actin in the perinuclear region has been proposed to shield the nucleus[8], it raises the question of why actin rapidly accumulates around the injury site. It is uncertain whether this accumulation is an effort to protect the cell from potential repeated injuries by forming a dense actin network around the wound, by encapsulating the AuNS, or if the immediate actin response is a component of PMR and the subsequent accumulation (Fig. 4.4C, yellow dashed

line) is due to its remodeling capacity. Nevertheless, given the specificity of this observation to the thermoplasmonic method, it is also possible that actin is interacting with the air-water interface during nanobubble formation.

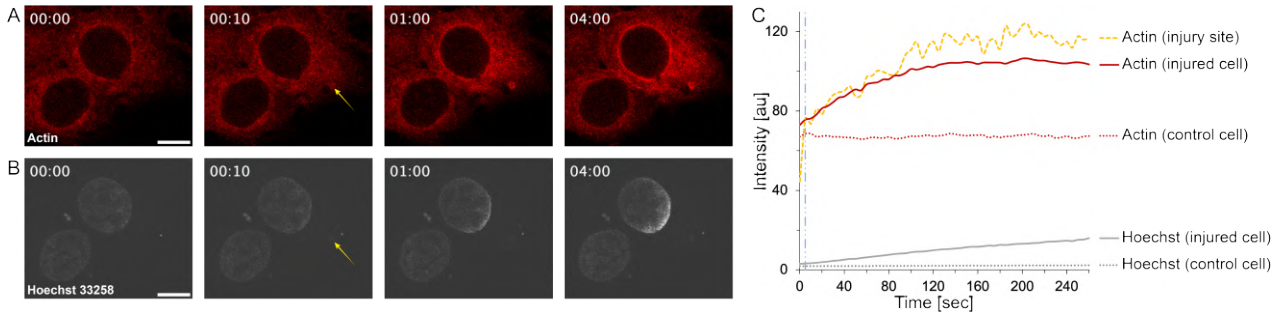


Figure 4.4: The confocal images illustrate the response of actin to plasma membrane disruption in MCF7 cells, facilitated by NIR irradiation of AuNSs. Actin was labeled with SPY650-FastAct (A), while extracellular residing Hoechst 33258 was used to assess plasma membrane rupture (B). In panel (C) the fluorescent intensity was measured as a function of time for the actin intensity at the perinuclear region (red line), at the injury site (yellow dashed line), and at the perinuclear rim of the neighboring control cell (red dotted line). Similarly, Hoechst 33258 was measured within the nucleus for the injured cell (gray line) and the control cell (gray dotted line). Images were captured before (00:00) and immediately after (00:10) thermoplasmonically induced plasma membrane injury, with the irradiation site marked by the yellow arrows. The scale bars denoted $10 \mu\text{m}$. Upon laser irradiation at 5 seconds (vertical blue dashed line), the actin accumulation at the injury site rapidly increased, as observed by the fluorescence intensity measurements.

In summary, the control experiment established the assembly of actin in the perinuclear region upon disruption of the plasma membrane, as indicated by the influx of extracellular impermeable Hoechst 33258, supporting previous reports claiming actin mechanotransduction to rely on the influx of extracellular calcium[152, 189]. Additionally, it has been previously reported that Ca^{2+} can trigger the disassembly of actin structures[122] and that the accumulation of actin observed in the present study is likely the result of an increase in the level of monomeric actin following this Ca^{2+} -dependent actin filament disassembly. While the previous studies have described reversible actin polymerization, the control experiment did not exhibit this phenomenon over the 4-minute observation period, with the accumulation of actin in the perinuclear region reaching a plateau within 3 minutes. However, it remains unclear if a prolonged observation period would reveal actin polymerization reversal since the thermoplasmonic rupture might be more severe, and hereby induce a more extensive actin response, than the injuries obtained in aforementioned studies [152, 189]. Taken together, the results suggest that peripheral plasma membrane injury may modulate nuclear function via local mechanical signaling from the cell periphery. The accumulation of actin at the injury site raises questions about whether it serves a protective, repair, or remodeling function, or whether it is a response to nanobubble formation. Further research is needed to explore these hypotheses.

4.7 Nuclear envelope disruption

Disrupting the rigid, double lipid bilayer, nucleus proved to be a challenging task, as often the more fluid plasma membrane was ruptured while the nucleus remains unaffected or only slightly deformed due to explosive thermoplasmonic heating. To confirm the lack of nuclear membrane disruption, the absence of NLS efflux from the nucleoplasm was noted, while the influx of Hoechst 33258 indicated plasma membrane rupture and led to actin accumulation in the perinuclear region, as presented in Figure 4.4. However, upon successful nuclear envelope disruption, the actin response was observed to fall within two distinct scenarios, depending on whether or not the plasma membrane was simultaneously disrupted, as depicted in Figures 4.5 and 4.6.

4.7.1 Simultaneous nuclear envelope and plasma membrane disruption

The first scenario employed confocal imaging to investigate the response of actin to the simultaneous disruption of the nuclear envelope and plasma membrane in MCF7 cells using AuNSs. This is schematically illustrated in Figure 4.5A, which shows a close-up view of the nucleus before, upon, and after irradiation which corresponds to the confocal images in Figure 4.5B.

Prior to irradiation, the actin filaments appeared homogeneously distributed within the cell and the nucleoplasm was identified by NLS (Fig. 4.5B, 00:00). The irradiation site, indicated by the yellow arrow, was located at the nuclear envelope where the AuNS aggregates generated tremendous heat upon irradiation. This caused a nuclear deformation at the injury site as well as a disruption of both the nuclear envelope and plasma membrane (Fig. 4.5B, 6 sec). These observations were supported by NLS rapidly flowing out of the nucleus into the cytosol and increased nuclear uptake of Hoechst 33258 over time. This resulted in an actin accumulation at the perinuclear region forming an actin rim around the nucleus that remained stable for the duration of the observation. The actin response was analyzed by its intensity at the nuclear rim as a function of time, as presented in Figure 4.5C. The analysis supported the observation that the actin intensity at the nuclear rim increased immediately after membrane injury (red line) compared to the low, constant actin intensity at the nuclear rim in the control cell (red dotted line). The intensity of NLS (blue line) exponentially decreased until it was homogeneously dispersed within the cytosol, whereby the NLS intensity remained stable. Furthermore, Hoechst 33258 was observed to increase within the nucleus upon laser irradiation (gray line), indicating PM disruption. This increase was only observed in the injured cell compared to the control cell (gray dotted line), confirming that the upconcentration was due to PM rupture and not by Hoechst 33258 permeating the cell membrane.

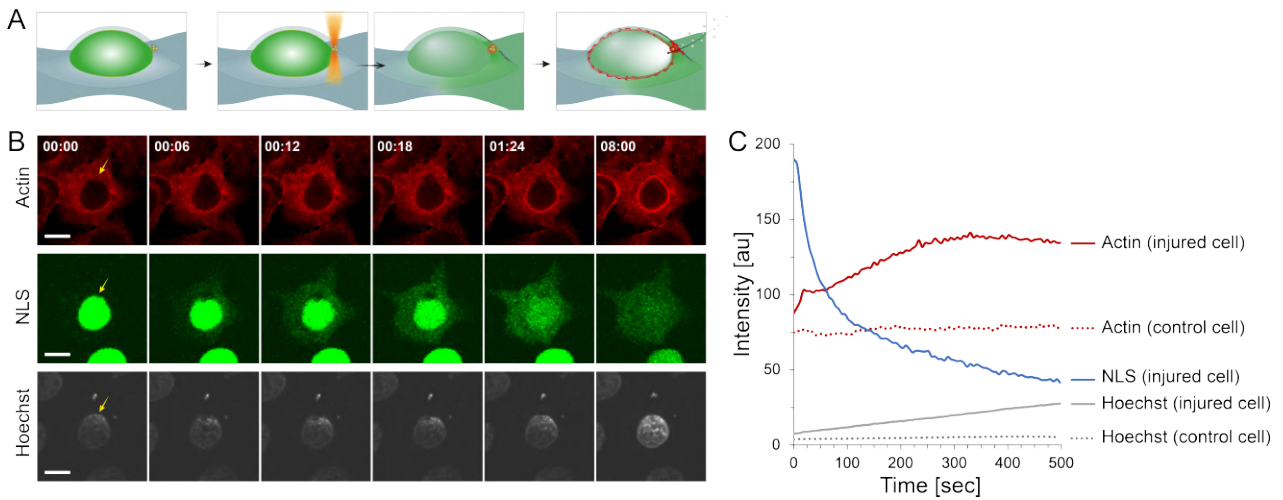


Figure 4.5: The first scenario is depicted in which NIR laser irradiation of endocytosed AuNS aggregates disrupts both the nuclear envelope and plasma membrane. The schematic provides a close-up view of the nucleus before, during, and after irradiation (A), with the injury site highlighted by yellow arrows, as demonstrated in the confocal images (B). The confocal images were obtained for actin, NLS, and Hoechst 33258, with 00:00 representing pre-irradiation, 00:06 denoting upon irradiation, and 00:12 post-irradiation, with scale bars measuring 10 μm . In panel (C), the fluorescent intensity was measured as a function of time for actin at the perinuclear region of the injured cell (red line) and the perinuclear rim of a neighboring control cell (red dotted line). The NLS intensity within the nucleus decreased exponentially after laser irradiation (blue line), while Hoechst 33258 increased over time within the nucleus for the injured cell (gray line) and remained constant within the control cell (gray dotted line). The Hoechst 33258 images were enhanced for better visualization.

The findings suggest a mechanotransductive role for actin, as it appeared to polymerize at the nuclear envelope, as depicted in Figure 4.5B and C. In contrast to Figure 4.3, actin did not display reversible polymerization or significant localization at the injury site, and further exhibit a slight deformation at the nuclear injury site. Notably, the actin response for Figure 4.5 was only followed for 8 min, in contrast to 14 min for Figure 4.3, in which actin was not fully reversed after 8 min. However, actin seemed to accumulate and create a dense layer surrounding the nucleus, potentially to safeguard it from further harm[8]. It is noteworthy that actin only appeared to accumulate at the nuclear envelope of the injury site following the confinement of the nuclear deformation to its initial state. The absence of actin prior to the reestablished nuclear volume might indicate the involvement of other membrane repair mechanisms. To investigate whether a genuine repair mechanism is taking place at the nuclear membrane, CHMP4B, tagged with GFP, could be used as a positive control marker. CHMP4B is the primary component of the ESCRT-III complex, which is one of the few components known to participate in nuclear envelope repair[168]. Detection of CHMP4B at the injured nucleus would therefore verify the occurrence of actual repair after thermoplasmonic nuclear rupture. Assuming that the nuclear membrane was repaired before the accumulation of actin at the rim of the repair site, it is plausible that actin could contribute to the reconstruction of the nuclear envelope. This could also explain the slight delay in the formation of a complete

actin rim around the nucleus reaching a maximum intensity at 5.5 min, as opposed to the 2 min post mechanical force stimuli[152] and to the observation in Figure 4.4 and Figure 4.3, where the latter nuclear disruption remains as an assumption. The prolonged observation of actin at the perinuclear region and its possible reversible mechanism could be delayed due to nuclear damage, where the repair of both nuclear and plasma membranes takes precedence.

4.7.2 Exclusive disruption of the nuclear envelope

The second scenario, presented in Figure 4.6, demonstrated a distinct response of actin to the selective disruption of the nuclear envelope without permeabilizing the plasma membrane. The schematic depiction of the cell nucleus in Figure 4.6A corresponds to the confocal imaging observations presented in Figure 4.6B, which were subsequently analyzed in Figure 4.6C using a methodology similar to that employed in the first scenario. Prior to irradiation, actin filaments were homogeneously distributed within the cell (Fig. 4.6B, 00:00). The nucleoplasm was visualized by nuclear localization signals (NLS), while AuNSs aggregated at the nuclear envelope constituting the irradiation site (denoted by the yellow arrow). Upon irradiation and subsequent thermoplasmonic heat generation, the nuclear envelope was disrupted without causing nuclear deformation (Fig. 4.6B, 6 sec). The disruption was confirmed by NLS flowing out of the nucleus into the cell cytosol at an exponential rate (Fig. 4.6C, blue line), becoming constant as NLS is homogeneously distributed throughout the cell. The lack of Hoechst 33258 influx confirmed that the plasma membrane was not disrupted, which was further verified by the constant Hoechst intensity within the nucleus over time (Fig. 4.6C, gray line) similar to the background Hoechst 33258 signal (gray dotted line). Moreover, actin accumulation was not observed at the perinuclear region, further indicating that the plasma membrane remained intact, while actin was observed to accumulate at the injury site immediately after laser irradiation. The analysis showed a constant actin intensity around the nuclear rim over time (Fig. 4.6C, red dotted line), which appeared unaffected by the internal injury. However, the intensity of actin at the injury site (red line) increased rapidly upon irradiation and subsequently assembled into a stable structure surrounding the AuNS aggregates. The accumulation of actin around the AuNS aggregates is visualized by the insert of the injury site in Figure 4.6B. The drop in actin intensity observed upon laser irradiation (Fig. 4.6C, 6 sec) is likely due to fluorescent quenching[140] and does not impact the actin mechanism itself. This was confirmed by an additional control experiment (Fig. A.5) conducted under the same conditions, where instead of labeling actin an empty RFP vector was employed as a control. This experiment, supported by previous findings[31, 131], confirmed that the observed actin response occurs independently of the fluorescent coupled protein, and is therefore not due to a methodical artifact created by vapor pressure or other factors. This supplementary finding proved RFP to be homogeneously distributed within the cell prior to irradiation (Fig. A.5A), quenched upon irradiation (Fig. A.5B), and homogeneously distributed immediately after irradiation (Fig. A.5C), without accumulating at any other part of the cell.

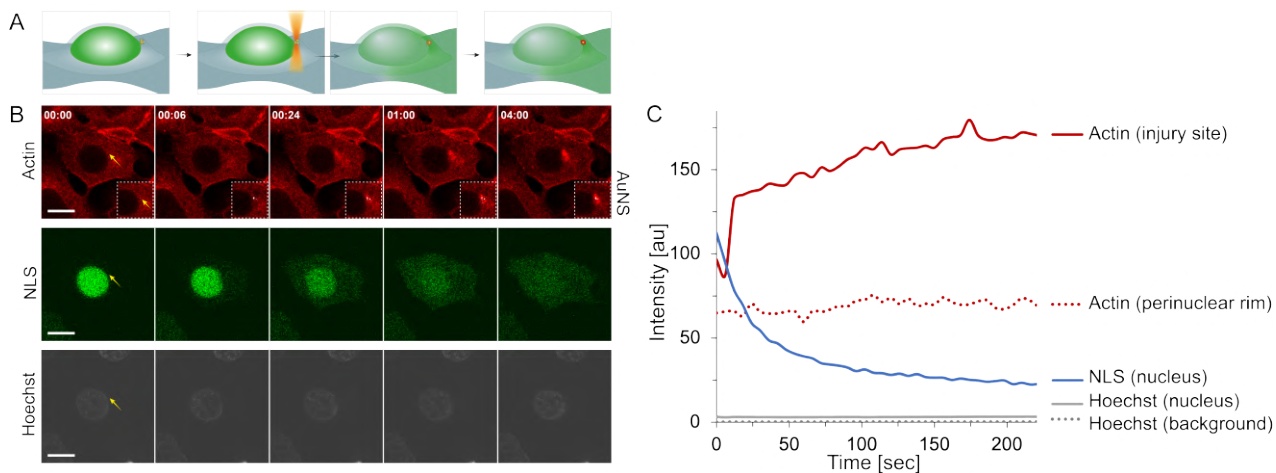


Figure 4.6: The second scenario depicts the disruption of the nuclear membrane upon laser irradiation of endocytosed AuNS aggregates. The schematic provides a detailed view of the nucleus before, during, and after irradiation (A), with the injury site highlighted by yellow arrows, as clearly demonstrated in the confocal images (B). Confocal images were obtained for actin, NLS, and Hoechst 33258, with the time points 00:00, 00:06, and 00:24 representing pre-irradiation, upon irradiation, and post-irradiation, respectively. In panel (C), the fluorescent intensity was measured over time for actin at the perinuclear region (red dotted line) and at the injury site (red line). The NLS intensity within the nucleus exhibited an exponential decrease upon laser irradiation (blue line), while Hoechst 33258 remained constant over time (gray line) similar to the Hoechst background signal (gray dotted line), indicating no plasma membrane disruption. The AuNSs are visualized by their reflection, as white dots, at the injury site, depicted in the (red) insert in panel (B). Moreover, the Hoechst 33258 images were enhanced for better visualization (C), and the scale bars measure $10 \mu\text{m}$.

The results of the quantitative analysis corroborated the qualitative observation, indicating that the disruption was limited to the nuclear envelope. Since the outer nuclear membrane is continuous with the endoplasmic reticulum (ER)[172], it is presumed that the ER was also disrupted. The endoplasmic reticulum (ER) functions as a repository for calcium within the cellular environment. Notably, the calcium concentration within the ER ranges from $100\text{-}800 \mu\text{M}$, which stands in contrast to the cytosol's calcium concentration of 100 nM and the extracellular milieu's concentration of $1\text{-}2 \text{ mM}$ [194]. Following ER disruption, the cell would be expected to experience an increase in intracellular calcium, which has been suggested to trigger the specific mechanosensing mechanism that leads to actin assembly in the perinuclear region[169]. The present study suggests that an intracellular calcium boost resulting from ER leakage is insufficient for actin polymerization in the perinuclear region, strongly indicating that the mechanotransduction is specifically dependent on extracellular calcium influx, consistent with the findings by Wales et al.[189]. However, the accumulation of actin at the injury site remained an open question. It is unclear whether it is an attempt to shield the cell from potential repeated injuries by creating a dense actin network at the injury site (Figure 4.3) or by encapsulating the AuNSs (Figure 4.4), or whether it is a marker of membrane repair, where the immediate actin response is part of the membrane repair mechanism, and its further accumulation (as seen in Figure 4.4C, denoted by the yellow dashed line, and in Figure 4.6C,

represented by the red line) is due to its membrane remodeling/reorganization ability. Notably, as this observation is specific to the thermoplasmonic method, as well as temperatures exceeding $\sim 200^{\circ}\text{C}$ can induce nanobubble formation at the AuNP surface[74, 135, 136], it could also be an indication of actin interacting with the air-water interface upon nanobubble formation. In conclusion, the preliminary findings, combined with previous research, suggest that extracellular calcium influx is a requirement for the mechanosensing mechanism of perinuclear actin. Moreover, exploring repair mechanisms at the nuclear membrane following disruption is an area of significant interest. One potential method of inquiry is through the labeling of the CHMP4B component of the ESCRT-III complex, which is among the few known components involved in the process of nuclear envelope repair[168]. Through this approach, it may be possible to determine whether repair mechanisms are activated in response to exclusive nuclear membrane rupture or in conjunction with plasma membrane disruption.

4.8 Concluding remarks

Numerous studies have focused on exploring the role of actin, where its dynamic nature has been proposed to be involved in several mechanisms, including its mechanosensing ability, which enables actin remodeling at the perinuclear space in response to mechanical and biochemical stimuli[152, 189]. This chapter aims to investigate the response of actin to selective and localized disruption of the nuclear envelope and to gain insight into its reorganizing properties and potential contribution to intracellular membrane repair in living cells.

This study focused on optimizing the selective puncturing method of the nuclear envelope using plasmonic gold nanoparticles since the puncturing of the rigid nucleus posed a significant challenge. Therefore, the 95 experiments included a variety of experimental conditions, such as investigation of the response of either ANXA4 or actin to thermoplasmonic disruption of the plasma membrane and/or the nuclear membrane. The nuclear membrane was visualized by labeling the NUP153 component of the nuclear pore complex or indirectly by labeling Lamin B1, a component of the underlying nuclear membrane lamina. Additionally, to verify nuclear envelope rupture, the nuclear localization signal (NLS) was tagged to observe its efflux out of the nucleus upon rupture. The rupture of the plasma membrane was confirmed by the influx of the extracellular residing, membrane impermeable, DNA-specific Hoechst 33258, which accumulates within the nucleus upon plasma membrane rupture. The initial findings of this study demonstrated that actin remodeling occurs in response to membrane disruption. After successful disruption of the nuclear envelope, the actin response was found to conform to two distinct scenarios, depending on the presence or absence of concurrent plasma membrane disruption, as illustrated in Figures 4.5 and 4.6.

Following plasma membrane disruption, actin was observed to assemble as a dense struc-

ture surrounding the nucleus, which was observed in the majority of the experiments. This observation is consistent with previous studies, reporting that the assembly of actin around the nuclear rim is Ca^{2+} -dependent and triggered by plasma membrane disruption[152, 189]. In $\sim 5\text{-}10\%$ of the experiments, the perinuclear assembly of actin appeared to disassemble in the following minutes (Fig. 4.3). This finding is consistent with previous research reporting that perinuclear actin polymerization is a reversible process observed within two minutes in cells subjected to mechanical stimuli at the cell periphery[152]. However, the reversible process appeared to be prolonged for the thermoplasmonic method, possibly due to the extent of injury, as the thermoplasmonic approach may induce more severe injuries than the mechanical force induced on the plasma membrane using a bead on an AFM tip[152].

Moreover, following the disruption of the nuclear envelope and plasma membrane, actin disassembly at the perinuclear region was followed by its translocation to the injury site, where it seemed to form a plug (Fig. 4.3). Further investigation is required to determine the frequency of this response, given that it only was observed in $\sim 3\%$ of the experiments. Moreover, long-term imaging is recommended as this phenomenon appeared to occur after tens of minutes, whereas the majority of experiments were conducted on a shorter timescale. Furthermore, a notable response of actin to selective disruption of the nuclear envelope, without permeabilizing the plasma membrane, was observed in $\sim 4\%$ of the preliminary experiments, as demonstrated in Figure 4.6. In this scenario, actin was not observed to accumulate around the nucleus, indicating that the plasma membrane remained intact, which was further confirmed by the absence of Hoechst 33258 influx. However, actin was observed to accumulate at the injury site immediately following laser irradiation. Since the outer nuclear membrane is continuous with the endoplasmic reticulum (ER) [172], it can be assumed that the ER is simultaneously disrupted. The present study thus suggests that an increase in intracellular calcium resulting from ER leakage is insufficient for actin polymerization in the perinuclear region, strongly implying that mechanotransduction is specifically reliant on extracellular calcium influx, an observation consistent with the results of Wales et al.[189].

The accumulation of actin in the perinuclear region has been proposed to serve as a protective function, supporting and shielding the nucleus from potential harm[8]. However, this raises the question of why actin rapidly accumulates around the injury site. It remains unclear whether this accumulation is a defensive mechanism, aimed at protecting the cell from further injury by forming a dense actin network around the wound or by encapsulating the gold nanoparticles, as depicted in Figure 4.6 and 4.4. Alternatively, it could be a component of PMR and subsequent accumulation may be attributed to its remodeling capacity. To investigate whether repair mechanisms are taking place at the nuclear membrane, fluorescently labeled CHMP4B could be used as a positive control marker. CHMP4B is the primary component of the ESCRT-III complex, which is known to participate in nuclear envelope repair[168].

Detection of CHMP4B at the injured nucleus would therefore verify the occurrence of actual repair after thermoplasmonic nuclear rupture. Nevertheless, given that this observation has only been made using the thermoplasmonic approach, it is possible that the observed phenomenon is related to the unique thermoplasmonic properties of the method, where the actin response may be due to an interaction with the air-water interface of the nanobubble.

In summary, the preliminary findings demonstrated that peripheral plasma membrane injury triggers a mechanosensing mechanism, which is observed as actin assembly at the perinuclear region. This mechanism not only requires elevated Ca^{2+} levels, but specifically extracellular Ca^{2+} influx. Furthermore, while there is a need for further refinement of the thermoplasmonic technique, it has been demonstrated to enable selective disruption of the nuclear envelope, as evidenced by the efflux of NLS from the nucleus and the absence of Hoechst 333258 influx. Recently, the thermoplasmonic approach has been further developed, primarily relying on the formation of nanobubbles on the surface of AuNPs, using the Lumicks C-Trap. This optimized method has achieved an $\sim 80\%$ success rate of nuclear puncture along with plasma membrane permeabilization, which is a significant improvement compared to the $\sim 15\text{-}20\%$ success rate achieved during the development and optimization of the method presented in this chapter. However, since the Lumicks C-Trap lacks a reflection mode, co-localization between the laser focus and the particle of interest can be challenging. Therefore, brightfield imaging is used as an alternative method to assess the particle's position. Further testing and optimization of the method is however still necessary to achieve a higher success rate of selective nuclear envelope puncture.

5

Synapse formation and T-cell activation

During the period of my residency at the Dutch research center AMOLF, I had the opportunity to collaborate with Dr. Nebojša Jukić and Guusje Mouton from the Physics of Cellular Interaction group under the leadership of Dr. Kristina Ganzinger. The current investigation was part of a broader research initiative aimed at designing a novel two-dimensional experimental platform utilizing giant plasma membrane vesicles (GPMVs) extracted from tumor cell membranes. This platform had the potential to enhance the understanding of the biophysical mechanisms underlying the formation of immunological synapses and to investigate fundamental attributes of immune receptors and their ligands, including their spatiotemporal arrangement, response to forces, and effect on cellular activation and cytotoxicity.

The preliminary findings of the collaboration revealed that both complete and incomplete $\gamma\delta$ T-cell receptors had the ability to interact with tumor cells, detecting and actively searching for antigen-presenting tumor membranes through the extension, twisting, and retraction of finger-like protrusions, resulting in intracellular calcium fluxes. Moreover, the formation of immunological synapses, observed as a close contact between T-cells and tumor cells, resulted in T-cell activation and ultimately tumor cell lysis due to the cytotoxic nature of the T-cells. Additionally, T-cell interaction with GPMVs was investigated since the two-dimensional experimental platform was intended to be constructed from GPMVs. Despite observing T-cell activation upon interaction with tumor cells, no activation was observed when the T-cells were co-incubated with GPMVs derived from the same tumor cell line. These findings raised several questions regarding the properties of the GPMV membrane.

5.1 The immune system

The immune system is a complex network of cells, chemicals, and processes that serve to protect the body against harmful invaders, such as bacteria and viruses, as well as cancer cells, with the primary function to prevent infections and diseases[195]. The immune system can be categorized into two primary compartments: innate immunity and adaptive immunity based on their primary mechanism of action[196]. Innate immunity is a rapid defense mechanism that is antigen-independent, hereby less specific, and serves as the first line of defense against invasive pathogens. Adaptive immunity, on the other hand, is antigen-dependent and antigen-specific and is crucial when innate immunity fails to eliminate invaders. Although

adaptive immunity has a slower response time compared to innate immunity, cells of the adaptive immune compartment have a remarkable capacity to differentiate into memory cells, allowing for faster antigen recognition and a more rapid and efficient immune response upon subsequent exposure to the antigen[197].

The innate and adaptive immune responses are not mutually exclusive, but rather complementary mechanisms of defense. A defect in either mechanism can lead to both autoimmunity and immunodeficiency. Autoimmunity arises from self-reactive T-cells, which cause the immune system to attack its own healthy cells and tissue, resulting in autoimmune diseases such as Addison's disease, multiple sclerosis, arthritis, type I diabetes, and celiac disease, among others. In contrast, immunodeficiency occurs when the immune system's ability to fight infectious disease is compromised or absent, as observed for diseases such as leukemia and AIDS[198, 199]. Moreover, the adaptive immune response plays a critical role in effective immunization against infectious diseases, with T-cells acting as vital mediators and considered the key component in the immune response[195, 200]. Overall, a better understanding of the intricate mechanisms of the immune system is necessary to advance therapeutics for both autoimmunity and immunodeficiency.

5.1.1 T-cells

T-lymphocytes, also referred to as T-cells, are a specialized type of white blood cells. To carry out their function, T-cells are required to recognize and integrate signals from neighboring cells, which initiates signaling cascades. Ultimately, this process results in cytokine secretion, which is capable of modulating the behavior of other immune cells and triggering direct or indirect cytotoxic activity[4]. Additionally, T-cells are essential in the formation of long-lasting immune memory[200]. To recognize target cells, such as tumor cells, T-cells must form specialized close contacts with the target cells, referred to as immunological synapses[3].

$\alpha\beta$ T-cells, a vital component of the adaptive immune system, are activated through interaction with antigen-presenting major histocompatibility (MHC) molecules located on the surface of target cells. This interaction is facilitated by T-cell receptors (TCRs), a unique antigen-binding protein located on the T-cell membrane surface[201]. However, encountering tumor cells can present a unique challenge for T-cells since tumor cells share much of their surface antigen repertoire with the cells they originate from. Nevertheless, specific tumor antigens have been identified that enable T-cells to recognize and target tumor cells. This breakthrough has led to the development of adoptive T-cell therapies for certain types of cancer. However, downregulation or structural changes of these antigens can result in tumor antigen escape, ultimately reducing the effectiveness of chimeric antigen receptor (CAR) T-cell targeting, and recognition[202], which is an immunotherapeutic method that uses genetically engineered T-cells to target and eliminate cancer cells in the body[203].

$\gamma\delta$ T-cells, on the other hand, are a distinct subpopulation of T-cells characterized by the unique expression of a T-cell receptor (TCR) composed of γ and δ chains[201], as depicted in Figure 5.1. Their role in pathogen and parasite recognition has been well-established, and they have also been shown to play a critical role in tumor surveillance[204]. Unlike conventional $\alpha\beta$ T-cells, which recognize specific peptide antigens presented on major histocompatibility complex (MHC) molecules, $\gamma\delta$ T-cells are not MHC-restricted[205, 206]. Instead, they detect metabolic changes in target cells, specifically phosphoantigen content, which is altered in tumor cells or during infection by pathogens[207], as well as recognizing unconventional antigens such as stress molecules[205, 208]. These reported cytotoxic and antitumor lymphocytes are often found in tumor tissues and are considered a favorable prognostic factor[209]. Due to their ability to rapidly detect general metabolic changes, $\gamma\delta$ T-cells are considered part of the rapid innate immune system. However, as they also have the ability to generate immunological memory, this flexible response has been proposed to serve as a bridge between the innate and adaptive immune responses[210]. Additionally, $\gamma\delta$ T-cells communicate with multiple immune cells surrounding the tumor microenvironment[209], making them attractive candidates for adoptive immune T-cell therapies[211].

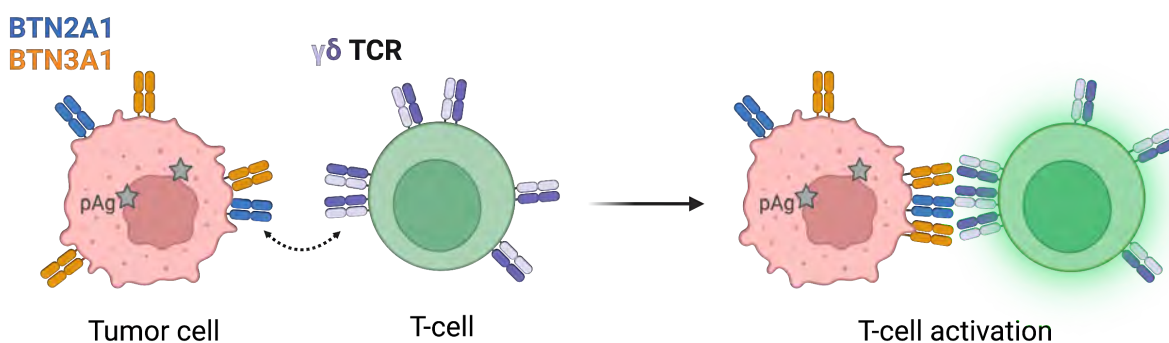


Figure 5.1: A schematic representation of a tumor cell featuring butyrophilins BTN2A1 and BTN3A1 integrated into its surface, along with a $\gamma\delta$ T-cell with its corresponding $\gamma\delta$ T-cell receptor (TCR). The figure portrays the two cells before (left) and after (right) the formation of immunological synapses mediated by the immune receptors and their corresponding ligands. This engagement triggers the activation of the T-cell, as indicated by the elevated intensity of intracellular calcium.

Despite their potential as immunotherapeutic agents, the development of $\gamma\delta$ T-cell-based therapies has been hindered by a lack of understanding of the mechanism of $\gamma\delta$ TCR signaling, which differs fundamentally from $\alpha\beta$ TCR signaling. While the principal molecules involved in immunological synapse formation in $\alpha\beta$ T-cells have been identified, $\gamma\delta$ T-cell synapses cannot be reconstituted using bottom-up approaches due to incomplete insight into the molecular components involved. Bottom-up reconstitution systems have played a crucial role in investi-

gating the organization and function of immune synapses in $\alpha\beta$ T-cells, leading to a greater understanding of the biophysical principles that govern synapse formation [212]. These studies have demonstrated that T-cell receptors (TCRs) exhibit specific patterns of spatiotemporal organization during T-cell activation[213], with force-dependent receptor-ligand interactions implicated in this activation process[214, 215]. Accordingly, a thorough comprehension of the molecular components and biophysical principles underlying $\gamma\delta$ T-cell synapse organization and function is imperative for the development of effective $\gamma\delta$ T-cell-based therapies.

5.1.1.1 The importance of butyrophilins for phosphoantigen sensing

V γ 9V δ 2 T-cells present a prominent subset involved in tumor surveillance[197] and are often targeted in $\gamma\delta$ T-cell-based immunotherapies[209]. These cells are stimulated by phosphoantigens (pAg) within antigen-presenting cells[216] and interact with the transmembrane protein family butyrophilins (BTNs), which belong to the immunoglobulin superfamily. BTNs are encoded by genes clustered in the extended MHC region of the human genome and classified into three subfamilies: BTN1, BTN2, and BTN3[205]. Notably, tumor cells express both butyrophilin 2A1 (BTN2A1) and butyrophilin 3A1 (BTN3A1), illustrated in Figure 5.1, where the presence of the latter is significantly correlated with patient prognosis[205]. The γ chain of the $\gamma\delta$ TCR interacts directly with BTN2A1[216, 217], while BTN3A1 is essential for $\gamma\delta$ T-cell pAg sensing. The intracellular domain of BTN3A1 is believed to bind to pAgs, inducing a conformational change that allows it to interact with BTN2A1[208], as well as induce a conformational change in BTN2A1, increasing its affinity of $\gamma\delta$ TCR for BTN2A1. The resulting complex formed by BTN2A1 and BTN3A1 binds to the γ chain of the V γ 9V δ 2 cell, thereby enabling effective tumor surveillance[217, 218].

5.1.1.2 T-cell activation

During target recognition by $\alpha\beta$ T-cells, their $\alpha\beta$ T-cell receptors (TCRs) engage with antigen-presenting target cells, resulting in the formation of an immunological synapse, triggered by rapid cytoskeletal rearrangements and an increase in intracellular calcium concentration[219]. This leads to the secretion of cytolytic granules and/or cytokines by T-cells, ultimately eliminating the target cells[4]. Specifically, TCR engagement with peptides conjugated to major histocompatibility complexes (pMHCs) on tumor cells triggers the Ca^{2+} signal transduction pathway. This pathway begins with the rapid release of intracellular Ca^{2+} from endoplasmic reticulum (ER) Ca^{2+} stores[143, 26]. This is followed by the opening of Ca^{2+} release-activated Ca^{2+} channels (CRAC) in the plasma membrane[220, 221], a process known as store-operated Ca^{2+} entry (SOCE)[4]. The SOCE process facilitates a 10^4 -fold Ca^{2+} concentration gradient across the plasma membrane, leading to passive Ca^{2+} influx[33], hence a significant increase in intracellular Ca^{2+} upon immunological synapse formation. The elevated Ca^{2+} concentration is critical for inducing rapid cytoskeleton-dependent polarization involving actin cytoskeleton rearrangements and microtubule reorientation, ultimately sup-

porting T-cell effector functions[4]. According to Joseph et al.[4], the remodeling of the actin cytoskeleton is a critical process for Ca^{2+} signaling, which was determined by the inhibition of actin polymerization using Cytochalasin D, showing reduced T-cell Ca^{2+} mobilization and activation. Overall, the interaction and synapse formation between T-cells and tumor cells, which is facilitated by the $\gamma\delta$ TCR and the BTN2A1 and BTN3A1 complex, leads to T-cell activation, remodeling of the actin cytoskeleton, and a significant increase in intracellular calcium levels. As a result, monitoring the Ca^{2+} levels within the T-cell using a calcium probe serves as an efficient approach to assess T-cell activation and synapse formation.

5.2 The research objective

The project aimed to investigate fundamental aspects related to the biology of $\gamma\delta$ T-cell immune synapses and generate knowledge that could ultimately be applied to inform the development of innovative cancer therapies. To achieve this goal, the project was divided into subprojects that focused on understanding the biophysical principles underlying $\gamma\delta$ T-cell activation and its correlation with cytolytic efficacy.

One of the initial subprojects of the study aimed to develop a novel experimental platform derived from cell membranes. This platform would facilitate the exploration of biophysical phenomena that occur during immunological synapse formation and allow for the investigation of fundamental attributes of immune receptors and their ligands. Specifically, the platform would enable the examination of spatiotemporal organization and response to forces at the molecular level, and how this impacts cellular activation and cytotoxicity.

As the research project is currently in its early stages, this chapter will only provide a brief overview of the development of the membrane-derived experimental platform, see Section 5.3 for further details. The primary objective, which is elaborated on in Section 5.4, was to investigate the interaction between $\gamma\delta$ T-cells and tumor membranes, with a specific focus on determining whether V γ 9V δ 6 T-cells can form immunological synapses with tumor membranes, ultimately resulting in T-cell activation.

5.3 The novel experimental platform

The initial objective was to investigate the interaction and synapse formation between $\gamma\delta$ T-cells and tumor membranes using a novel two-dimensional membrane-derived experimental platform. The platform involved the generation of giant plasma membrane vesicles (GPMVs) from select tumor cells lines, with GPMVs retaining native-like membrane and protein composition, orientation, and diffusivity[222, 223], as depicted in Figure 5.2.

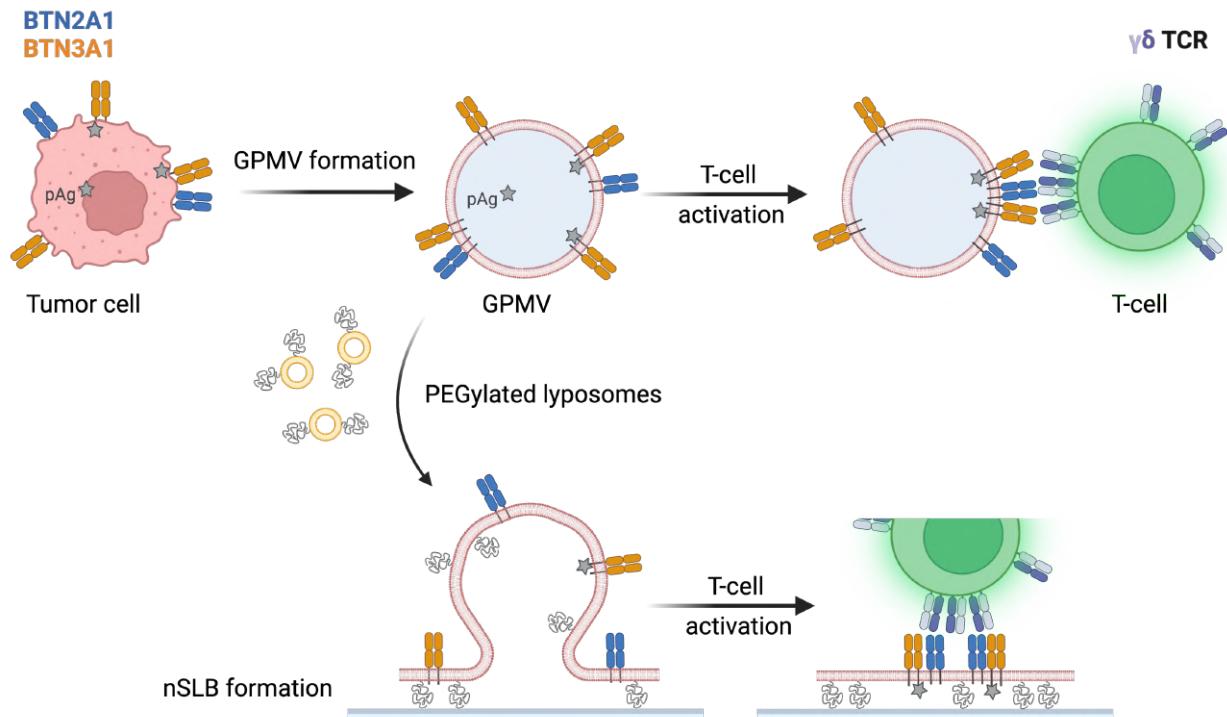


Figure 5.2: Schematic illustration depicting the developmental process of a two-dimensional cell membrane-derived experimental platform. Specifically, the platform is generated using giant plasma membrane vesicles (GPMVs) derived from tumor cells, which possess native-like membrane composition. Consequently, T-cells can interact with the GPMV membrane and form immunological synapses. This results in T-cell activation, which is evidenced by an elevation in intracellular calcium concentration. To establish a stable membrane bilayer, GPMVs are incubated with PEGylated liposomes, which triggers their bursting onto the glass surface, thereby generating a native-supported lipid bilayer (nSLB). This nSLB platform can be employed to examine $\gamma\delta$ T-cell activation and synapse formation at the molecular level.

The GPMVs were derived from tumor cell membranes using N-Ethylmaleimide (NEM), a vesiculating agent that is recognized for its capacity to produce maximal bleb yield while reducing negative impacts on membrane protein stability that might arise due to non-specific crosslinking or off-target effects. In order to form a native-supported lipid bilayer (nSLB), synthetic liposomes were added to the GPMVs before deposition onto a glass surface[224]. This step promoted the bursting of the otherwise stable GPMVs upon contact with the surface. Additionally, the synthetic liposomes were PEGylated, enabling the membrane proteins to move freely within the nSLB, while concurrently prohibiting their interaction with the surface[225]. The orientation of the membrane proteins was determined by measuring the diffusion of fluorescently labeled anti-CD45 antibodies. The antibodies would localize on the nSLB only if the GPMVs, adhered to the substrate, ruptured in the correct orientation with the outer GPMV membrane facing upwards. Furthermore, a fully confluent bilayer was an-

anticipated to be obtained by adjusting the GPMV:liposome ratio, creating a platform that is suitable for single-molecule imaging of the contact between T-cells and the planar antigen-presenting nSLB[226].

However, the development of the nSLB platform proved to be more challenging than originally anticipated, necessitating further investigation, and testing to achieve the desired outcome. The initial findings indicated a formation of patches rather than uniform nSLB bilayers, despite varying the GPMV:liposome ratio between 1:1 and 1:10. Additionally, the study required further investigation to determine the extent to which the GPMV components contribute to the formation of the nSLB patches, or if it mainly consisted of synthetic liposomes, and whether the GPMVs ruptured in the correct orientation. The absence of anti-CD45 antibodies on the adhered GPMV membrane patches, in contrast to the observation of anti-CD45 antibodies on non-disrupted GPMV surfaces, suggested that the GPMV patches were formed in an undesirable orientation with the inner leaflet facing upwards. Despite these limitations, the experimental platform derived from cell membranes holds great promise for various applications, including high-resolution microscopy studies and single-molecule force spectroscopy. While the primary objective of this platform was to explore $\gamma\delta$ T-cell synapses and advance the understanding of the fundamental principles of $\gamma\delta$ T-cell biology, it has the potential to broaden its application beyond the scope of this project by investigating other immune cell synapses. Therefore, this platform could lay the foundation for the development of innovative biophysical approaches that can enhance the development of T-cell based immunotherapies.

5.4 Exploring the formation of immunological synapses

Instead of using a supported lipid bilayer, the study turned to a complementary experimental platform, which involved investigating the possible activation of T-cells, specifically by immunological synapse formation, upon direct interaction with tumor cells or GPMVs harvested from the same tumor cell line. This study was conducted to verify the ability of both tumor cells and GPMVs to activate T-cells, where the T-cell activation by GPMVs was of particular importance for the formation of the nSLB. The tumor cell model selected for this study was from the RPMI8226 B lymphoid cancer cell line, while the T-cells were mimicked by Jurkat76 T-cells engineered to express defined $\gamma\delta$ T-cell receptors (TEGs) with the deletion of the α and β chains[227]. Consequently, any detected T-cell activation could be attributed to $\gamma\delta$ TCR-mediated signaling, correlated to one variable, namely the donor $\gamma\delta$ TCR sequence. Given that different $\gamma\delta$ TCR TEGs vary in their ability to be activated by antigen-presenting cells[228], two distinct donors, CL5 and LM1 TEGs, were selected for the study. This selection was based on their unique characteristics, as depicted schematically in Figure 5.3. The T-cells expressing complete, full-length, $\gamma\delta$ TCRs, namely the CL5 T-cells, are expected to form immunological synapses with the tumor membrane, leading to T-cell activation. In contrast,

the nonfunctional length mutant 1 T-cells, abbreviated as LM1 T-cells, are not expected to facilitate T-cell activation as the γ TCR chain is truncated. The LM1 T-cells were included as a negative control to establish a baseline level for T-cell activation. Both the tumor cells and T-cells were obtained from the laboratory of Zsolt Sebestyén, Center of Translational Immunology, UMC Utrecht.

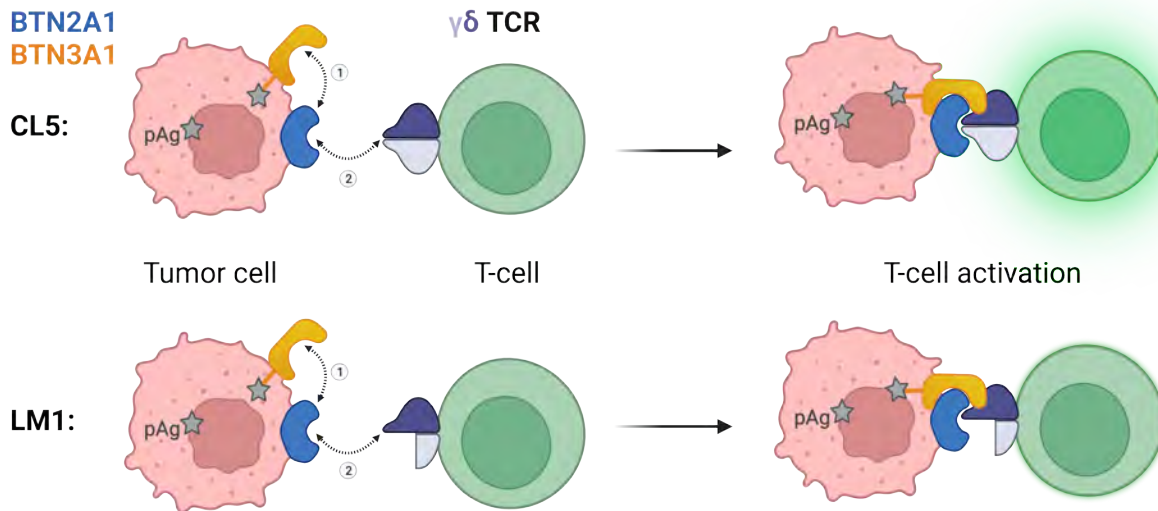


Figure 5.3: A simplified and schematic representation of the interaction between the BTN2A1-BTN3A1 complex, which is expressed on tumor cells, and the $\gamma\delta$ T-cell immune receptor. Specifically, two T-cell donors are illustrated, namely the CL5 T-cell possessing a full-length $\gamma\delta$ T-cell receptor (TCR), and the LM1 mutant T-cell featuring a truncated γ chain in its TCR. Upon interaction between the T-cells and the tumor cell, the intracellular domain of the BTN3A1 protein binds to internal phosphoantigen (pAg), thereby triggering a conformational change leading to the formation of the BTN2A1-BTN3A1 complex. Subsequently, the γ chain of the $\gamma\delta$ TCR directly interacts with the BTN2A1 protein present in the complex, ultimately enabling T-cell activation and the formation of an immunological synapse. This process results in an elevation of intracellular calcium concentration observed in CL5 T-cells, identifying T-activation, in contrast to LM1 T-cells due to their truncated γ chain.

Fluorescent confocal imaging was utilized to visualize the interactions and synapse formations between T-cells and tumor cells for a duration of 60 minutes. A hallmark of immunological synapse formation is the reorganization of the actin cytoskeleton, which is rapidly followed by an influx of Ca^{2+} ions. To assess T-cell activation for both donors, the elevation in internal Ca^{2+} concentration was monitored using the cytosolic calcium probe, Fluo-4-AM, as illustrated in Figure 5.3. The plasma membrane of tumor cells and tumor cell-derived GP-MVs was labeled with CellMask red for visualization. Specifically, the observation of T-cell and tumor cell interactions was carried out using a Nikon Ti-E Eclipse confocal microscope equipped with a 100x oil immersion objective. The experimental conditions were maintained at a constant temperature of 37°C and a CO_2 concentration of 5% by placing the cells in an incubator chamber, ensuring optimal conditions for the experiment. Moreover, to enhance baseline T-cell activation, tumor cells were treated with the activating anti-BTN3A 20.1 anti-

body prior to co-incubation with T-cells. This is thought to induce the same conformational changes in BTN3A1 as pAg binding to the cytosolic domain of BTN3A1. It is an essential way of mimicking the pAg effect through binding of the 20.1 antibody on an extracellular epitope on BTN3A1[208], thus the antibody, specific to BTN3A1, has been reported to ensure robust $\gamma\delta$ T-cell activation upon interaction with the tumor membrane[229].

5.4.1 T-cell recognition and response to tumor cells

This section aims to elaborate on the response of $\gamma\delta$ T-cells to tumor cells that have undergone pre-treatment with the BTN3A1-specific 20.1 antibody. The T-cell response was assessed in both the presence and absence of tumor cells. In instances where tumor cells were absent, T-cells were observed to be stable, based on their minimal mobility and lack of interactions with each other. The intracellular calcium signal was consistently maintained, and only minor Ca^{2+} fluxes were observed (Fig. A.6A). Notably, the presence of a constant calcium signal is not attributed to T-cell activation. Instead, it is a result of the intracellular calcium concentration in resting T-cells, which typically ranges between 50-100 nM and is necessary for maintaining cellular homeostasis[4]. Upon exposure to tumor cells, a significant increase in T-cell mobility, deformation, and calcium fluctuations was detected (Fig. A.6B). These observations strongly suggest that T-cells are not activated significantly in isolation; rather, their enhanced activity in the presence of tumor cells indicates their capacity to recognize the presence of antigens presented on the tumor surface.

The interaction between T-cells and tumor cells triggers a complex signaling cascade that culminates in the formation of immunological synapses and the secretion of cytokines, chemokines, and cytolytic granules[4, 196]. This elaborate process leads to the direct elimination of tumor cells in close contact with T-cells, while also facilitating T-cell communication and the recruitment of other immune cells to the target site[196]. This phenomenon is presumably observed in Figure A.7, where $\gamma\delta$ T-cells (CL5) are seemingly recruited and directed towards a tumor cell. This is indicated by the considerable T-cell deformation and calcium fluctuations observed upon interaction with the tumor, which appear to occur in conjunction with high mechanical activity as the tumor cell is being pulled and pushed out of the focal plane. The tumor cell is presumed to ultimately die based on its vigorous blebbing, a vesiculation process that is believed to be closely associated with the underlying actin cytoskeleton [31]. Additionally, T-cell mobility and the formation of protrusive extensions are intricately linked to actin remodeling. The direct attachment of the actin cytoskeleton to the plasma membrane provides structural support to the cell membrane[150], while its interaction with intermediate filaments and microtubules is essential for maintaining cell shape and overall organization [230]. Besides its structural role, the dynamic actin network plays a crucial role in T-cell crawling by generating flat protrusions known as lamellipodia[231]. Moreover, T-cells are capable of initiating contact with other cells through the formation of actin-rich filopodia,

which extend or retract as finger-like protrusions from the cell surface[231, 19]. The highly dynamic structure of filopodia facilitates various cellular functions such as growth, shrinking, axial twisting, and buckling, which collectively enable cells to explore their extracellular space in three dimensions[19]. These dynamic processes have been extensively studied and proven crucial for cellular communication, sensing, mobility, and interaction with other cells. [8, 19, 169, 189, 232].

5.4.1.1 The active search for tumor cells

$\gamma\delta$ T-cells were frequently observed exploring their environment and sensing the surface of neighboring cells, regardless of whether they were fellow T-cells or tumor cells. In order to sense the tumor cell surface, T-cells were seen to form finger-like protrusions, as depicted in Figure 5.4A. These protrusions, presumed to be filopodia, were observed to extend (Fig. 5.4A, frame 2), twist, and retract (Fig. 5.4A, frame 4) as the tumor and T-cell approached each other during the 60-minute observation period. This mechanism appeared to elicit an elevation in intracellular calcium. To determine the extent of the Ca^{2+} increase the T-cell was tracked and its mean calcium intensity was measured over time using the TrackMate plugin available through Fiji distribution of ImageJ[233].

Given that individual T-cells exhibited a baseline Ca^{2+} intensity prior to imaging, the elevation in intracellular Ca^{2+} intensity served as an indicator of T-cell activation. The Ca^{2+} intensity of the T-cell of interest, denoted by the blue arrow, appeared to fluctuate, with significant Ca^{2+} intensity peaks observed over time, as illustrated in Figure 5.4B. However, the observed Ca^{2+} peaks were detected prior to the formation of an established contact between the T-cell and tumor cell and seemed to be dependent on the movement of filopodia. Since an elevation in Ca^{2+} intensity was considered to be indicative of T-cell activation, it appeared that the T-cell was activated before it established close contact with the tumor cell, hence prior to the formation of an immunological synapse, possibly due to the brief contact between the filopodia and tumor membrane.

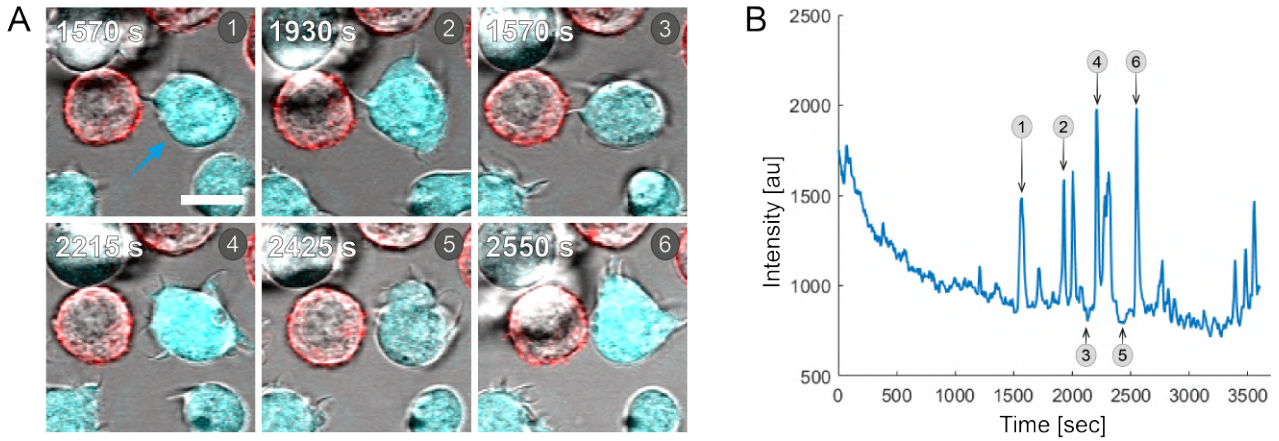


Figure 5.4: A T-cell is observed to actively sense its environment and search for a tumor cell via finger-like protrusions. (A) The confocal fluorescence microscopy images display the cytosolic calcium response of a $\gamma\delta$ T-cell (CL5) during its interaction with a tumor cell (RPMI8226), identified by its red-stained plasma membrane. Their behavior was monitored for 60 minutes, where various time points are depicted in frames 1-6. The scale bar measures $12 \mu\text{m}$. (B) The mean calcium intensity within the T-cell of interest, denoted by the blue arrow, was quantified as a function time, where the corresponding calcium intensities for frames 1-6 are highlighted in the intensity plot.

The process of filopodia formation and movement by T-cells necessitates the remodeling of actin. The assembly of actin filaments depends on Ca^{2+} influx, which can enter the protrusions both through Ca^{2+} channels and voltage-gated membrane channels, which governs force-dependent cell movement[234]. Furthermore, Efremov et al.[234] reported Ca^{2+} fluxes within filopodia in response to mechanical stretching, persisting for several minutes after force release, indicating the presence of a filopodia memory effect. Such an effect could trigger a global Ca^{2+} response by the cell[234], potentially accounting for the observed Ca^{2+} elevations within T-cells. Notably, Ca^{2+} influx could also be facilitated by stretch-sensitive channels [192, 193] or reversible membrane ruptures [49, 54] during cellular exploration and crawling[6]. As such, fluctuations in Ca^{2+} levels may be more likely attributed to actin polymerization within protrusions, rather than actin remodeling during synapse formation. It is plausible to hypothesize that the substantial reorganization of the actin cytoskeleton, which has been demonstrated to be crucial for T-cell activation[4], may elicit intracellular bursts of Ca^{2+} originating from the endoplasmic reticulum[143, 169]. This could then initiate the T-cell Ca^{2+} signaling cascade, thus promoting T-cell activation. However, it is important to mention that this remains a speculative notion. It is well established that T-cell activation and their subsequent effector functions necessitate T-cell receptor (TCR) signaling, which requires close contact with an antigen-presenting membrane[209].

5.4.2 Immunological synapse formation upon tumor cells interaction

In addition to the searching abilities, T-cells have been observed in close proximity to tumor cells, leading to the formation of immunological synapses, as illustrated in Figure 5.5. The confocal images display two T-cells (CL5), indicated by the yellow and orange arrows in Figure 5.5A, actively seeking neighboring tumor cells. As a result of this process, the T-cells underwent significant deformation as they crawled, searched, and initiated contact with the target tumor cells, which was observed as an elevation in cytosolic Ca^{2+} . The calcium intensity, quantified in Figure 5.5B and represented by the yellow and orange lines for the respective yellow and orange-denoted T-cells, revealed calcium fluctuations throughout the observation period.

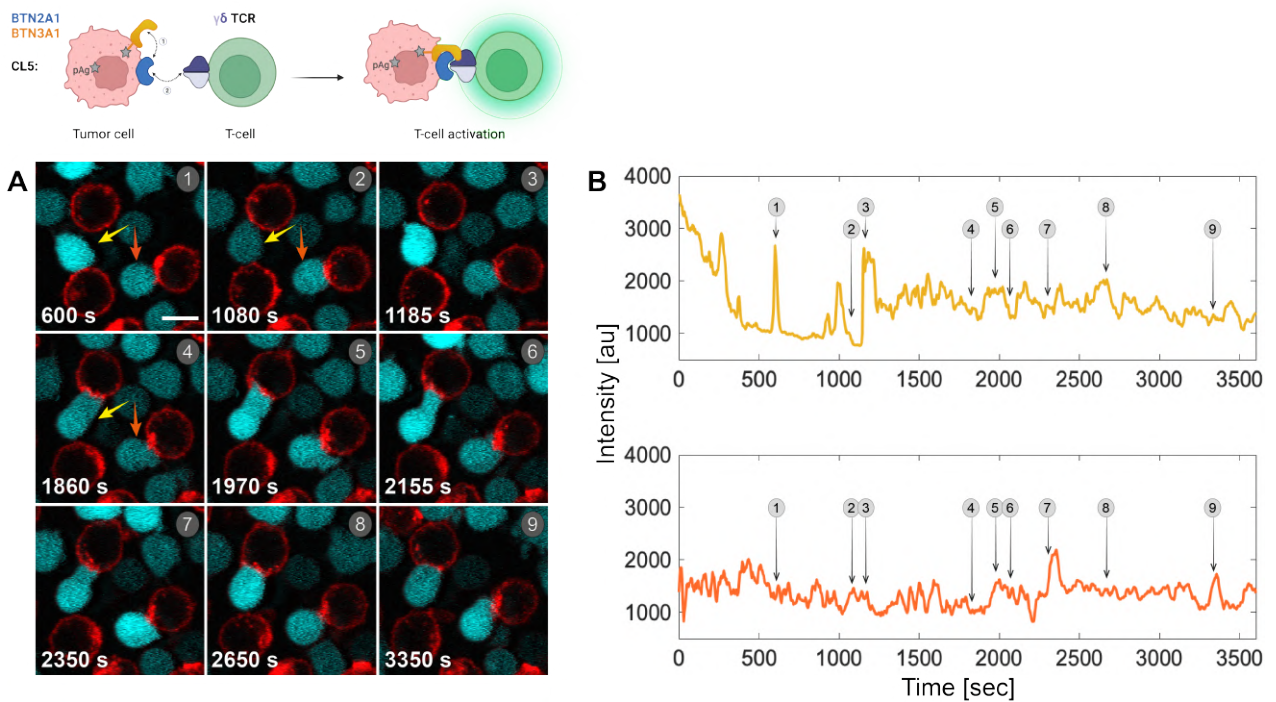


Figure 5.5: Immunological synapse formation upon T-cell and tumor cell interaction. The confocal images (A) illustrate the cytosolic calcium response in two $\gamma\delta$ T-cells (CL5), denoted by the yellow and orange arrow, during their interaction with tumor cells (RPMI8226), identified by their red-stained membrane. The images are captured at various time points, given by frames 1-9, and the scale bar measures $12 \mu\text{m}$. (B) The mean calcium intensity within the T-cells was measured over 60 minutes and is illustrated as a yellow or orange intensity plot for the respective yellow and orange-denoted T-cells. The highlighted calcium intensities in (B) correspond to frames 1-9 from panel A.

Notably, the yellow-denoted T-cell (in fact being a $\gamma\delta$ TCR-expressing Jurkat cell) exhibited significant peaks and fluctuations in calcium intensity, while searching and interacting with the tumor cell surface, as depicted in Figure 5.5 (frames 1-3). However, upon establishing contact between the T-cell and tumor cell, the fluctuation in Ca^{2+} intensity decreased signifi-

cantly and became relatively stable, as evidenced by the observation and quantification from frame 5 to 9. The formation of an immunological synapse, a hallmark of which is the flattened contact area between the T-cell and tumor cell due to strong membrane adhesion and cytoskeletal rearrangements (Fig. 5.5A, frame 4), was observed for multiple T-cell - tumor cell interactions, with the tumor membrane signal accumulating at the contact area. T-cell searching and interaction are known to be mediated by Ca^{2+} -dependent actin polymerization. Following this process, it is possible that the cell pumps out excess intracellular Ca^{2+} to maintain cell homeostasis[162], resulting in a feedback loop as long as the T-cells are in motion. This phenomenon could explain the observed calcium fluctuations prior to the established cell-cell contact. Additionally, the formation of an immunological synapse necessitates TCR signaling, via the BTN2A1/BTN3A1 interaction[209], and requires a steady influx of extracellular Ca^{2+} , initiated by Ca^{2+} -mediated signaling cascades, such as the store-operated Ca^{2+} entry (SOCE) process[4]. This process could explain the decrease in Ca^{2+} fluctuations as the two cells form an immunological synapse, where the steady Ca^{2+} level is maintained by the passive Ca^{2+} influx mediated by the 10^4 -fold Ca^{2+} gradient across the membrane[33].

The T-cell denoted by the orange arrow was also observed to interact with a neighboring tumor cell and undergo deformation, although with less significant Ca^{2+} intensity peaks than those observed for the yellow-denoted T-cell. Notably, the Ca^{2+} fluctuation pattern of the orange-denoted T-cell was similar to the pattern observed when the yellow-labeled T-cell had established contact with the tumor cell, rather than when it was in the process of searching for the tumor cell. It is plausible that the orange-labeled T-cell had already established contact with the tumor cell before initial imaging, as the two cells were found in close proximity upon imaging. Additionally, the orange-denoted T-cell exhibited deformation as it interacted with the tumor membrane, and the tumor membrane appeared to accumulate at the contact area, although this accumulation may potentially be a membrane artifact as it was present already upon initial imaging. Furthermore, it is worth noting that the variation in cytosolic Ca^{2+} intensity between the two T-cells may be attributed to several factors, such as differences in individual cell cycles, the efficiency of calcium probe uptake, or a combination of multiple mechanisms occurring during their interactive process.

As these findings are preliminary, further experiments are needed to determine the generalizability of the calcium intensity pattern as an indicator of immunological synapse formation. Nevertheless, the results clearly demonstrate that full-length $\gamma\delta$ TCR-expressing Jurkat cells are capable of detecting and interacting with tumor cells, with the additional recruitment of other T-cells to the tumor cell (Fig. 5.5A, frames 7-9) could suggest an ability to communicate with other immune cells in the tumor environment, as previously reported by Park et al.[209]. Additionally, this study revealed that T-cells can form immunological synapses with the tumor membrane, which is activated as the $\gamma\delta$ TCR detects the phosphoantigen content

within the tumor cell through its interaction with the BTN3A1-BTN2A1 complex at the tumor surface. This activation ultimately leads to tumor cell lysis, based on the assumption that $\gamma\delta$ T-cells are cytotoxic and antitumor lymphocytes[209].

5.4.2.1 Modified immune receptors facilitate tumor interaction

In order to gain further insight into the Ca^{2+} patterns observed during CL5 T-cell interactions, and to establish a baseline for $\gamma\delta$ T-cell activation, the study was replicated using the LM1 T-cell variant with a truncated γ chain in its $\gamma\delta$ TCRs. The LM1 T-cells were therefore expected to be less capable of forming immunological synapses with tumor cells, and thereby exhibit reduced activation. The study was carried out under the same experimental conditions as previously described, where LM1 T-cell activation was monitored using a calcium probe along with red membrane-stained tumor cells that had been pre-treated with the 20.1 antibody specific for BTN3A1.

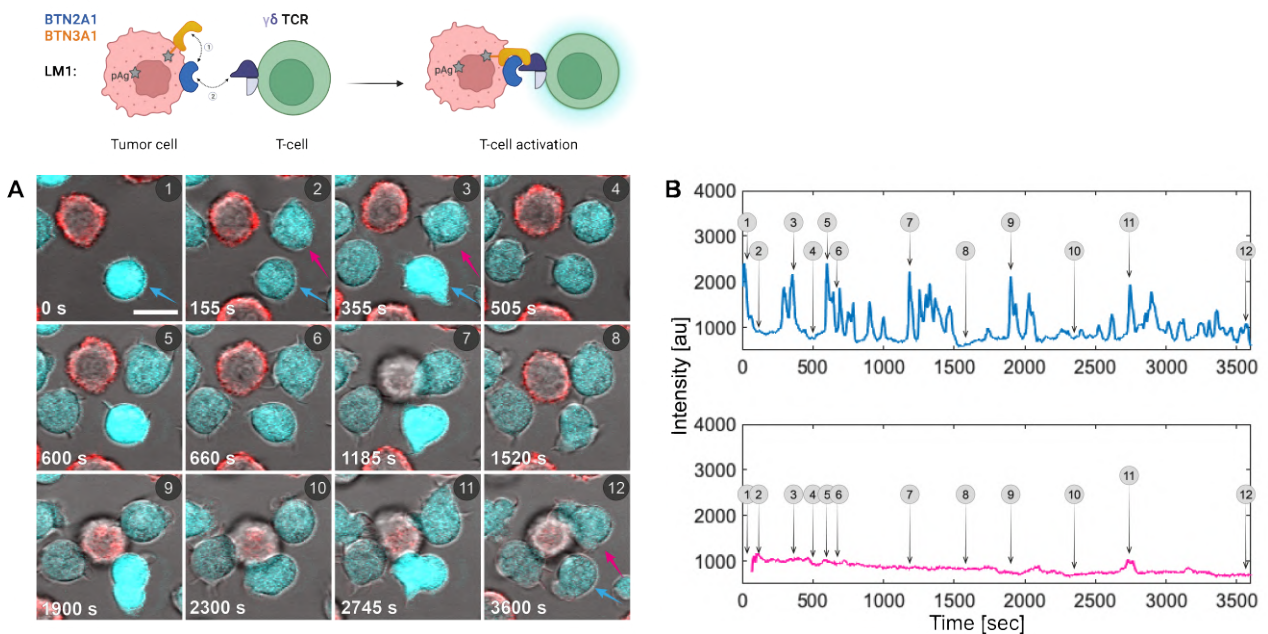


Figure 5.6: Interaction between T-cells, expressing a truncated $\gamma\delta$ TCR, and a tumor cell. The confocal images (A) portray the cytosolic calcium response in two modified $\gamma\delta$ T-cells (LM1), denoted by the blue and magenta arrow, during their interaction with a tumor cell (RPMI8226), identified by its red-stained membrane. The images are depicted at various time points, given by frames 1-12, and the scale bar measures $12 \mu\text{m}$. (B) The mean calcium intensity within the T-cells was tracked for 60 min and presented as either a blue or magenta intensity plot for the respective blue or magenta-denoted T-cells. The highlighted calcium intensities in (B) correspond to frames 1-12 in panel A.

The overall fluctuations in Ca^{2+} intensity for the LM1 T-cells, indicated by the blue and magenta arrows, were found to be lower than that of the CL5 T-cells. However, as depicted in Figure 5.6A, the LM1 T-cells exhibited a similar pattern of behavior, as for the CL5 donor, in their movement and search for tumor cells, which involved deformation and formation of

protrusions resulting in fluctuations in Ca^{2+} levels, particularly for T-cell denoted by the blue arrow (Fig. 5.6A and B, blue line). This T-cell was observed to detect two adjacent tumor cells in frame 7 (Fig. 5.6A), leading to an increase in its calcium concentration (Fig. 5.6B, frame 7). Simultaneously, the magenta-denoted T-cell was seen to deform around the tumor cell and push it out of the focal plane (Fig. 5.6A, frame 7), while extending a protrusion, presumably to interact with the neighboring, blue-denoted T-cell (Fig. 5.6A, frame 8). However, this interactive behavior did not result in significant Ca^{2+} fluctuations within the magenta-denoted T-cell (Fig. 5.6B, magenta line).

However, the observations suggest that the LM1 T-cells are activated, which is noteworthy given that T-cell activation is only triggered by direct interaction between the TCR and the surface BTN complex[209]. Interestingly, the cytosolic calcium intensity of the magenta-denoted T-cell, which had been relatively stable, was found to peak in frame 11 (Fig. 5.6B, magenta), coinciding with a peak in calcium intensity within the blue-denoted T-cell (Fig. 5.6B, blue line). Although this simultaneous Ca^{2+} elevation could be coincidental, it could also indicate a form of communication between the two T-cells that were interacting with the same tumor cell and with each other via filopodia protrusions (Fig. 5.6A, frame 8).

The preliminary findings suggest that the LM1 T-cell variant, despite its truncated γ chain, retains the capacity to detect, interact, and form immunological synapses with the tumor surface. Although this ability may have been reduced, which may account for the diminished fluctuations in Ca^{2+} , it was evident that this capability had not been completely abolished. Furthermore, the LM1 T-cells were observed to exert mechanical forces on the tumor cells upon interaction, resulting in tumor cell displacement in all three dimensions as illustrated in Figure 5.6 (frame 7-12). Considering that the LM1 mutant was not anticipated to establish an interaction with the BTN2A1-BTN3A1 complex, the results of this study suggest that the process of synapse formation is more complex than the simplistic model depicted in Figure 5.3, which portrays an interaction between the BTN2A1-BTN3A complex and the TCR γ chain. Therefore, it would be of interest to repeat the experiment to replicate the experiment using a different mutant, where both the γ and δ chains of the TCR were truncated which should serve as a negative control. This would not only establish a baseline for activation but also provide further insights into the T-cell response upon encountering tumor cells. In the event of T-cell activation, it would be worthwhile to examine the mechanism by which synapse formation is facilitated by $\gamma\delta$ T-cells.

Additionally, further research is necessary to determine if the observations made for the $\gamma\delta$ TCR donors are applicable to the overall T-cell response in a tumor cell environment. Moreover, a more statistical analysis of T-cell activation, interaction, and potential patterns for cytosolic calcium elevations could be achieved by determining the center of each cell and

measuring the distance between their centroids as the T-cells move and interact with tumor cells and potentially other T-cells. This approach could assess the approximate distance following T-cell activation to ascertain whether T-cell activation can be facilitated by T-cell protrusions interacting with the tumor cell or if close contact must be established before activation. Cell-cell contact could be identified by the distance between the centroids, where a distance smaller than the combined radius of the two cells would be considered as close contact, indicative of immunological synapse formation. Accordingly, a distance larger than the combined radius of the two cells would not be considered contact, which could further provide information about the extent of the distance for which the T-cells were activated. This approach, however, would require resolving the limitations of TrackMate[233], which tracks cells as spherical particles and was unable to identify the tumor cells due to the exclusive plasma membrane labeling. This limitation could be overcome by using a cytosolic protein, such as ANXA5, to visualize tumor cells, which would provide additional information about their viability[137]. Alternatively, the programmed tracking could be expanded upon. Nevertheless, limitations may arise from cell movement in the vertical direction, as the resolution is confined to the focal plane.

5.4.3 T-cell interaction with GPMVs derived from tumor cells

The interaction between T-cells and the tumor cell membrane revealed that the butyrophilin proteins, specifically BTN2A1 and BTN3A1, present on the tumor membrane, were able to engage with the $\gamma\delta$ T-cell receptor and facilitate immunological synapse formation. The initial objective was to create a native-supported lipid bilayer (nSLB) using GPMVs derived from tumor cells. Thus, it was crucial to verify that T-cells could be activated and form immunological synapses when interacting with the GPMV membrane. Since T-cells were observed to effectively interact with the RPMI8226 tumor cell line, GPMVs were generated from the same tumor line. GPMVs, being blebs directly derived from the plasma membrane, consist of the same lipid bilayer and embedded proteins as the cell, while lacking the cytoskeletal network[223]. Therefore, GPMVs are considered the most physiologically relevant system for constructing planar-supported membranes[222], and for studying membrane-related behavior as to characterize synapse formation patterns. Consequently, T-cell activation upon interaction with GPMVs would validate the presence of the BTN2A1-BTN3A1 complex on the model tumor cell membrane, a prerequisite for the 2D membrane-derived experimental platform.

The experimental procedure followed for this study was similar to that of the cell-cell interaction analysis, with the exception that the GPMVs were pre-seeded into the chamber prior to T-cell addition. This step was deemed necessary as GPMVs are significantly lighter than T-cells and require additional time to settle on the surface. The difference in size between T-cells and GPMVs was pronounced, with T-cells having a diameter of $\sim 12 \mu\text{m}$ (Fig.

5.7B), while GPMVs were measured to have a diameter ranging between 2-7 μm (Fig. 5.7C). As a result, only one of the two could be observed within the focal plane at a time. Since the primary interest was the activation of T-cells, the focal plane was locked in at the mid-section of the $\gamma\delta$ T-cells (illustrated by the yellow dashed line in Figure 5.7D). This enabled optimal observation of the CL5 $\gamma\delta$ T-cell response to RPMI8226-derived GPMVs, which was monitored for 60 minutes. As the mobile GPMVs were observed to diffuse throughout the imaging solution, they could only be tracked during their transition in and out of the focal plane, as depicted in Figure 5.8A.

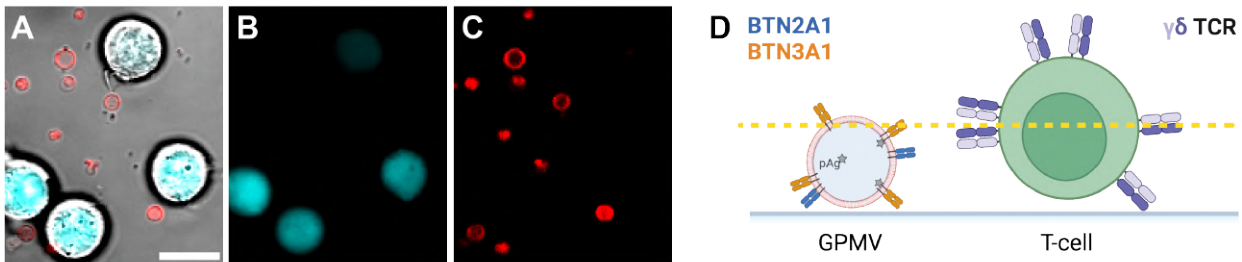


Figure 5.7: The experimental conditions for investigating the interactions between tumor-derived GPMVs and T-cells. Confocal imaging was employed to visualize the co-incubation of T-cells and GPMVs, with a scale bar of 12 μm (A). Due to the size difference between the entities, only one could be in focus at any given time. The cytosolic calcium probe, within the $\sim 12 \mu\text{m}$ sized T-cells (B), appears blurry as the T-cells are out of focus. Conversely, the in-focus GPMVs (C), measuring 2-7 μm in size, are distinguished by their red-stained membrane. As the calcium activity of the T-cells was of primary interest, the focus plane was locked at the midsection of the $\gamma\delta$ T-cell (D), denoted by the yellow dashed line. This approach ensured that the T-cell signal remained in focus throughout the observation period, while the GPMVs were monitored as they diffused in and out of the focal plane.

Figure 5.8 depicts the T-cell behavior, and its corresponding cytosolic calcium level, upon interaction with pre-seeded GPMVs. Unlike the previous response to tumor cell interactions, the cytosolic calcium level remained stable throughout the observation period and no significant intensity fluctuations were noted (Fig. 5.8B). However, the T-cell was observed to undergo deformation over time and detect a pre-seeded GPMV (Fig. 5.8A, frame 4), after which the T-cell appeared to wrap around the GPMV. At this point, a marginal increase in the calcium intensity was detected over time (Fig. 5.8B); nevertheless, the minimal Ca^{2+} increase and absence of oscillations implied that the membrane composition of tumor-derived GPMVs varied from that of tumor cells. It is unclear whether this response results from the presence of inactive BTNs on the tumor GPMV surface or if they are entirely absent. Despite observing a few instances of T-cell deformation, the overall lack of T-cell activation and mobility indicates that the $\gamma\delta$ T-cell receptors were incapable of detecting the BTN2A1 and BTN3A1 proteins on the presumed antigen-presenting GPMV surface. Another possible explanation for the absence of Ca^{2+} response during GPMV interaction could be attributed to the lack of mechanical rigidity in the GPMVs. Living cells have an actin cortex, that is con-

siderably stiffer than the GPMV membrane. Therefore, when T-cells establish contact with living cells, they encounter mechanical stresses that facilitate the opening of Ca^{2+} channels. In contrast, GPMVs are composed solely of a nanoscale lipid bilayer that provides minimal resistance and, consequently, cannot exert tension on the contact area between the T-cell and GPMV, which could elucidate the lack of Ca^{2+} influx. Another hypothesis is that the GPMV surface area is too small for $\gamma\delta\text{TCRs}$ to encounter sufficient $\text{BTN3A1}/\text{BTN2A1}$ proteins to activate.

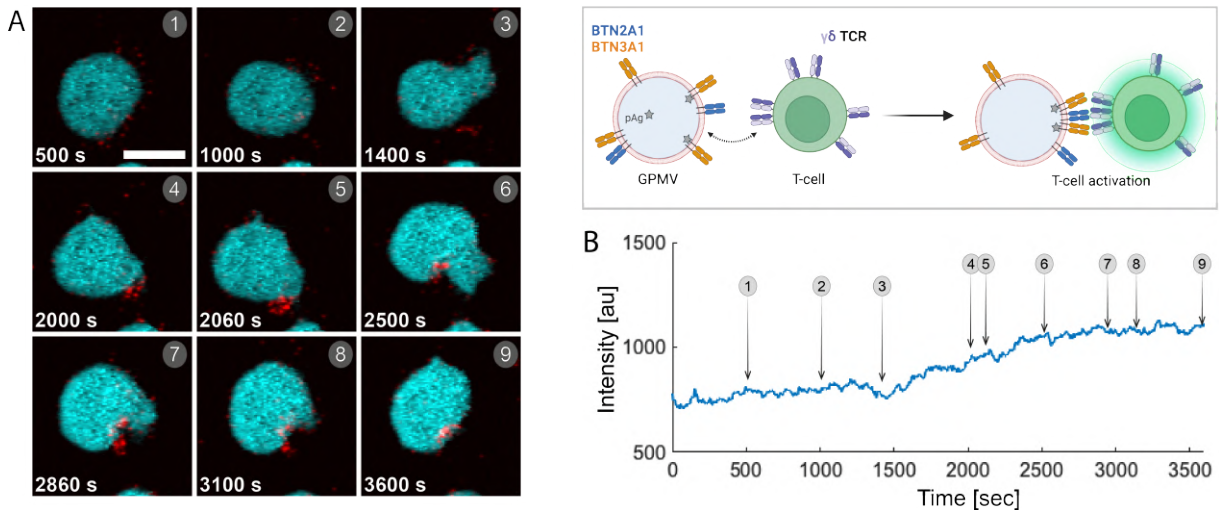


Figure 5.8: The T-cell response to GPMVs that were harvested from tumor cells. (A) The confocal images depict the cytosolic calcium response in $\gamma\delta$ T-cells (CL5) as they interact with GPMVs derived from tumor cells (RPMI8226), which are distinguished by their red-stained membrane. The images are captured at various time points, given by frames 1-9, and the scale bar measures $12\ \mu\text{m}$. (B) The mean calcium intensity within the T-cell was monitored for 60 minutes and displayed as a calcium intensity plot, where the highlighted calcium intensities corresponds to frames 1-9 from panel A.

5.4.3.1 BTN3A1 localization on tumor cell membranes

The results of the experiments indicate that the activation of $\gamma\delta$ T-cells occurred primarily through cell-cell interaction, whereas activation through GPMV interaction was either significantly less effective or non-existent. Since GPMVs are expected to express all the membrane components of the tumor cell[222, 223], including BTNs, the migration of BTN3A1 to the GPMV surface was investigated upon vesiculation of RPMI8226 tumor cells. Specifically, the cell membranes were stained with CellMask green, and GPMVs were chemically derived via the use of the vesicular agent NEM, as depicted in Figure 5.9A. Subsequently, the cells and GPMVs were treated with the 20.1 antibody that specifically targets BTN3A1 , which was coupled with Alexa Fluor 647.

The results demonstrated the presence of the green plasma membrane stain on both the

plasma membrane of the cell remnant and the GPMVs (Fig. 5.9A1), indicating that the GPMVs were indeed composed of tumor cell membranes. However, the BTN3A1-specific antibody was observed solely at the cell remnant membrane and not at the GPMV membrane (Fig. 5.9A2), strongly suggesting that the BTN3A1 proteins were either inactive or did not migrate with the plasma membrane to the GPMV during NEM-induced vesiculation. In order to evaluate the potential impact of the blebbing agent on protein migration into GPMVs, it may be worthwhile to explore alternative vesiculation agents, such as the actin-depolymerizing drug latrunculin B along with mechanical vesiculation[225, 235]. In a separate experiment, spontaneous blebbing was observed in a dying tumor cell without the use of NEM or other vesicular agents, as illustrated in Figure 5.9B. The cell membranes were similarly labeled with CellMask green, and subsequently, the Alexa Fluor 647 tagged 20.1 antibody. While the green fluorescent stain highlighted both the cell plasma membrane and the blebs (Fig. 5.9B1), the BTN3A1 specific antibody was not detected at the bleb membrane (Fig. 5.9B2). These results clearly demonstrate that the BTN3A1-specific antibody was able to bind to the existing BTN3A1 proteins on the surface of the cells, indicating that the BTN3A1 proteins were either inactive or absent from the blebbing membrane during spontaneous blebbing. This further implies that the exclusion of BTN3A1 from GPMVs may not be NEM-specific, but rather a result of a more general mechanism. To gain further insight into the localization of the BTN3A1 protein, a construct that genetically expresses fluorescently labeled BTN3A1 could be employed to investigate whether BTN3A1 is incorporated into GPMVs upon vesiculation.

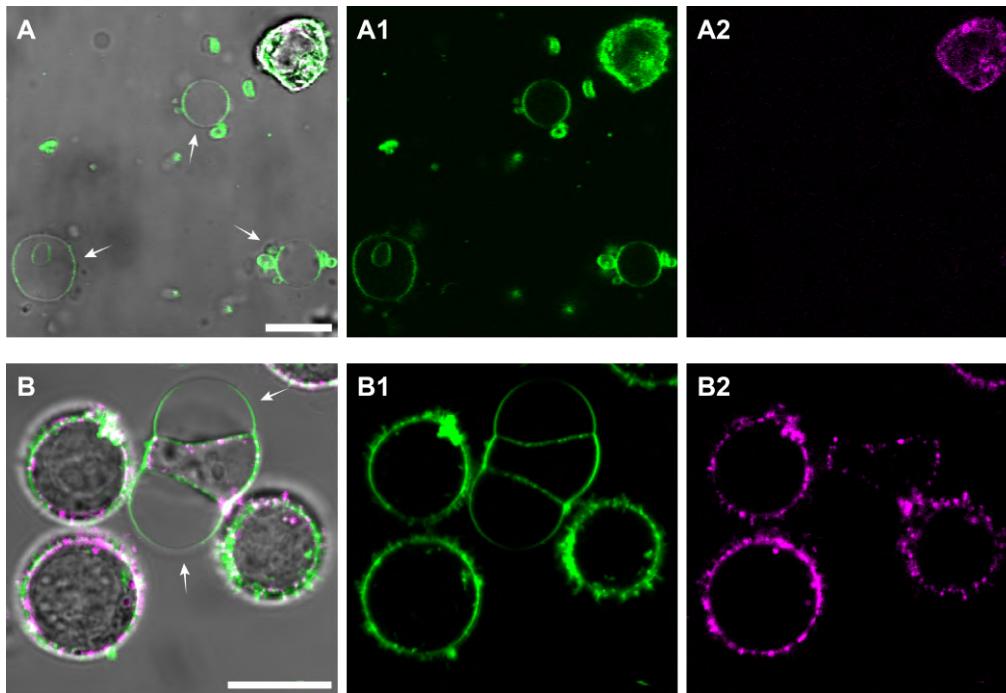


Figure 5.9: The confocal images visualize cells, GPMVs and blebs, and in particular the BTN3A1 localization. (A) Illustrates GPMVs derived from RPMI8226 tumor cells following NEM vesiculation, while spontaneous blebs generated from the same, non-treated tumor cell line are displayed in (B). The green fluorescent plasma membrane staining probe localized at the plasma membrane of cells and GPMV (A1), as well as at the naturally occurring blebs (B1). Conversely, the fluorescent-labeled 20.1 antibody, which specifically binds to the BTN3A1 protein, was only observed at the cell membranes and not on the GPMV surface (A1) or the blebbing membrane (B1). This suggests that the BTN3A1 proteins may either be inactive or entirely excluded during GPMV/bleb formation. The GPMVs and bleb are indicated by the white arrows, and the scale bars measure 12 μm .

5.5 Concluding remarks

Although the initial goal of creating a novel two-dimensional experimental platform could not be achieved within the predetermined four-month timeframe, this project generated a multitude of inquiries that necessitate additional investigation, particularly concerning the composition of giant plasma membrane vesicles (GPMV) and T-cell activation upon tumor cell interaction. However, the main findings of the study showed that when $\gamma\delta$ T-cells were co-incubated with RPMI8226 tumor cells, the T-cell exhibited enhanced mobility, as they were able to detect the antigens presented on the surface of the tumor cells, and actively searched throughout the extracellular environment by extending, twisting, and retracting their finger-like protrusions[19]. Furthermore, the interactions between T-cells and neighboring cells were found to be force-dependent, regardless of a complete or modified $\gamma\delta$ T-cell receptor (TCR). These processes resulted in elevated cytosolic calcium levels, which were assessed using a calcium probe to measure T-cell activation.

Previous studies have proposed that T-cell activation occurs only through direct interaction between the T-cell receptor (TCR) and the antigen-presenting tumor surface[209], in our case the BTN2A1 and BTN3A1 protein complex, where the γ TCR chain supposedly binds to BTN2A1 of the complex[217, 218]. T-cell activation is mediated by various signaling cascades, including actin remodeling and Ca^{2+} influx, which are critical for the formation of the immunological synapses[4, 219]. The fluctuations in Ca^{2+} intensity within T-cells could therefore be indicative of T-cell activation, and hence synapse formation, although the most significant calcium fluctuations were observed prior to the establishment of close contact. This cell-cell contact was determined by the flattened surface area at the contact site, which is a hallmark of immunological synapse formation. Notably, the Ca^{2+} fluctuations were primarily observed during filopodia movement, which is a process that involves the formation of protrusions by actin polymerization, a process that is also known to be regulated by Ca^{2+} influx[8, 4, 19]. Consequently, it is plausible that the Ca^{2+} elevation and fluctuations result from the interplay of the aforementioned Ca^{2+} -dependent mechanisms, which in turn may even act in concert. Further investigation is necessary to expand upon this proposition, specifically concerning intracellular calcium elevation in relation to the T-cells' proximity to the tumor cells.

Furthermore, the study demonstrated T-cell recruitment, whereby T-cells formed immunological synapses with tumor cells, eventually resulting in tumor cell lysis due to their cytolytic attribute[209, 4, 205]. In conclusion, the pronounced T-cell activation upon tumor interaction raised the pressing question of whether the BTN2A1 and BTN3A1 protein complex is inactive or entirely absent from the tumor-derived GPMV surface, as none of the T-cells were observed to be activated upon interaction with GPMVs. This issue would have to be addressed before the development of the novel membrane-derived experimental platform. Notably, while most T-cells did not exhibit interactive behaviors with GPMVs, the findings depicted in Figure 5.8 clearly demonstrated that T-cells respond to GPMVs. Thus, it could be worthwhile to explore this interaction using the method proposed by Cespedes et al. [236], where a rigid silica bead can be coated with tumor cell-derived plasma membrane to investigate the effects of individual proteins and complexes upon T-cell interaction.

6

Conclusion and future work

The thesis presented various aspects of protein response to cell membrane disruption, specifically discussing the involvement of annexin and actin in plasma membrane repair. Additionally, a section of the thesis is dedicated to the investigation of T-cell activation through its interaction with cancer cells.

To study the intricate repair mechanisms in a near-native environment, an optical platform was developed that utilizes thermoplasmonic heating. This platform facilitated the investigation of the role of annexin A5 and annexin A2, as well as the actin response, to highly local membrane injuries in living cells. When the thermoplasmonic approach is integrated with confocal microscopy, the membrane puncturing method can provide a mechanistic understanding of membrane dynamics in cells and membrane model systems, as well as quantitative information on protein response to membrane damage, including protein recruitment and their biophysical function[73].

Notably, low laser power induces membrane permeabilization, while high laser power can generate temperatures around the NP that exceed the boiling point of water, where temperatures between 200 and 300°C leads to the formation of nanobubbles surrounding the nanoparticles[74, 135, 136]. To further reduce the extent of heating, even smaller nanoparticles, like gold nanorods or nanomatryoshkas[70], that resonate with NIR light could be used, enabling intracellular precise punctures in endosomes, the endoplasmic reticulum, and the nuclear envelope[73].

Annexins

In order to gain insights into the mechanism behind the upconcentration of proteins near the wound site during plasma membrane repair (PMR), the role of annexins was investigated. This was accomplished by utilizing gold nanoparticles to induce plasma membrane ruptures, and subsequently monitoring the protein response.

The findings suggested that the recruitment of both annexin A5 (ANXA5) and annexin A2 (ANXA2) is crucial for the process of wound healing. Specifically, the results indicate that ANXA5 and ANXA2 form a scaffold at the wound perimeter. Notably, a significant Ca^{2+}

influx was observed as a prerequisite for the recruitment and accumulation of ANXA at the site of injury, where ANXA2 translocation appeared to unfold in a sequential manner, with the time of wound closure being of utmost priority. However, further investigation would have to be done on this subject to gain a comprehensive understanding of the relationship between wound closure time, wound size, and the corresponding resealing strategies. Furthermore, it would be of great interest to investigate the interplay between annexins during membrane repair, where future studies could utilize ANXA co-incubation in cells or model membranes.

Previous studies have reported on the ability of several annexins to induce membrane curvature[128], where wound repair was hypothesized to depend on the membrane stabilizing step governed by ANXA5. The wound geometry has been proposed to involve an inward budding, forming a funnel-shaped membrane [31]. Intriguingly, the current study, using thermoplasmonics, demonstrated a stable annexin ring around the site of injury. Future studies, using thermoplasmonics, should focus on the possibility of triggering Ca^{2+} influx at lower laser powers, before the initiation of nanobubbles, while simultaneously imaging components of the PMR machinery. This could potentially lead to the transient recruitment of PMR-associated proteins and subsequent healing of the damaged membrane.

An alternative ANXA5-mediated PMR model was proposed, suggesting that ANXA5 induces a local membrane curvature upon membrane disruption, while the underlying actin cytoskeleton inhibits the rolling of the membrane. The damaged membrane is then locally bent and folded on top of itself. This process was proposed to be mediated by the N-terminal region of the ANXA5 protein, which facilitates the interaction between two ANXA5 proteins and thus “closes” the pocket. This was based on ANXA5’s ability to aggregate GUVs when added to a GUV-containing suspension[54]. Another suggestion, building upon this model, is that the membrane was explosively displaced upon nanobubble formation. Here, ANXA5 induces rolling at the free membrane edges, which is then attached to the PM creating a membrane pocket. Either way, ANXA5 was suggested to mediate PMR by preventing further expansion of the wound, leading to successful membrane restoration through alternative repair mechanisms, potentially by vesicle recruitment and clustering at the injury site[31, 127].

Following inhibition of actin polymerization and subsequent disruption of the actin cytoskeleton, a distinct response of ANXA2 was observed, characterized by the nucleation of vesicle structures from the ANXA2 ring structure, which resembled the shape of flower petals, a structure referred to as the “Annexin flower”. The impact of actin disruption revealed a correlation between the actin cytoskeleton and the ANXA2 blebbing mechanism and was thought to be linked to the established ANXA2-induced blebbing mechanism of patch membranes[131]. Thus, the present findings demonstrate a direct biophysical effect of ANXA2-induced blebbing within living cells. Additionally, these vesicular structures, or blebs, remained stable and

appeared to form membrane adhesion with the adjacent bleb membranes, which supports previous studies reporting ANXA2-mediated vesicle aggregation[116, 157, 158]. However, further studies need to be performed to confirm the nature of these blebs e.g., by the addition of extracellular dyes which could diffuse into the lumen of possible inward-forming blebs.

To gain a more comprehensive understanding of the biophysical response of ANXA2 to membrane injury, it would be advantageous to isolate its mechanism in model membrane systems such as giant plasma membrane vesicles (GPMVs) or giant unilamellar vesicles (GUVs). By doing so, a cell-free environment can be established where the proteins can be quantitatively investigated. For comparative reasons, ANXA2 can be encapsulated within GUVs, similar to the ANXA5 in vitro experiments conducted by Moreno et al.[54], for further investigation. This approach could provide insights into the mechanisms underlying the formation of the ANXA2 ring structure at the injury site and potentially elucidate how the blebs are formed and expand into the Annexin flower. However, unlike in cells, the holes inflicted on GUVs tend to continue to expand, followed by destabilization of the vesicle. Imaging the hole evolution using confocal microscopy could therefore be challenging due to the rapid expansion of the hole diameter, alternatively, a spinning disk confocal could be utilized for faster imaging. Such experiments could confirm the differences seen between ANXA2 and other annexins in terms of curvature generation around free edges.

An important future step is to resolve how cells are healing after a thermoplasmonic membrane rupture, which could be done by imaging other structures, such as endosomes, which could in fact play a role in sealing the wound and stop the influx of Ca^{2+} . Therefore, it is of great interest to further investigate the content of the wound, and the recruitment, and fusion of endosomes and lysosomes to the injury site, which could shed light on the events occurring within the wound and offer insights into the operation of the PMR machinery in living cells.

Nuclear envelope disruption

In collaboration with the Danish Cancer Society Research Center, a study was conducted to investigate the actin response to nuclear envelope disruption in breast cancer cells. The preliminary findings revealed a large-scale reorganization of the actin cytoskeleton during and after mechanical disruption. Furthermore, the rapid actin polymerization at the perinuclear region was not solely dependent on elevated intracellular calcium levels, but specifically on extracellular calcium influx prior to its assembly.

To investigate if a repair mechanism is taking place at the nuclear envelope, the CHMP4B protein could be labeled, as a positive control marker. CHMP4B is a primary component of the ESCRT-III complex, which is among the few components known to be involved in nuclear envelope repair[168]. Hence, the detection of CHMP4B at the injured nucleus would

therefore confirm repair after thermoplasmonic nuclear rupture and potentially provide further information of whether actin contributes to the reconstruction of the internal membrane. In this context, it may also be of interest to investigate the role of ANXA7, which is known to interact with ESCRT III[47]. This approach could potentially elucidate whether the repair mechanisms and actin recruitment are triggered by nuclear envelope rupture alone or require simultaneous disruption of the plasma membrane. The primary goal for this part will therefore be to optimize the current platform in performing selective punctures of the nuclear membrane and avoid any damage to the plasma membrane. So far, no method has been developed for efficient and selective puncturing of nuclear membranes and hence these preliminary results and this platform holds great promise for nuclear repair studies.

Future developments of the thermoplasmonic method

Despite the potential limitations of the thermoplasmonic method, including the manual alignment of the laser and confocal focus, which may introduce variability in membrane rupture efficiency, and the formation of nanobubbles, this technique provides a distinctive tool for investigating cellular responses and plasma membrane repair in an almost native environment while maintaining cell viability.

When using microscopes that do not have a reflection mode, such as the Lumicks C-Trap, achieving co-localization between the laser focus and the particle of interest can be difficult. To address this challenge, alternative imaging modes, such as brightfield, can be used, and a slow raster scan can be conducted around the anticipated position of the particle. Additionally, less efficient techniques such as fluorescent AuNP labeling can be considered as an alternative[73].

Additionally, exploring the lipid concentration at the injury site could provide a better understanding of the nature of the wound, where a variation in lipid order could be assessed by incorporating membrane order-sensitive probes, such as push-pull pyrene[138] or Laurdan[127], and offer a more nuanced depiction of the components involved in plasma membrane repair. To gain a deeper insight into the nature of the wound and into the biophysical role and interaction of key proteins involved in membrane repair at the single-molecule level, the thermoplasmonic approach could be combined with other imaging techniques, such as the stochastic optical reconstruction microscopy (STORM). This combination could provide comprehensive information on the injury site, including the wound geometry and location of annexin proteins, and identification of other key players responsible for restoring the membrane surface[73].

T-cell activation

The preliminary findings obtained during the residency at the Dutch research center, AMOLF, revealed that both complete and incomplete $\gamma\delta$ T-cell receptor-expressing Jurkat cells had the capacity to interact with cancer cells by detecting and actively searching for antigen-presenting tumor membranes through the extension, twisting, and retraction of finger-like protrusions, resulting in intracellular calcium fluxes. Moreover, the formation of immunological synapses, indicating T-cell activation, was observed as a close contact between T-cells and tumor cells, ultimately resulting in cancer cell death due to the cytotoxic nature of T-cells[4, 209]. However, given the preliminary nature of the findings, further experiments are necessary to determine the calcium intensity pattern, as a hallmark for synapse formation is a dramatic increase in the cytosolic calcium concentration[4], and to investigate whether the Ca^{2+} fluctuations arise due to T-cell movement or immunological synapse formation. This could potentially be achieved through statistical analysis of the T-cell activation, depending on its proximity to neighboring cells, providing information on whether the cells were in close contact, hence forming an immunological synapse, upon T-cell activation or giving an estimate of the distance for which the T-cells were activated. However, as the cellular response is monitored by confocal microscopy, limitations may arise from force-dependent cell movement in the vertical direction, as the resolution is confined to the focal plane.

Furthermore, the findings showed that T-cells were not activated upon engagement with GPMVs derived from tumor cells by NEM-induced vesiculation. Since it was expected that the GPMV model consisted of both the complex plasma membrane and the cytosolic fluid content of the tumor cells[223], it was anticipated that T-cells would exhibit a similar interactive response as with the tumor cells. The complete lack of T-cell activation indicates that the designated butyrophilins (BTNs) were either inactive or entirely absent on the antigen-presenting GPMV membrane. To assess the potential impact of the blebbing agent on protein migration into GPMVs, alternative vesicular agents such as the actin-depolymerizing drug latrunculin B or mechanical vesiculation could be explored[225, 235]. However, since the BTNs were neither identified on spontaneously formed blebs, this further suggested that the exclusion of BTNs from GPMVs may not be NEM-specific, but instead be a result of a more general mechanism. Therefore, further research into the GPMV's composition is required. This could be accomplished by employing a construct that genetically expresses fluorescently labeled BTN3A1, which would reveal whether the BTN3A1 proteins were incorporated into GPMVs upon vesiculation.

Bibliography

- [1] “Cancer - key facts,” *The World's Health Organization*, vol. <https://www.who.int/news-room/factsheets/detail/cancer>, (accessed: 16.04.2023).
- [2] K. Poulsen, “Kræft i danmark,” *The Danish Cancer Society*, 2020.
- [3] M. Norcross, “A synaptic basis for t-lymphocyte activation,” in *Annales de l'Institut Pasteur/Immunologie*, vol. 135, pp. 113–134, Elsevier, 1984.
- [4] N. Joseph, B. Reicher, and M. Barda-Saad, “The calcium feedback loop and t cell activation: how cytoskeleton networks control intracellular calcium flux,” *Biochimica et Biophysica Acta (BBA)-Biomembranes*, vol. 1838, no. 2, pp. 557–568, 2014.
- [5] D. Hanahan and R. A. Weinberg, “Hallmarks of cancer: the next generation,” *cell*, vol. 144, no. 5, pp. 646–674, 2011.
- [6] T. L. Boye and J. Nylandsted, “Annexins in plasma membrane repair,” *Biological chemistry*, vol. 397, no. 10, pp. 961–969, 2016.
- [7] P. Bendix, A. Simonsen, C. Florentsen, S. Häger, A. Mularski, A. Zanjani, G. Moreno-Pescador, M. Klenow, S. Sønder, H. Danielsen, *et al.*, “Interdisciplinary synergy to reveal mechanisms of annexin-mediated plasma membrane shaping and repair. *cells*. 9: 1029,” 2020.
- [8] M. L. Ebstrup, C. Dias, A. S. B. Heitmann, S. L. Sønder, and J. Nylandsted, “Actin cytoskeletal dynamics in single-cell wound repair,” *International Journal of Molecular Sciences*, vol. 22, no. 19, p. 10886, 2021.
- [9] T. Hianik and V. I. Paschnik, *Bilayer lipid membranes. Structure and mechanical properties*. Springer Science & Business Media, 1995.
- [10] M. Chabanon, J. C. Stachowiak, and P. Rangamani, “Systems biology of cellular membranes: a convergence with biophysics,” *Wiley Interdisciplinary Reviews: Systems Biology and Medicine*, vol. 9, no. 5, p. e1386, 2017.
- [11] M. Aktas, L. Danne, P. Möller, and F. Narberhaus, “Membrane lipids in *agrobacterium tumefaciens*: biosynthetic pathways and importance for pathogenesis,” *Frontiers in plant science*, vol. 5, p. 109, 2014.
- [12] T. Harayama and H. Riezman, “Understanding the diversity of membrane lipid composition,” *Nature reviews Molecular cell biology*, vol. 19, no. 5, pp. 281–296, 2018.
- [13] G. Van Meer, “Voelker dr feigenson gw nat,” *Rev. Mol. Cell Biol*, vol. 9, pp. 112–124, 2008.
- [14] G. L. Nicolson, “Cell membrane fluid–mosaic structure and cancer metastasis,” *Cancer research*, vol. 75, no. 7, pp. 1169–1176, 2015.
- [15] A. G. Clark, O. Wartlick, G. Salbreux, and E. K. Paluch, “Stresses at the cell surface during animal cell morphogenesis,” *Current Biology*, vol. 24, no. 10, pp. R484–R494, 2014.
- [16] S. N. Koerdt and V. Gerke, “Annexin a2 is involved in ca²⁺-dependent plasma membrane repair in primary human endothelial cells,” *Biochimica et Biophysica Acta (BBA)-Molecular Cell Research*, vol. 1864, no. 6, pp. 1046–1053, 2017.
- [17] T. Svitkina, “The actin cytoskeleton and actin-based motility,” *Cold Spring Harbor perspectives in biology*, vol. 10, no. 1, p. a018267, 2018.

- [18] J. Zimmerberg and M. M. Kozlov, “How proteins produce cellular membrane curvature,” *Nature reviews Molecular cell biology*, vol. 7, no. 1, pp. 9–19, 2006.
- [19] N. Leijnse, Y. F. Barooji, M. R. Arastoo, S. L. Sønder, B. Verhagen, L. Wullkopf, J. T. Erler, S. Semsey, J. Nylandsted, L. B. Oddershede, *et al.*, “Filopodia rotate and coil by actively generating twist in their actin shaft,” *Nature Communications*, vol. 13, no. 1, p. 1636, 2022.
- [20] S. Pöyry and I. Vattulainen, “Role of charged lipids in membrane structures — insight given by simulations,” *Biochimica et Biophysica Acta (BBA) - Biomembranes*, vol. 1858, pp. 2322–2333, 2016.
- [21] V. Gerke, C. E. Creutz, and S. E. Moss, “Annexins: linking ca^{2+} signalling to membrane dynamics,” *Nature reviews Molecular cell biology*, vol. 6, no. 6, pp. 449–461, 2005.
- [22] H. T. McMahon and J. L. Gallop, “Membrane curvature and mechanisms of dynamic cell membrane remodelling,” *Nature*, vol. 438, no. 7068, pp. 590–596, 2005.
- [23] W. T. Snead and J. C. Stachowiak, “Structure versus stochasticity—the role of molecular crowding and intrinsic disorder in membrane fission,” *Journal of molecular biology*, vol. 430, no. 16, pp. 2293–2308, 2018.
- [24] E. E. Strehler and D. A. Zacharias, “Role of alternative splicing in generating isoform diversity among plasma membrane calcium pumps,” *Physiological reviews*, 2001.
- [25] E. C. David, “Calcium signaling,” *Cell*, vol. 47, pp. 423–431, 1995.
- [26] R. S. Lewis, “Calcium signaling mechanisms in t lymphocytes,” *Annual review of immunology*, vol. 19, no. 1, pp. 497–521, 2001.
- [27] A. Bouter, R. Carmeille, C. Gounou, F. Bouvet, S. Degrelle, D. Evain-Brion, and A. Brisson, “Annexin-a5 and cell membrane repair,” *Placenta*, vol. 36, pp. S43–S49, 2015.
- [28] O. Gajic, J. Lee, C. H. Doerr, J. C. Berrios, J. L. Myers, and R. D. Hubmayr, “Ventilator-induced cell wounding and repair in the intact lung,” *American journal of respiratory and critical care medicine*, vol. 167, no. 8, pp. 1057–1063, 2003.
- [29] P. L. McNeil and R. Khakee, “Disruptions of muscle fiber plasma membranes. role in exercise-induced damage.,” *The American journal of pathology*, vol. 140, no. 5, p. 1097, 1992.
- [30] Q. Yu and P. L. McNeil, “Transient disruptions of aortic endothelial cell plasma membranes.,” *The American journal of pathology*, vol. 141, no. 6, p. 1349, 1992.
- [31] T. L. Boye, K. Maeda, W. Pezeshkian, S. L. Sønder, S. C. Haeger, V. Gerke, A. C. Simonsen, and J. Nylandsted, “Annexin a4 and a6 induce membrane curvature and constriction during cell membrane repair,” *Nature communications*, vol. 8, no. 1, pp. 1–11, 2017.
- [32] N. Reymond, B. B. d’Agua, and A. J. Ridley, “Crossing the endothelial barrier during metastasis,” *Nature Reviews Cancer*, vol. 13, no. 12, pp. 858–870, 2013.
- [33] J. Jaiswal, “Calcium—how and why?,” *Journal of biosciences*, vol. 26, no. 3, pp. 357–363, 2001.
- [34] A. J. Jimenez and F. Perez, “Plasma membrane repair: the adaptable cell life-insurance,” *Current opinion in cell biology*, vol. 47, pp. 99–107, 2017.
- [35] C. Cai, H. Masumiya, N. Weisleder, N. Matsuda, M. Nishi, M. Hwang, J.-K. Ko, P. Lin, A. Thornton, X. Zhao, *et al.*, “Mg53 nucleates assembly of cell membrane repair machinery,” *Nature cell biology*, vol. 11, no. 1, pp. 56–64, 2009.
- [36] L. Heilbrunn, “The surface precipitation reaction of living cells,” *Proceedings of the American Philosophical Society*, vol. 69, no. 1, pp. 295–301, 1930.

- [37] R. A. Steinhardt, G. Bi, and J. M. Alderton, “Cell membrane resealing by a vesicular mechanism similar to neurotransmitter release,” *Science*, vol. 263, no. 5145, pp. 390–393, 1994.
- [38] B. Alberts, A. Johnson, J. Lewis, M. Raff, K. Roberts, P. Walter, *et al.*, *Molecular biology of the cell*, vol. 4. New York: Garland Science USA, 2002.
- [39] X. Cheng, X. Zhang, L. Yu, and H. Xu, “Calcium signaling in membrane repair,” in *Seminars in cell & developmental biology*, vol. 45, pp. 24–31, Elsevier, 2015.
- [40] X. Cheng, X. Zhang, Q. Gao, M. Ali Samie, M. Azar, W. L. Tsang, L. Dong, N. Sahoo, X. Li, Y. Zhuo, *et al.*, “The intracellular ca^{2+} channel *mcoln1* is required for sarcolemma repair to prevent muscular dystrophy,” *Nature medicine*, vol. 20, no. 10, pp. 1187–1192, 2014.
- [41] A. Mularski, S. L. Sønder, A. S. B. Heitmann, M. P. Pandey, H. Khandelia, J. Nylandsted, and A. C. Simonsen, “Interplay of membrane crosslinking and curvature induction by annexins,” *Scientific Reports*, vol. 12, no. 1, p. 22568, 2022.
- [42] S. T. Cooper and P. L. McNeil, “Membrane repair: mechanisms and pathophysiology,” *Physiological reviews*, vol. 95, no. 4, pp. 1205–1240, 2015.
- [43] C. Dias and J. Nylandsted, “Plasma membrane integrity in health and disease: significance and therapeutic potential,” *Cell discovery*, vol. 7, no. 1, pp. 1–18, 2021.
- [44] S. K. Tang and W. F. Marshall, “Self-repairing cells: How single cells heal membrane ruptures and restore lost structures,” *Science*, vol. 356, no. 6342, pp. 1022–1025, 2017.
- [45] M. T. Abreu-Blanco, J. M. Verboon, and S. M. Parkhurst, “Single cell wound repair: Dealing with life’s little traumas,” *Bioarchitecture*, vol. 1, no. 3, pp. 114–121, 2011.
- [46] M. T. Abreu-Blanco, J. M. Verboon, and S. M. Parkhurst, “Cell wound repair in *drosophila* occurs through three distinct phases of membrane and cytoskeletal remodeling,” *Journal of Cell Biology*, vol. 193, no. 3, pp. 455–464, 2011.
- [47] S. L. Sønder, T. L. Boye, R. Tölle, J. Dengjel, K. Maeda, M. Jäättelä, A. C. Simonsen, J. K. Jaiswal, and J. Nylandsted, “Annexin a7 is required for *escrt iii*-mediated plasma membrane repair,” *Scientific reports*, vol. 9, no. 1, pp. 1–12, 2019.
- [48] N. W. Andrews, P. E. Almeida, and M. Corrotte, “Damage control: cellular mechanisms of plasma membrane repair,” *Trends in cell biology*, vol. 24, no. 12, pp. 734–742, 2014.
- [49] V. Idone, C. Tam, J. W. Goss, D. Toomre, M. Pypaert, and N. W. Andrews, “Repair of injured plasma membrane by rapid ca^{2+} -dependent endocytosis,” *The Journal of cell biology*, vol. 180, no. 5, pp. 905–914, 2008.
- [50] S. P. Lauritzen, T. L. Boye, and J. Nylandsted, “Annexins are instrumental for efficient plasma membrane repair in cancer cells,” in *Seminars in cell & developmental biology*, vol. 45, pp. 32–38, Elsevier, 2015.
- [51] S. C. Häger and J. Nylandsted, “Annexins: players of single cell wound healing and regeneration,” *Communicative & integrative biology*, vol. 12, no. 1, pp. 162–165, 2019.
- [52] J. K. Jaiswal, S. P. Lauritzen, L. Scheffer, M. Sakaguchi, J. Bunkenborg, S. M. Simon, T. Kallunki, M. Jäättelä, and J. Nylandsted, “S100a11 is required for efficient plasma membrane repair and survival of invasive cancer cells,” *Nature communications*, vol. 5, no. 1, pp. 1–13, 2014.
- [53] A. Draeger, K. Monastyrskaya, and E. B. Babychuk, “Plasma membrane repair and cellular damage control: the annexin survival kit,” *Biochemical pharmacology*, vol. 81, no. 6, pp. 703–712, 2011.

- [54] G. S. Moreno-Pescador, D. S. Aswad, C. D. Florentsen, A. Bahadori, M. R. Arastoo, H. M. D. Danielsen, A. S. B. Heitmann, T. L. Boye, J. Nylandsted, L. B. Oddershede, *et al.*, “Thermoplasmonic nano-rupture of cells reveals annexin v function in plasma membrane repair,” *Nanoscale*, vol. 14, no. 21, pp. 7778–7787, 2022.
- [55] B. Zhivotovsky and S. Orrenius, “Calcium and cell death mechanisms: a perspective from the cell death community,” *Cell calcium*, vol. 50, no. 3, pp. 211–221, 2011.
- [56] A. S. B. Heitmann, A. A. H. Zanjani, M. B. Klenow, A. Mularski, S. L. Sønder, F. W. Lund, T. L. Boye, C. Dias, P. M. Bendix, A. C. Simonsen, *et al.*, “Phenothiazines alter plasma membrane properties and sensitize cancer cells to injury by inhibiting annexin-mediated repair,” *Journal of Biological Chemistry*, vol. 297, no. 2, 2021.
- [57] W. M. Bement, C. A. Mandato, and M. N. Kirsch, “Wound-induced assembly and closure of an actomyosin purse string in xenopus oocytes,” *Current biology*, vol. 9, no. 11, pp. 579–587, 1999.
- [58] N. Weisleder, N. Takizawa, P. Lin, X. Wang, C. Cao, Y. Zhang, T. Tan, C. Ferrante, H. Zhu, P.-J. Chen, *et al.*, “Recombinant mg53 protein modulates therapeutic cell membrane repair in treatment of muscular dystrophy,” *Science translational medicine*, vol. 4, no. 139, pp. 139ra85–139ra85, 2012.
- [59] A. Defour, S. Sreetama, and J. K. Jaiswal, “Imaging cell membrane injury and subcellular processes involved in repair,” *JoVE (Journal of Visualized Experiments)*, no. 85, p. e51106, 2014.
- [60] I. R. Sudji, Y. Subburaj, N. Frenkel, A. J. García-Sáez, and M. Wink, “Membrane disintegration caused by the steroid saponin digitonin is related to the presence of cholesterol,” *Molecules*, vol. 20, no. 11, pp. 20146–20160, 2015.
- [61] E. Babiychuk, K. Monastyrskaya, S. Potez, and A. Draeger, “Intracellular ca^{2+} operates a switch between repair and lysis of streptolysin o-perforated cells,” *Cell Death & Differentiation*, vol. 16, no. 8, pp. 1126–1134, 2009.
- [62] L. Nygård Skalman, M. R. Holst, E. Larsson, and R. Lundmark, “Plasma membrane damage caused by listeriolysin o is not repaired through endocytosis of the membrane pore,” *Biology open*, vol. 7, no. 10, p. bio035287, 2018.
- [63] G. Moreno-Pescador, C. D. Florentsen, H. Østbye, S. L. Sønder, T. L. Boye, E. L. Veje, A. K. Sonne, S. Semsey, J. Nylandsted, R. Daniels, *et al.*, “Curvature-and phase-induced protein sorting quantified in transfected cell-derived giant vesicles,” *ACS nano*, vol. 13, no. 6, pp. 6689–6701, 2019.
- [64] K. A. Swaggart, A. R. Demonbreun, A. H. Vo, K. E. Swanson, E. Y. Kim, J. P. Fahrenbach, J. Holley-Cuthrell, A. Eskin, Z. Chen, K. Squire, *et al.*, “Annexin a6 modifies muscular dystrophy by mediating sarcolemmal repair,” *Proceedings of the National Academy of Sciences*, vol. 111, no. 16, pp. 6004–6009, 2014.
- [65] E. Lukianova-Hleb, Y. Hu, L. Latterini, L. Tarpani, S. Lee, R. A. Drezek, J. H. Hafner, and D. O. Lapotko, “Plasmonic nanobubbles as transient vapor nanobubbles generated around plasmonic nanoparticles,” *ACS nano*, vol. 4, no. 4, pp. 2109–2123, 2010.
- [66] A. Vogel, J. Noack, G. Hüttman, and G. Paltauf, “Mechanisms of femtosecond laser nanosurgery of cells and tissues,” *Applied physics B*, vol. 81, no. 8, pp. 1015–1047, 2005.
- [67] L. Minai, D. Yeheskely-Hayon, L. Golan, G. Bisker, E. J. Dann, and D. Yelin, “Optical nanomanipulations of malignant cells: controlled cell damage and fusion,” *Small*, vol. 8, no. 11, pp. 1732–1739, 2012.
- [68] D. Yeheskely-Hayon, L. Minai, L. Golan, E. J. Dann, and D. Yelin, “Optically induced cell fusion using bispecific nanoparticles,” *Small*, vol. 9, no. 22, pp. 3771–3777, 2013.

- [69] J. C. Fraire, G. Houthaeye, J. Liu, L. Raes, L. Vermeulen, S. Stremersch, T. Brans, G. G.-D. Barriga, S. De Keulenaer, F. Van Nieuwerburgh, *et al.*, “Vapor nanobubble is the more reliable photothermal mechanism for inducing endosomal escape of sirna without disturbing cell homeostasis,” *Journal of Controlled Release*, vol. 319, pp. 262–275, 2020.
- [70] L. Jauffred, A. Samadi, H. Klingberg, P. M. Bendix, and L. B. Oddershede, “Plasmonic heating of nanostructures,” *Chemical reviews*, vol. 119, no. 13, pp. 8087–8130, 2019.
- [71] K. C. Neuman and A. Nagy, “Single-molecule force spectroscopy: optical tweezers, magnetic tweezers and atomic force microscopy,” *Nature methods*, vol. 5, no. 6, pp. 491–505, 2008.
- [72] X. Deán-Ben, S. Gottschalk, B. Mc Larney, S. Shoham, and D. Razansky, “Advanced optoacoustic methods for multiscale imaging of in vivo dynamics,” *Chemical Society Reviews*, vol. 46, no. 8, pp. 2158–2198, 2017.
- [73] H. M. D. Danielsen, M. Arastoo, G. Moreno-Pescador, and P. M. Bendix, “A thermoplasmonic approach for the investigation of plasma membrane repair in living cells and model membranes,” *Journal of Visualized Experiments*, 2023.
- [74] P. M. Bendix, S. N. S. Reihani, and L. B. Oddershede, “Direct measurements of heating by electromagnetically trapped gold nanoparticles on supported lipid bilayers,” *ACS nano*, vol. 4, no. 4, pp. 2256–2262, 2010.
- [75] A. Kyrsting, P. M. Bendix, D. G. Stamou, and L. B. Oddershede, “Heat profiling of three-dimensionally optically trapped gold nanoparticles using vesicle cargo release,” *Nano letters*, vol. 11, no. 2, pp. 888–892, 2011.
- [76] Y. He, K. Laugesen, D. Kamp, S. A. Sultan, L. B. Oddershede, and L. Jauffred, “Effects and side effects of plasmonic photothermal therapy in brain tissue,” *Cancer Nanotechnology*, vol. 10, no. 1, pp. 1–11, 2019.
- [77] C. D. Florentsen, A.-K. V. West, H. M. D. Danielsen, S. Semsey, P. M. Bendix, and L. B. Oddershede, “Quantification of loading and laser-assisted release of rna from single gold nanoparticles,” *Langmuir*, vol. 34, no. 49, pp. 14891–14898, 2018.
- [78] A. Samadi, H. Klingberg, L. Jauffred, A. Kjær, P. M. Bendix, and L. B. Oddershede, “Platinum nanoparticles: a non-toxic, effective and thermally stable alternative plasmonic material for cancer therapy and bioengineering,” *Nanoscale*, vol. 10, no. 19, pp. 9097–9107, 2018.
- [79] A. Bahadori, A. R. Lund, S. Semsey, L. B. Oddershede, and P. M. Bendix, “Controlled cellular fusion using optically trapped plasmonic nano-heaters,” in *Optical Trapping and Optical Micromanipulation XIII*, vol. 9922, pp. 125–134, SPIE, 2016.
- [80] A. Bahadori, L. B. Oddershede, and P. M. Bendix, “Hot-nanoparticle-mediated fusion of selected cells,” *Nano Research*, vol. 10, no. 6, pp. 2034–2045, 2017.
- [81] A. Bahadori, G. Moreno-Pescador, L. B. Oddershede, and P. M. Bendix, “Remotely controlled fusion of selected vesicles and living cells: a key issue review,” *Reports on Progress in Physics*, vol. 81, no. 3, p. 032602, 2018.
- [82] A. Rørvig-Lund, A. Bahadori, S. Semsey, P. M. Bendix, and L. B. Oddershede, “Vesicle fusion triggered by optically heated gold nanoparticles,” *Nano letters*, vol. 15, no. 6, pp. 4183–4188, 2015.
- [83] G. Moreno-Pescador, M. R. Arastoo, S. Chiantia, R. Daniels, and P. M. Bendix, “Thermoplasmonic induced vesicle fusion for investigating membrane protein phase affinity,” *bioRxiv*, pp. 2022–09, 2022.

- [84] G. S. M. Pescador, D. S. Asward, M. R. Arastoo, H. M. D. Danielsen, C. D. Florentsen, A. Bahadori, J. Nylandsted, L. B. Oddershede, and P. M. Bendix, “Investigating plasma-membrane repair employing thermoplasmonics,” *Biophysical Journal*, vol. 120, no. 3, p. 45a, 2021.
- [85] R.-J. Essiambre, “Arthur ashkin: Father of the optical tweezers,” *Proceedings of the National Academy of Sciences*, vol. 118, no. 7, p. e2026827118, 2021.
- [86] “The nobel prize in physics 2018,” *Nobel Prize outreach AB 2023*, vol. <https://www.nobelprize.org/prizes/physics/2018/summary>, (accessed: 30.01.2023).
- [87] L. B. Oddershede, C. Krafft, P. Roesch, and J. Popp, “Optical tweezers techniques - from chapter: Methods and applications in: Handbook of molecular biophysics,” 2009.
- [88] M. Minsky, “Memoir on inventing the confocal scanning microscope,” *Scanning*, vol. 10, no. 4, pp. 128–138, 1988.
- [89] P. M. Bendix, L. Jauffred, K. Norregaard, and L. B. Oddershede, “Optical trapping of nanoparticles and quantum dots,” *IEEE journal of selected topics in quantum electronics*, vol. 20, no. 3, pp. 15–26, 2013.
- [90] K. Svoboda and S. M. Block, “Biological applications of optical forces,” *Annual review of biophysics and biomolecular structure*, vol. 23, no. 1, pp. 247–285, 1994.
- [91] A. Rohrbach and E. H. Stelzer, “Trapping forces, force constants, and potential depths for dielectric spheres in the presence of spherical aberrations,” *Applied optics*, vol. 41, no. 13, pp. 2494–2507, 2002.
- [92] A. Ashkin, “Forces of a single-beam gradient laser trap on a dielectric sphere in the ray optics regime,” *Biophysical journal*, vol. 61, no. 2, pp. 569–582, 1992.
- [93] A. Kyrsting, P. M. Bendix, and L. B. Oddershede, “Mapping 3d focal intensity exposes the stable trapping positions of single nanoparticles,” *Nano letters*, vol. 13, no. 1, pp. 31–35, 2013.
- [94] G. Mie, “Beiträge zur optik trüber medien, speziell kolloidaler metallösungen,” *Annalen der physik*, vol. 330, no. 3, pp. 377–445, 1908.
- [95] N. G. Khlebtsov and L. A. Dykman, “Optical properties and biomedical applications of plasmonic nanoparticles,” *Journal of Quantitative Spectroscopy and Radiative Transfer*, vol. 111, no. 1, pp. 1–35, 2010.
- [96] H. Goldenberg and C. Tranter, “Heat flow in an infinite medium heated by a sphere,” *British journal of applied physics*, vol. 3, no. 9, p. 296, 1952.
- [97] S. Eustis and M. A. El-Sayed, “Why gold nanoparticles are more precious than pretty gold: noble metal surface plasmon resonance and its enhancement of the radiative and nonradiative properties of nanocrystals of different shapes,” *Chemical society reviews*, vol. 35, no. 3, pp. 209–217, 2006.
- [98] U. Kreibig and M. Vollmer, *Optical properties of metal clusters*, vol. 25. Springer Science & Business Media, 2013.
- [99] C. F. Bohren and D. R. Huffman, *Absorption and scattering of light by small particles*. John Wiley & Sons, 2008.
- [100] N. G. Khlebtsov, “Optics and biophotonics of nanoparticles with a plasmon resonance,” *Quantum electronics*, vol. 38, no. 6, p. 504, 2008.
- [101] S. Link and M. A. El-Sayed, “Shape and size dependence of radiative, non-radiative and photothermal properties of gold nanocrystals,” *International reviews in physical chemistry*, vol. 19, no. 3, pp. 409–453, 2000.

- [102] J. A. Webb and R. Bardhan, “Emerging advances in nanomedicine with engineered gold nanostructures,” *Nanoscale*, vol. 6, no. 5, pp. 2502–2530, 2014.
- [103] Z. Qin and J. C. Bischof, “Thermophysical and biological responses of gold nanoparticle laser heating,” *Chemical Society Reviews*, vol. 41, no. 3, pp. 1191–1217, 2012.
- [104] L. D. Landau and E. M. Lifshitz, *Fluid Mechanics: Landau and Lifshitz: Course of Theoretical Physics, Volume 6*, vol. 6. Elsevier, 2013.
- [105] J. C. Jaeger and H. S. Carslaw, *Conduction of heat in solids*. Clarendon P Oxford, United Kingdom, 1959.
- [106] J. T. Jørgensen, K. Norregaard, P. Tian, P. M. Bendix, A. Kjaer, and L. B. Oddershede, “Single particle and pet-based platform for identifying optimal plasmonic nano-heaters for photothermal cancer therapy,” *Scientific Reports*, vol. 6, no. 1, pp. 1–10, 2016.
- [107] S. Oldenburg, “Light scattering from gold nanoshells, diss. rice university, 2000.”
- [108] A. C. Richardson, N. Reihani, and L. B. Oddershede, “Combining confocal microscopy with precise force-scope optical tweezers,” in *Optical Trapping and Optical Micromanipulation III*, vol. 6326, pp. 560–569, SPIE, 2006.
- [109] J. Vangindertael, R. Camacho, W. Sempels, H. Mizuno, P. Dedecker, and K. Janssen, “An introduction to optical super-resolution microscopy for the adventurous biologist,” *Methods and applications in fluorescence*, vol. 6, no. 2, p. 022003, 2018.
- [110] A. Fine, “Confocal microscopy: Principles and practice,” *Cold Spring Harbor Protocols*, vol. 2007, no. 10, pp. pdb-top22, 2007.
- [111] R. W. Cole, T. Jinadasa, and C. M. Brown, “Measuring and interpreting point spread functions to determine confocal microscope resolution and ensure quality control,” *Nature protocols*, vol. 6, no. 12, pp. 1929–1941, 2011.
- [112] S. Dunst and P. Tomancak, “Imaging flies by fluorescence microscopy: principles, technologies, and applications,” *Genetics*, vol. 211, no. 1, pp. 15–34, 2019.
- [113] T. Numata, H. Tatsuta, Y. Morita, Y. Otani, and N. Umeda, “Localized thermal processing with a laser-trapped and heated metal nanoparticle,” *IEEEJ Transactions on Electrical and Electronic Engineering*, vol. 2, no. 3, pp. 398–401, 2007.
- [114] V. Gerke and S. E. Moss, “Annexins: from structure to function,” *Physiological reviews*, vol. 82, no. 2, pp. 331–371, 2002.
- [115] S. E. Moss and R. O. Morgan, “The annexins,” *Genome biology*, vol. 5, no. 4, pp. 1–8, 2004.
- [116] P. Drücker, M. Pejic, H.-J. Galla, and V. Gerke, “Lipid segregation and membrane budding induced by the peripheral membrane binding protein annexin a2,” *Journal of Biological Chemistry*, vol. 288, no. 34, pp. 24764–24776, 2013.
- [117] T. Togo, J. M. Alderton, G.-Q. Bi, and R. A. Steinhardt, “The mechanism of facilitated cell membrane resealing,” *Journal of cell science*, vol. 112, no. 5, pp. 719–731, 1999.
- [118] C. S. Eddleman, M. L. Ballinger, M. E. Smyers, H. M. Fishman, and G. D. Bittner, “Endocytotic formation of vesicles and other membranous structures induced by ca²⁺ and axolemmal injury,” *Journal of Neuroscience*, vol. 18, no. 11, pp. 4029–4041, 1998.
- [119] N. J. Lennon, A. Kho, B. J. Bacsikai, S. L. Perlmutter, B. T. Hyman, and R. H. Brown, “Dysferlin interacts with annexins a1 and a2 and mediates sarcolemmal wound-healing,” *Journal of Biological Chemistry*, vol. 278, no. 50, pp. 50466–50473, 2003.

- [120] D. Bansal, K. Miyake, S. S. Vogel, S. Groh, C.-C. Chen, R. Williamson, P. L. McNeil, and K. P. Campbell, “Defective membrane repair in dysferlin-deficient muscular dystrophy,” *Nature*, vol. 423, no. 6936, pp. 168–172, 2003.
- [121] L. L. Scheffer, S. C. Sreetama, N. Sharma, S. Medikayala, K. J. Brown, A. Defour, and J. K. Jaiswal, “Mechanism of Ca^{2+} -triggered ESCRT assembly and regulation of cell membrane repair,” *Nature communications*, vol. 5, no. 1, p. 5646, 2014.
- [122] L. M. Godin, J. Vergen, Y. Prakash, R. E. Pagano, and R. D. Hubmayr, “Spatiotemporal dynamics of actin remodeling and endomembrane trafficking in alveolar epithelial type I cell wound healing,” *American Journal of Physiology-Lung Cellular and Molecular Physiology*, vol. 300, no. 4, pp. L615–L623, 2011.
- [123] K. Miyake, P. L. McNeil, K. Suzuki, R. Tsunoda, and N. Sugai, “An actin barrier to resealing,” *Journal of cell science*, vol. 114, no. 19, pp. 3487–3494, 2001.
- [124] C. A. Mandato and W. M. Bement, “Contraction and polymerization cooperate to assemble and close actomyosin rings around *Xenopus* oocyte wounds,” *The Journal of cell biology*, vol. 154, no. 4, pp. 785–798, 2001.
- [125] J. K. Jaiswal and J. Nylandsted, “S100 and annexin proteins identify cell membrane damage as the achilles heel of metastatic cancer cells,” *Cell cycle*, vol. 14, no. 4, pp. 502–509, 2015.
- [126] E. Babiychuk, K. Monastyrskaya, S. Potez, and A. Draeger, “Blebbing confers resistance against cell lysis,” *Cell Death & Differentiation*, vol. 18, no. 1, pp. 80–89, 2011.
- [127] Y.-C. Lin, C. Chipot, and S. Scheuring, “Annexin-V stabilizes membrane defects by inducing lipid phase transition,” *Nature communications*, vol. 11, no. 1, pp. 1–13, 2020.
- [128] A. Bouter, C. Gounou, R. Bérat, S. Tan, B. Gallois, T. Granier, B. L. d’Estaintot, E. Pöschl, B. Brachvogel, and A. R. Brisson, “Annexin-A5 assembled into two-dimensional arrays promotes cell membrane repair,” *Nature communications*, vol. 2, no. 1, pp. 1–9, 2011.
- [129] C. D. Florentsen, A. Kamp-Sonne, G. Moreno-Pescador, W. Pezeshkian, A. A. H. Zanjani, H. Khandelia, J. Nylandsted, and P. M. Bendix, “Annexin A4 trimers are recruited by high membrane curvatures in giant plasma membrane vesicles,” *Soft matter*, vol. 17, no. 2, pp. 308–318, 2021.
- [130] A. C. Simonsen and L. A. Bagatolli, “Structure of spin-coated lipid films and domain formation in supported membranes formed by hydration,” *Langmuir*, vol. 20, no. 22, pp. 9720–9728, 2004.
- [131] T. L. Boye, J. C. Jeppesen, K. Maeda, W. Pezeshkian, V. Solovyeva, J. Nylandsted, and A. C. Simonsen, “Annexins induce curvature on free-edge membranes displaying distinct morphologies,” *Scientific Reports*, vol. 8, no. 1, pp. 1–14, 2018.
- [132] A. Miyagi, C. Chipot, M. Rangl, and S. Scheuring, “High-speed atomic force microscopy shows that annexin V stabilizes membranes on the second timescale,” *Nature nanotechnology*, vol. 11, no. 9, pp. 783–790, 2016.
- [133] M. Menke, M. Ross, V. Gerke, and C. Steinem, “The molecular arrangement of membrane-bound annexin A2-s100A10 tetramer as revealed by scanning force microscopy,” *Chembiochem*, vol. 5, no. 7, pp. 1003–1006, 2004.
- [134] G. Moreno-Pescador, I. Qoqaj, V. T. Ruhoff, J. F. Iversen, J. Nylandsted, and P. M. Bendix, “Effect of local thermoplasmonic heating on biological membranes,” in *Optical Trapping and Optical Micromanipulation XVI*, vol. 11083, pp. 24–34, SPIE, 2019.

- [135] G. Baffou, J. Polleux, H. Rigneault, and S. Monneret, “Super-heating and micro-bubble generation around plasmonic nanoparticles under cw illumination,” *The Journal of Physical Chemistry C*, vol. 118, no. 9, pp. 4890–4898, 2014.
- [136] K. Sasikumar, Z. Liang, D. G. Cahill, and P. Keblinski, “Curvature induced phase stability of an intensely heated liquid,” *The Journal of Chemical Physics*, vol. 140, no. 23, p. 234506, 2014.
- [137] L. Bendall and D. Green, “Autopsy of a cell,” *Leukemia*, vol. 28, no. 6, pp. 1341–1343, 2014.
- [138] Y. Niko, P. Didier, Y. Mely, G.-i. Konishi, and A. S. Klymchenko, “Bright and photostable push-pull pyrene dye visualizes lipid order variation between plasma and intracellular membranes,” *Scientific reports*, vol. 6, no. 1, pp. 1–9, 2016.
- [139] S. Li, T. Zhang, Z. Zhu, N. Gao, and Q.-H. Xu, “Lighting up the gold nanoparticles quenched fluorescence by silver nanoparticles: a separation distance study,” *RSC advances*, vol. 6, no. 63, pp. 58566–58572, 2016.
- [140] C. Zhang, M.-S. Liu, and X.-H. Xing, “Temperature influence on fluorescence intensity and enzyme activity of the fusion protein of gfp and hyperthermophilic xylanase,” *Applied microbiology and biotechnology*, vol. 84, pp. 511–517, 2009.
- [141] F. Bouvet, M. Ros, E. Bonedeau, C. Croissant, L. Frelin, F. Saltel, V. Moreau, and A. Bouter, “Defective membrane repair machinery impairs survival of invasive cancer cells,” *Scientific Reports*, vol. 10, no. 1, pp. 1–16, 2020.
- [142] S. Nakielny, S. Shaikh, B. Burke, and G. Dreyfuss, “Nup153 is an m9-containing mobile nucleoporin with a novel ran-binding domain,” *The EMBO Journal*, vol. 18, no. 7, pp. 1982–1995, 1999.
- [143] A. Raffaello, C. Mammucari, G. Gherardi, and R. Rizzuto, “Calcium at the center of cell signaling: interplay between endoplasmic reticulum, mitochondria, and lysosomes,” *Trends in biochemical sciences*, vol. 41, no. 12, pp. 1035–1049, 2016.
- [144] M. Menke, V. Gerke, and C. Steinem, “Phosphatidylserine membrane domain clustering induced by annexin a2/s100a10 heterotetramer,” *Biochemistry*, vol. 44, no. 46, pp. 15296–15303, 2005.
- [145] E. Morel and J. Gruenberg, “The p11/s100a10 light chain of annexin a2 is dispensable for annexin a2 association to endosomes and functions in endosomal transport,” *PLoS One*, vol. 2, no. 10, p. e1118, 2007.
- [146] U. Rescher, D. Ruhe, C. Ludwig, N. Zobiack, and V. Gerke, “Annexin 2 is a phosphatidylinositol (4, 5)-bisphosphate binding protein recruited to actin assembly sites at cellular membranes,” *Journal of cell science*, vol. 117, no. 16, pp. 3473–3480, 2004.
- [147] E. Morel, R. G. Parton, and J. Gruenberg, “Annexin a2-dependent polymerization of actin mediates endosome biogenesis,” *Developmental cell*, vol. 16, no. 3, pp. 445–457, 2009.
- [148] A. Torchi, F. Simonelli, R. Ferrando, and G. Rossi, “Local enhancement of lipid membrane permeability induced by irradiated gold nanoparticles,” *ACS nano*, vol. 11, no. 12, pp. 12553–12561, 2017.
- [149] R. Xiong, K. Raemdonck, K. Peynshaert, I. Lentacker, I. De Cock, J. Demeester, S. C. De Smedt, A. G. Skirtach, and K. Braeckmans, “Comparison of gold nanoparticle mediated photoporation: vapor nanobubbles outperform direct heating for delivering macromolecules in live cells,” *ACS nano*, vol. 8, no. 6, pp. 6288–6296, 2014.
- [150] D. V. Köster and S. Mayor, “Cortical actin and the plasma membrane: inextricably intertwined,” *Current opinion in cell biology*, vol. 38, pp. 81–89, 2016.

- [151] D. Goddette and C. Frieden, “Actin polymerization. the mechanism of action of cytochalasin d.,” *Journal of Biological Chemistry*, vol. 261, no. 34, pp. 15974–15980, 1986.
- [152] X. Shao, Q. Li, A. Mogilner, A. D. Bershadsky, and G. Shivashankar, “Mechanical stimulation induces formin-dependent assembly of a perinuclear actin rim,” *Proceedings of the National Academy of Sciences*, vol. 112, no. 20, pp. E2595–E2601, 2015.
- [153] J.-Y. Tinevez, U. Schulze, G. Salbreux, J. Roensch, J.-F. Joanny, and E. Paluch, “Role of cortical tension in bleb growth,” *Proceedings of the National Academy of Sciences*, vol. 106, no. 44, pp. 18581–18586, 2009.
- [154] G. T. Charras, C.-K. Hu, M. Coughlin, and T. J. Mitchison, “Reassembly of contractile actin cortex in cell blebs,” *The Journal of cell biology*, vol. 175, no. 3, pp. 477–490, 2006.
- [155] G. Charras and E. Paluch, “Blebs lead the way: how to migrate without lamellipodia,” *Nature reviews Molecular cell biology*, vol. 9, no. 9, pp. 730–736, 2008.
- [156] A. Bharadwaj, M. Bydoun, R. Holloway, and D. Waisman, “Annexin a2 heterotetramer: structure and function,” *International journal of molecular sciences*, vol. 14, no. 3, pp. 6259–6305, 2013.
- [157] O. Lambert, V. Gerke, M.-F. Bader, F. Porte, and A. Brisson, “Structural analysis of junctions formed between lipid membranes and several annexins by cryo-electron microscopy,” *Journal of molecular biology*, vol. 272, no. 1, pp. 42–55, 1997.
- [158] O. Lambert, N. Cavusoglu, J. Gallay, M. Vincent, J. L. Rigaud, J.-P. Henry, and J. Ayala-Sanmartin, “Novel organization and properties of annexin 2-membrane complexes,” *Journal of Biological Chemistry*, vol. 279, no. 12, pp. 10872–10882, 2004.
- [159] D. Hakobyan, V. Gerke, and A. Heuer, “Modeling of annexin a2—membrane interactions by molecular dynamics simulations,” *PloS one*, vol. 12, no. 9, p. e0185440, 2017.
- [160] A. V. Harrist, E. V. Ryzhova, T. Harvey, and F. Gonzalez-Scarano, “Anx2 interacts with hiv-1 gag at phosphatidylinositol (4, 5) bisphosphate-containing lipid rafts and increases viral production in 293t cells,” *PLoS One*, vol. 4, no. 3, p. e5020, 2009.
- [161] K. Sandvig and A. Llorente, “Proteomic analysis of microvesicles released by the human prostate cancer cell line pc-3,” *Molecular & Cellular Proteomics*, vol. 11, no. 7, pp. M111–012914, 2012.
- [162] M. B. Klenow, A. S. B. Heitmann, J. Nylandsted, and A. C. Simonsen, “Timescale of hole closure during plasma membrane repair estimated by calcium imaging and numerical modeling,” *Scientific Reports*, vol. 11, no. 1, pp. 1–12, 2021.
- [163] T.-W. Chen, T. J. Wardill, Y. Sun, S. R. Pulver, S. L. Renninger, A. Baohan, E. R. Schreier, R. A. Kerr, M. B. Orger, V. Jayaraman, *et al.*, “Ultrasensitive fluorescent proteins for imaging neuronal activity,” *Nature*, vol. 499, no. 7458, pp. 295–300, 2013.
- [164] F.-C. Tsai, A. Seki, H. W. Yang, A. Hayer, S. Carrasco, S. Malmersjö, and T. Meyer, “A polarized ca²⁺, diacylglycerol and stim1 signalling system regulates directed cell migration,” *Nature cell biology*, vol. 16, no. 2, pp. 133–144, 2014.
- [165] R. Bagur and G. Hajnóczky, “Intracellular ca²⁺ sensing: its role in calcium homeostasis and signaling,” *Molecular cell*, vol. 66, no. 6, pp. 780–788, 2017.
- [166] A. Samadi, P. M. Bendix, and L. B. Oddershede, “Optical manipulation of individual strongly absorbing platinum nanoparticles,” *Nanoscale*, vol. 9, no. 46, pp. 18449–18455, 2017.
- [167] H. Klingberg, L. B. Oddershede, K. Loeschner, E. H. Larsen, S. Loft, and P. Møller, “Uptake of gold nanoparticles in primary human endothelial cells,” *Toxicology Research*, vol. 4, no. 3, pp. 655–666, 2015.

- [168] M. Raab, M. Gentili, H. de Belly, H.-R. Thiam, P. Vargas, A. J. Jimenez, F. Lautenschlaeger, R. Voituriez, A.-M. Lennon-Duménil, N. Manel, *et al.*, “Escrt iii repairs nuclear envelope ruptures during cell migration to limit dna damage and cell death,” *Science*, vol. 352, no. 6283, pp. 359–362, 2016.
- [169] P. M. Davidson and B. Cadot, “Actin on and around the nucleus,” *Trends in Cell Biology*, vol. 31, no. 3, pp. 211–223, 2021.
- [170] L. K. Srivastava, Z. Ju, A. Ghagre, and A. J. Ehrlicher, “Spatial distribution of lamin a/c determines nuclear stiffness and stress-mediated deformation,” *Journal of cell science*, vol. 134, no. 10, p. jcs248559, 2021.
- [171] J. Lu, T. Wu, B. Zhang, S. Liu, W. Song, J. Qiao, and H. Ruan, “Types of nuclear localization signals and mechanisms of protein import into the nucleus,” *Cell communication and signaling*, vol. 19, no. 1, pp. 1–10, 2021.
- [172] E. C. Schirmer and L. Gerace, “Organelar proteomics: the prizes and pitfalls of opening the nuclear envelope,” *Genome biology*, vol. 3, no. 4, pp. 1–4, 2002.
- [173] C. Smythe, H. E. Jenkins, and C. J. Hutchison, “Incorporation of the nuclear pore basket protein nup153 into nuclear pore structures is dependent upon lamina assembly: evidence from cell-free extracts of xenopus eggs,” *The EMBO journal*, vol. 19, no. 15, pp. 3918–3931, 2000.
- [174] J. Lammerding, “Mechanics of the nucleus,” *Comprehensive physiology*, vol. 1, no. 2, p. 783, 2011.
- [175] B. E. White, M. K. White, Z. A. Nima Alsudani, F. Watanabe, A. S. Biris, and N. Ali, “Cellular uptake of gold nanorods in breast cancer cell lines,” *Nanomaterials*, vol. 12, no. 6, p. 937, 2022.
- [176] D. Chen, N. A. Monteiro-Riviere, and L. W. Zhang, “Intracellular imaging of quantum dots, gold, and iron oxide nanoparticles with associated endocytic pathways,” *Wiley Interdisciplinary Reviews: Nanomedicine and Nanobiotechnology*, vol. 9, no. 2, p. e1419, 2017.
- [177] R. Shukla, V. Bansal, M. Chaudhary, A. Basu, R. R. Bhonde, and M. Sastry, “Biocompatibility of gold nanoparticles and their endocytotic fate inside the cellular compartment: a microscopic overview,” *Langmuir*, vol. 21, no. 23, pp. 10644–10654, 2005.
- [178] A. M. Alkilany and C. J. Murphy, “Toxicity and cellular uptake of gold nanoparticles: what we have learned so far?,” *Journal of nanoparticle research*, vol. 12, pp. 2313–2333, 2010.
- [179] J. Gruenberg, “The endocytic pathway: a mosaic of domains,” *Nature reviews Molecular cell biology*, vol. 2, no. 10, pp. 721–730, 2001.
- [180] L. A. Dykman and N. G. Khlebtsov, “Uptake of engineered gold nanoparticles into mammalian cells,” *Chemical reviews*, vol. 114, no. 2, pp. 1258–1288, 2014.
- [181] C. Freese, M. I. Gibson, H.-A. Klok, R. E. Unger, and C. J. Kirkpatrick, “Size-and coating-dependent uptake of polymer-coated gold nanoparticles in primary human dermal microvascular endothelial cells,” *Biomacromolecules*, vol. 13, no. 5, pp. 1533–1543, 2012.
- [182] S.-H. Wang, C.-W. Lee, A. Chiou, and P.-K. Wei, “Size-dependent endocytosis of gold nanoparticles studied by three-dimensional mapping of plasmonic scattering images,” *Journal of nanobiotechnology*, vol. 8, pp. 1–13, 2010.
- [183] H. T. McMahon and E. Boucrot, “Molecular mechanism and physiological functions of clathrin-mediated endocytosis,” *Nature reviews Molecular cell biology*, vol. 12, no. 8, pp. 517–533, 2011.
- [184] J. Lopez-Andarias, J. Saarbach, D. Moreau, Y. Cheng, E. Derivery, Q. Laurent, M. Gonzalez-Gaitan, N. Winssinger, N. Sakai, and S. Matile, “Cell-penetrating streptavidin: a general tool for bifunctional delivery with spatiotemporal control, mediated by transport systems such as adaptive benzopolysulfane networks,” *Journal of the American Chemical Society*, vol. 142, no. 10, pp. 4784–4792, 2020.

- [185] R. L. Mellgren, “A plasma membrane wound proteome: reversible externalization of intracellular proteins following reparable mechanical damage,” *Journal of Biological Chemistry*, vol. 285, no. 47, pp. 36597–36607, 2010.
- [186] A. Livne, E. Bouchbinder, and B. Geiger, “Cell reorientation under cyclic stretching,” *Nature communications*, vol. 5, no. 1, p. 3938, 2014.
- [187] N. X. Chen, K. D. Ryder, F. M. Pavalko, C. H. Turner, D. B. Burr, J. Qiu, and R. L. Duncan, “Ca²⁺ regulates fluid shear-induced cytoskeletal reorganization and gene expression in osteoblasts,” *American Journal of Physiology-Cell Physiology*, vol. 278, no. 5, pp. C989–C997, 2000.
- [188] E. Tzima, M. Irani-Tehrani, W. B. Kiosses, E. Dejana, D. A. Schultz, B. Engelhardt, G. Cao, H. DeLisser, and M. A. Schwartz, “A mechanosensory complex that mediates the endothelial cell response to fluid shear stress,” *Nature*, vol. 437, no. 7057, pp. 426–431, 2005.
- [189] P. Wales, C. E. Schuberth, R. Aufschnaiter, J. Fels, I. García-Aguilar, A. Janning, C. P. Dlugos, M. Schäfer-Herte, C. Klingner, M. Wälte, *et al.*, “Calcium-mediated actin reset (caar) mediates acute cell adaptations,” *Elife*, vol. 5, p. e19850, 2016.
- [190] K. Ohashi, S. Fujiwara, and K. Mizuno, “Roles of the cytoskeleton, cell adhesion and rho signalling in mechanosensing and mechanotransduction,” *The journal of biochemistry*, vol. 161, no. 3, pp. 245–254, 2017.
- [191] W. C. Ruder, E. D. Pratt, N. Z. Brandy, D. A. LaVan, P. R. LeDuc, and J. F. Antaki, “Calcium signaling is gated by a mechanical threshold in three-dimensional environments,” *Scientific reports*, vol. 2, no. 1, pp. 1–6, 2012.
- [192] S. Munevar, Y.-l. Wang, and M. Dembo, “Regulation of mechanical interactions between fibroblasts and the substratum by stretch-activated ca²⁺ entry,” *Journal of cell science*, vol. 117, no. 1, pp. 85–92, 2004.
- [193] B. Coste, B. Xiao, J. S. Santos, R. Syeda, J. Grandl, K. S. Spencer, S. E. Kim, M. Schmidt, J. Mathur, A. E. Dubin, *et al.*, “Piezo proteins are pore-forming subunits of mechanically activated channels,” *Nature*, vol. 483, no. 7388, pp. 176–181, 2012.
- [194] S. Samtleben, J. Jaepel, C. Fecher, T. Andreska, M. Rehberg, and R. Blum, “Direct imaging of er calcium with targeted-esterase induced dye loading (ted),” *Journal of visualized experiments: JoVE*, no. 75, 2013.
- [195] A.-s. Kone, S. Ait Ssi, S. Sahraoui, and A. Badou, “Btn3a: A promising immune checkpoint for cancer prognosis and treatment,” *International Journal of Molecular Sciences*, vol. 23, no. 21, p. 13424, 2022.
- [196] J. S. Marshall, R. Warrington, W. Watson, and H. L. Kim, “An introduction to immunology and immunopathology,” *Allergy, Asthma & Clinical Immunology*, vol. 14, no. 2, pp. 1–10, 2018.
- [197] P. Parham, “The immune system, 4th edn. garland science,” 2014.
- [198] L. D. Notarangelo, “Primary immunodeficiencies,” *Journal of Allergy and Clinical Immunology*, vol. 125, no. 2, pp. S182–S194, 2010.
- [199] J. Chinen and W. T. Shearer, “Secondary immunodeficiencies, including hiv infection,” *Journal of Allergy and Clinical Immunology*, vol. 125, no. 2, pp. S195–S203, 2010.
- [200] V. Kumar, A. K. Abbas, and J. C. Aster, *Robbins basic pathology e-book*. Elsevier Health Sciences, 2017.

- [201] J. M. Boulter, M. Glick, P. T. Todorov, E. Baston, M. Sami, P. Rizkallah, and B. K. Jakobsen, “Stable, soluble t-cell receptor molecules for crystallization and therapeutics,” *Protein engineering*, vol. 16, no. 9, pp. 707–711, 2003.
- [202] D. J. Hicklin, F. M. Marincola, and S. Ferrone, “Hla class i antigen downregulation in human cancers: T-cell immunotherapy revives an old story,” *Molecular medicine today*, vol. 5, no. 4, pp. 178–186, 1999.
- [203] R. C. Sterner and R. M. Sterner, “Car-t cell therapy: current limitations and potential strategies,” *Blood cancer journal*, vol. 11, no. 4, p. 69, 2021.
- [204] B. Silva-Santos, K. Serre, and H. Norell, “ $\gamma\delta$ t cells in cancer,” *Nature reviews immunology*, vol. 15, no. 11, pp. 683–691, 2015.
- [205] J.-L. Blazquez, A. Benyamine, C. Pasero, and D. Olive, “New insights into the regulation of $\gamma\delta$ t cells by btn3a and other btn/btnl in tumor immunity,” *Frontiers in immunology*, vol. 9, p. 1601, 2018.
- [206] A. Morath and W. W. Schamel, “ $\alpha\beta$ and $\gamma\delta$ t cell receptors: Similar but different,” *Journal of leukocyte biology*, vol. 107, no. 6, pp. 1045–1055, 2020.
- [207] H.-J. Gober, M. Kistowska, L. Angman, P. Jenö, L. Mori, and G. De Libero, “Human t cell receptor $\gamma\delta$ cells recognize endogenous mevalonate metabolites in tumor cells,” *The Journal of experimental medicine*, vol. 197, no. 2, pp. 163–168, 2003.
- [208] C. Harly, Y. Guillaume, S. Nedellec, C.-M. Peigné, H. Mönkkönen, J. Mönkkönen, J. Li, J. Kuball, E. J. Adams, S. Netzer, *et al.*, “Key implication of cd277/butyrophilin-3 (btn3a) in cellular stress sensing by a major human $\gamma\delta$ t-cell subset,” *Blood, The Journal of the American Society of Hematology*, vol. 120, no. 11, pp. 2269–2279, 2012.
- [209] J. H. Park and H. K. Lee, “Function of $\gamma\delta$ t cells in tumor immunology and their application to cancer therapy,” *Experimental & Molecular Medicine*, vol. 53, no. 3, pp. 318–327, 2021.
- [210] Y. h. Chien and M. Bonneville, “Gamma delta t cell receptors,” *Cellular and Molecular Life Sciences CMLS*, vol. 63, pp. 2089–2094, 2006.
- [211] Z. Sebestyén, I. Prinz, J. Déchanet-Merville, B. Silva-Santos, and J. Kuball, “Translating gammadelta ($\gamma\delta$) t cells and their receptors into cancer cell therapies,” *Nature reviews Drug discovery*, vol. 19, no. 3, pp. 169–184, 2020.
- [212] P. F. Céspedes, D. Beckers, M. L. Dustin, and E. Sezgin, “Model membrane systems to reconstitute immune cell signaling,” *The FEBS Journal*, vol. 288, no. 4, pp. 1070–1090, 2021.
- [213] A. Grakoui, S. K. Bromley, C. Sumen, M. M. Davis, A. S. Shaw, P. M. Allen, and M. L. Dustin, “The immunological synapse: a molecular machine controlling t cell activation,” *Science*, vol. 285, no. 5425, pp. 221–227, 1999.
- [214] D. K. Das, Y. Feng, R. J. Mallis, X. Li, D. B. Keskin, R. E. Hussey, S. K. Brady, J.-H. Wang, G. Wagner, E. L. Reinherz, *et al.*, “Force-dependent transition in the t-cell receptor β -subunit allosterically regulates peptide discrimination and pmhc bond lifetime,” *Proceedings of the National Academy of Sciences*, vol. 112, no. 5, pp. 1517–1522, 2015.
- [215] B. Liu, W. Chen, B. D. Evavold, and C. Zhu, “Accumulation of dynamic catch bonds between tcr and agonist peptide-mhc triggers t cell signaling,” *Cell*, vol. 157, no. 2, pp. 357–368, 2014.
- [216] M. M. Karunakaran, C. R. Willcox, M. Salim, D. Paletta, A. S. Fichtner, A. Noll, L. Starick, A. Nöhren, C. R. Begley, K. A. Berwick, *et al.*, “Butyrophilin-2a1 directly binds germline-encoded regions of the v γ 9v δ 2 tcr and is essential for phosphoantigen sensing,” *Immunity*, vol. 52, no. 3, pp. 487–498, 2020.

- [217] M. Rigau, S. Ostrouska, T. S. Fulford, D. N. Johnson, K. Woods, Z. Ruan, H. E. McWilliam, C. Hudson, C. Tutuka, A. K. Wheatley, *et al.*, “Butyrophilin 2a1 is essential for phosphoantigen reactivity by $\gamma\delta$ t cells,” *Science*, vol. 367, no. 6478, p. eaay5516, 2020.
- [218] L. Boutin and E. Scotet, “Towards deciphering the hidden mechanisms that contribute to the antigenic activation process of human $v\gamma9v\delta2$ t cells,” *Frontiers in immunology*, vol. 9, p. 828, 2018.
- [219] R. A. Mariuzza, P. Agnihotri, and J. Orban, “The structural basis of t-cell receptor (tcr) activation: An enduring enigma,” *Journal of Biological Chemistry*, vol. 295, no. 4, pp. 914–925, 2020.
- [220] M. Hoth and R. Penner, “Depletion of intracellular calcium stores activates a calcium current in mast cells,” *Nature*, vol. 355, no. 6358, pp. 353–356, 1992.
- [221] A. Zweifach and R. S. Lewis, “Mitogen-regulated ca^{2+} current of t lymphocytes is activated by depletion of intracellular ca^{2+} stores.” *Proceedings of the National Academy of Sciences*, vol. 90, no. 13, pp. 6295–6299, 1993.
- [222] E. Sezgin, “Giant plasma membrane vesicles to study plasma membrane structure and dynamics,” *Biochimica et Biophysica Acta (BBA)-Biomembranes*, p. 183857, 2022.
- [223] P.-C. Chiang, K. Tanady, L.-T. Huang, and L. Chao, “Rupturing giant plasma membrane vesicles to form micron-sized supported cell plasma membranes with native transmembrane proteins,” *Scientific reports*, vol. 7, no. 1, p. 15139, 2017.
- [224] P.-Y. Peng, P.-C. Chiang, and L. Chao, “Mobile lipid bilayers on gold surfaces through structure-induced lipid vesicle rupture,” *Langmuir*, vol. 31, no. 13, pp. 3904–3911, 2015.
- [225] H. Pace, L. Simonsson Nystrom, A. Gunnarsson, E. Eck, C. Monson, S. Geschwindner, A. Snijder, and F. Hook, “Preserved transmembrane protein mobility in polymer-supported lipid bilayers derived from cell membranes,” *Analytical chemistry*, vol. 87, no. 18, pp. 9194–9203, 2015.
- [226] Y. Kaizuka, A. D. Douglass, R. Varma, M. L. Dustin, and R. D. Vale, “Mechanisms for segregating t cell receptor and adhesion molecules during immunological synapse formation in jurkat t cells,” *Proceedings of the National Academy of Sciences*, vol. 104, no. 51, pp. 20296–20301, 2007.
- [227] V. Marcu-Malina, S. Heijhuurs, M. van Buuren, L. Hartkamp, S. Strand, Z. Sebestyen, K. Scholten, A. Martens, and J. Kuball, “Redirecting $\alpha\beta$ t cells against cancer cells by transfer of a broadly tumor-reactive $\gamma\delta$ t-cell receptor,” *Blood, The Journal of the American Society of Hematology*, vol. 118, no. 1, pp. 50–59, 2011.
- [228] A. Vyborova, D. X. Beringer, D. Fasci, F. Karaiskaki, E. van Diest, L. Kramer, A. de Haas, J. Sanders, A. Janssen, T. Straetemans, *et al.*, “ $\gamma9\delta2$ t cell diversity and the receptor interface with tumor cells,” *The Journal of clinical investigation*, vol. 130, no. 9, pp. 4637–4651, 2020.
- [229] A. Palakodeti, A. Sandstrom, L. Sundaresan, C. Harly, S. Nedellec, D. Olive, E. Scotet, M. Bonneville, and E. J. Adams, “The molecular basis for modulation of human $v\gamma9v\delta2$ t cell responses by cd277/butyrophilin-3 (btn3a)-specific antibodies,” *Journal of Biological Chemistry*, vol. 287, no. 39, pp. 32780–32790, 2012.
- [230] A. F. Pegoraro, P. Janmey, and D. A. Weitz, “Mechanical properties of the cytoskeleton and cells,” *Cold Spring Harbor perspectives in biology*, vol. 9, no. 11, p. a022038, 2017.
- [231] S. J. Heasman and A. J. Ridley, “Multiple roles for rhoa during t cell transendothelial migration,” *Small GTPases*, vol. 1, no. 3, pp. 553–563, 2010.
- [232] L. Blanchoin, R. Boujemaa-Paterski, C. Sykes, and J. Plastino, “Actin dynamics, architecture, and mechanics in cell motility,” *Physiological reviews*, vol. 94, no. 1, pp. 235–263, 2014.

- [233] D. Ershov, M.-S. Phan, J. W. Pylvänäinen, S. U. Rigaud, L. Le Blanc, A. Charles-Orszag, J. R. Conway, R. F. Laine, N. H. Roy, D. Bonazzi, *et al.*, “Trackmate 7: integrating state-of-the-art segmentation algorithms into tracking pipelines,” *Nature methods*, vol. 19, no. 7, pp. 829–832, 2022.
- [234] A. K. Efremov, M. Yao, Y. Sun, Y. H. Tee, M. P. Sheetz, A. D. Bershadsky, B. Martinac, and J. Yan, “Application of piconewton forces to individual filopodia reveals mechanosensory role of l-type ca²⁺ channels,” *Biomaterials*, vol. 284, p. 121477, 2022.
- [235] H. P. Pace, J. K. Hannestad, A. Armonious, M. Adamo, B. Agnarsson, A. Gunnarsson, S. Micciulla, P. Sjøvall, Y. Gerelli, and F. Hook, “Structure and composition of native membrane derived polymer-supported lipid bilayers,” *Analytical chemistry*, vol. 90, no. 21, pp. 13065–13072, 2018.
- [236] P. F. Cespedes and M. L. Dustin, “Preparation of bead-supported lipid bilayers to study the particulate output of t cell immune synapses.,” *Journal of Visualized Experiments: Jove*, no. 182, 2022.

Appendices

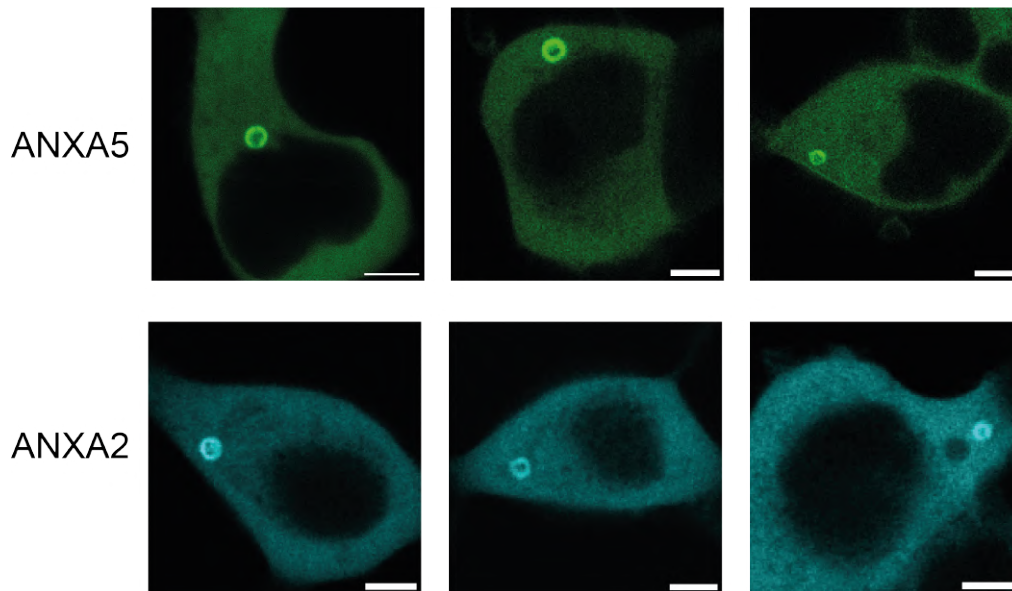
Annexins and Plasma Membrane disruption (Chapter 3)**ANXA5 and ANXA2 ring structures upon plasma membrane disruption**

Figure A.1: Confocal images of HEK293T cells transfected with either ANXA5 or ANXA2 depict plasma membrane injuries surrounded by ANXA rings. The scale bars measure 5 μm .

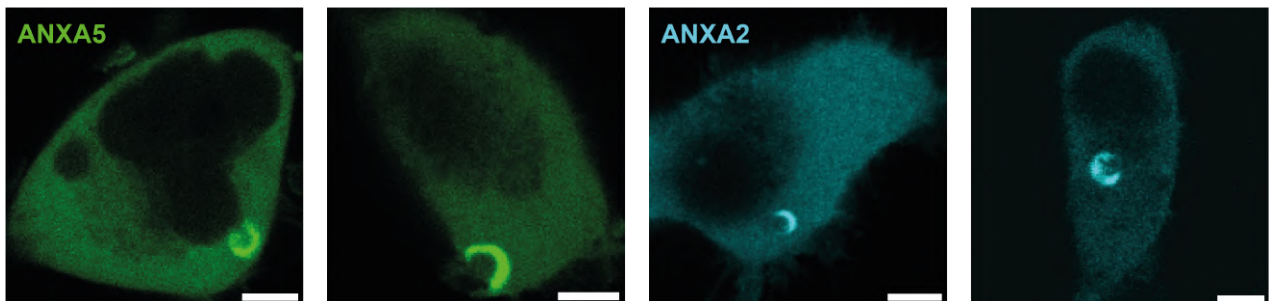


Figure A.2: Confocal images of HEK293T cells transfected with either ANXA5 or ANXA2 depict plasma membrane injuries surrounded by fractions of ANXA rings. The scale bars measure 5 μm .

ANXA5 and ANXA4 response in GUVs

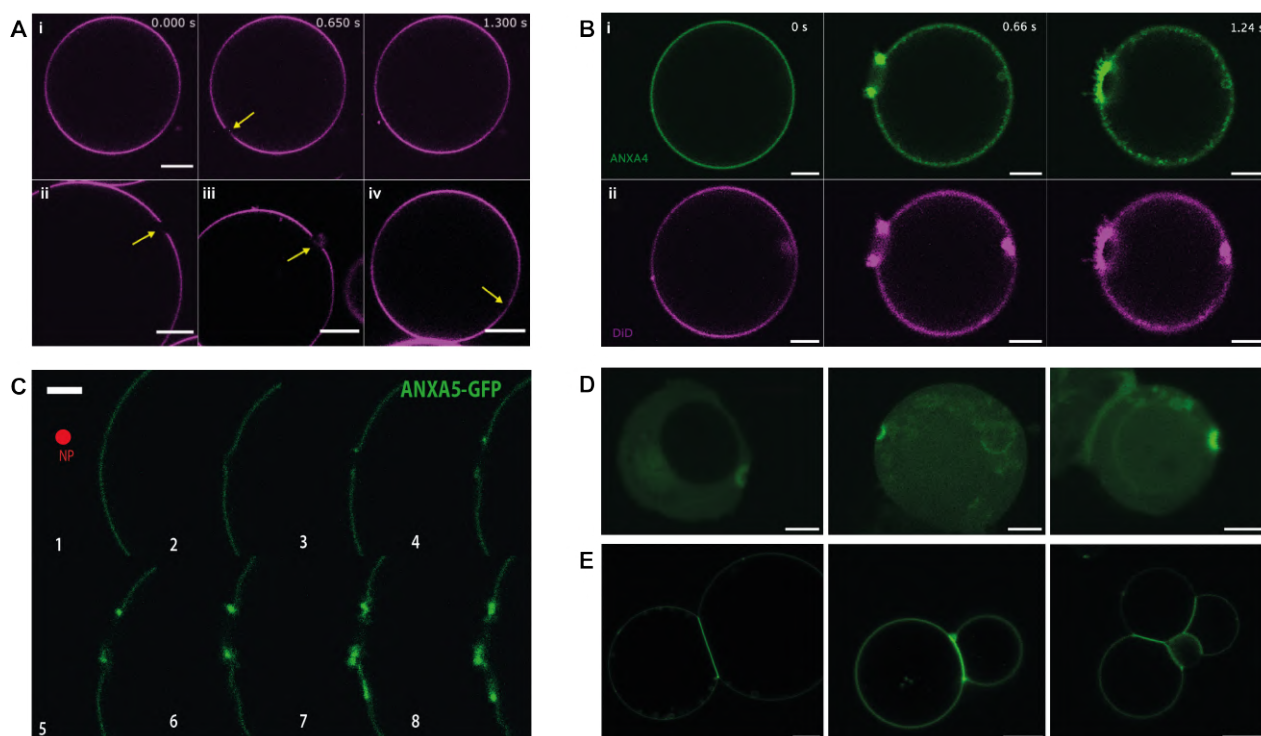


Figure A.3: Confocal images showcase plasmonic membrane rupture and its associated phenomena. (A) GUV control experiments with the PM labeled with DiD. In the absence of ANXA, no rolling or ring-like structures were observed. The yellow arrows denote thermoplasmonic-induced puncture sites. (i) Time sequence of a GUV membrane puncture and subsequent repair, along with (ii-iv) individual GUV punctures. All scale bars measure $10 \mu\text{m}$. (B) The GUV was punctured and monitored over time. (i) Encapsulated ANXA4 was observed bound to the membrane, forming a ring structure at the injury site. (ii) The membrane was also labeled with DiD and the scale bars measure $5 \mu\text{m}$. (C) ANXA5 response upon GUV rupture was imaged over time, illustrating membrane rolling. The scale bar measures $5 \mu\text{m}$. (D) Three individual HEK293T cells expressing ANXA5 were injured from the side. All scale bars measure $5 \mu\text{m}$. (E) ANXA5 mediated vesicle aggregation. Purified ANXA5 was added to the solution, causing strong binding of GUVs. The scale bars measure $10 \mu\text{m}$. All figures were adapted from Moreno et al.[54].

ANXA2 filled vesicles protrude from the injury site

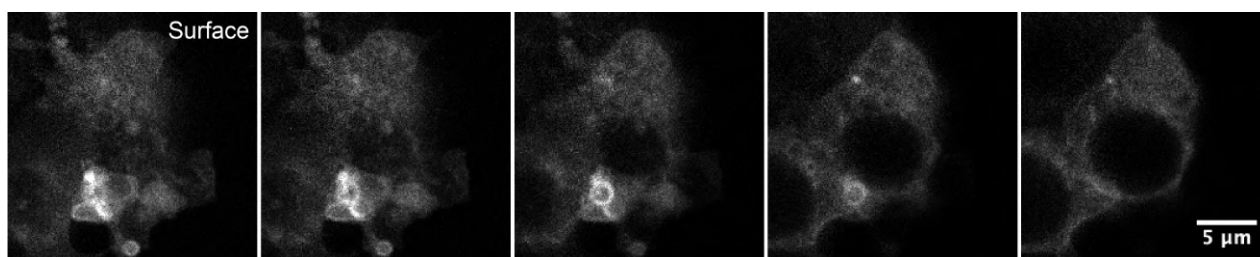


Figure A.4: Actin-intact HEK293T cell expressing ANXA2. The confocal images are obtained as a z-stack captured from the cell surface into the cytosol. ANXA2-filled blebs are observed to bud outwards from the injury site, as they are only observed at the surface.

Actin and Nuclear Envelope disruption (Chapter 4)

Fluorescent-tag control experiment

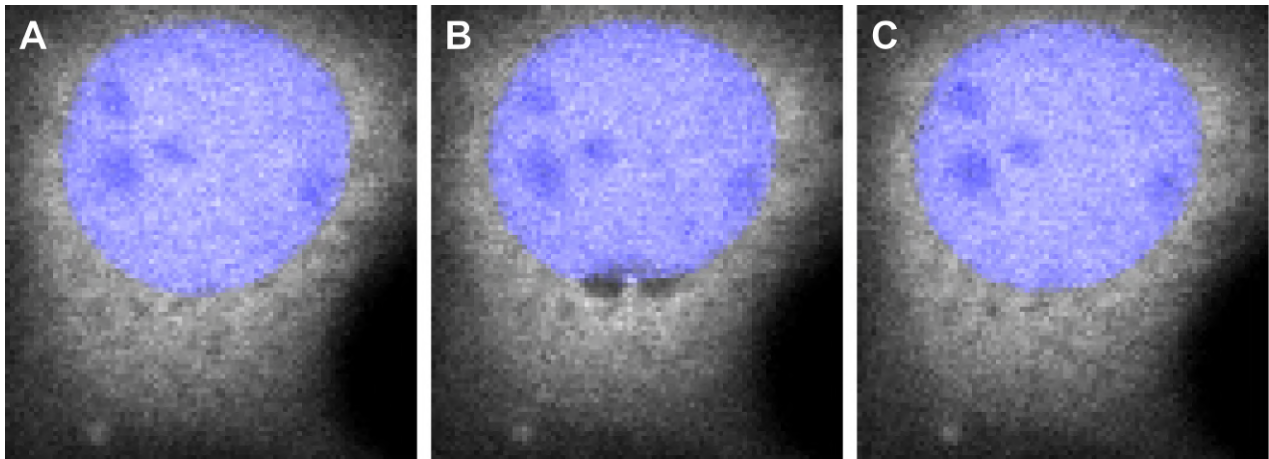


Figure A.5: Control for interaction between fluorescent molecules (RFP) and a thermoplasmonically induced nanobubble. The confocal images illustrate a MCF7 cell expressing cytosolic RFP and NLS (blue) in the nucleus. To investigate whether the observed actin response occurs independently of the fluorescent coupled protein, an empty-RFP vector was used instead of actin-RFP, as a control. (A) Prior to irradiation, RFP is uniformly distributed throughout the cell. (B) Subsequent to irradiation, the RFP fluorophore is quenched at the irradiation site. (C) Following irradiation, the RFP signal appears evenly distributed throughout the cell, without any accumulation at other locations.

Synapse formation and T-cell activation (Chapter 5)

The behavior of T-cell in the absence and presence of tumor cells

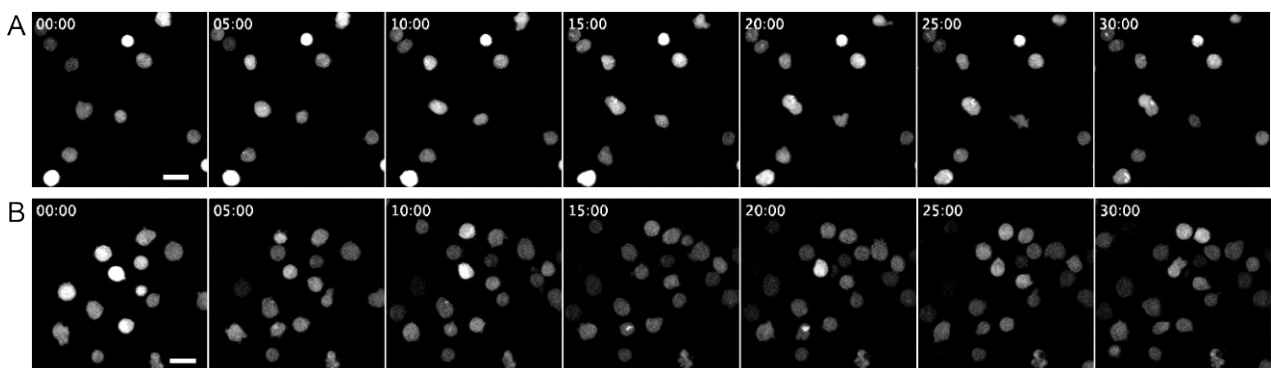


Figure A.6: The behavior of CL5 T-cell in the absence (A) and presence (B) of tumor cells was observed through confocal imaging. (A) The T-cells showed a stable cytosolic Ca^{2+} signal, minimal movement, and interaction in the absence of tumor cells. However, (B) in the presence of tumor cells, the T-cells exhibited an increase in movement, searching capacity, and interaction with neighboring cells, observed as Ca^{2+} intensity fluctuations. The scale bars measure $20 \mu\text{m}$.

The speculated cytotoxic attribute of T-cells

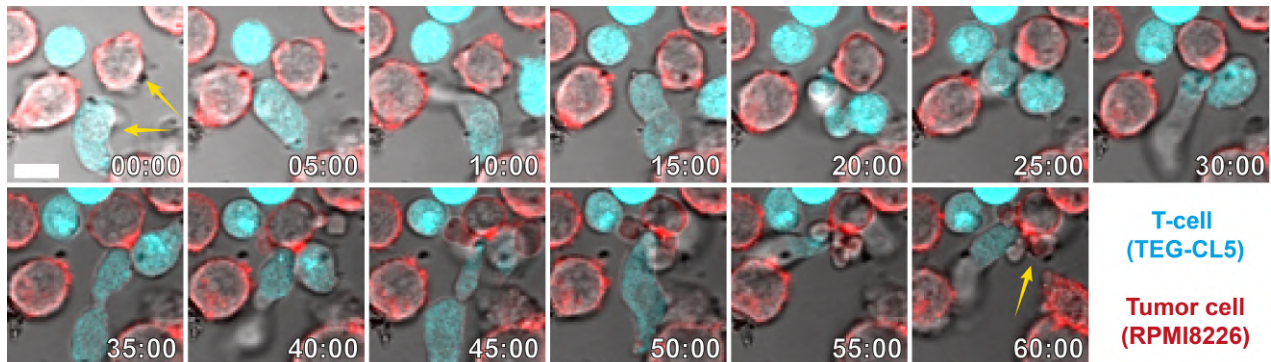






Figure A.7: The confocal images depict the proposed cytotoxic attribute of CL5 T-cells as they interact with a tumor cell. The two cells, denoted by the yellow arrows, were of particular interest. The T-cell was observed to undergo extensive deformation as it interacted with the tumor cell. Furthermore, the T-cell was activated, indicated by the formation of immunological synapses with the tumor cell (25min), and additional T-cell recruitment to the tumor cell of interest. Ultimately, this led to tumor cell lysis, which was observed as extensive tumor cell blebbing, particularly at the contact site (45-60 min). The scale bar measures 12 μm .

B

Publications

Review

Interdisciplinary Synergy to Reveal Mechanisms of Annexin-Mediated Plasma Membrane Shaping and Repair

Poul Martin Bendix^{1,*}, Adam Cohen Simonsen^{2,*}, Christoffer D. Florentsen¹, Swantje Christin Häger³, Anna Mularski², Ali Asghar Hakami Zanjani², Guillermo Moreno-Pescador¹, Martin Berg Klenow², Stine Lauritzen Sønder³, Helena M. Danielsen¹, Mohammad Reza Arastoo¹, Anne Sofie Heitmann³, Mayank Prakash Pandey², Frederik Wendelboe Lund², Catarina Dias³, Himanshu Khandelia^{2,*} and Jesper Nylandsted^{3,4,*}

¹ Niels Bohr Institute, University of Copenhagen, DK-2100 Copenhagen, Denmark; florentsen@nbi.ku.dk (C.D.F.); moreno@nbi.dk (G.M.-P.); helena.danielsen@nbi.ku.dk (H.M.D.); mohammadreza.arastoo@nbi.ku.dk (M.R.A.)

² Department of Physics, Chemistry and Pharmacy, University of Southern Denmark, DK-5230 Odense, Denmark; mularski@sdu.dk (A.M.); zanjani@sdu.dk (A.A.H.Z.); klenow@sdu.dk (M.B.K.); pandey@sdu.dk (M.P.P.); fwl@sdu.dk (F.W.L.)

³ Membrane Integrity, Cell Death and Metabolism Unit, Center for Autophagy, Recycling and Disease, Danish Cancer Society Research Center, DK-2100 Copenhagen, Denmark; swantjehchristinhaeger@gmail.com (S.C.H.); stilau@cancer.dk (S.L.S.); anhe@cancer.dk (A.S.H.); cad@cancer.dk (C.D.)

⁴ Department of Cellular and Molecular Medicine, Faculty of Health Sciences, University of Copenhagen, DK-2200 Copenhagen, Denmark

* Correspondence: bendix@nbi.ku.dk (P.M.B.); adam@memphys.sdu.dk (A.C.S.); hkhandel@sdu.dk (H.K.); jnl@cancer.dk (J.N.)

Received: 2 April 2020; Accepted: 19 April 2020; Published: 21 April 2020



Abstract: The plasma membrane surrounds every single cell and essentially shapes cell life by separating the interior from the external environment. Thus, maintenance of cell membrane integrity is essential to prevent death caused by disruption of the plasma membrane. To counteract plasma membrane injuries, eukaryotic cells have developed efficient repair tools that depend on Ca^{2+} - and phospholipid-binding annexin proteins. Upon membrane damage, annexin family members are activated by a Ca^{2+} influx, enabling them to quickly bind at the damaged membrane and facilitate wound healing. Our recent studies, based on interdisciplinary research synergy across molecular cell biology, experimental membrane physics, and computational simulations show that annexins have additional biophysical functions in the repair response besides enabling membrane fusion. Annexins possess different membrane-shaping properties, allowing for a tailored response that involves rapid bending, constriction, and fusion of membrane edges for resealing. Moreover, some annexins have high affinity for highly curved membranes that appear at free edges near rupture sites, a property that might accelerate their recruitment for rapid repair. Here, we discuss the mechanisms of annexin-mediated membrane shaping and curvature sensing in the light of our interdisciplinary approach to study plasma membrane repair.

Keywords: annexin; plasma membrane repair; membrane curvature; membrane curvature sensing; membrane shaping; interdisciplinary research; cell rupture; membrane damage

1. Introduction

Membranes of eukaryotic cells play fundamental roles in organizing cellular compartments and cluster specific molecules to generate signaling platforms. Beyond defining the physical cell boundary, the plasma membrane serves a dual purpose: it allows the communication and exchange of solutes with the extracellular environment, while guarding the cell from its surroundings. In addition, the plasma membrane facilitates cell–cell interactions and adhesion and regulates the architecture of the cell. Thus, it is crucial that the plasma membrane is kept intact to ensure cell survival.

The plasma membrane is composed of both structural and signaling lipids, as well as embedded proteins. The major structural lipids are glycerophospholipids (such as phosphatidylserine and phosphatidylcholine), sterols, and sphingolipids (e.g., sphingomyelin) [1]. Of note, the enrichment of sphingolipids and sterols, like cholesterol, aids in resisting mechanical stress [2]. Plasma membrane topology is shaped by the geometrical properties of its lipids, in combination with both integrated and peripheral proteins, including components of the cytoskeleton [3]. Glycerophospholipids with small head groups, such as phosphatidylethanolamines and phosphatidic acid, are cone-shaped and have the propensity to induce membrane curvature, thus lipid shape is intimately related to membrane shape [3,4]. Moreover, the surface charge of membranes influences its interaction with proteins, including curvature inducing regulators, and is determined by the head group charge of individual lipids [5,6]. This is exemplified by the family of annexin proteins that are characterized by their capacity to bind negatively charged phospholipids in a Ca^{2+} -dependent manner, to exert their various functions in membrane organization, trafficking, and repair [7].

Unlike prokaryotic cells, which are shielded by a cell wall, mammalian cells are primarily protected by their plasma membrane and appear more susceptible to cell injuries. To counteract the eminent threat that membrane damage would impose on cellular homeostasis, robust repair mechanisms have evolved to ensure that membrane holes are sealed within the timeframe of tens-of-seconds to maintain cell integrity [8,9]. If disruptions to the plasma membrane are not repaired rapidly, the resultant pronounced osmotic and ionic imbalances would lead to cell death. Skeletal muscle and cardiac muscle cells are classical examples of cells that, due to their high mechanic activity, need to cope with extensive plasma membrane disruptions [10]. Similarly, epithelial cells in the gut and skin fibroblasts are exposed to both mechanical and chemical stimuli and experience regular wounding [11]. However, it seems that all cell types can potentially experience plasma membrane injury and have the capacity to repair lesions [12].

Deficiency in plasma membrane repair is associated with several diseases. The best established link between repair deficiency and disease phenotype is observed in muscular dystrophies, such as dysferlin-deficient muscular dystrophy, where a failure to repair repeated membrane lesions leads to progressive muscle wasting [13]. Inversely, our research supports that enhanced plasma membrane repair plays a role in helping metastatic breast cancer cells cope with the physical stress imposed during invasion [14,15].

The importance of Ca^{2+} for membrane repair was recognized in 1930 by Heilbrunn, who discovered that sea urchin eggs failed to repair upon mechanical damage when the surrounding solution was depleted of Ca^{2+} [16]. Despite the scarce knowledge regarding membranes and cell compartmentalization at the time, this discovery pointed to Ca^{2+} as a fundamental trigger of plasma membrane repair. In intact resting cells the intracellular free Ca^{2+} concentrations in the cytoplasm are in the nanomolar range (~ 100 nM), while extracellular Ca^{2+} concentrations are in the millimolar range [17]. This steep Ca^{2+} gradient is important for signaling events and is established by actively pumping Ca^{2+} into the extracellular space and intracellular Ca^{2+} stores, which is also crucial to prevent Ca^{2+} cytotoxicity. Upon plasma membrane injury, the Ca^{2+} gradient leads to a rapid and pronounced flux of Ca^{2+} into the cell's cytoplasm, which poses a threat to the cell [18,19]. However, this rise in Ca^{2+} acts at the same time as the triggering event for plasma membrane repair mechanisms.

2. Annexins in Repair

Several functions have been reported for annexins, and most of them include their involvement in membrane trafficking events [20]. Interestingly, during the last two decades more evidence regarding their role in plasma membrane repair has emerged [20–23]. Most proteins that play a role in plasma membrane repair have the ability to bind Ca^{2+} and become activated upon injury-induced Ca^{2+} influx. However, the recruitment of repair components to the injured plasma membrane can also be facilitated via complex formation with other Ca^{2+} -binding proteins. This is exemplified by recent data showing a link between the Ca^{2+} -dependent, phospholipid-binding protein annexin A7 (ANXA7), and the shedding of damaged membrane during repair facilitated by the endosomal sorting complex required for transport III (ESCRT-III) complex [22]. In detail, ANXA7 localizes to the injury site where it forms a complex with apoptosis-linked gene 2 (ALG-2) and ALG-2-interacting protein X (ALIX) [23]. ANXA7 facilitates thereby anchoring of ALG-2 to the damaged plasma membrane, where ALG-2 can assemble the ESCRT-III complex and drive shedding of damaged membrane [22].

Accumulating evidence indicates that annexins are instrumental for coping with plasma membrane injuries, although their exact mode of action is not well characterized. Annexins are a family of proteins (in mammals: ANXA1–11 and ANXA13) which share a structurally conserved C-terminal domain and the functional property of being able to bind anionic phospholipids in a Ca^{2+} -dependent manner. Binding to membranes is mediated by their core domain, which consists of four characteristic structural annexin repeats [24]. The N-terminal domain varies in length and composition and is responsible for the interaction with other proteins, giving rise to different functional properties [24].

Work on dysferlin-deficient mouse muscle cells pioneered the hypothesis that annexins function in plasma membrane repair. ANXA1 and ANXA2 were found to associate with dysferlin upon muscle cell membrane injury. Since ANXA1 and ANXA2 were known to cause aggregation and fusion of liposomes *in vitro* [25], Lennon et al. proposed that the annexins could aid repair by facilitating fusion of vesicles with the injured plasma membrane [26]. Wounding experiments, using laser injury, confirmed that ANXA1 localizes to the injury site and that inhibition of ANXA1 function impedes plasma membrane repair [27].

Involvement of ANXA1 and ANXA6 could also be detected in microvesicle shedding of streptolysin O (SLO) pores [28]. Furthermore, data from the Protein Data Bank (PDB), where annexins have been crystallized, show that annexins have varying Ca^{2+} binding affinity, which adds another level of complexity to plasma membrane repair mechanisms. In line with this, ANXA6 was shown to have higher Ca^{2+} sensitivity than ANXA1, which led to differential recruitment patterns depending on the extent of the membrane lesions [28]. The importance of ANXA6 in muscle cell plasma membrane repair was recognized when mutations of the ANXA6 gene were found to negatively impact the phenotype of dysferlinopathy (a group of rare muscular dystrophies with recessive mutations in the dysferlin gene). Focal laser injury experiments revealed that ANXA6 localizes to the site of injury within seconds forming a repair cap [29,30]. Later work showed that ANXA6 localization to the injury site in muscle cells is actin-dependent and coincides with recruitment of ANXA1, ANXA2, and ANXA5 [31].

Even though the function of annexins in plasma membrane repair was initially merely explained by the ability of annexins to aid vesicle fusion, research now indicates that other mechanisms play a role for annexin-mediated wound closure. ANXA5, for example, was shown to assemble into 2D protein arrays around the injury site, preventing wound expansion [32,33]. To that end, using supported membrane models we have identified membrane binding and shaping features of other annexins that are independent of vesicle fusion events, pointing to a direct effect of annexins on membranes [34]. For example, ANXA4 was shown to generate a curvature force at free membrane edges because of its Ca^{2+} -dependent homo-trimerization, while binding of ANXA6 led to a constriction force [35]. Therefore, it is likely that annexins possess different membrane-shaping properties, allowing for a tailored response that meets the needs of repair. In concert with other described processes, such as actin remodeling, annexins lead to efficient and rapid repair.

Interestingly, certain annexins, which are central components in plasma membrane repair, also display strong affinity for high membrane curvatures as we have shown recently in Moreno-Pescador et al. [36]. This suggests that membrane shaping and curvature sensing are coupled in a feedback loop where initial curvature generation by annexins leads to further recruitment of more annexins. It is therefore essential that the effect of biophysical cues, like membrane curvature, are thoroughly investigated for a comprehensive understanding of the activity and function of annexins.

3. Interdisciplinary Approaches to Address Annexin Function

Given their complexity and rapid dynamics, detailed mechanisms of annexin-mediated membrane shaping and repair can only be resolved by incorporating sophisticated physical methods for assessing biophysical parameters like curvature and tension. Thus, interdisciplinary research within biophysics, molecular simulations, and molecular and cellular biology is needed to understand these mechanisms. This approach proved successful, as exemplified in recent studies showing that annexin family members share a common ability of membrane curvature induction, which seems to be important for their function in repair [24,25]. Here, the impact of annexins on planar membranes with stable, free edges are relevant for studying the membrane conformation near a hole.

The annexin core domain has a convex shape at its membrane-binding interface [21]. Thus, membrane-association of annexins can generally be expected to induce spontaneous membrane curvature and possibly produce membrane shape changes. The shape changes generated by annexins depend crucially on the initial membrane geometry and on the presence of free membrane edges in particular. Thus, the use of membrane model systems prepared with specific geometries allow the systematic study of the interplay between annexin binding, membrane shape, and shape remodeling.

Supported planar membranes in a stacked conformation are prepared using spincoating with the secondary membranes existing as isolated patches on the primary membrane. The patches have stable, free edges at their borders and have minimal interactions with the solid support due to the presence of the primary membrane [26]. These membrane patches serve as useful models for the plasma membrane near the injury site and address the experimental challenge that a membrane containing a hole is often unstable and the hole is short-lived. The planar patches allow out-of-plane bending, away from the supported surface and can be used for monitoring shape changes induced by different proteins. To this end, the impact of different annexin family members on the morphology of membrane patches with free edges were recently examined [24].

Notably, the annexin members ANXA4 and ANXA5 were both found to induce rolling of the patch starting from the free membrane edges at the patch border. Complete roll-up of a cell-sized membrane patch (50–100 μm) occurs over a time scale of 5–10 s. This result shows that membrane binding of ANXA4 and ANXA5 under physiological conditions induces spontaneous curvature. The curvature generation can be expected to also occur near a plasma membrane hole when Ca^{2+} briefly enters the cytoplasm and cytosolic annexin binds to the negatively charged internal leaflet.

In order to model curvature generation around a plasma membrane hole, it has proven useful to describe the system using theoretical modeling of the membrane curvature energy.

According to the classical theory by Helfrich [27], the curvature elastic energy H_{curve} of a membrane with area A can be written as:

$$H_{\text{curve}} = \int_A \left[\frac{1}{2} k_c (\bar{c} - c_0)^2 + k_G \bar{c}_G \right] dA \quad (1)$$

where k_c is the mean curvature elastic modulus [J], k_G is the gaussian curvature elastic modulus [J], and c_0 is the spontaneous curvature [m^{-1}]. The local curvature of the membrane is described by the two principal radii of curvature, R_1 and R_2 . The mean curvature is defined as: $\bar{c} = \frac{1}{R_1} + \frac{1}{R_2}$ and the gaussian curvature as: $\bar{c}_G = \frac{1}{R_1} \frac{1}{R_2}$.

H_{curve} describes the curvature energy associated with a membrane of a general shape, for example a curved membrane near a plasma membrane hole. The spontaneous curvature c_0 , is a quantity

describing the tendency of a membrane to spontaneously curve with a curvature radius ($1/c_0$). The effect of annexin binding to a membrane is potentially complex, but it can approximately be modeled as a non-zero value of c_0 . When describing a membrane containing a hole, there will additionally exist a tension force (edge tension) associated with the formation of the free edge. In a simple picture, the edge tension acts to contract the hole while the curvature energy (H_{curve} equation) acts oppositely, by bending the membrane out-of-plane and increasing the edge radius. As previously shown [28], an equilibrium configuration is possible that balances the curvature and tension energies to create a stable neck-like shape of the membrane near the hole. We propose that ending of the membrane near a plasma membrane hole, via a mechanism as described above, plays a functional role in the plasma membrane repair process. In a cellular system, membrane re-shaping is envisioned to involve the concerted action of several annexins plus other repair proteins to rapidly bend, constrict, and finally seal the hole (Figure 1A–C).

Members of the family of human annexins were shown to induce distinctly different morphologies in the planar membrane patches [24]. This was observed despite the fact that the annexins all contain a membrane-binding core domain, which is highly conserved. In addition to large scale (cooperative) rolling as induced by ANXA4 and ANXA5, rolling in a fragmented morphology was observed for ANXA3 and ANXA13. Rolling was not observed for ANXA1 and ANXA2, which instead both induced a blebbing/folding type morphology of the membrane patch (Figure 1D,E). ANXA7 and ANXA11 induce rolling, in addition to the generation of lens-shaped membrane inclusions containing the protein and phosphatidylserine lipids. In total, the morphologies induced by annexins in membrane patches correlate well with a dendrogram of their amino acid sequences [24]. This points to an important functional role of the N-terminal annexin domain in reshaping membranes.

A deeper insight into the interplay between molecular curvatures and the rich polymorphic membrane shapes, which can be induced by annexins, will require theoretical simulations and also development of assays for studying membrane shaping in 3D, e.g., surrounding a membrane hole, and to study curvature sensing by this large class of proteins.

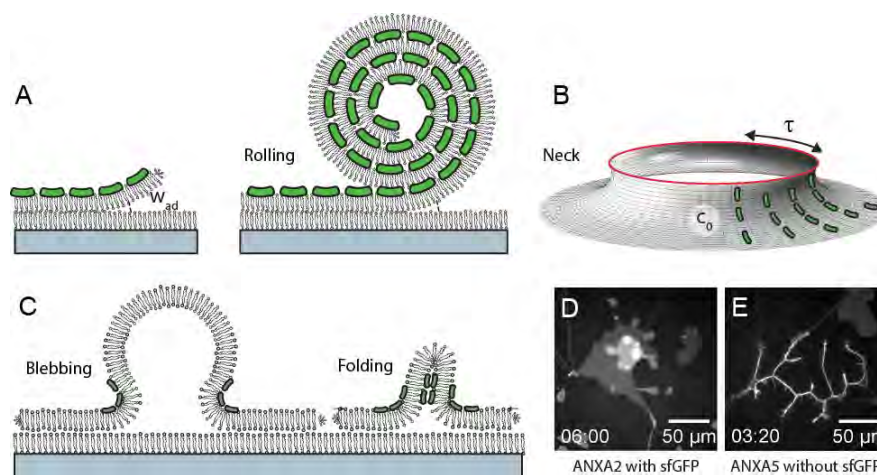


Figure 1. Binding of annexins (green) to a planar membrane patch with free edges and adhesion energy w_{ad} inducing spontaneous curvature and a rolling morphology of the patch (A). Translation to the geometry of a membrane hole (B) where the edge tension τ and the spontaneous curvature c_0 acts to create a stable neck conformation. Example of blebbing/folding morphologies induced by ANXA1 and ANXA2 (C) and examples of fluorescence data for patches (POPC: 1-palmitoyl-2-oleoyl-sn-glycero-3-phosphocholine, POPS: (1-palmitoyl-2-oleoyl-sn-glycero-3-phospho-L- serine), 9:1 ratio, DiDC18) showing blebbing (D) and rolling (E).

More specifically, the recent developments in super-resolution microscopy, like stochastic optical reconstruction microscopy (STORM) [29] and stimulated emission depletion (STED) [30], will be

valuable for investigating the shape evolution of the injured site. STORM has been used to image the cortical actin of cells with great detail [31] and could be used for resolving the rearrangement of cortical actin, which is known to regulate both plasma membrane shape and tension. Finally, faster imaging modes like STED or high speed-atomic force microscopy (AFM) could capture the steps in the formation of a hole and the subsequent membrane healing.

4. Annexins Are Recruited by Membrane Curvature

Proteins with the ability to shape membranes into highly curved structures often have the ability to sense high membrane curvatures. Such proteins include the well-studied Bin/amphiphysin/Rvs BAR domain containing proteins, which have all been verified as both curvature generators and sensors of specific membrane curvatures that correlate with their molecular shape [32–34]. The curvature sensing ability of annexins has only recently been recognized [35,36] despite the convex shape of the conserved membrane binding core domain, present in all annexins. Naively, one could expect that the convex shape, of the membrane binding domain, would imply that all annexins could be potential sensors of negative membrane curvatures. However, looking at the non-trivial curvature generation by different annexins this argument could be too simple, in particular considering the complex protein–protein interactions, variable Ca^{2+} sensitivity, and the variability in the N-terminal domains amongst the annexins.

Our studies, using isolated giant plasma membranes vesicles (GPMVs), have shown that both ANXA4 [36] and ANXA5 [35] are efficient sensors of negative membrane curvatures. Optical manipulation of the GPMVs was used to extract nanotubes which exhibit extreme membrane curvatures as shown in several studies on giant unilamellar vesicles (GUVs) [34]. Using GPMVs isolated from living cells expressing ANXAs coupled to GFP circumvents the step of protein encapsulation used in studies with artificial vesicles and also allows the curvature sensing to be investigated in a more physiologically-relevant environment with complex lipid and protein composition (See Figure 2A–C). Using optical manipulation, nanotubes were extracted from the vesicles (Figure 2D–F) and protein sorting between the nanotube and the vesicle membrane was quantified by the relative sorting parameter, S :

$$S = \frac{(I_{prot}/I_{mem})_{tube}}{(I_{prot}/I_{mem})_{vesicle}} \quad (2)$$

where S is a measure of the relative density of protein on the tube $(I_{prot})_{tube}$ versus the quasi-flat surface on the vesicle, $(I_{prot})_{vesicle}$. The intensity from a lipid analog in the membrane, $(I_{mem})_{tube}$ scales with the tube diameter and $(I_{mem})_{vesicle}$ is used for normalization to account for possible different concentrations of membrane dye in different vesicles.

As shown in Figure 2E,G the density of ANXA5 was found to increase significantly within nanotubes extracted from GPMVs which were derived from HEK293T cells. The increase in density of ANXA5 ranged up to 10–15 times higher than the density on the quasi-flat region on the vesicle membrane (Figure 2G) although with significant heterogeneity in the sorting as shown in Figure 2E,G,H. Interestingly, the curvature sensing of the cognate protein ANXA2 did show a majority of sorting values below 1 indicating a slightly negative affinity for the curvatures within the nanotubes (Figure 2F–G). These results indicate that proteins from the annexin family can differ remarkably in curvature sensing despite the similarly shaped membrane binding core domain. Furthermore, we recently found that ANXA4 senses membrane curvature with a similar effect as ANXA5 and the curvature sensing was dependent on the ability of ANXA4 to form trimers [36]. The curvature sensing and membrane rolling induced by ANXA4 and ANXA5, but not ANXA2, could together indicate that trimerization is critical for membrane curvature sensing and curvature induction. Beyond these results, future experiments should test whether the two dimensional curvature of annexins can discriminate between spherical and cylindrical curvatures in similar assays as used in Li et al. [37].

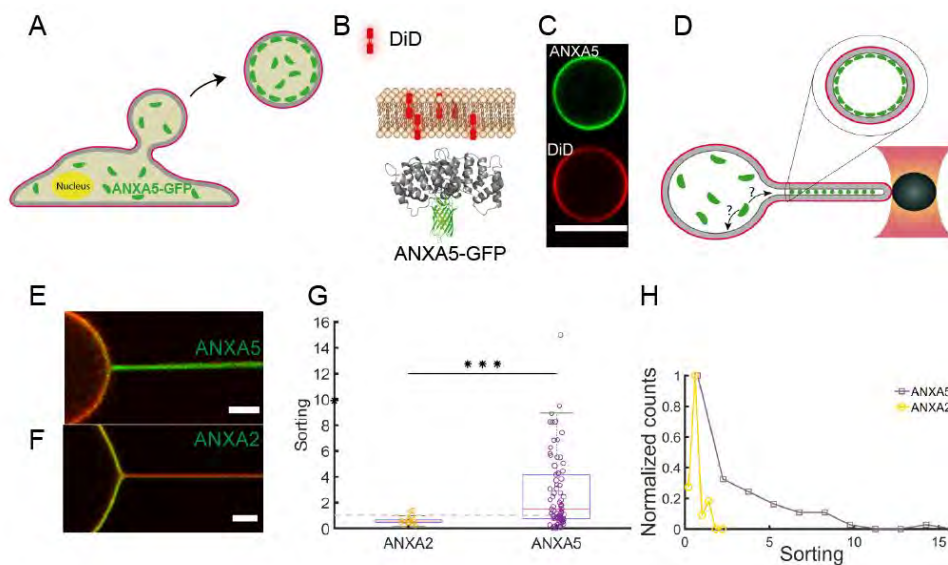


Figure 2. Membrane curvature sensing of ANXA2 and ANXA5 measured in lipid nanotubes extracted from Giant Plasma Membrane Vesicles (GPMVs). (A) GPMVs are derived from HEK293T cells expressing ANXA2-GFP or ANXA5-GFP. (B) GFP tagged annexins bind to the inner side of the lipophilic carbocyanine DiD labeled membrane. (C) Images of DiD (red) labeled GPMVs containing ANXA5-GFP (green). (D) Schematic of optical manipulation of the vesicles to form nanotubes with radius $\sim 50\text{nm}$ and length $10\mu\text{m}$. (E) Overlay image of a GPMV and nanotube containing GFP tagged ANXA5 and DiD membrane label. (F) Overlay image of a GPMV and nanotube containing GFP tagged ANXA2 and membrane label DiD. (G) Quantification of curvature sorting for ANXA2 and ANXA5, respectively. The dashed line represents Sorting = 1 corresponding to no sorting. $*** p = 0.004$. (H) The Sorting values from (G) plotted as a histogram which reveals significant heterogeneity in the Sorting by ANXA5. Reproduced with permission from [35].

Consistent with the rolling and sensing experiments discussed above multiscale simulations have revealed that ANXA4 trimers both induce and sense membrane curvatures [36]. All-atom (AA) molecular dynamics (MD) simulations provide molecular details of the interactions of annexins with lipid membranes of various compositions. Coarse-grained MD simulations, where multiple heavy atoms in a molecule are represented by single beads, are used to analyze the interactions of multiple annexin molecules with a bilayer surface, and the micron-scale scaffolding of annexins on a membrane surface [38]. Large-scale membrane conformations induced by annexins are probed by Monte-Carlo simulations, where the membrane is modeled as a fluid triangulated surface, and the annexin molecules are modeled as a vector field that induced local curvature changes in the membrane [36]. The three different computational techniques constitute an inter-coupled multi-scale simulation strategy where annexin-membrane interactions are investigated from the molecular level all the way to mesoscale fluctuations in membrane shape.

We used all-atom simulations to calculate the annexin-induced curvature upon POPC (1-Palmitoyl-2-oleoylphosphatidylcholine):POPS (1-Palmitoyl-2-oleoylphosphatidylserine) (4:1 ratio) lipid membranes in the presence of Ca^{2+} . Simulations of ANXA4 reveal that the ANXA4 trimer induces a significant negative average mean curvature of $0.0024 \pm 0.0002 \text{ nm}^{-1}$ on the bilayer. The curvature is calculated by fitting the coordinates of the lipid head group phosphorus atoms by a two-dimensional Fourier series. The simulations also reveal a significant accumulation of PS lipids below the annexin trimer surface, which is to be expected because Ca^{2+} ions cross-link between anionic amino acids on the annexin trimer and anionic POPS lipids [39]. It is worth noting that although such lipid reorganization can be observed in all-atom simulations on time-scales of hundreds of nanoseconds, the diffusion of lipids in the membrane plane is slow, and is best examined by coarse-grained simulations on longer time scales. The trimer of ANXA5 has a similar impact on bilayer properties, while the effect of

monomers of ANXA4 and ANXA5 differ in their interaction with the bilayer surface, compared to their trimer forms (unpublished data). Future studies along the lines described in the previous section are needed to test the theoretical predictions in experimental model systems using GUVs with controlled membrane curvatures and known protein densities.

The curvature calculated from the all-atom MD simulations is fed as a parameter into the Monte-Carlo simulations, which show that ANXA4 trimers accumulate on the inner membrane of highly curved nanotubes, and are desorbed from the less curved membrane surface (Figure 3). The data are in excellent agreement with the curvature-sensing experiments presented in Figure 2, which show a significant increase in the concentration of ANXA5 within nanotubes compared to the flat GPMV surface. The Monte-Carlo method described here simulates the distribution of annexins on a closed membrane surface. We are currently developing a framework of the Monte-Carlo simulations where the effect of annexins onto a free membrane edge can be investigated. Such a setup will open the possibility of investigating the effect of multiple annexins on the shape evolution of a free membrane edge, bringing us even closer to simulating the mechanism of membrane repair.

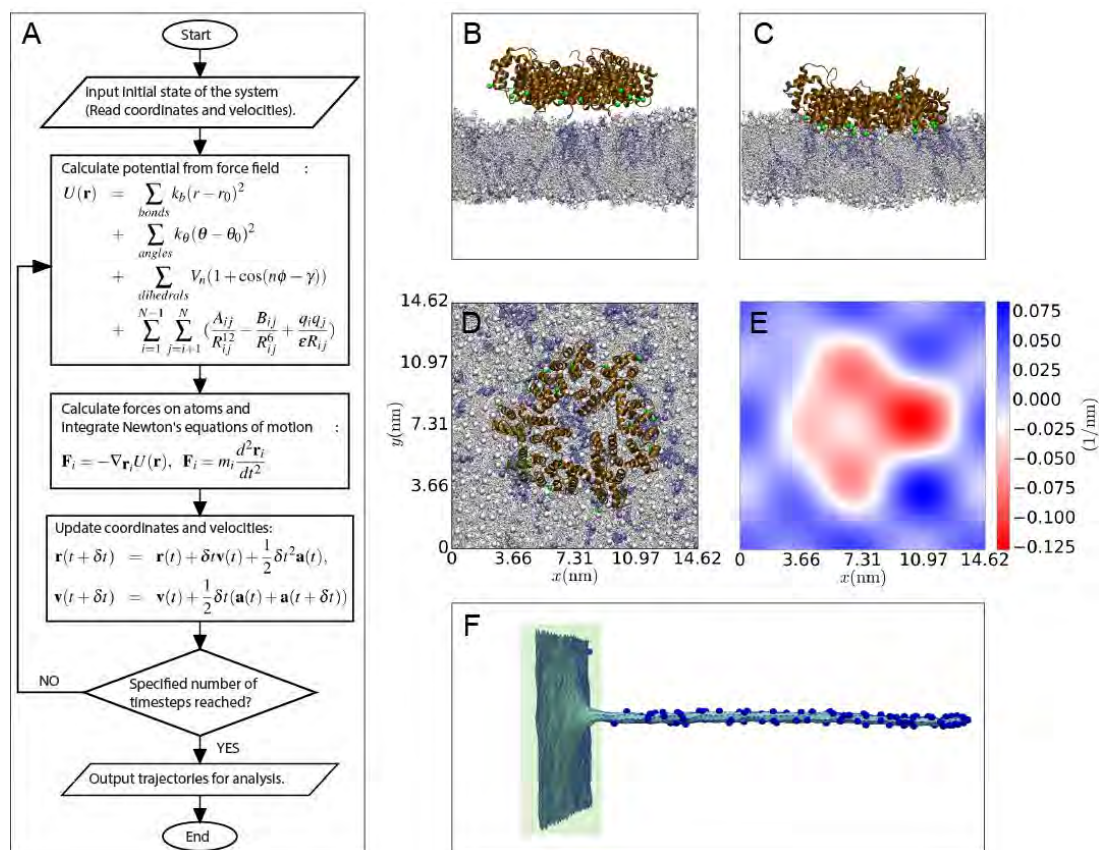


Figure 3. (A) An overview of the molecular dynamics (MD) procedure, with a simple form of force field and velocity-Verlet integration algorithm. The integration timestep in all-atom MD is usually 2 fs. (B) Initial simulation setup of the ANXA4 trimer near a POPC:POPS (4:1) bilayer. (C) Final snapshot showing the indentation of the membrane. (D) Top view of the final snapshot. (E) The 2D curvature profile for a surface passing through the center of the membrane in panel C. (F) Monte-Carlo simulation snapshot of ANXA4 protein affinity for a membrane patch (flat) and a highly curved nanotube generated by pulling a vertex from a flat membrane. Note that the proteins are depicted on the outer surface for clarity.

5. Annexin Scaffolding

Some members of the annexin family have been shown to form large scale protein scaffolds at high protein densities. These scaffolds have been imaged by atomic force microscopy (AFM) and consist of

a regular lattice of trimers. High-speed AFM has even shown the dynamics of the protein lattice [40]. Protein immobility has also been measured for annexin bound plasma membrane nanotubes indicating that protein lattices can also form in highly curved regions. The functional role of these lattices in membrane repair remains unknown, however it was recently shown that ANXA5 can change the physical properties of the membrane [39]. Additionally, another function could be to provide friction to the membrane and stabilize the membrane rupture against further expansion [41].

6. Approaches to Inflict Damage to the Plasma Membrane

Many cell studies aimed at studying plasma membrane resealing use ablation laser to inflict spatial damage to the cell membrane. Here, a single and localized wound can be induced at the plasma membrane of cultured cells and repair can be followed using fast time-lapse imaging [13,41,42]. The main advantages include user's control over the extent of damage by adjusting the laser power and the ability to assess cellular repair kinetic and monitor the action of fluorescently-tagged proteins involved in repair (Figure 4) [43]. A possible drawback is that membrane damage triggered by UV-ablation laser induces local high temperatures at the injured membrane, which can potentially affect membrane proteins and lipids and create thermally-induced diffusion and denaturation artifacts. However, we and others have demonstrated tempo-spatial recruitment of repair proteins occurs within 10–45s of laser-induced plasma membrane injury [28,44], indicating that the repair machinery is not disabled by the collateral thermal damage. Importantly, complimentary methods to induce membrane injury, such as the use of glass bead injury, detergents, and scraping, show that the same repair proteins are recruited to damaged membrane (including annexins, actin, ESCRT III) as with laser injury and needed for repair [14,45]. This suggests that laser-induced plasma membrane injury can provide insight into repair mechanisms that are of biological significance, since all injuries (artificial and, potentially, physiological/pathological) converge the point of Ca^{2+} influx, which is the key stimulus for plasma membrane repair mechanisms.

An alternative method for inflicting cell injury is to use thermoplasmonic [46]. Irradiation of plasmonic nanostructures using near infrared (NIR) light results in an extremely localized temperature increase which can be used to disrupt plasma membranes. This strategy has been used for fusion of cells [47] and membrane vesicles [48]. Both pulsed lasers or continuous wave lasers can be used in combination with plasmonic nanoparticles for disrupting membranes [49–52]. We envision that this technique will provide a fruitful approach for investigation of plasma membrane repair in the future in particular when combined with predictions from theoretical calculation on the stability of membrane holes decorated with annexins scaffolds.

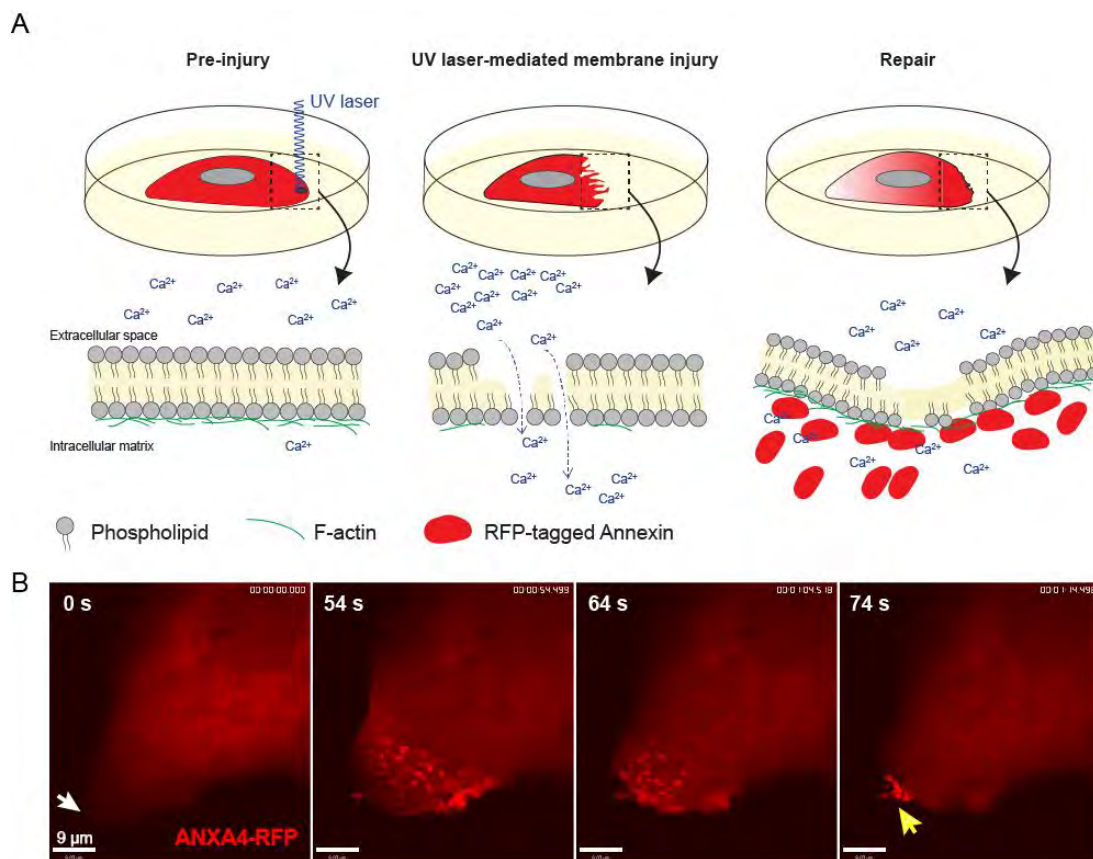


Figure 4. Plasma membrane injury inflicted by UV-laser ablation injury. **(A)** Schematic of ablation laser injury to monitor annexin behavior during plasma membrane repair. Ca^{2+} influx through the wounded membranes activates and enables annexin to bind and seal the hole by bending membrane and glue membrane edges together. **(B)** Sequential images from time-lapse movie of a MCF-7 breast carcinoma cell showing translocation behavior of ANXA4-RFP to the site of damage (white arrow) upon laser injury.

7. Concluding Remarks

This synergy fostered by interdisciplinary research achieves its full potential when different perspectives are integrated to comprehensively understand a complex cellular phenomenon. Here, we describe the development of new complementary strategies that, when combined, have elucidated mechanisms underlying membrane shaping and repair. Our recent findings, which could only be revealed through interdisciplinary collaboration, show that there is more to annexins than previously anticipated. In particular there are many unanswered questions in relation to the complex interaction between annexins and curved membranes, and how physical cues aid in membrane healing. We surmise that, a combination of novel membrane assays and high resolution imaging together with multiscale simulations will provide major progress in resolving the enigmatic process of membrane repair in the future.

Author Contributions: All authors contributed with manuscript writing and editing of this article. All authors have read and agreed to the published version of the manuscript.

Funding: Work presented here is supported by the Novo Nordisk Foundation Interdisciplinary Synergy Grant (NNF18OC0034936) and the Lundbeck Foundation (R218-2016-534).

Acknowledgments: We thank Dr. Weria Pezeshkian (University of Groningen) for providing the Monte-Carlo simulation snapshot in Figure 3F, and mapping the ANXA all-atom MD into a vertex-based model.

Conflicts of Interest: The authors declare no conflict of interest.

References

1. Harayama, T.; Riezman, H. Understanding the diversity of membrane lipid composition. *Nat. Rev. Mol. Cell Biol.* **2018**, *19*, 281–296. [[CrossRef](#)] [[PubMed](#)]
2. van Meer, G.; Voelker, D.R.; Feigenson, G.W. Membrane lipids: Where they are and how they behave. *Nat. Rev. Mol. Cell Biol.* **2008**, *9*, 112–124. [[CrossRef](#)] [[PubMed](#)]
3. McMahon, H.T.; Gallop, J.L. Membrane curvature and mechanisms of dynamic cell membrane remodelling. *Nature* **2005**, *438*, 590–596. [[CrossRef](#)] [[PubMed](#)]
4. Suetsugu, S.; Kurisu, S.; Takenawa, T. Dynamic shaping of cellular membranes by phospholipids and membrane-deforming proteins. *Physiol. Rev.* **2014**, *94*, 1219–1248. [[CrossRef](#)] [[PubMed](#)]
5. Peetla, C.; Vijayaraghavalu, S.; Labhasetwar, V. Biophysics of cell membrane lipids in cancer drug resistance: Implications for drug transport and drug delivery with nanoparticles. *Adv. Drug Deliv. Rev.* **2013**, *65*, 1686–1698. [[CrossRef](#)]
6. Poyry, S.; Vattulainen, I. Role of charged lipids in membrane structures—Insight given by simulations. *Biochim. Biophys. Acta* **2016**, *1858*, 2322–2333. [[CrossRef](#)]
7. Gerke, V.; Creutz, C.E.; Moss, S.E. Annexins: Linking Ca²⁺ signalling to membrane dynamics. *Nat. Rev. Mol. Cell Biol.* **2005**, *6*, 449–461. [[CrossRef](#)] [[PubMed](#)]
8. Hager, S.C.; Nylandsted, J. Annexins: Players of single cell wound healing and regeneration. *Commun. Integr. Biol.* **2019**, *12*, 162–165. [[CrossRef](#)]
9. Tang, S.K.Y.; Marshall, W.F. Self-repairing cells: How single cells heal membrane ruptures and restore lost structures. *Science* **2017**, *356*, 1022–1025. [[CrossRef](#)]
10. McNeil, P.L.; Khakee, R. Disruptions of muscle fiber plasma membranes. Role in exercise-induced damage. *Am J. Pathol.* **1992**, *140*, 1097–1109.
11. McNeil, P.L.; Ito, S. Molecular traffic through plasma membrane disruptions of cells in vivo. *J. Cell Sci.* **1990**, *96*, 549–556. [[PubMed](#)]
12. Moe, A.M.; Golding, A.E.; Bement, W.M. Cell healing: Calcium, repair and regeneration. *Semin. Cell Dev. Biol.* **2015**, *45*, 18–23. [[CrossRef](#)] [[PubMed](#)]
13. Bansal, D.; Miyake, K.; Vogel, S.S.; Groh, S.; Chen, C.C.; Williamson, R.; McNeil, P.L.; Campbell, K.P. Defective membrane repair in dysferlin-deficient muscular dystrophy. *Nature* **2003**, *423*, 168–172. [[CrossRef](#)] [[PubMed](#)]
14. Jaiswal, J.K.; Lauritzen, S.P.; Scheffer, L.; Sakaguchi, M.; Bunkenborg, J.; Simon, S.M.; Kallunki, T.; Jaattela, M.; Nylandsted, J. S100A11 is required for efficient plasma membrane repair and survival of invasive cancer cells. *Nat. Commun.* **2014**, *5*, 3795. [[CrossRef](#)] [[PubMed](#)]
15. Jaiswal, J.K.; Nylandsted, J. S100 and annexin proteins identify cell membrane damage as the Achilles heel of metastatic cancer cells. *Cell Cycle* **2015**, *14*, 502–509. [[CrossRef](#)]
16. Heilbrunn, L.V. The Surface Precipitation Reaction of Living Cells. *Proc. Am. Philos. Soc.* **1930**, *69*, 295–301.
17. Clapham, D.E. Calcium signaling. *Cell* **2007**, *131*, 1047–1058. [[CrossRef](#)]
18. Jaiswal, J.K. Calcium—how and why? *J. Biosci.* **2001**, *26*, 357–363. [[CrossRef](#)]
19. Zhivotovsky, B.; Orrenius, S. Calcium and cell death mechanisms: A perspective from the cell death community. *Cell Calcium* **2011**, *50*, 211–221. [[CrossRef](#)]
20. Boye, T.L.; Nylandsted, J. Annexins in plasma membrane repair. *Biol. Chem.* **2016**, *397*, 961–969. [[CrossRef](#)]
21. Gerke, V.; Moss, S.E. Annexins: From structure to function. *Physiol. Rev.* **2002**, *82*, 331–371. [[CrossRef](#)]
22. Bouter, A.; Carmeille, R.; Gounou, C.; Bouvet, F.; Degrelle, S.A.; Evain-Brion, D.; Brisson, A.R. Review: Annexin-A5 and cell membrane repair. *Placenta* **2015**, *36*, S43–S49. [[CrossRef](#)] [[PubMed](#)]
23. Draeger, A.; Monastyrskaya, K.; Babiychuk, E.B. Plasma membrane repair and cellular damage control: The annexin survival kit. *Biochem. Pharmacol.* **2011**, *81*, 703–712. [[CrossRef](#)] [[PubMed](#)]
24. Boye, T.L.; Jeppesen, J.C.; Maeda, K.; Pezeshkian, W.; Solovyeva, V.; Nylandsted, J.; Simonsen, A.C. Annexins induce curvature on free-edge membranes displaying distinct morphologies. *Sci. Rep.* **2018**, *8*, 10309. [[CrossRef](#)] [[PubMed](#)]
25. Drucker, P.; Pejic, M.; Galla, H.J.; Gerke, V. Lipid segregation and membrane budding induced by the peripheral membrane binding protein annexin A2. *J. Biol. Chem.* **2013**, *288*, 24764–24776. [[CrossRef](#)] [[PubMed](#)]
26. Simonsen, A.C.; Bagatolli, L.A. Structure of spin-coated lipid films and domain formation in supported membranes formed by hydration. *Langmuir* **2004**, *20*, 9720–9728. [[CrossRef](#)]

27. Helfrich, W. Elastic properties of lipid bilayers: Theory and possible experiments. *Z. Nat. C* **1973**, *28*, 693–703. [[CrossRef](#)]
28. Boye, T.L.; Maeda, K.; Pezeshkian, W.; Sonder, S.L.; Haeger, S.C.; Gerke, V.; Simonsen, A.C.; Nylandsted, J. Annexin A4 and A6 induce membrane curvature and constriction during cell membrane repair. *Nat. Commun.* **2017**, *8*, 1623. [[CrossRef](#)]
29. Rust, M.J.; Bates, M.; Zhuang, X. Sub-diffraction-limit imaging by stochastic optical reconstruction microscopy (STORM). *Nat. Methods* **2006**, *3*, 793–795. [[CrossRef](#)]
30. Hell, S.W.; Wichmann, J. Breaking the diffraction resolution limit by stimulated emission: Stimulated-emission-depletion fluorescence microscopy. *Opt. Lett.* **1994**, *19*, 780–782. [[CrossRef](#)]
31. Pan, L.; Yan, R.; Li, W.; Xu, K. Super-Resolution Microscopy Reveals the Native Ultrastructure of the Erythrocyte Cytoskeleton. *Cell Rep.* **2018**, *22*, 1151–1158. [[CrossRef](#)]
32. Sorre, B.; Callan-Jones, A.; Manzi, J.; Goud, B.; Prost, J.; Bassereau, P.; Roux, A. Nature of curvature coupling of amphiphysin with membranes depends on its bound density. *Proc. Natl. Acad. Sci. USA* **2012**, *109*, 173–178. [[CrossRef](#)]
33. Ramesh, P.; Baroji, Y.F.; Reihani, S.N.; Stamou, D.; Oddershede, L.B.; Bendix, P.M. FBAR syndapin 1 recognizes and stabilizes highly curved tubular membranes in a concentration dependent manner. *Sci. Rep.* **2013**, *3*, 1565. [[CrossRef](#)]
34. Prevost, C.; Zhao, H.; Manzi, J.; Lemichez, E.; Lappalainen, P.; Callan-Jones, A.; Bassereau, P. IRSp53 senses negative membrane curvature and phase separates along membrane tubules. *Nat. Commun.* **2015**, *6*, 8529. [[CrossRef](#)] [[PubMed](#)]
35. Moreno-Pescador, G.; Florentsen, C.D.; Ostbye, H.; Sonder, S.L.; Boye, T.L.; Veje, E.L.; Sonne, A.K.; Semsey, S.; Nylandsted, J.; Daniels, R.; et al. Curvature- and Phase-Induced Protein Sorting Quantified in Transfected Cell-Derived Giant Vesicles. *ACS Nano* **2019**, *13*, 6689–6701. [[CrossRef](#)] [[PubMed](#)]
36. Florentsen, C.; Kamp-Sonne, A.; Moreno-Pescador, G.; Pezeshkian, W.; Hakami Zanjani, A.A.; Khandelia, H.; Nylandsted, J.; Bendix, P.M. Annexin A4 trimers are recruited by high membrane curvatures in Giant Plasma Membrane Vesicles. *bioRxiv* **2020**. [[CrossRef](#)]
37. Li, X.; Matino, L.; Zhang, W.; Klausen, L.; McGuire, A.F.; Lubrano, C.; Zhao, W.; Santoro, F.; Cui, B. A nanostructure platform for live-cell manipulation of membrane curvature. *Nat. Protoc.* **2019**, *14*, 1772–1802. [[CrossRef](#)] [[PubMed](#)]
38. Marrink, S.J.; Risselada, H.J.; Yefimov, S.; Tieleman, D.P.; de Vries, A.H. The MARTINI force field: Coarse grained model for biomolecular simulations. *J. Phys. Chem. B* **2007**, *111*, 7812–7824. [[CrossRef](#)]
39. Lin, Y.C.; Chipot, C.; Scheuring, S. Annexin-V stabilizes membrane defects by inducing lipid phase transition. *Nat. Commun.* **2020**, *11*, 230. [[CrossRef](#)]
40. Miyagi, A.; Chipot, C.; Rangl, M.; Scheuring, S. High-speed atomic force microscopy shows that annexin V stabilizes membranes on the second timescale. *Nat. Nanotechnol.* **2016**, *11*, 783–790. [[CrossRef](#)]
41. Bouter, A.; Gounou, C.; Berat, R.; Tan, S.; Gallois, B.; Granier, T.; d’Estaintot, B.L.; Poschl, E.; Brachvogel, B.; Brisson, A.R. Annexin-A5 assembled into two-dimensional arrays promotes cell membrane repair. *Nat. Commun.* **2011**, *2*, 270. [[CrossRef](#)]
42. McNeil, P.L.; Kirchhausen, T. An emergency response team for membrane repair. *Nat. Rev. Mol. Cell Biol.* **2005**, *6*, 499–505. [[CrossRef](#)]
43. Jimenez, A.J.; Maiuri, P.; Lafaurie-Janvore, J.; Perez, F.; Piel, M. Laser induced wounding of the plasma membrane and methods to study the repair process. *Methods Cell Biol.* **2015**, *125*, 391–408. [[CrossRef](#)] [[PubMed](#)]
44. Sonder, S.L.; Boye, T.L.; Tolle, R.; Dengjel, J.; Maeda, K.; Jaattela, M.; Simonsen, A.C.; Jaiswal, J.K.; Nylandsted, J. Annexin A7 is required for ESCRT III-mediated plasma membrane repair. *Sci. Rep.* **2019**, *9*, 6726. [[CrossRef](#)]
45. Scheffer, L.L.; Sreetama, S.C.; Sharma, N.; Medikayala, S.; Brown, K.J.; Defour, A.; Jaiswal, J.K. Mechanism of Ca(2+)-triggered ESCRT assembly and regulation of cell membrane repair. *Nat. Commun.* **2014**, *5*, 5646. [[CrossRef](#)] [[PubMed](#)]
46. Moreno-Pescador, G.; Qoqaj, I.; Thusgaard Ruhoff, V.; Iversen, J.; Nylandsted, J.; Bendix, P.M. Effect of local thermoplasmonic heating on biological membranes. In Proceedings of the SPIE NANOSCIENCE + ENGINEERING, San Diego, CA, USA, 11–15 August 2019. [[CrossRef](#)]

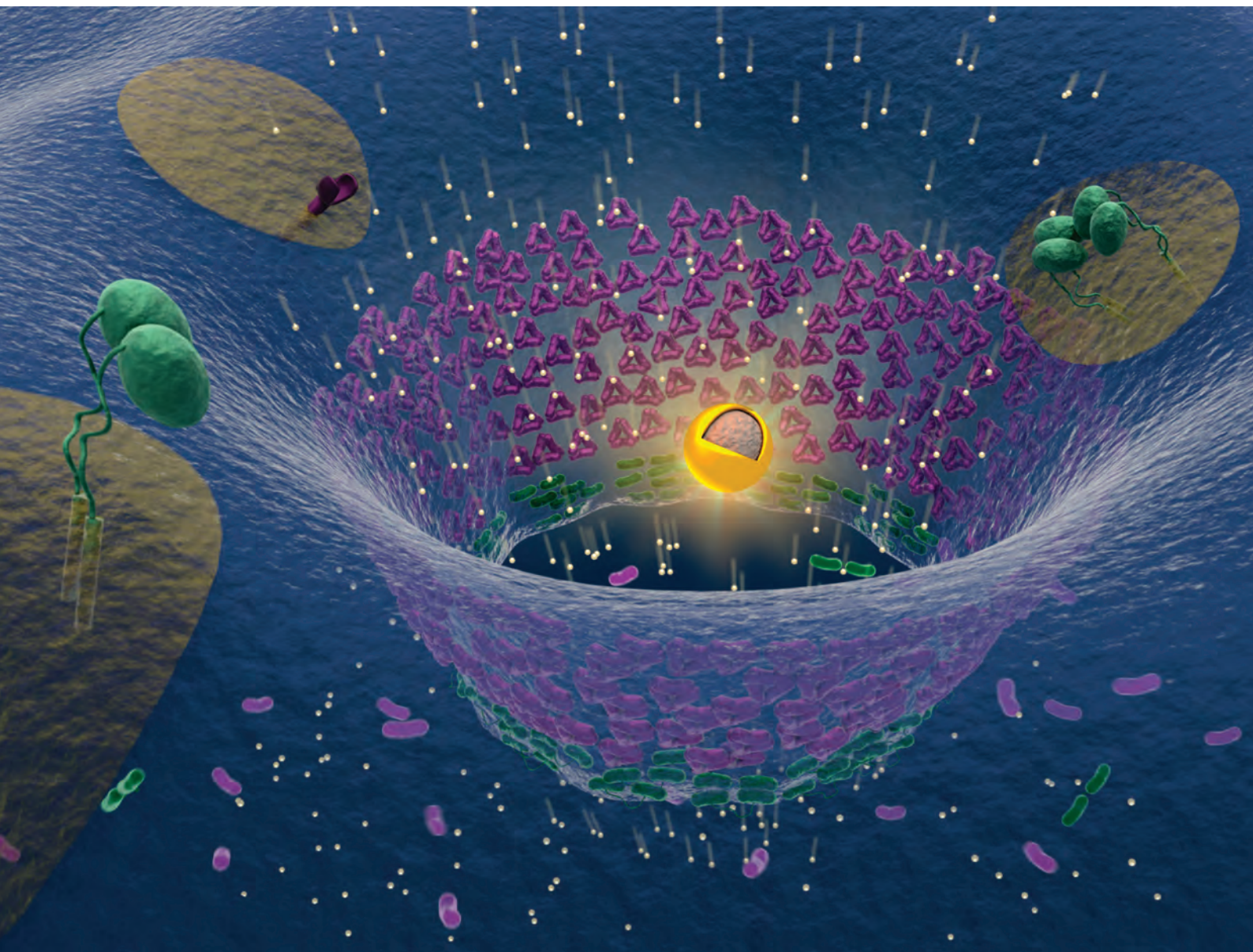
47. Bahadori, A.; Oddershede, L.B.; Bendix, P.M. Hot-nanoparticle-mediated fusion of selected cells. *Nano Res.* **2017**, *10*, 2034–2045. [[CrossRef](#)]
48. Rorvig-Lund, A.; Bahadori, A.; Semsey, S.; Bendix, P.M.; Oddershede, L.B. Vesicle Fusion Triggered by Optically Heated Gold Nanoparticles. *Nano Lett* **2015**, *15*, 4183–4188. [[CrossRef](#)]
49. Yeheskely-Hayon, D.; Minai, L.; Golan, L.; Dann, E.J.; Yelin, D. Optically induced cell fusion using bispecific nanoparticles. *Small* **2013**, *9*, 3771–3777. [[CrossRef](#)]
50. Minai, L.; Yeheskely-Hayon, D.; Golan, L.; Bisker, G.; Dann, E.J.; Yelin, D. Optical nanomanipulations of malignant cells: Controlled cell damage and fusion. *Small* **2012**, *8*, 1732–1739. [[CrossRef](#)]
51. Bahadori, A.; Moreno-Pescador, G.; Oddershede, L.B.; Bendix, P.M. Remotely controlled fusion of selected vesicles and living cells: A key issue review. *Rep. Prog. Phys.* **2018**, *81*, 032602. [[CrossRef](#)]
52. Lukianova-Hleb, E.; Hu, Y.; Latterini, L.; Tarpani, L.; Lee, S.; Drezek, R.A.; Hafner, J.H.; Lapotko, D.O. Plasmonic nanobubbles as transient vapor nanobubbles generated around plasmonic nanoparticles. *ACS Nano* **2010**, *4*, 2109–2123. [[CrossRef](#)] [[PubMed](#)]



© 2020 by the authors. Licensee MDPI, Basel, Switzerland. This article is an open access article distributed under the terms and conditions of the Creative Commons Attribution (CC BY) license (<http://creativecommons.org/licenses/by/4.0/>).

Nanoscale

rsc.li/nanoscale



ISSN 2040-3372

PAPER

Guillermo S. Moreno-Pescador, Poul Martin Bendix *et al.*
Thermoplasmonic nano-rupture of cells reveals annexin V
function in plasma membrane repair



Cite this: *Nanoscale*, 2022, **14**, 7778

Thermoplasmonic nano-rupture of cells reveals annexin V function in plasma membrane repair†

Guillermo S. Moreno-Pescador,^a Dunya S. Aswad,^a Christoffer D. Florentsen,^a Azra Bahadori,^b Mohammad R. Arastoo,^a Helena Maria D. Danielsen,^a Anne Sofie B. Heitmann,^c Theresa L. Boye,^c Jesper Nylandsted,^{c,d} Lene B. Oddershede^a and Poul Martin Bendix^a*

Maintaining the integrity of the cell plasma membrane (PM) is critical for the survival of cells. While an efficient PM repair machinery can aid survival of healthy cells by preventing influx of extracellular calcium, it can also constitute an obstacle in drug delivery and photothermal therapy. We show how nanoscopic holes can be created in a controlled fashion to the cell's plasma membrane, thus allowing identification of molecular components which have a pivotal role in PM repair. Cells are punctured by laser induced local heating of gold nanostructures at the cell surface which causes nano-ruptures in cellular PMs. Recruitment of annexin V near the hole is found to locally reshape the ruptured plasma membrane. Experiments using model membranes, containing recombinant annexin V, provide further biophysical insight into the ability of annexin V to reshape edges surrounding a membrane hole. The thermoplasmonic method provides a general strategy to monitor the response to nanoscopic injuries to the cell surface which offer new insight into how cells respond to photothermal treatment.

Received 16th December 2021,
Accepted 31st March 2022

DOI: 10.1039/d1nr08274d

rsc.li/nanoscale

Introduction

The eukaryotic membrane repair system involves cytoskeletal reorganization, membrane fusion events and membrane replacement.¹ Several members of the annexin (ANXA) protein family are Ca²⁺-sensitive phospholipid binding proteins that regulate endomembrane processes including vesicle fusion, segregation and repair.^{1,2} For example, metastatic breast cancer cells require enhanced PM repair to cope with increased frequency of injury.³ To cope with such surface stresses cells respond rapidly with recruitment of several types of proteins. Components of this molecular repair kit involves several members of the annexin protein family. The ANXA2/S100A11 complex has been shown to assist in resealing the PM by enabling polymerization of cortical F-actin and excision of damaged membrane.³ Recent results also show that ANXA4 and ANXA6 act in the early phase of PM repair in cervical and

breast cancer cells where they modulate wound edges by inducing curvature and constriction force, respectively.²

Annexin proteins exist predominantly in the cytosol of the cell and have been found to localize to sites of membrane repair activated by influx of calcium ions during – e.g. a membrane rupture.⁴ Upon binding of free Ca²⁺, annexin undergoes conformational changes, allowing it to bind to the negatively charged phospholipids abundant in the inner leaflet of the PM.^{5,6} The full scheme of the repair processes and whether they are conserved across different cellular tissues are still open questions. The specific role of annexins in membrane repair is not well understood which is mainly due to a focus on recruitment of proteins rather than the biophysical function which the proteins have on the ruptured membrane. Nevertheless, there are several proposed models of how annexins carry out cell membrane repair together with other proteins.¹ Recently, it was shown that several annexins have the capacity to both sense and induce curvature in model membranes^{2,7,8} and also to form protein scaffolds on membranes.^{7,9} However, the implications from these biophysical effects on repair in living cells remain elusive in part due to the difficulty in performing and imaging nanoscopic ruptures. Current approaches for inducing leakage of the PM include mechanical shaking using large beads,¹⁰ pulsed lasers⁶ or the use of bacterial toxins which insert into the PM and induce influx of Ca²⁺.¹¹ Pulsed lasers offer an effective way to disrupt the membranes, but may cause large holes and also

^aNiels Bohr Institute, University of Copenhagen, Blegdamsvej 17, 2100 København Ø, Denmark. E-mail: moreno@nbi.ku.dk, bendix@nbi.ku.dk

^bCenter for Chromosome Stability, University of Copenhagen, Blegdamsvej 3B, 2200 København N, Denmark

^cDanish Cancer Society Research Center, Strandboulevarden 49, DK-2100 Copenhagen, Denmark

^dDepartment of Cellular and Molecular Medicine, Faculty of Health Sciences, University of Copenhagen, DK-2200 Copenhagen N, Denmark

† Electronic supplementary information (ESI) available. See DOI: <https://doi.org/10.1039/d1nr08274d>

inflict damage to internal structures which are irradiated by the high-power pulses.

To elucidate the mechanism of action which annexins have in PM repair it is critical that nanoscopic holes can be applied to the PM in a controlled manner without extensive damage to the interior of the cells. We have developed a novel experimental assay based on thermoplasmonics to study the role of ANXAs in PM repair in live cells without compromising their viability which will allow for investigating some of the open questions regarding ANXAs role in the complex PM repair machinery.

Results and discussion

Thermoplasmonic injury to the PM

Rupture or damage of the cell's PM causes recruitment of a number of different membrane repair associated proteins to the site of injury. Using a combination of inorganic plasmonic nanoparticles and a highly focused $\lambda = 1064$ nm laser coupled to a confocal microscope, we examined the ANXA5 protein responses to PM injury.

By optically heating plasmonic nanoparticles^{12–15} near the PM (Fig. 1A/B/C) we formed nanoscopic holes in the PM of living cells. Local puncture of the PM leads to influx of Ca^{2+} which mediates binding of ANXA5 to the PM.¹⁶ Irradiation of plasmonic nanoparticles provides an efficient way to perturb the membrane of cells locally and has been successfully demonstrated as a method for: loading nanoparticles into GUVs¹⁷ and cells,^{18,19} photothermal-induced expression of proteins at the single cell level²⁰ or even fusing cells and membranes.²¹

Visualization of the cellular response to optically triggered local PM perturbation was carried out while imaging using confocal fluorescence microscopy. To achieve the best imaging of the ANXA5 response to rupture we chose to immobilize the nanoparticles on the surface underneath the cell. A near infrared laser ($\lambda = 1064$ nm) was used to irradiate gold nanoparticles (AuNP, $d = 200$ nm) or gold nanoshells (AuNSs, $d = 150$ nm). The AuNS are designed to be resonant with the NIR light and hence exhibit maximal absorption in the NIR region. The AuNPs are not resonant with the laser wavelength used here, but due to their large size and large amount of gold they exhibit higher order resonances and high absorption even in the NIR wavelength regime (see Fig. 1D and E). The solid AuNPs have been found to exhibit a higher thermal stability than the AuNSs,^{22,23} but in order to achieve the same heating as the AuNSs their diameter has to be slightly larger.

The high temperature region surrounding irradiated NPs extends only ~ 100 nm from the nanoparticle, see Fig. 1D and E.²⁴ This makes it possible to apply extremely localized and precise ruptures to the PM which are highly localized in all three dimensions. The exact size of the rupture remains to be investigated, but the thermal response of membranes has been investigated in both model membranes²⁵ and cells.^{26,27} Cell punctures will involve some denaturing of the underlying membrane actin cortex, but due to the extremely short

exposure of heat in our experiments it is uncertain how much the actin is influenced by the thermal pulse. However, in ref. 28 and 29 it was shown that NPs reaching temperatures of 200 °C locally ablated a region with a radius of approx. 200 nm which gives an upper limit of the potential damage caused by the transient (~ 1 second) heating carried out in this work. The effect from pulsed lasers, used in other studies² of membrane repair, is quite different since a laser can ablate internal cell material along the path of the laser light. Our novel approach allows us to test the cellular response to PM ruptures of nanoscopic dimensions in both cells and model membranes. Nanoscopic holes of this dimension may be frequently occurring during aggressive cellular migration and invasion^{1,30} and therefore investigation of protein recruitment in response to nanoscopic ruptures are relevant for understanding how living cells cope with ruptures.

The assay described in Fig. 1A was used to investigate the cellular rescue response to plasmonic injuries underneath human embryonic kidney 293T (HEK293T) cells on a glass surface. By immobilizing nanoparticles on the surface of the glass and seeding the cells on top, a two dimensional visualisation of the injury was obtained. Complementary, by trapping an AuNP and approaching the cell laterally, injuries at side of the cell could also be obtained (see Fig. 1C) which provides additional insight into how cells cope with damage of a PM not adhered to a substrate. In both cases the results show up-concentration of ANXA5 in a ring-like fashion around the wound site in HEK293T cells (see Fig. 1B, C, F and G).

To minimize the thermal effect on the cell we only briefly irradiated the NP for ~ 1 s which minimizes damages to proteins which typically need more time to unfold. The potential damage due to such a brief exposure will be highly localized as shown in ref. 28 and 27. The ANXA ring subsequently formed during a few seconds as shown in Fig. 1F and G.

The recruitment of protein to the site of injury is consistent with previously reported data of how a similar protein, ANXA4, responds to PM injuries applied using a pulsed laser source.² ANXA4 was recruited to the site of injury and the curvature induction effect of ANXA4 was proposed to curve the membrane away from the site of injury. The protein-shape and protein-structure of ANXA5 (Fig. 1H) resembles ANXA4 and we therefore anticipate that the internal membrane binding of ANXA5 around the holes in our experiments would generate some curvature in the membrane as schematically indicated in Fig. 1G and H.

Calculation of the ANXA ring sizes was based on the full-width-half-maximum of the intensity line profile as depicted in Fig. 2A. The resulting radii for a collection of more than 130 cells damaged *via* plasmonic heating of AuNPs and AuNSs are shown in Fig. 2B. Following irradiation, all injuries were observed to recruit ANXA5 to the wound site within seconds (see Fig. 1F and G), visible as a ring surrounding the wound. The ANXA5 ring size varied from hundreds of nanometers to several microns, suggesting that the injury varied from cell to cell due to slight differences in heating caused by the manual positioning the nanoparticle in the laser focus. Whether there

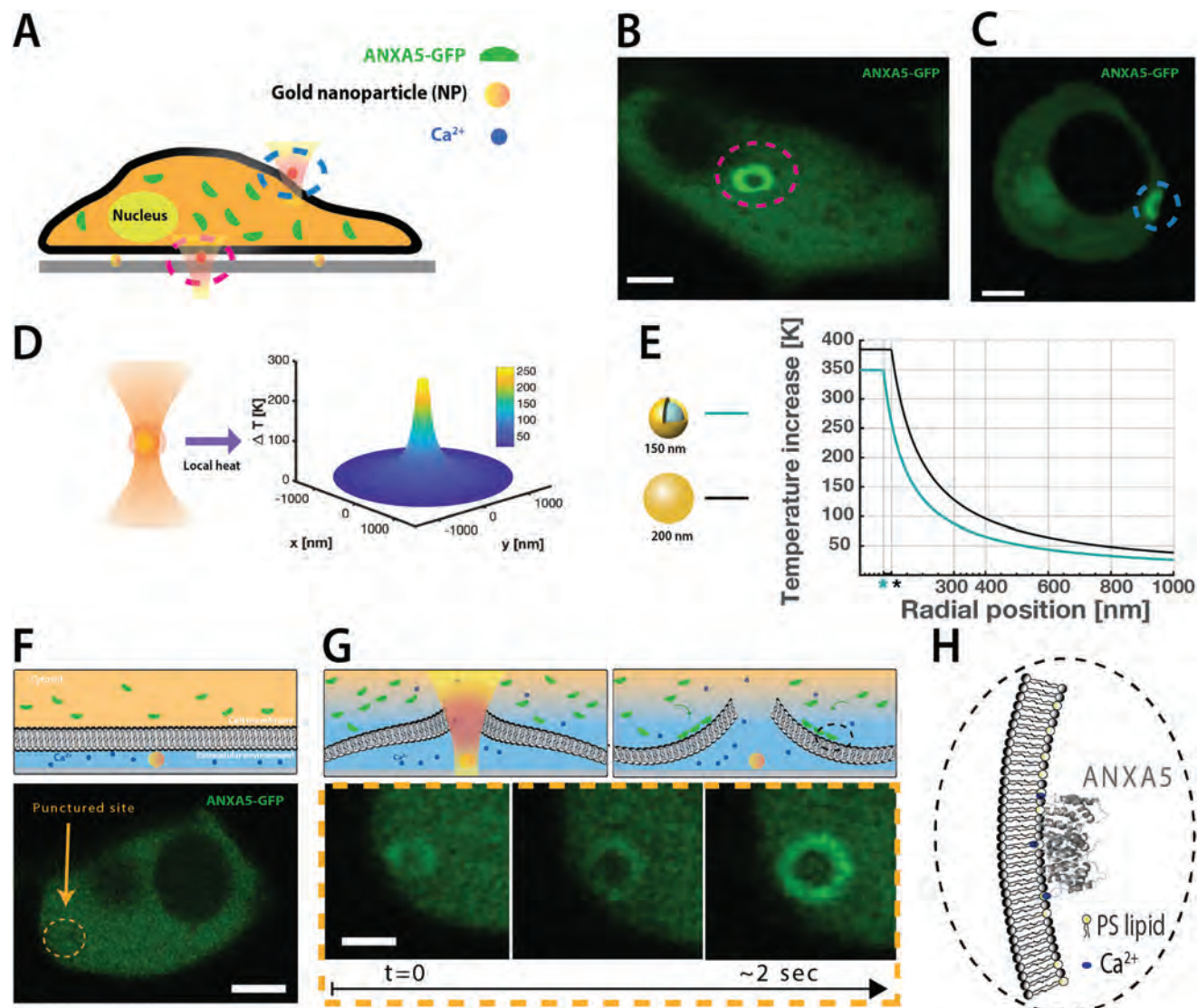


Fig. 1 Outline of the experimental assay for applying a nanorupture to a plasma membrane. (A) Schematic illustration of a ANXA5-GFP transfected cell plated on a glass with immobilized AuNSs. (B) Fluorescence confocal image from a ANXA5-GFP transfected HEK293T cell injury located below the cell created by irradiation of an immobilized AuNP. Scale bar is 5 μm . (C) Fluorescence confocal image from a ANXA5-GFP transfected HEK293T cell showing an injury on the side of the cell using an optically trapped AuNP. Scale bar is 5 μm . (D) Irradiation of a AuNS with a NIR laser induces localized heating from the particle. (E) The heating profile of two different size NPs (AuNP, $d = 200 \text{ nm}$ and AuNS, $d = 150 \text{ nm}$) used in this work at a laser intensity of $I = 7.6 \times 10^{10} \text{ W m}^{-2}$. Asterisks in the temperature profile mark the radii of the two types of particles. (F) Before the NPs are irradiated with NIR laser light, the plasma membrane is firmly adhered on top of the particles. Scale bar is 5 μm . (G) After the thermoplasmonic rupture, ANXA5-GFP up-concentrates in a ring-like fashion around the wounded site (confocal image in the bottom part) in less than two seconds after irradiation. Scale bar is 2 μm . (H) Illustration of Ca²⁺ mediated binding of ANXA5 to the PM. Crystal structure of ANXA5 from the PDB entry: 1a8a.

could exist differences in repair efficiency due to the cell cycle stage, the hole size in general or due to the amount of transfected ANXA5, is something that should be addressed in future experiments.

Cell viability was detected by monitoring the binding of ANXA5 on internal membranes. Excessive influx of Ca²⁺ leads to translocation of ANXA5 from the cytoplasm to internal membranes including the nuclear membrane and was detected in a few cases. In these few cases cell death occurred within a few minutes and such data were not used to quantify the shape of

the ANXA5 ring. The vast majority of thermoplasmonically ruptured cells showed no signs of ANXA5 binding to internal membranes, distal to the site of injury, even two hours after irradiation which is a sign of successful membrane repair.

For several injuries, only a fraction of a ring shape was observed (see ESI Fig. S1 panel D and G[†]). This phenomenon might be because the membrane disruption happens in an unfavorable way in parts of the injury, an asymmetric adhesion of the PM to the substrate or interactions with the actin cortex underlying the PM.

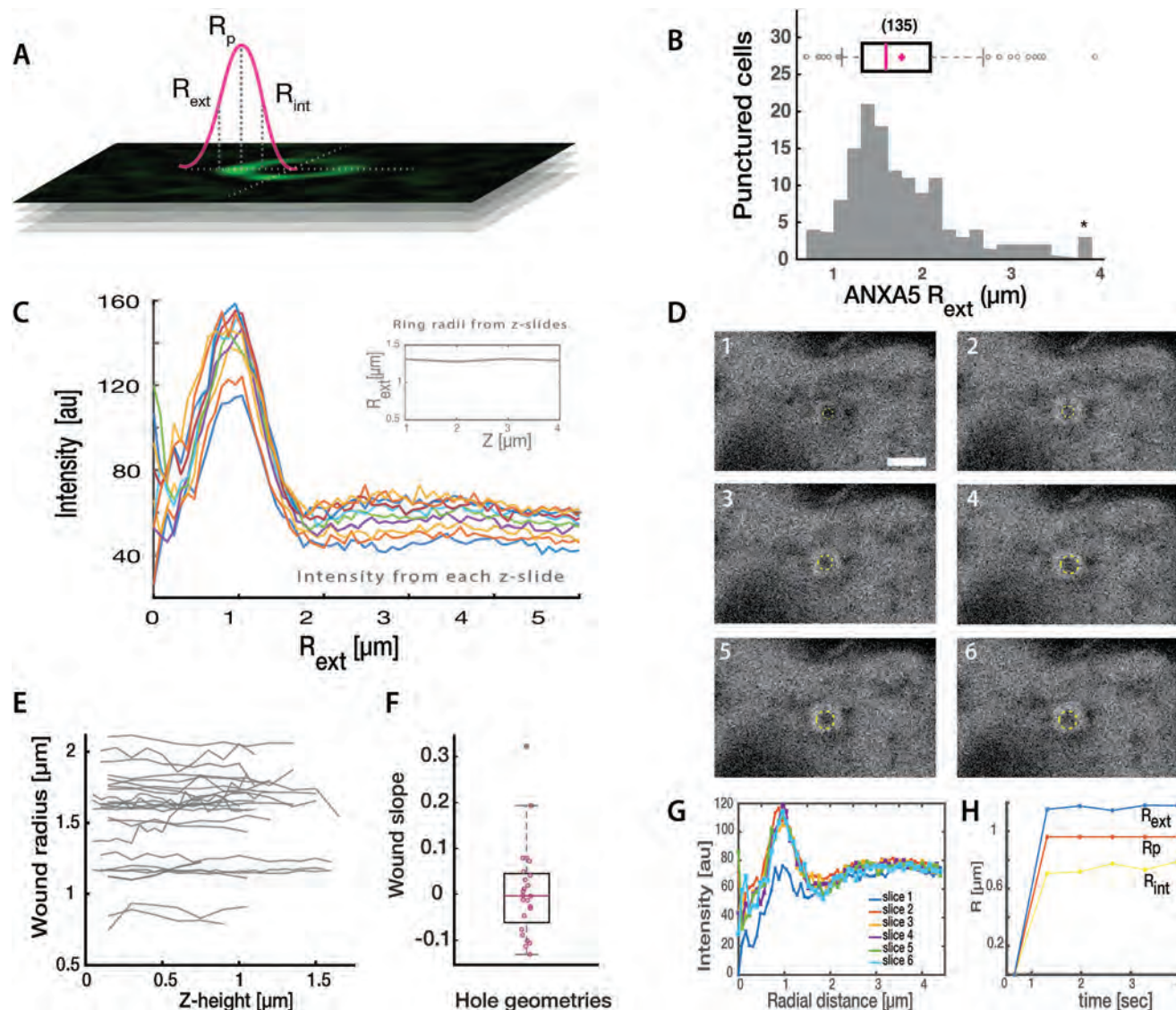


Fig. 2 Quantification of the ANXA5-GFP ring sizes surrounding the wounded sites. (A) Schematic of how the analysis is carried out with regard to radius determination. (B) Histogram of the ANXA5 ring radii measured for all experiments. A boxplot from the histogram has been placed on to the upper part of the graph. 135 cell punctures were analyzed. (C) Fluorescence intensity line profiles across the ANXA5-GFP rings for each slice of a z-stack. The inset shows the variation on the radius size along each slice of the z-stack. (D) Hole evolution over time. The time dependent hole evolution shows how ANXA5-GFP is upconcentrated immediately after injury. The ANXA5-GFP signature remained stationary for minutes following termination of heating. Scale bar is 2 μm . (E) Wound radii determined by the analysis method presented in (A) as a function of wound depth. 23 z-stacks from punctured-wounds were analyzed. (F) Slope of ring radius *versus* height extracted from the analysis data in (E). (G) Fluorescence intensity line profiles across the ANXA5-GFP rings for each time frame (0.66 seconds of time interval per frame). (H) Time evolution of the ANXA5-GFP ring radii from (D) calculated from the data in (G).

It has been reported that different members of the annexin family are able to roll membranes supported by a substrate² as well as being able to sense curvature.^{7,9} Such biophysical effects could lead to rolling of the membrane edges away from the hole and lead to a ring shaped structure if the membrane was free to roll.

To further investigate the actual three dimensional shape of the ANXA5 ring we performed confocal microscopy of each injury at several positions along the axial direction. ANXA5 rings induced by the thermoplasmonic-membrane rupture showed no change of the ring-size with height, see Fig. 2C.

The intensity profiles shown in Fig. 2C were observed in several other z-stacks and the extracted radius *versus* height was calculated for each injury, see Fig. 2E. The procedure behind the calculation of the ring sizes was the same as shown in Fig. 2A, keeping the same center coordinates for the ring in all images within the z-stack. From the analysis of the radii of each z-stack (see Fig. 2E), the slope of the resulting radius profile was calculated. A slope of zero value indicates no change in the radius of the ANXA5-ring along the z-direction.

As shown in Fig. 2F the slopes of radius *versus* height was close to zero in all cases. This strongly suggests that under these conditions the ANXA5 does not significantly bend the cell surface towards the cytoplasm, but rather forms a cluster of ANXA5 surrounding the site of injury. To test for a possible presence of a membrane roll resulting from ANXA5 binding to the PM we imaged the time evolution of the ring formation. As shown in Fig. 2D, G and H the ring reaches its final radius within ~ 1 s and within the time resolution of a confocal microscope we see no gradual increase in the width of the ring which is expected to be the case if the PM was rolling away from the site of injury. We note that rolling may still occur within the first second and level off due to adhesive contact to the substrate and the internal actin cortex.

To gain further insight into the response of cells when punctured at a location which is not in contact with an adhesive substrate, we also punctured cells from the side using plasmonic nanoparticles optically trapped in three dimensions. Such experiments also show an upconcentration of ANXA5 around the site of injury, see Fig. 1C and ESI Fig. S6.† Interestingly, these experiments occasionally showed a slight inward bending of the area enriched in ANXA5 as shown in Fig. 1C. This inward shape which was not visible when the ruptured site was in contact with the substrate could be a signature of an onset of rolling for a PM which is free to roll without adhesive resistance from a substrate.

To gain further mechanistic insight into the ability of membranes to roll following a rupture we used giant unilamellar vesicles (GUVs) encapsulating recombinant annexins as a minimal model system. GUVs can be readily punctured using thermoplasmonics which has been utilized for vesicle fusion²¹ and permeability studies of model membranes.³¹ Following the same experimental approach to generate punctures we encapsulated recombinant ANXA5-GFP or the cognate protein ANXA4-GFP inside GUVs by using the polyvinyl alcohol (PVA) gel hydration method (see ESI†). Briefly, a PVA gel coated glass slide is covered with the desired lipid mixture and incubated with a protein-containing growing buffer for GUV formation followed by isolation of the GUVs in an observation buffer.

The presence of millimolar concentrations of Ca^{2+} ions in the observation buffer facilitates the binding of ANXA5 to the internal membrane due to residual leakage of ions across the membrane during the handling of the GUVs like pipetting (see Fig. 3 and ESI Fig. S5†). A total number of $N = 11$ GUVs were punctured and two very distinct effects were observed consistently upon membrane rupture: (i) more severe ruptures using $P \approx 120$ mW and applied to GUVs encapsulating ANXA5, resulted in expansion of the hole and with an increasing membrane roll forming at the rim of the hole as shown in Fig. 3D. Moreover, using recombinant ANXA4 we were able to replicate ring-like upconcentration scaffolds in GUVs – see Fig. 3C. (ii) Under moderate heating exposure of $P \approx 50$ mW, small pores were formed and closed after a short time and we observed invaginating buds of the membrane forming inside the vesicle (Fig. 3B). There was a remarkable up-concentration

of ANXA5 in the neck region of this bud-like structure created after membrane rupture – see yellow circled area in Fig. 3B which is consistent with the curvature recruitment reported for ANXA5.⁹ The buds were not successfully released from the membrane after wound closure. Application of small injuries several times at the same location, resulted in accumulation of inward pointing buds before vesicle collapse (Fig. 3E).

Furthermore, control experiments (ESI Fig. S7†) done in GUVs only labelled with a lipophilic dye DiD and with the same lipid composition, showed that the membrane budding, rolling and bending does not occur in similar thermoplasmonic experiments when ANXAs are not bound to the membrane. Instead, holes sealed rapidly upon injury without any membrane deformation visible during imaging. The rapid closure of such holes is mediated by the line tension around the rim of the hole and is only possible when the membrane tension is not too high sufficiently high to further expand the hole.

These experiments embody very well the different effects that ANXAs have on pure membranes where no interactions with the cytoskeleton are present. The apparent rolling of membranes away from the site of injury shown in Fig. 3C and D and also for the membrane signal in ESI Fig. S5,† is a signature of the curvature induction by ANXA4 and A5 reported for supported bilayers^{2,7} and demonstrated here in a more biologically relevant three dimensional geometry. Additionally, accumulation of ANXA5 was observed at the neck regions connecting the spherical bud to the GUV membrane which is a clear signature of membrane curvature sensing by ANXA5 (yellow circle in Fig. 3B). The mechanism behind the budding events is unknown, but could result from ANXA5 induced inward bending of the membrane surrounding the hole into a funnel shape, followed by resealing of the funnel and subsequent formation of the spherical bud. Repeated injuries resulted in a several buds which were not released into the GUV lumen, but rather clustered near the site of injury Fig. 3E.

Several annexins have been shown to aggregate membrane vesicles and hence they have the ability to bridge or cluster apposing membranes as shown in Fig. 3E. ANXA5 isolated from chicken^{32,33} and human ANXA2³⁴ have been reported to mediate contact between apposing membranes through interactions between the N-terminals in the proteins. We have also observed the same interaction in human ANXA5. When recombinant ANXA5 was added in a 2 mM Ca^{2+} buffer it would bind to the GUV's membrane and in time aggregate the vesicles, see ESI Fig. S3.† Such interactions could well play a role in both the vesicle clustering and rolling behavior observed in Fig. 3.

Our experiments *ex vivo* and in model membranes show that ANXA5 mainly cluster around the site of injury in a ring like form. It is difficult from the current data to conclude whether the extensive rolling observed in model membranes (Fig. 3) also takes place in cells. Cells do indeed have an actin cortex underlying the PM which could inhibit the efficient rolling observed in model membranes exposed to ANXA5. However, we propose a more complex model of how ANXA5 could stabilize the PM around the wound area based on the results presented here – see Fig. 4B. Initial rolling will be coun-

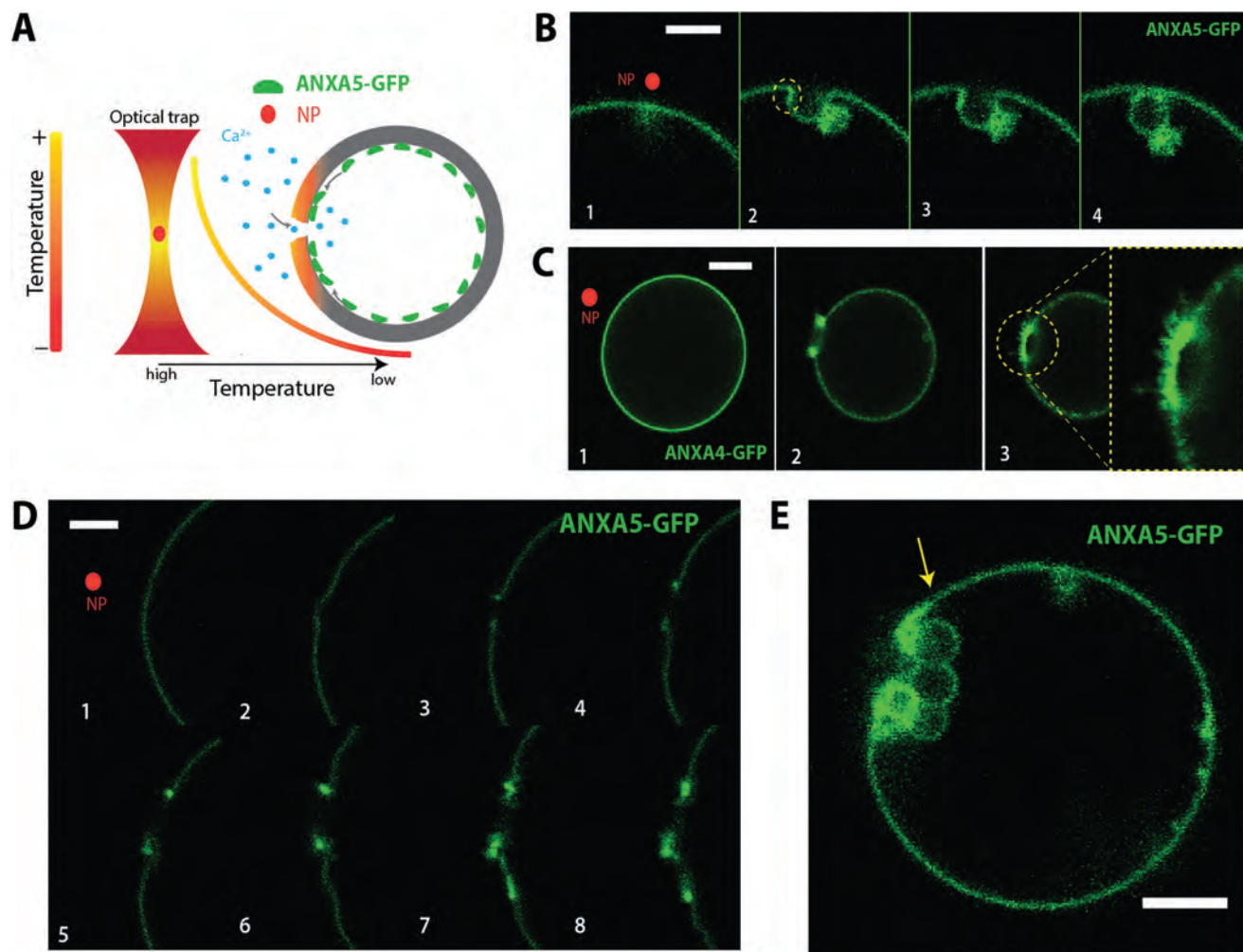


Fig. 3 Plasmonic rupture in GUVs with encapsulated GFP-ANXA5 or GFP-ANXA4. (A) Schematic illustration of the experiment with ANXA5 encapsulated in a GUV. A trapped AuNS in the vicinity of the GUV will generate enough heat to provoke rupturing of the membrane when sufficiently close. (B) Montage with the time evolution of a hole created in a GUV with ANXA5 bound to the membrane. Scale bar is 2 μm. (C) Montage with the time evolution of a GUV rupture with the cognate ANXA4 protein bound to the membrane. Scale bar is 10 μm. (D) Montage with the time evolution of a GUV rupture with ANXA5 bound to the membrane. Scale bar is 5 μm. (E) GUV after repeated thermoplasmonic puncturing. Scale bar is 10 μm.

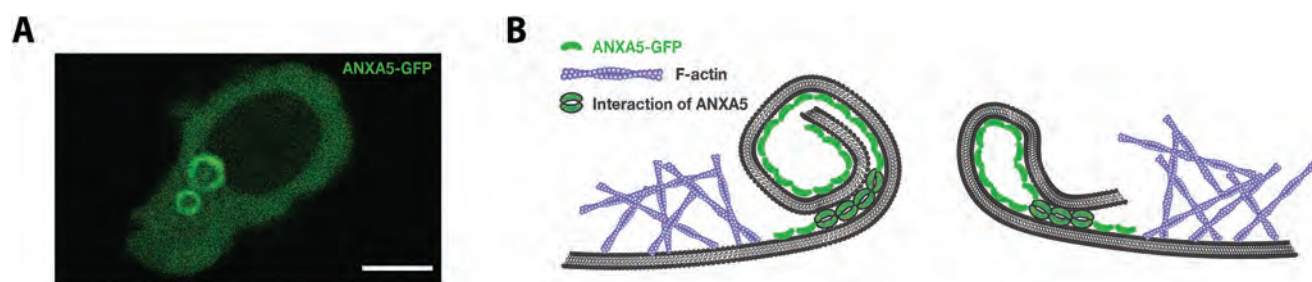


Fig. 4 Proposed model for the structure and action of ANXA5 at a wounded site. (A) Confocal fluorescence images from a thermoplasmonic experiment in ANXA5 transfected cells with two puncture sites. Scale bar is 10 μm. (B) Binding of ANXA5 to free edges induces local bending and interaction of ANXA5 molecules with the cytoskeleton arresting the membrane rolling deformation and stabilizing the wound. Once the membrane rupture is stabilized the leakage could be prevented by clustering of internal vesicles, not shown by this schematic.

teracted by the presence of the actin network, but the PM could be allowed to fold back onto itself by two ANXA5 proteins interacting *via* their N-terminals as shown in ESI Fig. S3.†

Moreover, extensive binding of ANXA5 to the PM surrounding the hole is known to result in a connected protein scaffold⁶ and could counteract expansion of the hole. This would allow

the cell to repair the hole through other mechanisms like clustering and fusion of internal vesicles to the ruptured membrane. Such a mechanism is in good agreement with the heterogeneity of the ANXA5-ring we found in our experiments.

Conclusion

The results presented here reveal how cells activate a molecular response to a photo thermal injury. These results are highly relevant to the emerging field of photo thermal therapy and offers an assay to investigate and identify molecular players employed by cells to survive local injuries. Cells are shown here to exhibit rapid recruitment of ANXA5 in response to membrane ruptures induced by thermoplasmonics. Upon irradiation of plasmonic gold nanostructures located on the plasma membrane, Ca^{2+} leaks into the cytoplasm and triggers ANXA5 binding to the internal PM. ANXA5 is found to form long lasting ring-like structures around the site of injury within few seconds following rupture of the PM. The fluorescent signal from the ring could arise from folding of the ANXA5 bound membrane caused by the curvature generation by the protein. The use of plasmonic puncturing of the cell surface combined with confocal imaging offers an excellent platform for identifying molecular components involved in surface repair and this approach should be extended in the future with novel nanoparticles like nanorods.³⁵ Considering the efficient uptake of nanoparticles in cells we envision that the precision provided by this approach will allow us to resolve the mechanisms employed by cells to heal internal damage in nuclear or endosomal membranes.

Experimental

Cell culture

HEK293T cells (ATCC) were cultured in Dulbecco's modified Eagle's medium supplemented with 10% fetal bovine serum (FBS) and 100 units per mL penicillin and $100 \mu\text{g mL}^{-1}$ streptomycin (Fisher). The cells were maintained in a humidified incubator with 5% CO_2 at 37 °C. Expression plasmid with turbo-GFP C-terminal tag containing human ANXA5 cDNA were purchased from OriGene Technologies. HEK293T cells were transiently transfected with the indicated plasmid using Lipofectamine LTX transfection reagent (Fischer) according to the manufacturer's protocol 24 h before they were used in experiments.

Reagents

Gold nanoparticle colloid suspension was prepared by adding 1 μL AuNP's (150 nm or 200 nm) from stock solution to 100 μL observation buffer and sonicating for 2–5 min before use. The AuNS are coated with Poly(ethylene glycol) (PEG) to prevent aggregation of the particles and stabilize them in solution. Gold nanoshells (AuNS) were also used, their core consisting

of a 120 ± 4 nm silica sphere upon which a thin gold shell (20 ± 7 nm) had been grown resulting in a total diameter of ~ 160 nm (Nanocomposix, CA USA). To generate C-terminal GFP-tagged recombinant Annexin A5 (ANXA5) protein, ANXA5 cDNA was subcloned into pETM11SUMO3sfGFP.³⁶ Proteins were produced using immobilized metal-affinity chromatography (IMAC) followed by fast protein liquid chromatography (FPLC).

Surface coating with particles

The nanoparticles used for the experiments were prepared a day prior to imaging. First an aliquot of particles was sonicated for 20–30 minutes to minimize aggregation. Poly-L-lysine (PLL) (Gibco) was used to make the particles and cells stick better to the surface of the microwell (MatTek 35 mm glass bottom dish). 500 μL PLL was added to the microwell and incubated for 10 minutes. The well was washed with distilled water (Gibco) and dried inside a flowhood. When the microwell was dry, the particles were added to the microwell together with 500 μL of DMEM.

Optical trapping and imaging

Confocal imaging was performed on a Leica SP5 confocal microscope into which an optical trap, based on a 1064 nm laser (Spectra Physics J201-BL-106C), was implemented.³⁷ Additionally an *xyz* nm-precision piezostage from Mad City Labs (USA) Nano-LP Series was also added to the microscope. Optical trapping was done at the focal plane of the microscope and by using a Leica PL APO, NA = 1.2, 63 \times water immersion objective to tightly focus the laser light. The optical trap was stationary, but the trap could be moved relative to the GUVs by translating the sample which was mounted on a piezoelectric stage (PI 731.20, Physik Instrumente, Germany) allowing lateral movements with nanometer precision. A glass bottom open chamber or microwell, containing either the GUVs or HEK293T cells, molecular fluorescent probes and gold nanoparticles, was mounted on the microscope and kept at room temperature during the experiment. The 488 nm argon laser line was used to excite the GFP fluorophores. To detect the scattered and reflected light from the AuNPs, a 613 nm or 476 nm laser line was used in reflection mode.

Plasmonic heating

The temperature profile around an irradiated NP can be found by solving the heat transfer equation³⁸ where the local heat intensity comes from light dissipation inside the irradiated NP,³⁹ the temperature increase $\Delta T(r)$ can be written as a function of distance to the source (r) as:⁴⁰

$$\Delta T(r) = \frac{VQ}{4\pi kr}, \quad r > R, \quad (1)$$

where R is the radius of the spherical NP, k is the thermal conductivity of water ($0.58 \text{ W m}^{-1} \text{ K}^{-1}$ in water at room temperature), V is the volume of the particle and Q is the local heat dissipation.⁴¹ From ref. 42, eqn (1) can be re-written

to relate the increase of temperature to the absorption cross section C_{abs} as

$$\Delta T(r) = \frac{IC_{\text{abs}}}{4\pi\kappa r}. \quad (2)$$

$\Delta T(r)$ is the temperature increase relative to ambient temperature and κ is the thermal conductivity. $Q = IC_{\text{abs}}$ is a measure of the generated heat (the amount of heat produced per unit time and volume inside the NP), largely contributed by Joule heating inside the NP. I is the intensity of the laser irradiation at the sample plane. The temperature profile around an irradiated NP is well described by eqn (1), which reaches a steady state within tens of nanoseconds, satisfying Laplace's equation. The solution for the temperature gradient will be a simple function of distance, r , to the surface of the NP with radius of R .

Through Mie based calculations,⁴³ we can calculate the absorption cross section, C_{abs} , from which the temperature profiles of irradiated strongly absorbing nanoparticles⁴⁴ can be obtained. Fig. 1B shows eqn (2) plotted as a function of distance to the particle center. For the case of the AuNS, the optical cross sections were directly obtained from the Mie Theory Calculator implemented at the Nanocompositix website (*i.e.* <https://nanocompositix.com/pages/mie-theory-calculator>). To calculate the power per surface area at the particle we assume a beam waist size of 500 nm of the focal spot of the NIR laser.

Vesicle swelling

Polyvinyl alcohol gel (PVA) (5%, 50 mM sucrose, 25 mM NaCl/Tris) was heated at 60 °C for 20 min. Glass slides were first cleaned in ethanol and dried with ultra spray, followed by heating in an air Plasma Cleaner model Harrick Plasma cleaner PDC-002. 90 μL of warm PVA gel was applied on the clean glass slides, after which they were heated in a 50 °C oven for 50 min. Subsequently, the vesicles were grown on top of the prepared PVA glass slides. A 50 μL glass Hamilton syringe was cleaned in chloroform to ensure minimum contamination. 30 μL of prepared lipid mix (95% DOPC, 5% DOPS) was added on top of the PVA gel layer on the glass slides. The applied lipid mix was dried with nitrogen for 30 seconds followed by vacuum drying for 2 hours. A clean vesicle chamber was used to grow the vesicles. 350 μL growing buffer (NaCl 70 mM, Tris (pH 7.4) 25 mM, sucrose 80 mM) with or without recombinant annexin was added to the chamber on top of the PVA-coated glass slide and the vesicles were left to form for ~1 hour. 340 μL of vesicle and buffer solution was collected from the chamber and deposited in an Eppendorf tube. 300 μL observation buffer (NaCl 70 mM, Tris (pH 7.4) 50 mM, glucose 55 mM) were added for the vesicles to sink to the bottom.

Protein encapsulation

Annexin A5 (900 nM) was added to the prepared cover glass. Followed by an addition of the prepared growing buffer at room temperature (total volume of 300 μL) was then set to form vesicles encapsulating GFP tagged ANXA4 or ANXA5 for

~1 hour. The vesicle solution was collected by pipetting directly from the cover glass into an Eppendorf tube together with 1000 μL observation buffer. The vesicles were set to sink for 5 minutes followed by centrifugation at 600 rcf for 10 minutes at 13 °C. Subsequently the added observation buffer was carefully removed from the top and down to ensure minimal loss of GUVs and to remove excess annexin on the outside.

Data analysis

All images were analyzed using Matlab (The MathWorks, Inc., Natick, Massachusetts, United States). Temperatures calculated in Fig. 1D and E were plotted using Matlab and calculations were based on the Mie equations.⁴³ Fig. 2 was calculated using an in-house Matlab workflow that is available on request. All confocal microscopy images were processed using Fiji ImageJ distribution.^{45,46} Additionally, in ESI Fig. S1–S3 and S5–S7† FigureJ plugin⁴⁷ was used.

Author contributions

Guillermo Moreno-Pescador: original-draft preparation, investigation, data curation, formal analysis, visualization, supervision. Dunya S. Aswad: data curation, investigation. Christoffer D. Florentsen: data curation, formal analysis. Azra Bahadori: data curation, investigation. Mohammad R. Arastoo: data curation, visualization, validation, investigation. Helena Maria D. Danielsen: investigation. Anne Sofie B. Heitmann: resources. Theresa L. Boye: resources. Jesper Nylandsted: supervision, funding acquisition. Lene B. Oddershede: supervision, funding acquisition. Poul Martin Bendix: writing–review editing, supervision, funding acquisition, project administration.

Conflicts of interest

The authors declare no competing financial interest.

Acknowledgements

This work is financially supported by Danish Council for Independent Research, Natural Sciences (DFR-4181-00196), by a Novo Nordisk Foundation Interdisciplinary Synergy Program 2018 (NNF18OC0034936), by the Scientific Committee Danish Cancer Society (R90-A5847-14-S2), the Lundbeck Foundation (R218-2016-534) and a Lundbeck Foundation Center of Excellence (Biomembranes in Nanomedicine).

Notes and references

- 1 T. L. Boye and J. Nylandsted, Annexins in plasma membrane repair, *Biol. Chem.*, 2016, **397**, 961–969.
- 2 T. L. Boye, K. Maeda, W. Pezeshkian, S. L. Sønder, S. C. Haeger, V. Gerke, A. C. Simonsen and J. Nylandsted,

- Annexin A4 and A6 induce membrane curvature and constriction during cell membrane repair, *Nat. Commun.*, 2017, **8**, 1623.
- 3 J. K. Jaiswal, S. P. Lauritzen, L. Scheffer, M. Sakaguchi, J. Bunkenborg, S. M. Simon, T. Kallunki, M. Jäättelä and J. Nylandsted, S100A11 is required for efficient plasma membrane repair and survival of invasive cancer cells, *Nat. Commun.*, 2014, **5**, 3795–3713.
 - 4 A. Draeger, K. Monastyrskaya and E. B. Babiychuk, Biochemical Pharmacology, *Biochem. Pharmacol.*, 2011, **81**, 703–712.
 - 5 J. H. Lorent, K. R. Levental, L. Ganesan, G. Rivera-Longsworth, E. Sezgin, M. Doktorova, E. Lyman and I. Levental, Plasma membranes are asymmetric in lipid unsaturation, packing and protein shape, *Nat. Chem. Biol.*, 2020, **16**, 644–652.
 - 6 A. Bouter, C. Gounou, R. Bérat, S. Tan, B. Gallois, T. Granier, B. L. d'Estaintot, E. Pöschl, B. Brachvogel and A. R. Brisson, Annexin-A5 assembled into two-dimensional arrays promotes cell membrane repair, *Nat. Commun.*, 2011, **2**, 1–9.
 - 7 C. D. Florentsen, A. Kamp-Sonne, G. Moreno-Pescador, W. Pezeshkian, A. A. Hakami Zanjani, H. Khandelia, J. Nylandsted and P. M. Bendix, Annexin A4 trimers are recruited by high membrane curvatures in Giant Plasma Membrane Vesicles, *Soft Matter*, 2020, **17**, 308–318.
 - 8 T. L. Boye, J. C. Jeppesen, K. Maeda, W. Pezeshkian, V. Solovyeva, J. Nylandsted and A. C. Simonsen, Annexins induce curvature on free-edge membranes displaying distinct morphologies, *Sci. Rep.*, 2018, 1–14.
 - 9 G. Moreno-Pescador, C. D. Florentsen, H. Østbye, S. L. Sønder, T. L. Boye, E. L. Veje, A. K. Sonne, S. Semsey, J. Nylandsted, R. Daniels and P. M. Bendix, Curvature- and Phase-Induced Protein Sorting Quantified in Transfected Cell-Derived Giant Vesicles, *ACS Nano*, 2019, **13**, 6689–6701.
 - 10 N. Weisleder, N. Takizawa, P. Lin, X. Wang, C. Cao, Y. Zhang, T. Tan, C. Ferrante, H. Zhu, P.-J. Chen, R. Yan, M. Sterling, X. Zhao, M. Hwang, M. Takeshima, C. Cai, H. Cheng, H. Takeshima, X. Rui-Ping and J. Ma, Recombinant MG53 Protein Modulates Therapeutic Cell Membrane Repair in Treatment of Muscular Dystrophy, *Sci. Transl. Med.*, 2012, **4**(139), 139ra85.
 - 11 L. N. Skalman, M. R. Holst, E. Larsson and R. Lundmark, Plasma membrane damage caused by listeriolysin O is not repaired through endocytosis of the membrane pore, *Biol. Open*, 2018, **7**(10), bio035287.
 - 12 G. Baffou, *Thermoplasmonics*, Cambridge University Press, 2017.
 - 13 G. Baffou, R. Quidant and C. Girard, Heat generation in plasmonic nanostructures: Influence of morphology, *Appl. Phys. Lett.*, 2009, **94**, 153109.
 - 14 G. Baffou and R. Quidant, Thermo-plasmonics: using metallic nanostructures as nano-sources of heat, *Laser Photonics Rev.*, 2013, **7**, 171–187.
 - 15 A. S. Urban, S. Carretero-Palacios, A. A. Lutich, T. Lohmüller, J. Feldmann and F. Jäckel, Optical trapping and manipulation of plasmonic nanoparticles: fundamentals, applications, and perspectives, *Nanoscale*, 2014, **6**, 4458–4474.
 - 16 M. B. Klenow, A. S. B. Heitmann, J. Nylandsted and A. C. Simonsen, Timescale of hole closure during plasma membrane repair estimated by calcium imaging and numerical modeling, *Sci. Rep.*, 2021, **11**, 4226.
 - 17 A. S. Urban, T. Pfeiffer, M. Fedoruk, A. A. Lutich and J. Feldmann, Single-step injection of gold nanoparticles through phospholipid membranes, *ACS Nano*, 2011, **5**, 3585–3590.
 - 18 S. Patskovsky, M. Qi and M. Meunier, Single point single-cell nanoparticle mediated pulsed laser optoporation, *Analyst*, 2020, **145**, 523–529.
 - 19 M. Li, T. Lohmüller and J. Feldmann, Optical injection of gold nanoparticles into living cells, *Nano Lett.*, 2015, **15**, 770–775.
 - 20 H. M. L. Robert, J. Savatier, S. Vial, J. Verghese, B. Wattellier, H. Rigneault, S. Monneret, J. Polleux and G. Baffou, Photothermal Control of Heat-Shock Protein Expression at the Single Cell Level, *Small*, 2018, **14**, e1801910.
 - 21 A. Bahadori, G. Moreno-Pescador, L. B. Oddershede and P. M. Bendix, Remotely controlled fusion of selected vesicles and living cells: a key issue review, *Rep. Prog. Phys.*, 2018, **81**, 032602.
 - 22 J. T. Jørgensen, K. Nørregaard, P. Tian, P. M. Bendix, A. Kjær and L. B. Oddershede, Single Particle and PET-based Platform for Identifying Optimal Plasmonic Nano-Heaters for Photothermal Cancer Therapy, *Sci. Rep.*, 2016, **6**, 30076.
 - 23 A. Samadi, H. Klingberg, L. Jauffred, P. M. Bendix, A. Kjær and L. B. Oddershede, Platinum nanoparticles: a non-toxic, effective and thermally stable alternative plasmonic material for cancer therapy and bioengineering, *Nanoscale*, 2018, **10**, 9097–9107.
 - 24 P. M. Bendix and L. B. Oddershede, Expanding the Optical Trapping Range of Lipid Vesicles to the Nanoscale, *Nano Lett.*, 2011, **11**, 5431–5437.
 - 25 J. Pan, F. A. Heberle, S. Tristram-Nagle, M. Szymanski, M. Koepfinger, J. Katsaras and N. Kučerka, Molecular structures of fluid phase phosphatidylglycerol bilayers as determined by small angle neutron and X-ray scattering, *Biochim. Biophys. Acta*, 2012, **1818**, 2135–2148.
 - 26 N. Gershfeld and M. Murayama, Thermal instability of red blood cell membrane bilayers: temperature dependence of hemolysis, *J. Membr. Biol.*, 1988, **101**, 67–72.
 - 27 A. Ebrahimi, L. Csonka and M. Alam, Analyzing Thermal Stability of Cell Membrane of Salmonella Using Time-Multiplexed Impedance Sensing, *Biophys. J.*, 2018, **114**, 609–618.
 - 28 J. T. Jørgensen, K. Nørregaard, P. Tian, P. M. Bendix, A. Kjaer and L. B. Oddershede, Single Particle and PET-based Platform for Identifying Optimal Plasmonic Nano-Heaters for Photothermal Cancer Therapy, *Sci. Rep.*, 2016, 1–10.

- 29 P. M. Bendix, S. N. S. Reihani and L. B. Oddershede, Direct Measurements of Heating by Electromagnetically Trapped Gold Nanoparticles on Supported Lipid Bilayers, *ACS Nano*, 2010, **4**, 2256–2262.
- 30 F. Bouvet, M. Ros, E. Bonedeau, C. Croissant, L. Frelin, F. Saltel, V. Moreau and A. Bouter, Defective membrane repair machinery impairs survival of invasive cancer cells, *Sci. Rep.*, 2020, **10**, 21821.
- 31 G. Moreno-Pescador, I. Qoqaj, V. T. Ruhoff, J. F. Iversen, J. Nylandsted and P. M. Bendix, *Optical Trapping and Optical Micromanipulation XVI*, 2019, pp. 24–34.
- 32 J. Turnay, A. Guzmán-Aránguez, E. Lecona, J. I. Barrasa, N. Olmo and M. A. Lizarbe, Key role of the N-terminus of chicken annexin A5 in vesicle aggregation, *Protein Sci.*, 2009, **18**, 1095–1106.
- 33 M. Lizarbe, J. Barrasa, N. Olmo, F. Gavilanes and J. Turnay, Annexin-Phospholipid Interactions. Functional Implications, *Int. J. Mol. Sci.*, 2013, **14**, 2652–2683.
- 34 P. Drücker, M. Pejic, H.-J. Galla and V. Gerke, Lipid Segregation and Membrane Budding Induced by the Peripheral Membrane Binding Protein Annexin A2, *J. Biol. Chem.*, 2013, **288**, 24764–24776.
- 35 J. Jiang, X. Che, Y. Qian, L. Wang, Y. Zhang and Z. Wan, Bismuth Sulfide Nanorods as Efficient Photothermal Theragnosis Agents for Cancer Treatment, *Front. Mater.*, 2020, **7**, 234.
- 36 A.-E. Saliba, I. Vonkova, S. Ceschia, G. M. Findlay, K. Maeda, C. Tischer, S. Deghou, V. van Noort, P. Bork, T. Pawson, J. Ellenberg and A.-C. Gavin, A quantitative liposome microarray to systematically characterize protein-lipid interactions, *Nat. Methods*, 2014, **11**, 47–50.
- 37 A. C. Richardson, N. Reihani and L. B. Oddershede, *Optical Trapping and Optical Micromanipulation III*, 2006, pp. 560–569.
- 38 A. O. Govorov, W. Zhang, T. Skeini, H. Richardson, J. Lee and N. A. Kotov, Gold nanoparticle ensembles as heaters and actuators: melting and collective plasmon resonances, *Nanoscale Res. Lett.*, 2006, **1**, 84–90.
- 39 C. F. Bohren and D. R. Huffman, *Absorption and Scattering of Light by Small Particles*, John Wiley & Sons, 2008.
- 40 H. S. Carslaw and J. C. Jaeger, *Conduction of heat in solids*, Clarendon Press, Oxford, 2nd edn, 1959.
- 41 L. D. Landau and E. M. Lifshitz, *Electrodynamics of Continuous Media*, Pergamon Press, 1960.
- 42 H. Goldenberg and C. J. Tranter, Heat flow in an infinite medium heated by a sphere, *Br. J. Appl. Phys.*, 1952, **3**, 296–298.
- 43 G. Mie, Beiträge zur Optik triiber Medden, speziell colloidalen Metallö sungem, *Ann. Phys.*, 1908, **25**, 1–69.
- 44 L. Jauffred, A. Samadi, H. Klingberg, P. M. Bendix and L. B. Oddershede, Plasmonic Heating of Nanostructures, *Chem. Rev.*, 2019, **119**, 8087–8130.
- 45 C. T. Rueden, J. Schindelin, M. C. Hiner, B. E. DeZonia, A. E. Walter, E. T. Arena and K. W. Eliceiri, ImageJ2: ImageJ for the next generation of scientific image data, *BMC Bioinf.*, 2017, **18**, 529–526.
- 46 J. Schindelin, I. Arganda-Carreras, E. Frise, V. Kaynig, M. Longair, T. Pietzsch, S. Preibisch, C. Rueden, S. Saalfeld, B. Schmid, J.-Y. Tinevez, D. J. White, V. Hartenstein, K. Eliceiri, P. Tomancak and A. Cardona, *Fiji: an open-source platform for biological-image analysis*, Nature Publishing Group, 2012, vol. 9, pp. 676–682.
- 47 J. Mutterer and E. Zinck, Quick-and-clean article figures with FigureJ, *J. Microsc.*, 2013, **252**, 89–91.

Thermoplasmonic nano-rupture of cells reveals Annexin V function in plasma membrane repair

Guillermo S. Moreno-Pescador,^{*,†} Dunya S. Aswad,[†] Christoffer D. Florentsen,[†]
Azra Bahadori,[‡] Mohammad R. Arastoo,[†] Helena Maria D. Danielsen,[†] Anne
Sofie B. Heitmann,[¶] Theresa L. Boye,[¶] Jesper Nylandsted,^{¶,§} Lene B.
Oddershede,[†] and Poul Martin Bendix^{*,†}

[†]*Niels Bohr Institute, University of Copenhagen, Blegdamsvej 17, 2100 København Ø,
Denmark*

[‡]*Center for Chromosome Stability, University of Copenhagen, Blegdamsvej 3B, 2200
København N, Denmark*

[¶]*Danish Cancer Society Research Center, Strandboulevarden 49, DK-2100 Copenhagen,
Denmark*

[§]*Department of Cellular and Molecular Medicine, Faculty of Health Sciences, University of
Copenhagen, DK-2200 Copenhagen N, Denmark.*

E-mail: moreno@nbi.ku.dk; bendix@nbi.ku.dk

Supporting Information Available

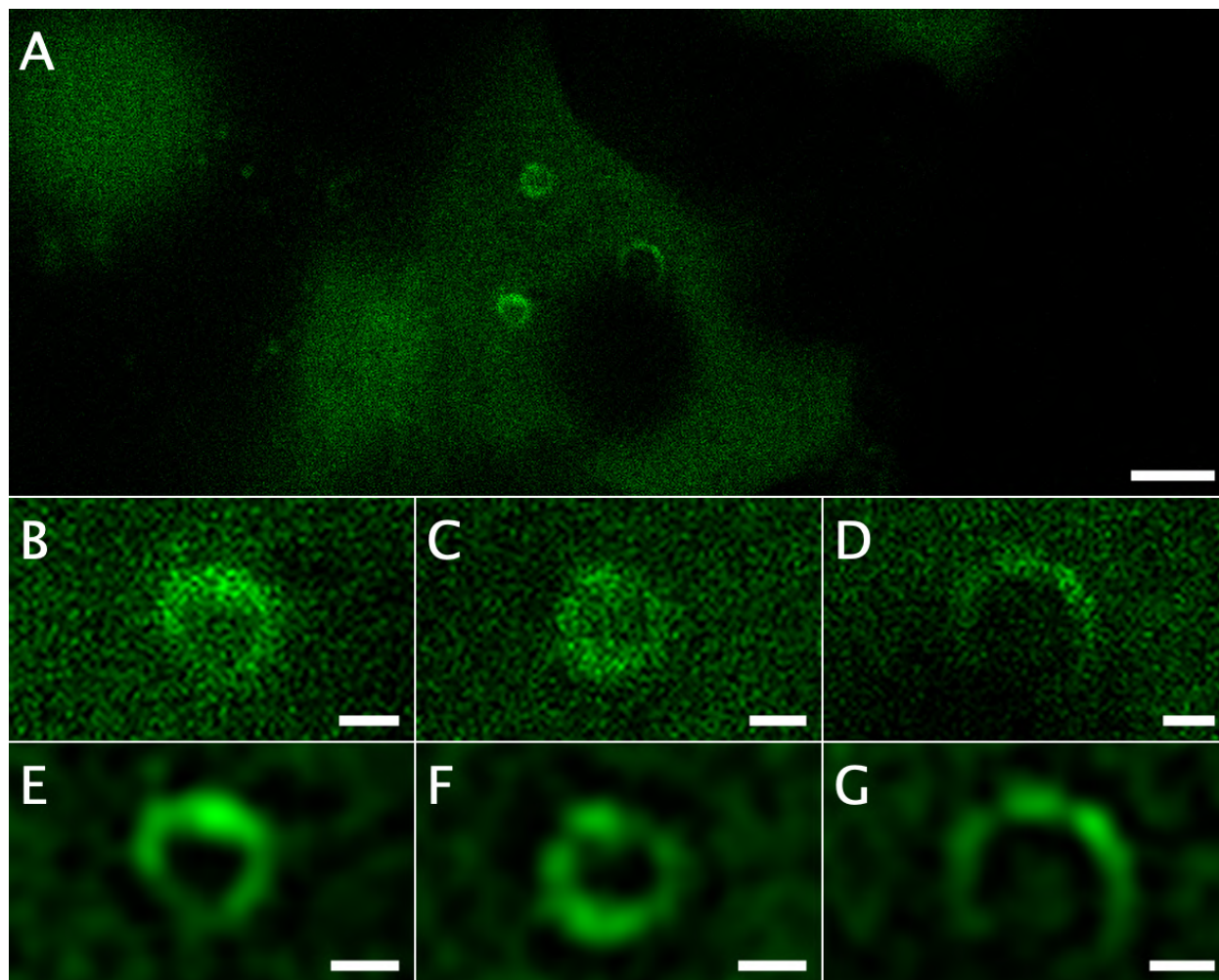


Fig. S 1: Membrane puncturing of a HEK293T cell. The cell is able to survive puncturing several times by activation of the PMR machinery. A) Cell with 3 punctures. Scale bar is 5 μm B), C) and D,) show the unedited rings from A. E), F) and G) show edited images using a Difference of Gaussian (DoG) filter of the images above. All scale bars, except for A), are 2 μm .

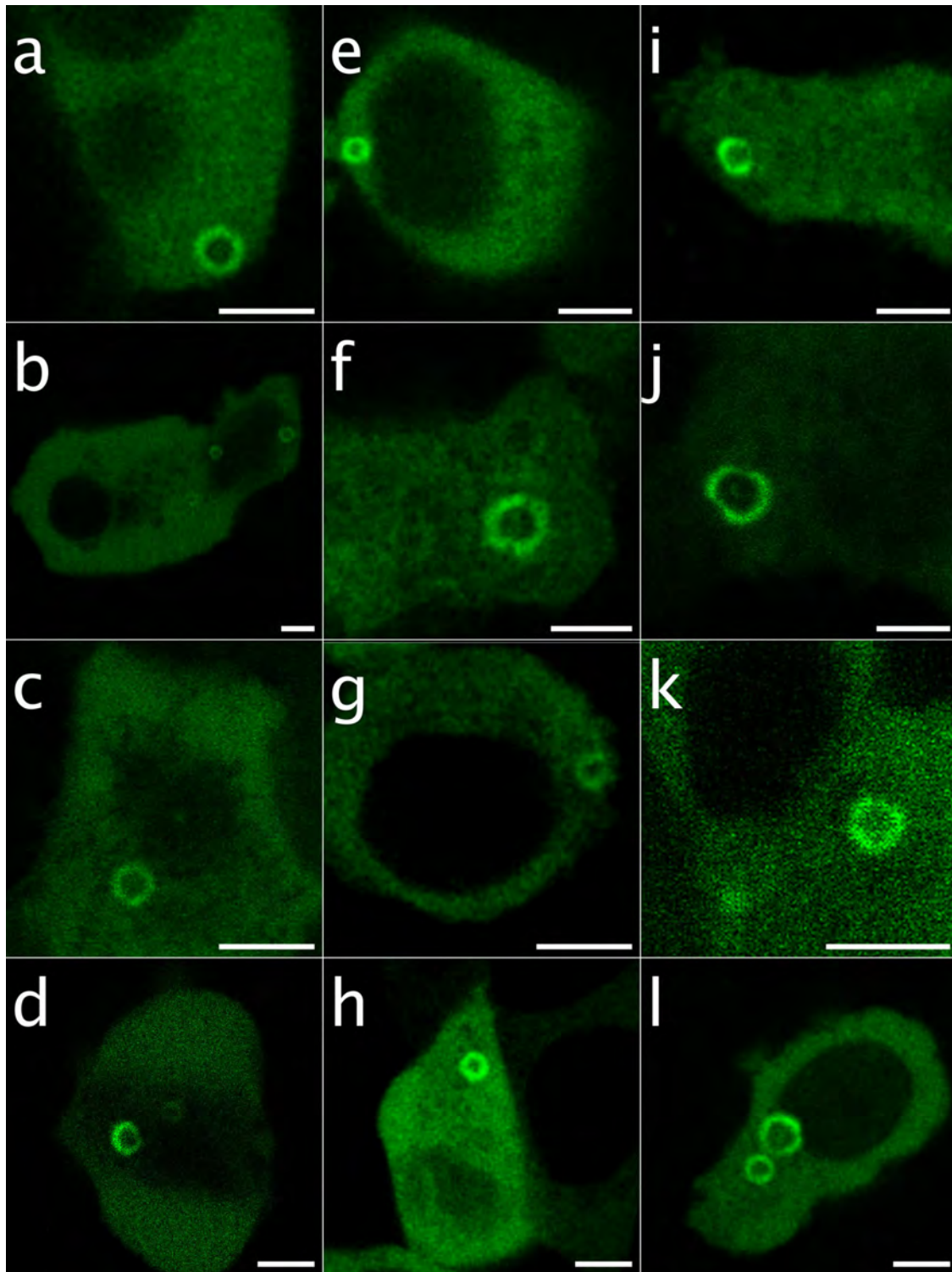


Fig. S 2: Examples of punctured HEK293T cells expressing ANXA5-gfp. All cells were punctured by plasmonic gold nanoparticles located between a coverglass and an adhering cell. Laser powers ranged from (add approximate laser levels). Scale bars are all $5 \mu\text{m}$.

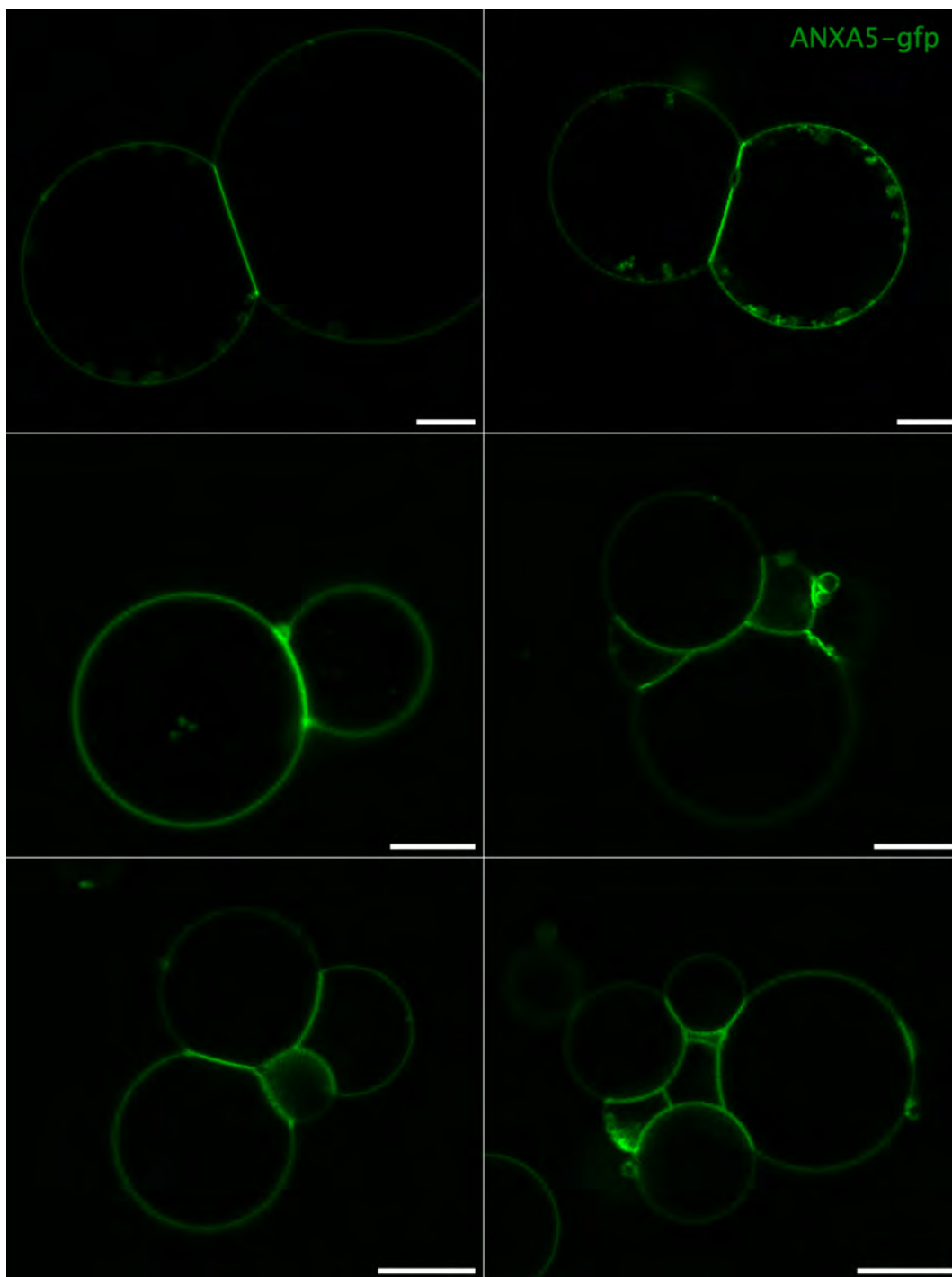


Fig. S 3: Interaction of C-terminal in between ANXA5 interacting at the interface between apposing vesicles. These are examples of GUVs prepared using electroformation (DOPC 90% + DOPS 10%) in a Ca^{2+} buffer of 2mM. Purified ANXA5-gfp was added in solution causing strong binding of GUVs. Scale bars are all 10 μ m.

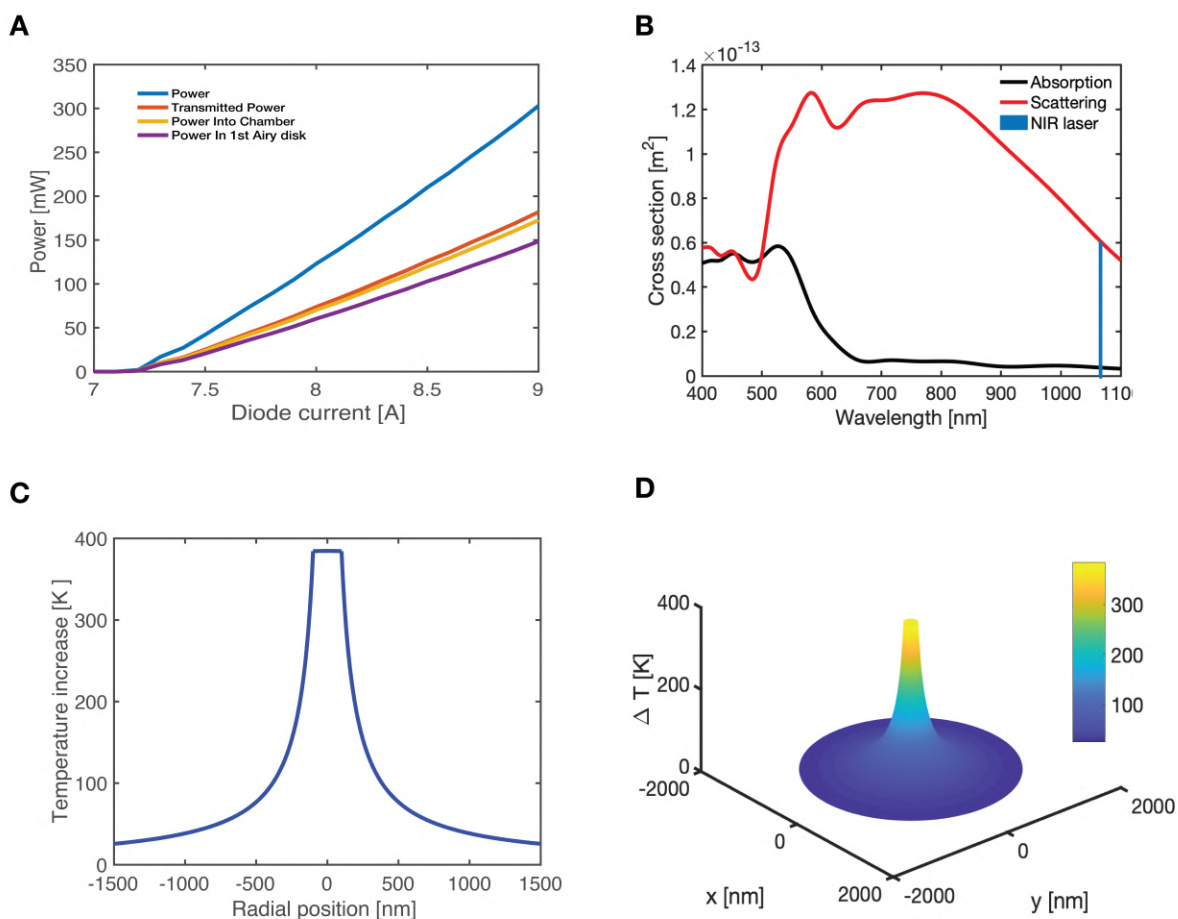


Fig. S 4: Calculations of thermoplasmonic heating for an irradiated 200 nm gold nanoparticle. (A) Power measurements of the experimental set up at different points of the NIR laser path. Blue, right after the fiber. Red and orange are before and after the objective respectively. Purple is the power measured in a sample. (B) Absorption and scattering cross sections calculated for a AuNP of 200 nm diameter. (C) Calculation of temperature increase around a 200 nm irradiated gold nanoparticle based on parameters shown in (A) and (B) and using a current of 8A. (D) 3D render of the same heating profile presented in (C).

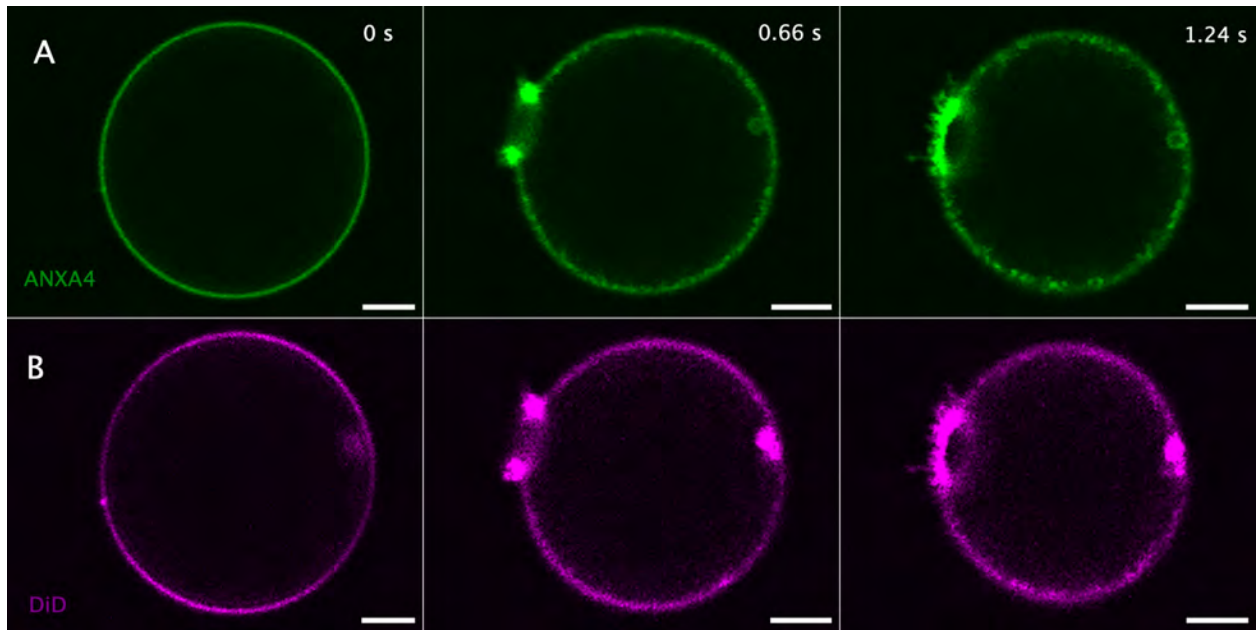


Fig. S 5: Example of punctured GUV with bound ANXA4-gfp and membrane DiD labeling. A) GFP-ANXA4 fluorescence channel with time interval in between frames. B) DiD fluorescence channel. The time interval in between frames is the same as for panel A). Scale bars are all $5 \mu\text{m}$.

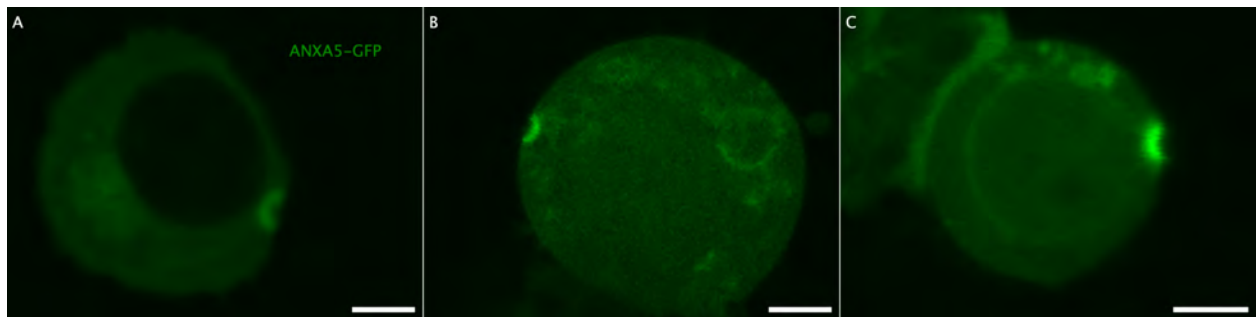


Fig. S 6: HEK293T cells expressing ANXA5 punctured from one side. Scale bars are all $5 \mu\text{m}$.

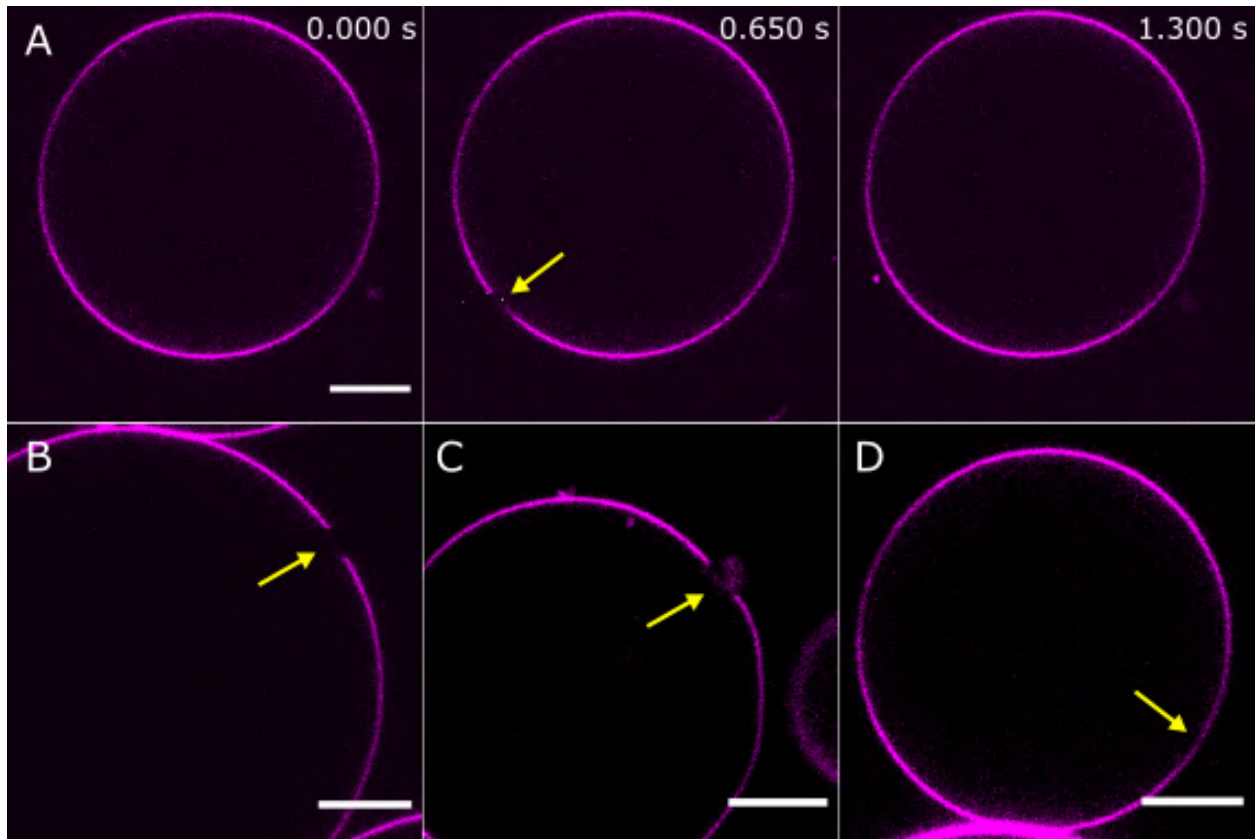


Fig. S 7: Control experiments with GUVs containing only labelled PM with DiD. We can not observe rolling, budding or rings-like structures when ANXAs are not present. Yellow arrows indicate the thermoplasmonic-induced puncture sites. A) Time sequence of a punctured whole and its repair. B) punctured whole C) Punctured whole D) Punctured whole. Scale bars are all $10\ \mu\text{m}$.

A thermoplasmonic approach for the investigation of plasma membrane repair in living cells and model membranes

Helena Maria D. Danielsen¹, Mohammad Reza Arastoo², Guillermo Moreno-Pescador³, and Poul Martin Bendix⁴

^{1,2,4} The Niels Bohr Institute, University of Copenhagen, 2100 Copenhagen, Denmark

³Plant and Environmental Sciences, University of Copenhagen, 1871 Frederiksberg, Denmark

E-MAIL ADDRESSES:

helena.danielsen@nbi.ku.dk

mohammadreza.arastoo@nbi.ku.dk

moreno@nbi.ku.dk

bendix@nbi.ku.dk

CORRESPONDING AUTHOR:

Poul Martin Bendix (bendix@nbi.ku.dk)

KEYWORDS:

biophysics, plasma membrane repair, optical tweezers, annexins, giant unilamellar vesicles, photothermal thermoplasmonics, membrane puncture

SHORT ABSTRACT:

The thermoplasmonic puncture method integrates confocal microscopy, optical tweezers, and gold nanoparticles to study protein responses during plasma membrane repair in cells and giant unilamellar vesicles. The technique enables rapid and localized membrane puncture, allowing identification of key proteins and their functional roles in the intricate plasma membrane repair machinery.

LONG ABSTRACT:

The cell membrane is crucial for cell survival, and ensuring its integrity is essential as the cell experiences injuries throughout its entire cycle. To maintain cell viability, cells have developed efficient plasma membrane repair mechanisms. To study the complex repair mechanisms, a method combining confocal microscopy, optical tweezers, and gold nanoparticles (AuNPs) is utilized to identify and investigate the role of key proteins, such as annexins, involved in surface repair in living cells and giant unilamellar vesicles.

The puncture approach employs a laser to induce highly localized heating upon NP irradiation. The use of near-infrared light minimizes phototoxicity in the biological sample, while the majority of the absorption takes place in the near-infrared resonant plasmonic nanoparticle. This thermoplasmonic method has been exploited for potential photothermal and biophysical research to enhance the understanding of intracellular mechanisms and cellular responses through vesicle and cell fusion studies. The approach has shown to be complementary to existing methods for membrane disruption, such as mechanically, chemically, or optically induced injuries, and provides a high level of control by inflicting extremely localized injuries. The extent of the injury is limited to the vicinity of the spherical nanoparticle, and no detrimental damage occurs along the beam path as opposed to pulsed lasers. Despite certain limitations, such as the formation of

nanobubbles, the thermoplasmonic method offers a unique tool for investigating cellular responses and plasma membrane repair in an almost native environment without compromising cell viability.

When integrated with confocal microscopy, the puncturing method can provide a mechanistic understanding of membrane dynamics in model membrane systems as well as quantitative information on protein responses to membrane damage, including protein recruitment and their biophysical function. Overall, the application of this method to reduced model systems can enhance our understanding of the intricate plasma membrane repair machinery in living cells.

INTRODUCTION:

The cell membrane, serving both as a physical barrier and a signaling platform, is vital for cell survival¹. Throughout its entire cell cycle, the plasma membrane (PM) is subjected to damage, such as mechanical²⁻⁵ and chemical⁶ stress-induced injuries. To maintain membrane integrity and ensure cell survival, the cell has developed robust plasma membrane repair (PMR) mechanisms. These mechanisms depend on various strategies, such as cytoskeleton reorganization, membrane fusion, and membrane replacement strategies⁷⁻¹¹, all of which rely on the recruitment of specific proteins. Notably, members of the annexin protein family have been identified as key proteins associated with the processes of PMR^{1, 9, 12-16}. Following PM injury, the cell experiences an influx of calcium ions (Ca^{2+}), which poses an immediate threat to the cell's survival¹⁷. In response to Ca^{2+} influx, annexin proteins, which are predominantly located in the cytosol, bind to the inner leaflet of the damaged plasma membrane as a part of the PMR strategies¹⁸. Annexin A2 (ANXA2) was one of the first members of the annexin family to be associated with PMR in dysferlin-deficient muscular dystrophy and was suggested to mediate repair by fusing intracellular vesicles to the PM near the injury site^{5, 19-21}. Subsequently, several functions have been attributed to annexins²², and their role in PMR has garnered increased attention in recent decades^{15, 18, 21, 22}. However, the exact role of annexins in PMR remains enigmatic.

This article proposes a method for investigating protein-membrane interaction and membrane dynamics in a controlled and highly localized manner, utilizing a combination of confocal microscopy, optical tweezers, and gold nanoparticles (AuNPs). This method enables the quantitative study of protein, lipid, and small molecule interactions in response to membrane damage and Ca^{2+} influx. Despite the complexity and multiplicity of components involved in the process of membrane repair, simplified membrane systems that mimic the plasma membrane have been employed to gain a mechanistic understanding of membrane dynamics and the response of annexin proteins to membrane disruption. The model membrane system is based on giant unilamellar lipid vesicles (GUVs) with a specified lipid composition. The GUVs were generated using the gel-assisted hydration method, specifically polyvinyl alcohol gel hydration, as described by Weinberger *et al.*²³, which allowed for efficient encapsulation of annexins into GUVs.

The utilization of near-infrared (NIR) laser irradiation on metallic nanoparticles (NPs) induces significant heating of the NP, making it an effective method to establish a local heat source exploited in biomedical applications²⁴. Consequently, the method was initially used to directly measure the temperature surrounding a single AuNP in both 2D and 3D biomimetic assays^{25, 26}. In these assays, the plasmonic nanoparticles were irradiated on a supported lipid bilayer or optically trapped near giant unilamellar lipid vesicles undergoing a local thermal phase transition upon local heating, enabling quantification and control of the exact temperature profile around the particle.

This reference temperature profile has been utilized when investigating or manipulating biological specimens. Further advancements in the method have facilitated the induction of nanoscopic pores in membranes²⁷, allowing for vesicle and cell fusion^{28, 29}. Other studies have investigated the behavior of peripheral membrane proteins in GUVs²⁹ and transmembrane proteins³⁰ by creating novel hybrid vesicles, while cell-specific drug delivery has also been explored to control and study cellular responses or gene expression^{28, 29, 31–33}. Recently, the method has been used to investigate protein responses to membrane damage^{32, 34, 35}.

Several methods exist for disrupting the plasma membrane to explore cellular responses and membrane repair. These include microneedle punctures, microbead shaking, and cell scraping, all of which can disrupt the cell membrane mechanically^{14, 36, 37}. Chemically induced damage can be achieved by adding detergents^{5, 38}, or bacterial toxins^{39, 40} that destabilize the lipid bilayer and generate membrane pores across the plasma membrane. Furthermore, optically induced injuries by continuous wave and pulsed lasers have been used to study PMR components, such as annexin proteins^{5, 14, 21, 41}, in combination with plasmonic nanoparticles^{42–45}. Despite the efficiency of high-power pulsed lasers, they can cause significant injuries and damage to the cell's interior along the beam path. Moreover, the detailed changes that occur in biological matter upon pulsed laser irradiation and whether it creates a well-defined pore remain to be further investigated. An alternative method is presented in this article, employing thermoplasmonics to induce nanoscopic holes in the PM in a controlled manner^{34, 35} without causing significant harm to the internal structures. This is accomplished by exposing plasmonic NPs to a highly focused NIR laser, resulting in an extremely localized temperature increase that can easily reach temperatures exceeding 200 °C^{25, 46, 47}. This process can be controlled by adjusting the laser intensity as well as the size, shape, and composition of the NPs⁴⁸. By employing this technique, researchers can explore the role of proteins in PM repair in living cells, which could help address some of the unanswered questions regarding the involvement of annexin proteins in membrane repair without compromising cell viability.

The optical trapping of plasmonic nanoparticles is well-established^{25, 49–52}. Therefore, it can be used to create nanoscopic holes in the PM for the purpose of studying the cellular response and repair mechanisms. More precisely, the puncture can be achieved through the optical heating of AuNPs in close proximity to the membrane, as shown in Figures 1A and B. This localized puncture allows for Ca²⁺ influx, which was verified by calcium sensing (Fig. 4), thus activating the PMR machinery. For cellular experiments, AuNPs with a diameter of 200 nm were immobilized on the surface beneath the cell to monitor the role of ANXA2 in PMR via confocal microscopy (Fig. 2). The NIR laser, with a wavelength of 1064 nm, irradiates the AuNP, exploiting its plasmonic properties (Fig. 1C), resulting in substantial local heating (Fig. 1D) in the biological transparency window⁴⁹ while causing minimal damage to the cell itself. The high-temperature region surrounding the AuNP rapidly decreases by 30–40% at a distance corresponding to the radius of the NP (Fig. 1E), allowing for an extremely confined injury in all three dimensions.

[Figure 1]:

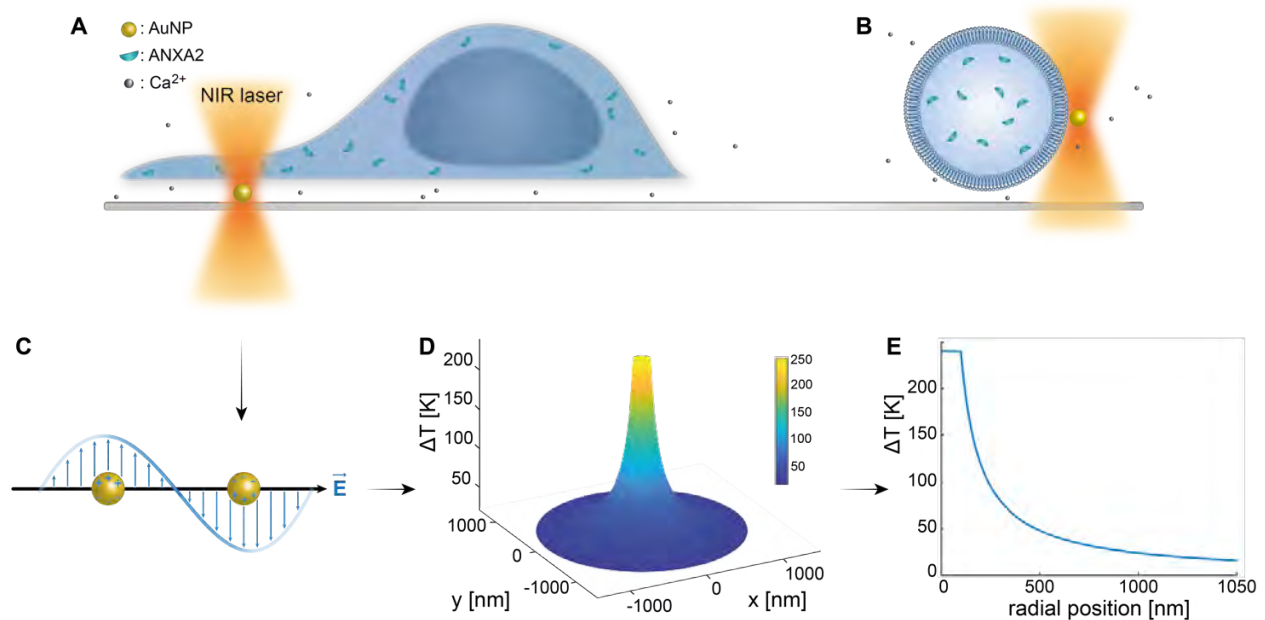


Figure text: The experimental method is schematically outlined as follows: (A) ANXA-transfected cells are situated on top of immobilized gold nanoparticles (AuNPs) on the surface, or (B) giant unilamellar vesicles (GUVs), with encapsulated ANXA, are situated in a medium containing AuNPs. A single AuNP is irradiated by the NIR optical trap, where the interaction between the incoming electromagnetic field and the conduction electrons leads to a collective oscillation of electrons within the NP (C). This process results in a highly confined yet significant increase in temperature (D). To estimate the temperature at the NP surface, Mie theory is employed, and a temperature profile (E) is calculated for an AuNP with a diameter of 200 nm and laser density $I = 6.36 \cdot 10^{12} \text{ W/m}^2$.

To minimize the thermal effect on cells, the AuNPs are only irradiated for ~ 1 second. This causes a transient and local burst of heating, which reduces the damage to proteins that typically require more time to unfold. Upon membrane puncture, annexin proteins are recruited in a fraction of a second, and within a few seconds, a ring is formed around the site of injury (Fig. 2B). This approach has also been applied to explore the involvement of ANXA5 in both living cells and model membranes¹⁶ in an effort to shed light on the complete scheme of the repair processes. While the primary focus has been on the correlating recruitment of various annexin proteins, the biophysical aspects of the repair mechanism have yet to be elucidated.

To fully implement the proposed method, three key components are required: confocal microscopy, optical tweezers, and plasmonic metal nanoparticles. Optical tweezers are used to trap the AuNP, which can be constructed following the procedure outlined by Neuman *et al.*⁴⁹. However, if building an optical tweezer proves to be too challenging, a tightly focused NIR laser can be used to irradiate AuNPs immobilized beneath the spreading cells. While spherical AuNPs were chosen for this protocol, a variety of plasmonic particles with tunable absorption spectra could also be utilized to achieve a highly localized temperature gradient within the NIR region⁴⁸.

Fluorescence imaging is necessary for observing the role of the labeled proteins, and therefore TIRF⁵³ could be considered as an alternative to confocal imaging. However, this technique only allows for surface imaging and would not be compatible with the model membrane vesicle experiments. Consequently, both the optical tweezers and confocal microscope are essential for precise localization of the nanoparticle and detailed investigation of the local area surrounding the cell injury. To effectively irradiate the nanoparticle with a diffraction-limited laser focus, it is necessary to visualize the nanoparticle. This can be optimally achieved by reflection microscopy, which is a standard imaging feature of Leica confocal microscopes. However, if reflection or scattering imaging is not available, alternative methods, such as the less efficient fluorescent AuNP labeling, may be considered.

In summary, the highly controllable and localized thermoplasmonic method presented in this study has the potential to serve as an excellent platform for investigating the molecular components involved in cellular responses and PM repair mechanisms in living cells. In addition to studying the protein response upon PM damage, this approach can also be utilized for the purpose of locally puncturing vesicles, thereby enabling an investigation of the protein response in both protein-protein and protein-membrane dynamics. Moreover, this method allows for a quantitative analysis of the interactions between proteins, lipids, and small molecules when membranes are disrupted. Collectively, these advances have the potential to shed light on some of the unresolved questions regarding the intricate and complex plasma membrane repair machinery.

PROTOCOL:

Preparations for cell membrane puncture experiments

1.1 Cell seeding (Day 1)

- 1.1.1 Human Embryonic Kidney (HEK293T) cells are cultured in Dulbecco's Modified Eagle's Medium (DMEM) supplemented with 10% Fetal Bovine Serum (FBS) and 1% Penicillin-Streptomycin (PS) in T25 tissue culture flasks at 37 °C in a 5% CO₂ humidifier incubator until they reach 70% confluency.
- 1.1.2 The cells are detached from the surface using 500 µL Trypsin-EDTA, and 200,000 HEK293T cells are seeded in a 35x10 mm cell culture dish with a total volume of 3 mL culture medium. The cells are then incubated at 37 °C in a 5% CO₂ humidifier incubator for 24 h.

NOTE: To prevent cell clustering in the middle of the dish, make sure to spread the cells evenly and avoid swirling the dish, as this can decrease transfection efficiency.

1.2 Cell transfection (Day 2)

NOTE: The transfected cells can be used up to 48 h after transfection.

- 1.2.1 Pipet the plasmid of interest, in this case annexin (ANXA) plasmids, and the lipofectamine (LTX) solution for 5 s before use.
- 1.2.2 Mix the following in a sterile Eppendorf tube in the specific order:

500 μ L Opti-MEM Reduced-Serum Medium (OptiMEM)
5 μ L LTX (4 times more than the plasmid)
1.25 μ L ANXA (1 μ g/ μ L)

- 1.2.3 Thoroughly but gently pipet the transfection mixture and incubate it at room temperature for 30 min before adding it dropwise to the cells.
- 1.2.4 Before adding the transfection mixture, remove the medium from the culture dish, gently wash the cells with 2 mL of phosphate buffered saline (PBS), and add 2000 μ L OptiMEM to the dish.
- 1.2.5 Incubate the cells together with the transfection mixture at 37 °C in a 5% CO₂ humidifier incubator for 2 h and 45 min before changing the medium to 3 mL culture medium.

1.3 Preparation of gold nanoparticle (AuNP) solution (Day 2)

- 1.3.1 Vortex the 200 nm AuNP stock solution for 10 s at maximum speed, sonicate for 5 min (max amplitude), and vortex again for 10 s.
- 1.3.2 Mix 150 μ L AuNPs with 850 μ L of distilled water to a total volume of 1 mL.

NOTE: The diluted AuNP solution can be stored in the fridge and reused for up to 1 month.

1.4 Preparation of the experimental dish (Day 2)

- 1.4.1 Coat the 35 mm bottom glass surface of the MatTek microwell dish with 150 μ L 0.01-0.1% Poly-L-Lysine (PLL) and incubate for 15 min at room temperature.
- 1.4.2 Wash the glass surface twice with 500 μ L of distilled water and let it air dry for ~10 min.
- 1.4.3 Add 80 μ L of AuNP solution dropwise to the dry PLL surface.

NOTE: Vortex (10 s), sonicate (5 min), and vortex (10 s) the diluted AuNP solution before adding it to the coated glass surface to minimize AuNP aggregates.

- 1.4.4 Wait for ~10 min before adding 1.5 mL of culture medium, and let the dish incubate at 37 °C overnight.

1.5 Preparation of the experimental chamber (Day 3)

NOTE: The experimental chamber can be prepared either on day 3 or 4, but the following preparations must be completed on the same day as the experiment.

- 1.5.1 Remove the medium from the cells in the culture dish and wash the cells with 2 mL PBS.

NOTE: This step is essential to remove any residual medium and debris that could interfere with the subsequent steps.

- 1.5.2 Add 500 μ L of TrypLE to the well and incubate for 1-3 min until the cells have detached from the culture dish.

- 1.5.3 Add 1.5 mL of fresh culture medium and pipette the cell solution to get a homogenous cell solution to minimize the likelihood of cell clusters.
- 1.5.4 Gently remove the medium from the AuNPs in the experimental MatTek well.
- 1.5.5 Add the cell solution (2 mL) to the MatTek well and allow it to incubate for at least 5 h before performing the experiment.

NOTE: For optimal experimental conditions, do not swirl the chamber, as this will cause the cells to cluster in the middle of the chamber.

2. The cell membrane puncture experiments

The experiments were conducted using a Leica SP5 confocal scanning microscope in conjunction with a 1064 nm trapping laser (Spectra Physics J201-BL-106C, Nd: YVO4 NIR laser)⁵⁴. Optical trapping is carried out at the focal plane utilizing a Leica PL APO 63x water-immersion objective with a numerical aperture (NA) of 1.2. Assuming that the focus is the size of an Airy disc, the focal beam width of the irradiation laser is ~540 nm in radius. The laser power (P) is converted to the corresponding laser intensity (I) by the laser power per area [W/cm^2].

The Leica Acousto-Optical Beam Splitter (AOBS) allows for simultaneous visualization of multiple fluorescent signals. When combined with photomultiplier tubes, the system can be configured to visualize metallic NPs via their scattering signal.

During the experimental sessions, a glass-bottom open chamber (35 mm bottom glass surface MatTek microwell dish) containing cells, molecular fluorescent probes, and gold nanoparticles is mounted on the microscope. During the experimental session, the optical trap remains stationary; however, the trap can be moved relative to the cells by translating the sample mounted on a piezoelectric stage (PI 731.20, Physik Instrumente, Germany), which allows for nanometer-precise lateral movements¹⁶.

2.1 Experimental settings for the cell membrane puncture experiments

- 2.1.1 The experimental setup comprises HEK293T cells that have been transfected with a protein of interest, in this case Annexin A2 plasmids, coupled with Green Fluorescent Protein (GFP). The cells are placed on top of single AuNPs that are immobilized on the glass surface (Fig. 1A).
- 2.1.2 Scanning confocal microscopy is performed using an Argon 488 nm laser to visualize the GFP fluorescence signal and a HeNe 633 nm laser to visualize the reflection from the AuNPs.
- 2.1.3 The optical tweezer, which operates with a 1064 nm NIR laser, irradiates a single AuNP at the surface for ~1 s, leading to a significant local increase in temperature and thereby disrupting the plasma membrane.

- 2.1.4 The particle in focus is irradiated with 200–295 mW, giving a temperature increase between 230–360 °K without taking the heat dissipation into the glass surface into account. The glass surface absorbs some of the heat, which consequently reduces the amount of heat that would have been released to the plasma membrane^{48, 55}.
- 2.1.5 In order to achieve an effective and localized PM injury and subsequent protein repair response, proper calibration of the focused NIR laser is imperative. This is achieved by capturing a single AuNP suspended in the same imaging medium and ensuring that the selected AuNP is in focus prior to irradiation.

NOTE: The nanoparticle is considered to be in focus when its scattering signal appears the sharpest, i.e., exhibiting clear edges and the absence of a halo around the particle, when observing it in confocal microscopy (Fig. 2C (ii)).

2.2 Cell and AuNP density conditions

- 2.2.1 To avoid overlap of plasma membranes, it is necessary to use single cells instead of clusters. The cells should be adhered to the surface and exhibit a flattened morphology (Fig. S1), which allows for the cell periphery to be punctured and prevents damage to the nuclear membrane (Fig. S2).
- 2.2.2 To prevent cellular uptake of the AuNP, cells should be incubated according to the protocol or until they have settled and flattened. It is important to note that excessive incubation time should be avoided. To further reduce the likelihood of endocytosis, PEGylated AuNPs are recommended over other alternatives.
- 2.2.3 It is imperative that the immobilized AuNPs are present as single particles and are adequately spaced apart from each other, as the presence of aggregates or close proximity could significantly increase the thermal gradient and result in elevated temperatures that may disrupt a substantial fraction of the cell.
- 2.2.4 It is recommended to replace the sample every 1-2 h, as prolonged exposure can lead to a deterioration in cell health, compromising their ability to respond accurately to injury in terms of membrane repair. This decline in cell health is typically observed by a change in cell shape as cells become rounder and more rigid, eventually culminating in cell death.

3. Preparation of Giant Unilamellar Vesicles (GUVs)

3.1 Preparation of the lipid mixture

- 3.1.1 The lipid composition of the GUVs used in this experiment consists of DOPC and DOPS lipids with a molar ratio of 4:1 (see Table 1). The lipid stock was aliquoted into 1.5 mL glass vials based on the experimental needs and stored at -20 °C.

NOTE: To prevent the oxidation of unsaturated lipids and extend their shelf life, it is recommended to replace the air with argon in the aliquoted vials.

3.1.2 Mixing of the lipids: Use glass Hamilton syringes for the chloroform-dissolved lipids

- 3.1.2.1 Clean a 50- μ L and a 500- μ L Hamilton syringe with chloroform five times to ensure they

are free of contaminants.

CAUTION: Chloroform must be handled in a fume hood due to its toxic effects.

3.1.2.2 Transfer the calculated volume of chloroform into a clean amber-glass vial, followed by adding the desired amount of each lipid. The desired amounts are specified in Table 1.

NOTE: To avoid cross-contamination between lipid stocks, ensure that the syringes are cleaned with chloroform as mentioned in step 3.1.2.1.

3.1.2.3 Finally, add the membrane dye and thoroughly mix the lipids by pipetting. Store the prepared lipid mixture at -20 °C for further use; the mixture can be stored for 2-3 weeks without any considerable damage to its lipids.

NOTE: Keep the lipids on ice at all times when they are out of the freezer.

3.2 Preparation of PVA gel

3.2.1 The GUV are prepared using the gel-assisted hydration method described by Weinberger *et al.*²³ with minor modifications.

3.2.2 To prepare the PVA gel, 5 g of polyvinyl alcohol (PVA) is dissolved in 100 mL of a buffer containing 50 mM sucrose, 25 mM NaCl, and 25 mM Tris (pH 7.4).

3.2.3 The PVA is heated and stirred until the solution becomes transparent. The solution is then cooled down to room temperature and stored in a fridge for further use.

NOTE: PVA is not easily dissolved in the buffer, and therefore, heating up to 85 °C is necessary.

3.3 Preparation of glass slides

3.3.1 Round glass slides (25 mm Ø) are cleaned with ethanol and air-dried. The slides are then treated with an air plasma cleaner (Harrick Plasma Cleaner PDG-002) to remove any residual contamination from the glass surface.

3.3.2 Preparation of PVA-coated glass slides

3.3.2.1 The PVA gel (5%) is warmed up to 60 °C for 30 min to increase its fluidity. 90 µL of the warm PVA is spread uniformly onto the glass slide and dried in a heating cabinet at 50 °C for 50 min.

3.3.2.2 Once the PVA glass slide is ready, 30 µL of the prepared lipid mixture is added using a Hamilton syringe and spread into a thin film using the edge of the needle.

3.3.2.3 The lipid mixture is then dried by evaporating its chloroform content under gentle nitrogen pressure. The glass slides are further dried under vacuum for 1.5–2 h.

NOTE: The lipids should be kept on ice at all times when they are out of the freezer.

3.4 Growing GUVs in a chamber

- 3.4.1 The in-house chamber, similar in design to reference⁵⁶, is assembled with the prepared glass slide.
- 3.4.2 In a separate Eppendorf tube, the recombinant protein of interest (in this case, ANXA5 or ANXA4) is diluted with a growing buffer (GB) consisting of 80 mM sucrose, 70 mM NaCl, and 25 mM Tris-HCl (pH 7.4) to a desired final concentration.
- 3.4.3 Then, 400 μ L of the diluted recombinant protein solution is added to the chamber, and the chamber is incubated at room temperature for 1 h to allow GUVs to grow from the deposited lipid coat. The same buffer, excluding the protein, is used as a negative control.

NOTE: The chamber is wrapped in parafilm to prevent buffer evaporation.

- 3.4.4 The GUVs are collected by transferring 400 μ L of the chamber content to an Eppendorf tube.
- 3.4.5 To remove any non-encapsulated proteins outside the GUVs, 1 mL of observation buffer (OB) containing 55 mM glucose, 70 mM NaCl, and 50 mM Tris-HCl (pH 7.4) is added to the collected solution, which is then centrifuge at 600 x g for 10 min at 13 °C.
- 3.4.6 After centrifugation, 1 mL of the supernatant is replaced with an equal volume of observation buffer. The GUVs are then dispersed by gentle pipetting and stored in the refrigerator until they are to be employed in GUV experiments.

4. The GUV puncture experiments

4.1 Chamber preparation

- 4.1.1 A 35-mm glass-bottom dish is used for the experiment. To prevent GUVs from sticking to the surface and bursting, the surface is coated with β -casein (5 mg/mL) for 15–30 min.
 - 4.1.1.1 To prepare the β -casein solution, 0.1 g of the protein is dissolved in a 20-mL buffer of 20 mM Tris (PH 7.5) and 100 mM NaCl, which is then filtered. The protein solution is aliquoted into small vials and frozen for further use.
- 4.1.2 The chamber is washed twice with observation buffer to remove any excess free β -caseins from the surface and is left to dry at room temperature.
- 4.1.3 In a separate Eppendorf tube, the formed GUVs are mixed with the OB. CaCl₂ is added to the mixture for the desired final concentration (in this case, 200 μ M).
- 4.1.4 150 nm gold nanoshells (AuNSs) are then added to the mixture in a ratio of 1:100. The final mixture contains 250 μ L of GUVs, 225 μ L of OB, 20 μ L of CaCl₂ (5 mM), and 5 μ L of the specified AuNSs.

4.2 Experimental setup

- 4.2.1 The mixture is transferred to the chamber, and the chamber is mounted on the microscope stage. Depending on the size of the chamber, either the entire mixture or a portion of it can be added.
- 4.2.2 Timing is critical since calcium ions can pass through the membrane and mediate the binding of the annexins to the internal leaflet of the membrane.
- 4.2.3 The same optical setup utilized for the cell puncturing experiments is used here.
- 4.2.4 The optical tweezers, with a power of ~ 125 mW, trap a single AuNS near the target GUV.
- 4.2.5 When the particle is trapped, it is brought into close contact with the GUV membrane, and the laser power is increased to ~ 300 mW. This produces a highly localized temperature increase, which disrupts the membrane and hence punctures the membrane at the target site.

[Table 1]:

Name	Volume (ml)	Solvent to add (ml)	Mass (mg)	Mol (μmol)	Concentration (mg/ml)	Concentration ($\mu\text{mol/ml}$)				
GUV	1	0,837	1,582	2	1,582	2				
Lipid				Stock		Mix				
DB	ID-L	Name	MW(g/mol)	g/L	mmol/L	Molar ratio	mg	μmol	μL of stock	
Avanti	850375	18:1 ($\Delta 9$ -Cis) PC	785,6	10	12,73	79,8	1,254	1,596	125,4	
Avanti	840035	18:1 PS	809,5	10	12,35	20	0,3238	0,4	32,38	
Custom		DiD	1052	0,83	0,789	0,2	0,0042	0,004	5,07	

Table text: The GUV composition was determined according to the table.

5. Measurements and data analysis for cell puncture and ANXA response

All images were analyzed using MatLab (The Mathworks, Inc., Natick, Massachusetts, United States), and the AuNP temperature profile (Figs. 1D and E) is based on Mie equation^{57, 58} and plotted using MatLab. Additionally, all confocal images were processed using the FIJI ImageJ distribution^{59, 60}.

To analyze the membrane injury, the region of interest, containing the punctured area, was first cropped using FIJI prior to analysis. An in-house Matlab workflow was then utilized to process each image, whereby the user manually marked the center of the ANXA ring and its outer perimeter. These markings were used to set the processing limits for the region of interest. The area was subsequently scanned radially within the set limits, and the fluorescence intensity was averaged over the full circle and stored for each radius step. The averaged intensities over the entire scanning range were then fitted to a one-dimensional Gaussian curve to identify the maxima (R_p) and full width at half maximum (FWHM) corresponding to R_{ext} and R_{int} , respectively, as depicted in Figure 3A. Finally, the size of the ANXA ring was calculated by determining the distance from the ring's center to R_{ext} .

To track the change in ANXA ring radius in the z-direction, the same Matlab analysis workflow as described in the previous section was applied to different confocal z-sections (Figs. 3C and E). The slope for each wound was then calculated based on the change in radii over the z-sections, as depicted in Figure 3F. Similarly, the evolution of the ANXA ring after thermoplasmonic rupture was tracked using the same Matlab analysis workflow over consecutive time points (see Figures 3D, G, and H).

6. Thermoplasmonics

Thermoplasmonics is a rapidly expanding field that merges the properties of optical light and plasmonic metal nanoparticles (NPs). The incoming light from the optical trap interacts with the metal NP and excites the conduction electrons within the NP. This induces a collective oscillation of electrons, known as plasmons (Fig. 1C). If the plasmons are in resonance with the electromagnetic field of the incoming light, the NP will experience localized surface plasmon resonance (LSPR), also referred to as plasmon resonance⁴⁸. This phenomenon leads to a significant increase in the absorption of light, which in turn generates heat through Joule heating caused by the friction between the electrons and the gold material. The heat is released into the surrounding environment, and an equilibrium temperature distribution is achieved within hundreds of nanoseconds⁴⁸. However, at temperatures exceeding ~200 °C, nanoscale bubbles may prevent thermal equilibrium and dramatically increase the local heating, leading to a small nanoscopic explosion^{25, 61, 62}. To achieve plasmon resonance in the NIR region of the spectrum, the shape, size, and composition of the NP can be adjusted to tune the plasmon resonance frequency to coincide with the wavelength of the laser. This maximizes the thermoplasmonic heating and makes the plasmonic NPs highly efficient light-to-heat converters^{48, 63, 64}.

The temperature distribution of an irradiated nanoparticle (NP) can be determined by solving the heat transfer equation⁶⁵. The temperature gradient is determined as a function of the distance, r , from the surface of the NP with radius R , as given by the following equation:

$$\Delta T(r) = \frac{VQ}{4\pi\kappa r}, r \geq R \quad (\text{Equation 1})$$

Where κ denotes the thermal conductivity of water (0.58 W/mK at ambient temperature), while Q represents the external heat source, which in this case is the NP. Q is a measure of the amount of heat generated per unit time and volume (V) within the NP. The majority of which is produced as Joule heating inside the NP⁴⁸, also known as thermoplasmonic heating.

Equation 1 can be expressed to relate the temperature increase to the absorption cross-section C_{abs} as follows⁶³:

$$\Delta T(r) = \frac{I C_{abs}}{4\pi\kappa r}, r \geq R \quad (\text{Equation 2})$$

Here, the temperature gradient $\Delta T(r)$ is a function of the distance, r , from the surface of the NP with radius R , relative to the ambient temperature. The thermal conductivity of water is represented by κ , and I denotes the laser intensity at the sample plane. Within tens of nanoseconds, the temperature distribution around the NP, generated by Equation 1, approaches a steady state, thus satisfying Laplace's equation^{16, 48}. The plasmonic heating of the NP is determined by the absorption cross-section, which in turn can be used to calculate the immediate heat production of the NP by multiplying C_{abs} with the known laser intensity, I ⁴⁸.

Mie theory uses a mathematical model to describe the scattering and absorption cross-sections of NPs⁵⁸. This theory allows for the calculation of the absorption cross section (C_{abs}) using

Mie-based calculations, from which the temperature profile of spherical NPs with a diameter greater than 20 nm can be determined⁴⁸. To predict the temperature profile, the in-house MatLab workflow based on Mie's equations for C_{abs} was used. The temperature profile in Figure 1E depicts Equation 2 as a function of distance to the particle center and reveals that the temperature gradient decreases by $\sim 40\%$ at a distance of R from the NP surface. This results in a significant, yet extremely confined, increase in temperature. Previous studies have shown that a focused NIR laser (1064 nm) can stably trap the NP, which provides a controlled approach for minimally invasive and highly localized membrane disruption^{25, 48-52}.

REPRESENTATIVE RESULTS:

In the present study, the thermoplasmonic method is used to investigate the annexin protein response to plasma membrane disruption. Protein recruitment and function are monitored by confocal imaging in both human embryonic kidney (HEK293T) cells and giant unilamellar vesicles (GUVs). To elaborate, Figure 2 illustrates the experimental conditions in which a focused NIR laser beam at 1064 nm is used to irradiate a single AuNP (Fig 2A), resulting in membrane injury and an influx of Ca^{2+} into the cell, activating the PMR machinery. Subsequently, annexins are rapidly recruited to the injury site, where they bind to the negatively charged phospholipids at the wound perimeter, forming a ring-like structure within seconds (Fig. 2B, i –iv). The model membrane experiments, using GUVs, demonstrated that membrane punctures were rapidly resealed in the absence of ANXA, as depicted in Figure 2C. However, in the presence of ANXA, a rapid accumulation of ANXA was observed at the injury site following membrane puncture (Fig. 2D). Notably, ANXA continued to roll the exposed edges, ultimately leading to the bursting of the GUV. This rolling mechanism is believed to arise from the ability of ANXA to induce curvature and bend lipid membranes²⁰.

[Figure 2]:

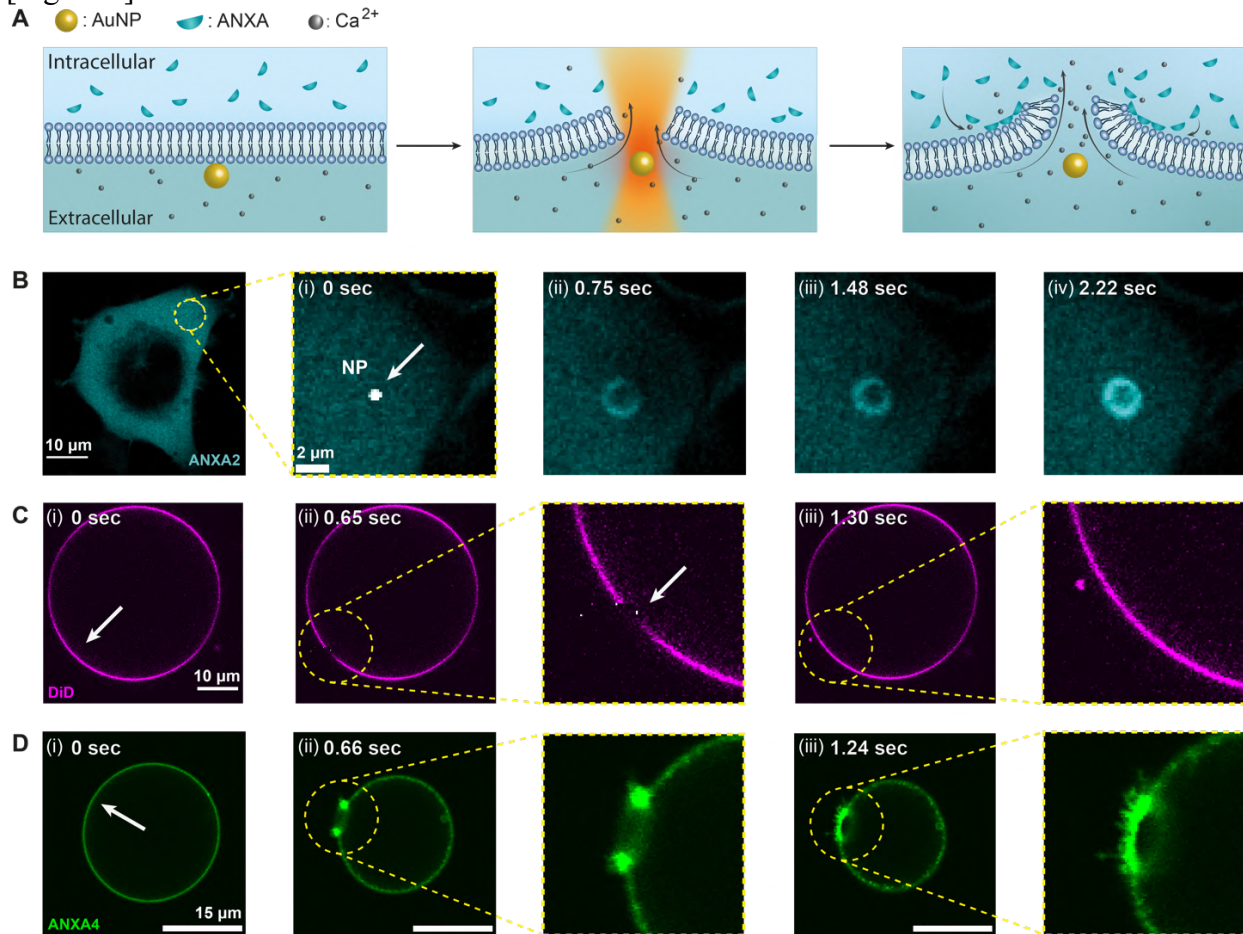


Figure text: Annexins (ANXAs) respond to thermoplasmonic-induced membrane disruption. Initially, (A) the plasma membrane acts as a barrier between the extracellular environment containing Ca^{2+} ions and the intracellular environment with encapsulated ANXAs. Upon irradiation with a near-infrared (NIR) laser, the gold nanoparticle generates substantial heat, causing the membrane to rupture and resulting in an influx of Ca^{2+} ions. Consequently, the plasma membrane repair (PMR) machinery is activated, which involves the recruitment of ANXAs to the site of injury, where they bind to negatively charged phospholipids. Confocal microscopy images of a cell containing ANXA2 (B) and a giant unilamellar vesicle (GUV) containing ANXA4 (D) demonstrate this process. Prior to the irradiation (i), the images show an intact cell, or GUV, with irradiation sites denoted by the white arrows. Upon nanoparticle irradiation (ii), (B) ANXAs are rapidly recruited to the injury site, forming a ring-like structure around the membrane wound (B ii-iv). Panel (C) shows a membrane-stained GUV without ANXA, which, upon puncture, reseals rapidly without observable membrane remodeling. On the other hand, panel (D) shows a GUV containing recombinant ANXA4, which is already bound to the membrane prior to irradiation (i) due to Ca^{2+} -leakage across the membrane. Upon puncture (ii), ANXA4 binds to the free edges, causing the GUV to collapse as the membrane is rolled away. Figures C and D are adapted, with permission, from Moreno *et al.*¹⁶.

The analysis of complete ANXA ring-like structures (Figs. 2B and S1) provides useful insights into the wound size and morphology. The radius of the ANXA ring structure can be determined

over time and space, as described in Section 5. Moreno *et al.*¹⁶ analyzed over 135 plasma membrane injuries in living cells, where the analysis of ANXA5 ring structures is depicted in Figure 3. The radius was determined by measuring the distance from the center of the ring to the external radius of the curve based on the full-width-half-maximum of the collapsed intensity profile (Fig. 3A). The findings illustrated a heterogeneous distribution of ANXA5 ring sizes (Fig. 3B), which remained constant over time (Figs. D, G, and H) and space (Figs. 3C, E, and F). These results suggest an accumulation of ANXA5 around the injury sites, indicative of an alternative ANXA5-mediated PMR strategy in living cells to the hypothesized funnel-like inward budding of the damaged membrane⁵.

[Figure 3]:

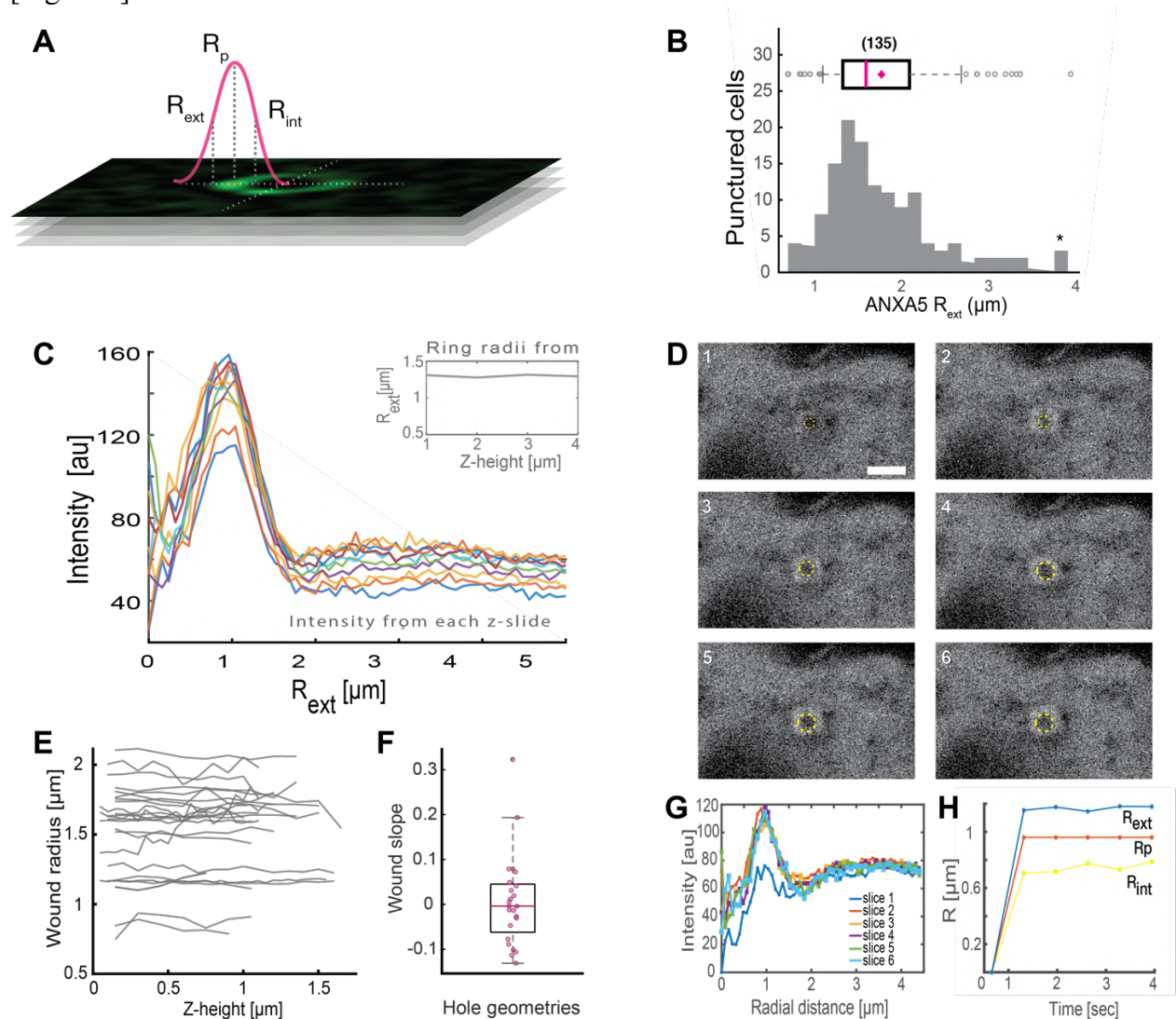


Figure text: The figure showcases the analysis of ANXA5 ring structures surrounding an injury site in living cells. (A) The schematic representation illustrates the analytical approach, which is based on the full-width-half maximum of the ANXA intensity line profile. (B) The histogram illustrates 135 measured ANXA5 ring radii. (C) Fluorescence intensity line profiles across an ANXA5-GFP ring for each z-section of the z-stack. (D) The confocal images illustrate the time evolution of a wound, where ANXA5-GFP accumulates at the wound perimeter immediately after

injury, followed by wound stabilization. The time frames, labeled 1-6, were captured at 0.66-second intervals per frame. (E) The radii of the wounds were determined as a function of wound depth based on the method presented in panel A. (F) The slope of the wound was analyzed as ANXA5 ring radii as a function of z-height based on the data extracted from panel E. (G) The fluorescence intensity line profiles were measured across the ANXA5-GFP ring from panel D, where each time interval 1-6 is denoted as slice 1-6. Finally, (H) the time evolution of the ANXA5-GFP ring radii is presented as a function of time calculated from the data in panel G. The figure is adapted with permission from Moreno *et al*¹⁶.

In comparison to the ring-like structures formed by disrupting the PM alone (Fig. S1), injuries in close proximity to the nucleus (Fig. S2A) may influence the evolution and geometry of the wound. Occasionally, only a fraction of the ANXA rings were evident (Figs. S2B and C), which can also be analyzed using the in-house MatLab analysis workflow (see Section 5), although additional data may be lost. Typically, ANXA ring formations observed in rounder cells (Fig. S2C) are located close to both the nucleus and the cell's periphery. As a consequence, a more elongated ring structure can be observed, which is suboptimal for the data analysis presented. Additionally, rounder cells appeared to be more susceptible to cell death following PM injury. Furthermore, when considering injuries resulting from the irradiation of AuNP aggregates, it is important to note that these injuries may be more severe and less controllable. This is due to the significant increase in thermoplasmonic heat, which can damage a large fraction of the cell. As a result, such injuries have not been incorporated into the ANXA5 ring analysis.

Moreover, the preliminary findings indicate that the disruption of the plasma membrane using thermoplasmonics results in elevated intracellular Ca^{2+} levels. This was observed even at low-intensity irradiation of single AuNPs, suggesting PM permeabilization³⁵, as depicted in Figure 4. The Ca^{2+} influx was observed in cells expressing a membrane-bound calcium probe, GCaMP6s-CAAX, which undergoes a conformational change upon Ca^{2+} influx and thus an increase in its intensity can be observed⁶⁶. The calcium intensity was quantified for the entire footprint of the cell over time. To eliminate background noise, the background Ca^{2+} level was subtracted prior to membrane disruption and post-membrane repair. The maximum intensity was determined by normalizing the mean Ca^{2+} intensity within the cell to one, resulting in an intensity curve exhibiting a rapid initial Ca^{2+} intensity increase followed by a slower decrease, as depicted in Figure 4B.

The cell reached a maximal calcium intensity at ~ 6.6 seconds, which is consistent with the findings of Klenow *et al.*⁶⁶, who suggested that the time of the calcium intensity peak ($t = t_c$) corresponds to the time required for wound closure. Nevertheless, while further investigations are required to establish the underlying mechanism of membrane repair and wound healing, the preliminary findings showed that this Ca^{2+} process was observed exclusively in the injured cell and not in the control cell. This confirms that the cell experienced Ca^{2+} influx upon thermoplasmonic membrane disruption, where the excess intracellular calcium is actively pumped out after successful PMR as the intracellular calcium level is no longer in competition with the Ca^{2+} influx, eventually achieving cell homeostasis⁶⁶.

[Figure 4]:

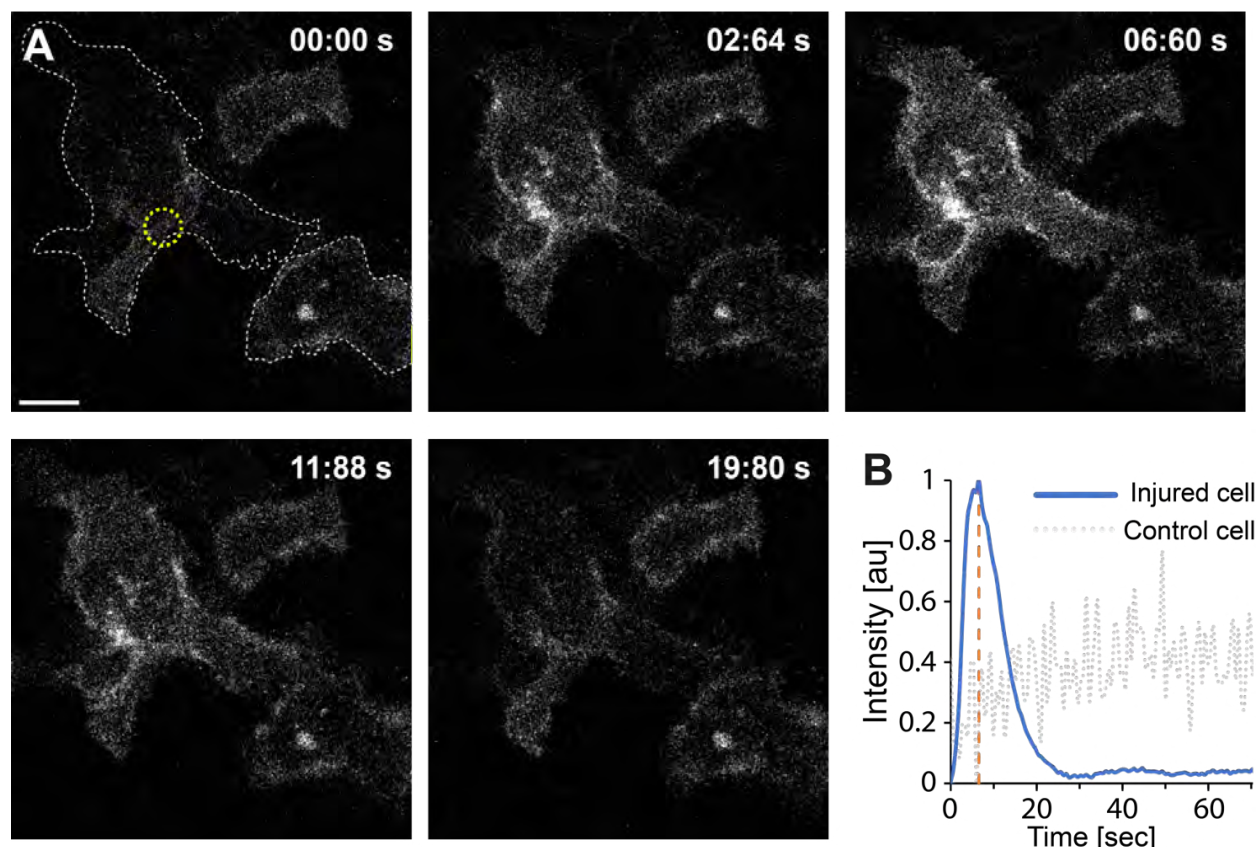


Figure text: A calcium influx was observed as the plasma membrane of a HEK293T cell was ruptured by thermoplasmonics. A series of confocal images show two cells (the cell of interest and a control cell) expressing the membrane-bound calcium probe, GCaMP6s-CAAX. The scale bar measures 10 μm . (A) Prior to irradiation, at 00:00 s, the footprint of the two cells is visualized by the gray dotted line, and the irradiation site is denoted by the yellow circle. Upon laser irradiation, a rapid influx of Ca^{2+} is observed, reaching a maximum intensity at ~ 6.6 seconds (B), denoted by the orange dashed line, a timepoint that is presumed to correspond to the time of wound closure⁶⁶. (B) The calcium intensity profile obtained from the GCaMP6s-CAAX probe in the injured cell (blue line) was compared to the Ca^{2+} intensity in a neighboring uninjured control cell (gray dotted line), showing a clear Ca^{2+} influx exclusively upon PM disruption.

DISCUSSION:

The study highlights the thermoplasmonic approach as a promising technique for exploring protein responses in living cells and model membranes following membrane disruption. This method not only provides extensive information on protein recruitment but also on the biophysical function of proteins involved in protein-membrane dynamics. Consequently, it facilitates the identification of molecular components responsible for surface repair and advances the understanding of the complex yet vital machinery of plasma membrane repair. Although various methods exist for inducing membrane disruption, such as mechanical, chemical, and optical techniques, these methods suffer from limitations, such as being non-specific to cells, generating multiple injuries to the cell membrane, or causing significant damage to the membrane and ablating internal cellular material along the laser path when using high-power pulsed lasers. While the integration of confocal microscopy and optical tweezers offers the most comprehensive information, alternative

imaging modalities could also be used. For instance, as the imaging of the plasmonic nanoparticle is achieved using reflection microscopy, a built-in imaging mode in Leica confocal microscopes, additional imaging techniques, such as darkfield microscopy^{67, 68}, other scattering methods like iSCAT^{69, 70}, or fluorescent labeling of the nanoparticle, could be employed for AuNP visualization, although this might limit the applicability of the method.

The presented method is capable of inducing nanoscopic holes in model membranes, enabling investigation of the synergy effects between different annexins. This is achieved by encapsulating differently labeled recombinant annexins, e.g., RFP and GFP, respectively, followed by thermoplasmonic puncture. This model system provides insight into how annexins interact with membranes in the vicinity of free edges, as demonstrated in Figure 2D. However, unlike in cells, the holes inflicted on GUVs continue to expand, followed by destabilization of the vesicle. The imaging of the hole evolution using confocal microscopy can be challenging due to the rapid expansion of the hole diameter, but can be accomplished by capturing several z-stacks over time. An alternative method would be to use a spinning disk confocal for faster imaging. Furthermore, the thermoplasmonic approach typically yields a limited number of optimal results per hour when applied to single cells or GUV experiments, usually two to three, at sample temperatures between 20 and 30 °C. To obtain the most accurate observation of protein-membrane dynamics, it is recommended to keep the cells in a hepes-containing buffer and replace the sample every hour. Alternatively, the experimental window could be extended by performing the experiments in a cell incubating chamber, i.e., at a constant temperature of 37 °C with 5% CO₂. Furthermore, combining this approach with other imaging techniques, such as stochastic optical reconstruction microscopy (STORM), could provide a deeper understanding of the biophysical function and interaction of key proteins involved in membrane repair on a single-molecule level. This could provide detailed information on the site of injury, including the wound geometry and location of annexin proteins, as well as identify other key players involved in repairing the membrane surface.

In order to achieve maximum effectiveness and precision in inducing membrane injury, it is imperative to verify the location of the laser focus prior to each experiment and ensure that the axial position of the laser focus coincides with the confocal focus. This alignment optimizes the intensity during AuNP imaging, which leads to a maximum local temperature increase and consequent membrane injury at lower laser power. This process is manually executed and therefore susceptible to variability in membrane rupture efficiency as the focus is manually translated to a position that coincides with the particle's location. In microscopes that lack a reflection mode, such as the Lumicks C-Trap, co-localization of the laser focus and particle can be challenging. In such cases, alternative imaging modes (e.g., bright field) can be employed, and a slow raster scan can be performed around the expected particle position. It should be noted that low laser power is likely to induce membrane permeabilization only, while high laser power can generate temperatures around the NP that exceed the boiling point of water, even if the glass surface has a cooling effect. It is estimated that the formation of nanobubbles surrounding the NPs occurs between 200 and 300°C^{25, 48}, where the explosive heat may result in either particle displacement from the laser focus or particle fragmentation. Notably, gold nanoshells do not tolerate high temperatures and will degrade under these conditions, as demonstrated by high-resolution microscopy⁵⁵.

This article provides a detailed protocol for using thermoplasmonics to perform highly localized

punctures in membranes, which is applicable to both cells and model membranes. To further reduce the extent of heating, smaller nanoparticles resonant with NIR light can be utilized, enabling intracellular punctures in endosomes, the endoplasmic reticulum, and the nuclear envelope. Such nanoparticles, including rods and nanomatryoshkas⁴⁸, can be used to investigate nuclear envelope repair by targeting endocytosed gold nanoparticles that are readily taken up at the cell surface and trafficked towards the nucleus⁷¹. Overall, this technique enables the identification and examination of key molecular components involved in PMR, elucidating their biophysical function and role while preserving the viability of the cells.

ACKNOWLEDGMENTS:

This work was financially supported by the Danish Council for Independent Research, Natural Sciences (DFR-4181-00196), by the Novo Nordisk Foundation Interdisciplinary Synergy Program 2018 (NNF18OC0034936), the Scientific Committee Danish Cancer Society (R90-A5847-14-S2), the Lundbeck Foundation (R218-2016-534) and a Lundbeck Foundation Center of Excellence (Biomembranes in Nanomedicine).

DISCLOSURES:

The authors have nothing to disclose.

REFERENCES

1. Bendix, P.M. *et al.* Interdisciplinary Synergy to Reveal Mechanisms of Annexin-Mediated Plasma Membrane Shaping and Repair. *Cells*. **9** (4), 1029, doi: 10.3390/cells9041029 (2020).
2. Gajic, O., Lee, J., Doerr, C.H., Berrios, J.C., Myers, J.L., Hubmayr, R.D. Ventilator-induced Cell Wounding and Repair in the Intact Lung. *American Journal of Respiratory and Critical Care Medicine*. **167**, 1057–1063, doi: 10.1164/rccm.200208-889oc (2003).
3. McNeil, P.L., Khakee, R. Disruptions of muscle fiber plasma membranes. Role in exercise-induced damage. *The American journal of pathology*. **140** (5), 1097–109 (1992).
4. Yu, Q.C., McNeil, P.L. Transient disruptions of aortic endothelial cell plasma membranes. *The American journal of pathology*. **141** (6), 1349–60 (1992).
5. Boye, T.L. *et al.* Annexin A4 and A6 induce membrane curvature and constriction during cell membrane repair. *Nature Communications*. **8**, doi: 10.1038/s41467-017-01743-6 (2017).
6. Bischofberger, M., Gonzalez, M.R., van der Goot, F.G. Membrane injury by pore-forming proteins. *Current Opinion in Cell Biology*. **21**, 589–595, doi: 10.1016/j.ceb.2009.04.003 (2009).
7. Tang, S.K.Y., Marshall, W.F. Self-Repairing Cells. *Science (New York, N.Y.)*. **356**, 1022–1025, doi: 10.1126/science.aam6496 (2017).
8. Abreu-Blanco, M.T., Verboon, J.M., Parkhurst, S.M. Single cell wound repair: Dealing with life's little traumas. *Bioarchitecture*. **1**, 114–121, doi: 10.4161/bioa.1.3.17091 (2011).
9. Sønders, S.L. *et al.* Annexin A7 is required for ESCRT III-mediated plasma membrane repair. *Scientific Reports*. **9**, doi: 10.1038/s41598-019-43143-4 (2019).
10. Andrews, N.W., Almeida, P.E., Corrotte, M. Damage control: cellular mechanisms of plasma membrane repair. *Trends in Cell Biology*. **24**, 734–742, doi:

- 10.1016/j.tcb.2014.07.008 (2014).
11. Idone, V., Tam, C., Goss, J.W., Toomre, D., Pypaert, M., Andrews, N.W. Repair of injured plasma membrane by rapid Ca²⁺-dependent endocytosis. *The Journal of Cell Biology*. **180**, 905–914, doi: 10.1083/jcb.200708010 (2008).
 12. Lauritzen, S.P., Boye, T.L., Nylandsted, J. Annexins are instrumental for efficient plasma membrane repair in cancer cells. *Seminars in Cell & Developmental Biology*. **45**, 32–38, doi: 10.1016/j.semcdb.2015.10.028 (2015).
 13. Häger, S.C., Nylandsted, J. Annexins: players of single cell wound healing and regeneration. *Communicative & Integrative Biology*. **12**, 162–165, doi: 10.1080/19420889.2019.1676139 (2019).
 14. Jaiswal, J.K. *et al.* S100A11 is required for efficient plasma membrane repair and survival of invasive cancer cells. *Nature Communications*. **5**, doi: 10.1038/ncomms4795 (2014).
 15. Draeger, A., Monastyrskaya, K., Babiychuk, E.B. Plasma membrane repair and cellular damage control: The annexin survival kit. *Biochemical Pharmacology*. **81**, 703–712, doi: 10.1016/j.bcp.2010.12.027 (2011).
 16. Moreno-Pescador, G.S. *et al.* Thermoplasmonic nano-rupture of cells reveals annexin V function in plasma membrane repair. *Nanoscale*. **14** (21), 7778–7787, doi: 10.1039/D1NR08274D (2022).
 17. Zhivotovsky, B., Orrenius, S. Calcium and cell death mechanisms: A perspective from the cell death community. *Cell Calcium*. **50**, 211–221, doi: 10.1016/j.ceca.2011.03.003 (2011).
 18. Gerke, V., Moss, S.E. Annexins: From Structure to Function. *Physiological Reviews*. **82**, 331–371, doi: 10.1152/physrev.00030.2001 (2002).
 19. Idone, V., Tam, C., Andrews, N.W. Two-way traffic on the road to plasma membrane repair. *Trends in Cell Biology*. **18**, 552–559, doi: 10.1016/j.tcb.2008.09.001 (2008).
 20. Boye, T.L. *et al.* Annexins induce curvature on free-edge membranes displaying distinct morphologies. *Scientific Reports*. **8**, doi: 10.1038/s41598-018-28481-z (2018).
 21. Bouter, A. *et al.* Annexin-A5 assembled into two-dimensional arrays promotes cell membrane repair. *Nature Communications*. **2**, doi: 10.1038/ncomms1270 (2011).
 22. Boye, T.L., Nylandsted, J. Annexins in plasma membrane repair. *Biological Chemistry*. **397**, doi: 10.1515/hsz-2016-0171 (2016).
 23. Weinberger, A. *et al.* Gel-Assisted Formation of Giant Unilamellar Vesicles. *Biophysical Journal*. **105**, 154–164, doi: 10.1016/j.bpj.2013.05.024 (2013).
 24. Numata, T., Tatsuta, H., Morita, Y., Otani, Y., Umeda, N. Localized thermal processing with a laser-trapped and heated metal nanoparticle. *IEEJ Transactions on Electrical and Electronic Engineering*. **2**, 398–401, doi: 10.1002/tee.20161 (2007).
 25. Bendix, P.M., Reihani, S.N.S., Oddershede, L.B. Direct Measurements of Heating by Electromagnetically Trapped Gold Nanoparticles on Supported Lipid Bilayers. *ACS Nano*. **4**, 2256–2262, doi: 10.1021/nn901751w (2010).
 26. Kyrsting, A., Bendix, P.M., Stamou, D.G., Oddershede, L.B. Heat Profiling of Three-Dimensionally Optically Trapped Gold Nanoparticles using Vesicle Cargo Release. *Nano Letters*. **11**, 888–892, doi: 10.1021/nl104280c (2011).
 27. Andersen, T., Kyrsting, A., Bendix, P.M. Local and transient permeation events are associated with local melting of giant liposomes. *Soft Matter*. **10** (24), 4268–4274, doi: 10.1039/C4SM00410H (2014).

28. Bahadori, A., Oddershede, L.B., Bendix, P.M. Hot-nanoparticle-mediated fusion of selected cells. *Nano Research*. **10**, 2034–2045, doi: 10.1007/s12274-016-1392-3 (2017).
29. Rørvig-Lund, A., Bahadori, A., Semsey, S., Bendix, P.M., Oddershede, L.B. Vesicle Fusion Triggered by Optically Heated Gold Nanoparticles. *Nano Letters*. **15**, 4183–4188, doi: 10.1021/acs.nanolett.5b01366 (2015).
30. Moreno-Pescador, G., Arastoo, M.R., Ruhoff, V.T., Chiantia, S., Daniels, R., Bendix, P.M. Thermoplasmonic Vesicle Fusion Reveals Membrane Phase Segregation of Influenza Spike Proteins. *Nano Letters*. doi: 10.1021/acs.nanolett.3c00371 (2023).
31. Bahadori, A., Lund, A.R., Semsey, S., Oddershede, L.B., Bendix, P.M. Controlled cellular fusion using optically trapped plasmonic nano-heaters. *SPIE Proceedings*. doi: 10.1117/12.2237848 (2016).
32. Bahadori, A., Moreno-Pescador, G., Oddershede, L.B., Bendix, P.M. Remotely controlled fusion of selected vesicles and living cells: a key issue review. *Reports on Progress in Physics*. **81**, 32602, doi: 10.1088/1361-6633/aa9966 (2018).
33. Moreno-Pescador, G., Arastoo, M.R., Chiantia, S., Daniels, R., Bendix, P.M. Thermoplasmonic induced vesicle fusion for investigating membrane protein phase affinity. doi: 10.1101/2022.09.19.508467.
34. Pescador, G.S.M. *et al.* Investigating Plasma-Membrane Repair Employing Thermoplasmonics. *Biophysical Journal*. **120** (3), 45a, doi: 10.1016/j.bpj.2020.11.519 (2021).
35. Moreno-Pescador, G.S., Qoqaj, I., Thusgaard Ruhoff, V., Iversen, J., Nylandsted, J., Bendix, P.M. Effect of local thermoplasmonic heating on biological membranes. *Optical Trapping and Optical Micromanipulation XVI*. doi: 10.1117/12.2530154 (2019).
36. Bement, W.M., Mandato, C.A., Kirsch, M.N. Wound-induced assembly and closure of an actomyosin purse string in *Xenopus* oocytes. *Current Biology*. **9**, 579–587, doi: 10.1016/s0960-9822(99)80261-9 (1999).
37. Weisleder, N. *et al.* Recombinant MG53 Protein Modulates Therapeutic Cell Membrane Repair in Treatment of Muscular Dystrophy. *Science Translational Medicine*. **4**, 139ra85-139ra85, doi: 10.1126/scitranslmed.3003921 (2012).
38. Sudji, I.R., Subburaj, Y., Frenkel, N., García-Sáez, A.J., Wink, M. Membrane disintegration caused by the steroid saponin digitonin is related to the presence of cholesterol. *Molecules*. **20** (11), doi: 10.3390/molecules201119682 (2015).
39. Babiychuk, E.B., Monastyrskaya, K., Potez, S., Draeger, A. Intracellular Ca²⁺ operates a switch between repair and lysis of streptolysin O-perforated cells. *Cell Death & Differentiation*. **16**, 1126–1134, doi: 10.1038/cdd.2009.30 (2009).
40. Nygård Skalman, L., Holst, M.R., Larsson, E., Lundmark, R. Plasma membrane damage caused by listeriolysin O is not repaired through endocytosis of the membrane pore. *Biology Open*. **7**, bio035287, doi: 10.1242/bio.035287 (2018).
41. Swaggart, K.A. *et al.* Annexin A6 modifies muscular dystrophy by mediating sarcolemmal repair. *Proceedings of the National Academy of Sciences*. **111**, 6004–6009, doi: 10.1073/pnas.1324242111 (2014).
42. Yehekely-Hayon, D., Minai, L., Golan, L., Dann, E.J., Yelin, D. Optically Induced Cell Fusion Using Bispecific Nanoparticles. *Small*. **9**, 3771–3777, doi: 10.1002/smll.201300696 (2013).
43. Minai, L., Yehekely-Hayon, D., Golan, L., Bisker, G., Dann, E.J., Yelin, D. Optical

- Nanomanipulations of Malignant Cells: Controlled Cell Damage and Fusion. *Small*. **8**, 1732–1739, doi: 10.1002/sml.201102304 (2012).
44. Lukianova-Hleb, E. *et al.* Plasmonic Nanobubbles as Transient Vapor Nanobubbles Generated around Plasmonic Nanoparticles. *ACS Nano*. **4**, 2109–2123, doi: 10.1021/nn1000222 (2010).
 45. Vogel, A., Noack, J., Hüttman, G., Paltauf, G. Mechanisms of femtosecond laser nanosurgery of cells and tissues. *Applied Physics B*. **81**, 1015–1047, doi: 10.1007/s00340-005-2036-6 (2005).
 46. Baffou, G., Polleux, J., Rigneault, H., Monneret, S. Super-heating and micro-bubble generation around plasmonic nanoparticles under cw illumination. *Journal of Physical Chemistry C*. **118** (9), doi: 10.1021/jp411519k (2014).
 47. Sasikumar, K., Liang, Z., Cahill, D.G., Keblinski, P. Curvature induced phase stability of an intensely heated liquid. *Journal of Chemical Physics*. **140** (23), doi: 10.1063/1.4883516 (2014).
 48. Jauffred, L., Samadi, A., Klingberg, H., Bendix, P.M., Oddershede, L.B. Plasmonic Heating of Nanostructures. *Chemical Reviews*. **119**, 8087–8130, doi: 10.1021/acs.chemrev.8b00738 (2019).
 49. Neuman, K.C., Nagy, A. Single-molecule force spectroscopy: optical tweezers, magnetic tweezers and atomic force microscopy. *Nature Methods*. **5** (6), 491–505, doi: 10.1038/nmeth.1218 (2008).
 50. Bendix, P.M., Jauffred, L., Norregaard, K., Oddershede, L.B. Optical Trapping of Nanoparticles and Quantum Dots. *IEEE Journal of Selected Topics in Quantum Electronics*. **20**, 15–26, doi: 10.1109/jstqe.2013.2287094 (2014).
 51. Samadi, A., Bendix, P.M., Oddershede, L.B. Optical manipulation of individual strongly absorbing platinum nanoparticles. *Nanoscale*. **9**, 18449–18455, doi: 10.1039/c7nr07374g (2017).
 52. Jørgensen, J.T., Norregaard, K., Tian, P., Bendix, P.M., Kjaer, A., Oddershede, L.B. Single Particle and PET-based Platform for Identifying Optimal Plasmonic Nano-Heaters for Photothermal Cancer Therapy. *Scientific Reports*. **6**, 30076, doi: 10.1038/srep30076 (2016).
 53. Niederauer, C., Seynen, M., Zomerdijk, J., Kamp, M., Ganzinger, K.A. The K2: Open-source simultaneous triple-color TIRF microscope for live-cell and single-molecule imaging. *HardwareX*. **13**, doi: 10.1016/j.ohx.2023.e00404 (2023).
 54. Richardson, A.C., Reihani, N., Oddershede, L.B. Combining confocal microscopy with precise force-scope optical tweezers. *SPIE Proceedings*. doi: 10.1117/12.680347 (2006).
 55. Samadi, A., Klingberg, H., Jauffred, L., Kjær, A., Bendix, P.M., Oddershede, L.B. Platinum nanoparticles: a non-toxic, effective and thermally stable alternative plasmonic material for cancer therapy and bioengineering. *Nanoscale*. **10**, 9097–9107, doi: 10.1039/C8NR02275E (2018).
 56. ThermoFisher Scientific Attofluor Cell Chamber, for microscopy. <https://www.thermofisher.com/order/catalog/product/A7816>.
 57. Kreibig, U., Vollmer, M. Theoretical Considerations. 13–201, doi: 10.1007/978-3-662-09109-8_2 (1995).
 58. Mie, G. Beiträge zur Optik trüber Medien, speziell kolloidaler Metallösungen. *Annalen der*

- Physik.* **330**, 377–445, doi: 10.1002/andp.19083300302 (1908).
59. Rueden, C.T. *et al.* ImageJ2: ImageJ for the next generation of scientific image data. *BMC Bioinformatics.* **18** (1), doi: 10.1186/s12859-017-1934-z (2017).
 60. Schindelin, J. *et al.* Fiji: An open-source platform for biological-image analysis. *Nature Methods.* **9** (7), doi: 10.1038/nmeth.2019 (2012).
 61. Baffou, G., Polleux, J., Rigneault, H., Monneret, S. Super-heating and micro-bubble generation around plasmonic nanoparticles under cw illumination. *Journal of Physical Chemistry C.* **118** (9), doi: 10.1021/jp411519k (2014).
 62. Sasikumar, K., Liang, Z., Cahill, D.G., Keblinski, P. Curvature induced phase stability of an intensely heated liquid. *Journal of Chemical Physics.* **140** (23), doi: 10.1063/1.4883516 (2014).
 63. Goldenberg, H., Tranter, C.J. Heat flow in an infinite medium heated by a sphere. *British Journal of Applied Physics.* **3**, 296–298, doi: 10.1088/0508-3443/3/9/307 (1952).
 64. Eustis, S., El-Sayed, M.A. Why gold nanoparticles are more precious than pretty gold: Noble metal surface plasmon resonance and its enhancement of the radiative and nonradiative properties of nanocrystals of different shapes. *Chem. Soc. Rev.* **35**, 209–217, doi: 10.1039/b514191e (2006).
 65. Landau, L.D., Lifshitz, E.M. *Fluid Mechanics: Landau and Lifshitz: Course of Theoretical Physics, Volume 6.* **6**. Elsevier. (2013).
 66. Klenow, M.B., Heitmann, A.S.B., Nylandsted, J., Simonsen, A.C. Timescale of hole closure during plasma membrane repair estimated by calcium imaging and numerical modeling. *Scientific Reports.* **11** (1), doi: 10.1038/s41598-021-82926-6 (2021).
 67. Li, T., Wu, X., Liu, F., Li, N. Analytical methods based on the light-scattering of plasmonic nanoparticles at the single particle level with dark-field microscopy imaging. *Analyst.* **142** (2), doi: 10.1039/c6an02384c (2017).
 68. Gibbs-Flournoy, E.A., Bromberg, P.A., Hofer, T.P.J., Samet, J.M., Zucker, R.M. Darkfield-Confocal Microscopy detection of nanoscale particle internalization by human lung cells. *Particle and Fibre Toxicology.* **8**, doi: 10.1186/1743-8977-8-2 (2011).
 69. Taylor, R.W., Sandoghdar, V. Interferometric Scattering Microscopy: Seeing Single Nanoparticles and Molecules via Rayleigh Scattering. *Nano Letters.* **19** (8), doi: 10.1021/acs.nanolett.9b01822 (2019).
 70. Wu, Y., Ali, M.R.K., Chen, K., Fang, N., El-Sayed, M.A. Gold nanoparticles in biological optical imaging. *Nano Today.* **24**, doi: 10.1016/j.nantod.2018.12.006 (2019).
 71. Klingberg, H., Oddershede, L.B., Loeschner, K., Larsen, E.H., Loft, S., Møller, P. Uptake of gold nanoparticles in primary human endothelial cells. *Toxicology Research.* **4** (3), doi: 10.1039/c4tx00061g (2015).

SUPPLEMENTARY FIGURES

TITLE:

A thermoplasmonic approach for the investigation of plasma membrane repair in living cells and model membranes

AUTHORS & AFFILIATIONS:

Helena Maria D. Danielsen¹, Mohammad Reza Arastoo², Guillermo Moreno-Pescador³, and Poul Martin Bendix⁴

^{1,2,4} The Niels Bohr Institute, University of Copenhagen, 2100 Copenhagen, Denmark

³Plant and Environmental Sciences, University of Copenhagen, 1871 Frederiksberg, Denmark

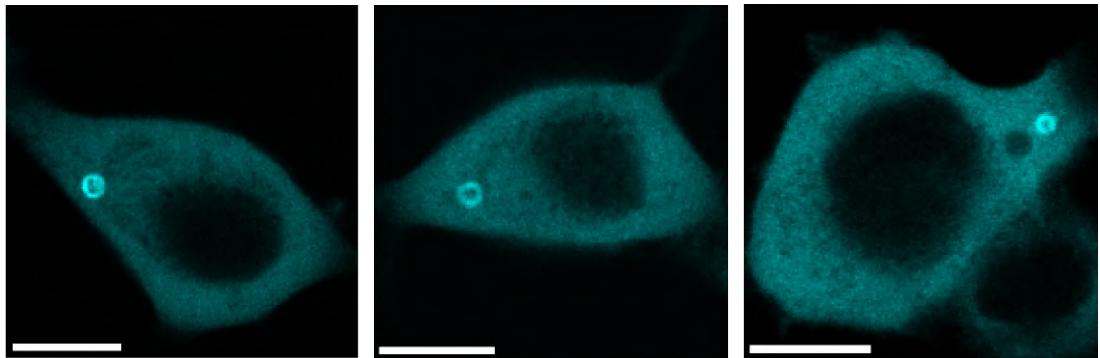


Figure S1:

Figure text: Confocal images of three individual HEK293T cells transfected with ANXA2-GFP after puncture. All cells show complete ANXA2 ring-like structures surrounding the injury site at the cell periphery. The scale bars measure 10 μ m.

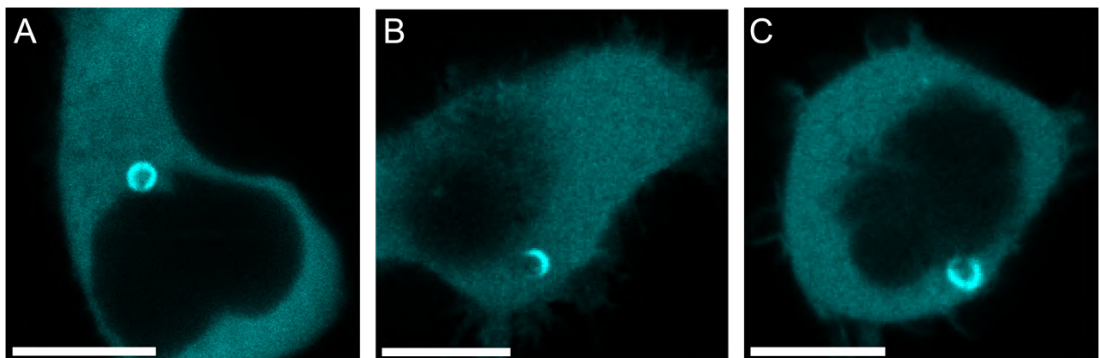


Figure S2:

Figure text: Confocal images of three individual HEK293T cells transfected with ANXA2-GFP after puncture. (A) A completely formed ANXA2 ring-like structure is observed near the nucleus. (B) Partially visualized ANXA2 ring formation. (C) An ANXA2 ring structure in close proximity to both the nucleus and the cell's periphery. The scale bars measure 10 μ m.